The decay of MHD turbulence and the primordial origin of magnetic fields in cosmic voids

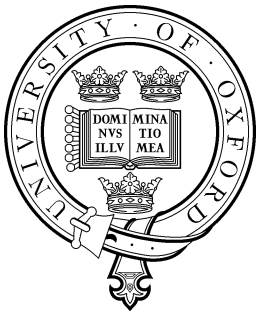

David N. Hosking
Merton College
University of Oxford

A thesis submitted for the degree of
Doctor of Philosophy in Astrophysics

Trinity 2022

The decay of MHD turbulence and the primordial origin of magnetic fields in cosmic voids

David N. Hosking

Merton College, University of Oxford

Submitted for the degree of Doctor of Philosophy in Astrophysics

Trinity 2022

The central result of this thesis is the solution of a decades-old problem in magnetohydrodynamic (MHD) turbulence theory: in the absence of energy injection, how do chaotic magnetic fields decay with time? We obtain novel predictions for the evolution of the magnetic energy and correlation scale by proposing that the field decays on reconnection timescales while respecting certain integral invariants that represent topological constraints. As is well known, the magnetic helicity is such an invariant for initially helical field configurations (Taylor, 1974), but does not constrain non-helical decay, where the volume-averaged magnetic-helicity density vanishes. For such a decay, we propose a new integral invariant — the "Saffman helicity invariant" — which is analogous to the Loitsyansky and Saffman invariants of hydrodynamic turbulence (Loitsyansky, 1939; Saffman, 1967), and that expresses the conservation of the random (scaling as volume$^{1/2}$) magnetic helicity contained in any sufficiently large volume. We verify that the Saffman helicity invariant is indeed well-conserved in our numerical simulations. We formulate a general principle of decay of turbulent systems subject to conservation of Saffman-like invariants, and propose how it may be applied to magnetohydrodynamic (MHD) turbulence with a strong mean magnetic field and to isotropic MHD turbulence with initial equipartition between the magnetic and kinetic energies.

We apply our theory of MHD decay to the evolution of primordial magnetic fields in the early Universe. This has become a popular problem in recent years due to the possibility that the weak magnetic field hosted by the intergalactic medium (IGM) in voids could be a relic from the early Universe [see Durrer & Neronov (2013); Subramanian (2016); Vachaspati (2021) and references therein]. If so, accurate measurement of

void fields combined with a theory of turbulent decay could be used to constrain cosmological models of the early Universe. Previous models of MHD decay have predicted that the present-day strength of fields generated at the electroweak phase transition (EWPT) should be too low to explain the observed scattering by void fields of γ-rays from TeV blazars (Neronov & Vovk, 2010; Wagstaff & Banerjee, 2016; Taylor *et al.*, 2011). However, our new theory indicates that the accepted models greatly underpredict the present-day strength of relic fields. Our new estimates restore the consistency of the EWPT-relic hypothesis with observational constraints; moreover, we find that efficient magnetogenesis at the EWPT could produce relics with the strength that is believed sufficient to resolve the Hubble tension (Jedamzik & Pogosian, 2020; Galli *et al.*, 2022) and explain galaxy-cluster magnetic fields without requiring dynamo amplification after structure formation (Banerjee & Jedamzik, 2003).

Further to this thesis' core narrative on decaying MHD turbulence, we address two additional problems that are also related to the dynamics of statistically isotropic, homogeneous turbulence. The first is the role of the Saffman invariant (and its generalisations) in constraining the dynamics of *forced*, rather than decaying, turbulence. We show that the physical interpretation of the Saffman integral as a measure of the strength of local momentum fluctuations leads to a natural physical picture of the "large-scale thermalisation" phenomenon reported in recent numerical studies (Dallas *et al.*, 2015; Cameron *et al.*, 2017; Alexakis & Biferale, 2018; Alexakis & Brachet, 2019). The second is the dynamical effect that statistically isotropic "tangled" magnetic fields have on their host medium. We derive a mean-field theory of magnetoelasticity that elucidates the important role of "intermittency" in the magnetic field, and present (to the best of our knowledge) the first simulations of "magnetoelastic waves", showing their evolution to be in good agreement with the predictions of our mean-field theory.

Acknowledgements

I am indebted to my supervisor, Alex Schekochihin, for his support and encouragement. He has shown great confidence in me, permitting me a lot of freedom to pursue the research questions that I thought were most interesting. Nonetheless, he has always been on hand to provide encouragement and nudges towards fruitful new approaches and topics. Our conversations have been thought-provoking, confidence-inspiring and rib-tickling; I consider him a good friend as well as a mentor.

I am grateful to Steven Balbus and Lorenzo Sironi for their supervision — I have learnt much about plasma astrophysics from them both. It is a pleasure also to acknowledge the inspiring and helpful conversations I have had with Santiago Benavides, Ben Chandran, Peter Davidson, Nuno Loureiro, John Magorrian, John Miller, François Rincon, Dmitry Uzdensky, and Muni Zhou about the work contained in this thesis. I thank Geoffroy Lesur for providing me with an up-to-date version of the Snoopy code.

I am indebted to a number of mentors that have shaped the course of my education. Of particular importance were Alan Barr, James Binney and Simon Hooker, who, together with Alex, formed an inspirational team of tutors during my time as an undergraduate at Merton College, Oxford. I am grateful to a number of school teachers who had an immeasurable influence on my interest in physics and mathematics: prominent among these were James Chew, Justine Hart and Matt Porter at Helston Community College. Most of all, I am grateful to David Finney, former headteacher of Trannack Primary School; it is to him that I owe my interest in solving maths puzzles.

My fiancé Amelia has been a source of unwavering support and love over the past few years — I am hugely grateful to her for keeping me sane and happy

as I worked to complete my doctorate (even in spite of a global pandemic). Finally, I thank my family — Mum for her encouragement, affirmation and support in times of crisis (GCSE statistics report!), Dad for his love and belief in me, and Jim for all the hilarity (even when we were working days). This thesis is dedicated to them.

Contents

List of Figures

Chapter 1

Introduction

1.1 Kolmogorov's theory of decaying turbulence

The nature of the decay of magnetohydrodynamic (MHD) turbulence is an important outstanding problem in fluid dynamics, with far-reaching consequences in astrophysics, from the evolution of primordial magnetic fields in cosmology (Banerjee & Jedamzik, 2004; Durrer & Neronov, 2013; Subramanian, 2016) to the dynamics of the solar wind (Chen *et al.*, 2011). Naturally, the subject of decaying turbulence is one with a long history. In the hydrodynamic case, the basic problem of determining the exponent of the energy-decay power law was solved by Kolmogorov, in the third of his seminal 1941 papers on turbulence (Kolmogorov, 1941*a*). Kolmogorov's approach can be summarised as follows: (*i*) identify an ideal invariant that is better conserved than the kinetic energy, then (*ii*) posit a decay of the kinetic energy, occurring on the dynamical timescale, that conserves the invariant. In the case of hydrodynamic turbulence, Kolmogorov identified the Loitsyansky integral (Loitsyansky, 1939),

$$I_{\boldsymbol{L}} = -\int \mathrm{d}^3\boldsymbol{r}\, r^2 \langle \boldsymbol{u}(\boldsymbol{x}) \cdot \boldsymbol{u}(\boldsymbol{x}+\boldsymbol{r}) \rangle, \tag{1.1}$$

as the relevant invariant. Physically, the invariance of $I_{\boldsymbol{L}}$ is a consequence of conservation of angular momentum $\boldsymbol{L} = \int \mathrm{d}^3\boldsymbol{r}\, \boldsymbol{r} \times \boldsymbol{u}$ (Landau & Lifshitz, 1959; Davidson, 2013).

Equation (1.1) implies the scaling $U^2 L^5 \sim \text{const}$, where L is the correlation scale of the turbulence, and U is the typical velocity at that scale. Together with the

identification of the dynamical timescale as $\tau \sim L/U$, this is enough to fix the decay rate of the kinetic energy $E = U^2/2$, as

$$\frac{\mathrm{d}E}{\mathrm{d}t} \sim -\frac{E}{\tau} \sim -\frac{E^{3/2}}{L} \propto -E^{17/10}, \tag{1.2}$$

which results in Kolmogorov's decay laws

$$E \propto t^{-10/7}, \quad L \propto t^{2/7}. \tag{1.3}$$

These laws describe, and have been confirmed to good precision numerically for (Ishida *et al.*, 2006; Davidson, 2013), hydrodynamic turbulence where correlations in the velocity field decay rapidly with distance [called 'Batchelor turbulence', after Batchelor & Proudman (1956)]. If they do not, then the Saffman integral (Saffman, 1967)

$$I_{\boldsymbol{P}} = \int \mathrm{d}^3\boldsymbol{r} \langle \boldsymbol{u}(\boldsymbol{x}) \cdot \boldsymbol{u}(\boldsymbol{x}+\boldsymbol{r}) \rangle, \tag{1.4}$$

may control the decay instead. $I_{\boldsymbol{P}}$ is finite for, and conserved by, hydrodynamic turbulence initialised with strong long-range spatial correlations, corresponding to a kinetic-energy spectrum $\propto k^2$ at the largest scales.[1] In this case $U^2L^3 \sim$ const and Kolmogorov's argument yields the decay laws

$$E \propto t^{-6/5}, \quad L \propto t^{2/5}. \tag{1.5}$$

Such turbulence is known as 'Saffman turbulence' (Davidson, 2013). Physically, the conservation of $I_{\boldsymbol{P}}$ is related to the conservation of linear momentum, $\boldsymbol{P} \equiv \int \mathrm{d}^3\boldsymbol{x}\, \boldsymbol{u}$, much as the conservation of the Loitsyansky integral is related to angular-momentum conservation. Note, however, that $\langle \boldsymbol{u} \rangle = \langle \boldsymbol{r} \times \boldsymbol{u} \rangle = 0$: the Loitsyansky and Saffman integrals encode conservation of *fluctuations* in these quantities, in a sense to be made precise later.

[1] We shall return to the specific conditions for the applicability of each integral and their relationships to the energy spectrum in Chapter 2, and discuss these topics in depth in Chapter 4, where we consider the evolution of long-range correlations in hydrodynamic turbulence.

1.2 Challenges for a theory of decaying magnetohydrodynamic turbulence

In Chapter 2 of this thesis, we show how Kolmogorov's philosophy can be adapted to MHD turbulence. Historically, two problems have hindered such attempts. First, there appear to exist a number of different regimes, depending on properties of the initial conditions (Stribling & Matthaeus, 1990, 1991; Ting *et al.*, 1986; Wan *et al.*, 2012). Restricting attention (for the moment) to the magnetically dominated case, where initial magnetic energy is much greater than kinetic, there are two canonical possibilities. First, there are helical field configurations, where the volume-averaged magnetic-helicity density, $\langle h \rangle = \langle \boldsymbol{A} \cdot \boldsymbol{B} \rangle$, is non-zero. Then, conservation of $\langle h \rangle$ [a phenomenon sometimes referred to as 'selective decay' (Taylor, 1974; Montgomery *et al.*, 1978)] provides a scaling that can be used to constrain the decay laws, $B^2 L \sim \text{const}$ (Hatori, 1984; Biskamp & Müller, 1999; Son, 1999), where B is the typical size of the magnetic field at the correlation scale L. However, magnetic helicity is not sign-definite, so there also exist non-helical field configurations, for which $\langle h \rangle \ll B^2 L$. For such fields, the conservation of $\langle h \rangle$ does not impose a constraint. We will show that the decay of these fields is still controlled by helicity conservation in a manner formally analogous to the control of the decay of hydrodynamic turbulence by angular- and linear-momentum conservation — via an invariant that we shall call the "Saffman helicity invariant",

$$I_H = \int \mathrm{d}^3 \boldsymbol{r} \langle h(\boldsymbol{x}) h(\boldsymbol{x} + \boldsymbol{r}) \rangle, \tag{1.6}$$

for the obvious analogy to (1.4). Indeed, we shall argue that I_H, $I_{\boldsymbol{L}}$ and $I_{\boldsymbol{P}}$ are members of a family of "Saffman-like" integral invariants that can be used to impose the conservation of sign-indefinite quantities as constraints on general forms of decaying turbulence.

Second, since, besides velocity, MHD has an additional field, $\boldsymbol{B}$, there is no longer a dimensional inevitability in the identification of the decay timescale, as there was in hydrodynamics. Previous treatments (Hatori, 1984; Biskamp & Welter, 1989; Biskamp & Müller, 1999; Son, 1999) have assumed the Alfvénic scaling $U \sim B$ in order to determine the ideal timescale uniquely, though this is not well reproduced in numerics,

where $B \gg U$ appears to be maintained if it was true initially, and, furthermore, for helical magnetic fields, a faster decay of the kinetic energy than the magnetic energy is often observed (Biskamp & Müller, 1999; Müller & Biskamp, 2000; Christensson *et al.*, 2001; Banerjee & Jedamzik, 2004; Frick & Stepanov, 2010; Berera & Linkmann, 2014; Brandenburg & Kahniashvili, 2017).

1.3 The role of magnetic reconnection

In fact, it is intuitively clear that relaxation on ideal timescales may not be possible for a strong initial magnetic field, because of the topological constraints imposed by magnetic-flux freezing. As was hypothesised by J.B. Taylor, magnetic fields with non-trivial topologies relax via the reconnection of magnetic field lines (Taylor, 1974, 1986), which transfers magnetic energy to larger scales. Reconnection, therefore, provides a physical explanation for the inverse transfer of magnetic energy observed in both helical and non-helical decaying MHD turbulence (Biskamp & Bremer, 1994; Müller & Biskamp, 2000; Müller *et al.*, 2012; Zrake, 2014; Brandenburg *et al.*, 2015; Reppin & Banerjee, 2017; Park, 2017; Zhou *et al.*, 2020; Bhat *et al.*, 2021). However, unless the values of the dissipation coefficients are sufficiently small for reconnection to occur in the plasmoid-dominated (Uzdensky *et al.*, 2010) or stochastic (Lazarian *et al.*, 2020) regime, magnetic reconnection occurs in the so-called 'Sweet-Parker' regime (Sweet, 1958; Parker, 1957), and is *slow* — its rate is proportional to a negative fractional power of the Lundquist number, $S = BL/\eta$, where η is the fluid resistivity. It should therefore be expected that the decay will proceed on the Sweet-Parker reconnection timescale, not the ideal one. The critical Lundquist number at which magnetic reconnection becomes fast (i.e., independent of S) is very large, $\sim 10^4$ (Uzdensky *et al.*, 2010), much larger than the typical Reynolds numbers at which (1.3) becomes a good description of the decay of hydrodynamic turbulence ($\mathrm{Re} \simeq 10^2$, see Ishida *et al.* 2006). The requirement of such a large Lundquist number (corresponding to very thin current sheets), together with the large scale separation between the box size and the energy-containing scale needed to eliminate finite-box-size effects, mean that direct numerical simulations aiming to measure decay laws will generally be in the slow-reconnection

regime[2]. In Zhou *et al.* (2019), it was demonstrated that two-dimensional MHD turbulence indeed decays on the Sweet-Parker timescale, and similar evidence has been presented for three-dimensional, non-helical turbulence too (Bhat *et al.*, 2021), though it was interpreted as arising from the two-dimensional decay mechanism put forward by Zhou *et al.* (2019). One of the main goals of Chapter 2 will be to verify the reconnection-controlled nature of the three-dimensional decay in both the helical and non-helical cases, and to establish the corresponding decay laws for both energies.

Sweet-Parker reconnection is defined by the conditions of (*i*) efficient conversion of magnetic energy to kinetic energy of reconnection outflows, and (*ii*) a balance between the inductive term, $\nabla \times (\boldsymbol{u} \times \boldsymbol{B})$, and the resistive dissipation term in the MHD induction equation, so that reconnection occurs in a time-invariant manner. This last requirement means that reconnection-controlled decaying turbulence in the Sweet-Parker regime is sensitive to the precise form of the dissipation term. Importantly, this means that different decay power laws are expected in numerical simulations depending on whether Laplacian dissipation, $\propto \eta \nabla^2 \boldsymbol{B} \equiv \eta_2 \nabla^2 \boldsymbol{B}$, or hyper-dissipation, $\propto \eta_n \nabla^n \boldsymbol{B}$, is employed. This fact has not been widely appreciated, and can be used to test whether reconnection indeed governs the decay timescale: simulations at moderately large (but not so large so as to be in the 'fast' reconnection regime) Lundquist numbers should exhibit different decay power laws depending on the order of hyper-dissipation, n. Such simulations turn out to be in excellent agreement with these expectations, as we confirm in Chapter 2.

1.4 Magnetic fields in cosmic voids

Hydrodynamic turbulence that is well described by Kolmogorov's decay theory as described in Section 1.1 is a somewhat abstract concept, as naturally occurring turbulence is rarely statistically homogeneous and isotropic at the largest scales [although experimentally generated "grid turbulence" is to reasonable approximation; see, e.g., Davidson (2011)]. On the other hand, there are astrophysical systems where *MHD* turbulence

[2]In two dimensions, the computational cost is becoming just about affordable — see the study of MHD turbulence in the plasmoid-dominated regime by Dong *et al.* (2018). Even there, however, only a moderate scale separation between the box and energy-containing scales was possible, so it is doubtful such simulations could give a measurement of the decay rate free of finite-box-size effects.

may exist in an approximately isotropic and homogeneous form. Galaxy clusters are one example — observations suggest that clusters are permeated by $u \sim B$ turbulence with an outer scale of $\sim$ 10kpc (Vogt & Enßlin, 2005), much smaller than the characteristic cluster size ($\sim$ 100kpc). This turbulence, which is believed to be sourced by "feedback" from the cluster's Active Galactic Nucleus (AGN), could be well described by the decay theories advanced in Chapter 2 during periods of AGN quiescence.

A second example, which is arguably the most popular application of theories of turbulent MHD decay, are the primordial magnetic fields (PMFs) that, according to some cosmological models, were generated in a statistically homogeneous and isotropic configuration in the early Universe, during inflation or at phase transitions [see e.g., Durrer & Neronov (2013); Subramanian (2016); Vachaspati (2021) for reviews]. An attractive and increasingly popular idea is that the magnetic fields present in the voids of large-scale cosmic structure might be relics of these PMFs. Unpolluted by the magnetic fields generated by collapsed structures like galaxies and clusters (and unadulterated by dynamo-inducing flows), it has been suggested that the void magnetic fields may simply be the result of a turbulent MHD decay between magnetogenesis and the present day. This suggests the remarkable possibility that measurement of the void fields might be combined with a theory of MHD decay to provide constraints on early-Universe physics.

Although precise measurement of void magnetic fields is not yet possible, a lower bound on their strength can be deduced from observations of high-energy γ-rays generated by TeV blazars and subsequently scattered by void fields (Neronov & Vovk, 2010; Wagstaff & Banerjee, 2016; Taylor *et al.*, 2011). Such measurements reveal the void fields to be relatively strong; attempts to convert the observational lower bound to a constraint on primordial fields using accepted theory [essentially, a porting of Kolmogorov's laws (1.3) from kinetic to magnetic energy] lead to the conclusion that, if non-helical ($\langle h \rangle = 0$), the relic fields would need to have had enormous energy at the electroweak phase transition (EWPT) — larger than the radiation density of the Universe — to be the progenitor of the void fields (Wagstaff & Banerjee, 2016). This conclusion has prompted research into exotic mechanisms of magnetic-helicity generation at the EWPT (since helical fields decay more slowly than non-helical ones).

However, it turns out that under the decay theory we advance in Chapter 2, there is no inconsistency between the scenario of non-helical magnetic-field generation at the EWPT and the observational constraints on voids. The application of this theory to the problem of PMF decay will be the subject of Chapter 3, where we shall find that that both key insights of Chapter 2 — the existence of the Saffman helicity invariant (1.6) and the control of the decay timescale by magnetic reconnection (a process that is extremely slow in the large-Prandtl-number early Universe) — conspire to greatly increase the expected strength of relic fields. In fact, the calculation presented in Chapter 3 indicates that efficient magnetogenesis could generate magnetic fields whose strength at recombination is around the critical value ($\sim 10^{-11}\,\mathrm{G}$) that some previous studies have indicated could provide a resolution of the Hubble tension (Jedamzik & Pogosian, 2020; Galli *et al.*, 2022), while simultaneously explaining the $\sim \mu$G magnetic fields in galaxy clusters without requiring post-collapse dynamo amplification (Banerjee & Jedamzik, 2003)

1.5 The role of Saffman integrals in forced turbulence

In Chapter 4, we put aside the subject of decaying turbulence and investigate the role of the Saffman integral (1.4) in constraining the large-scale dynamics of *forced* turbulence. Recent numerical studies have shown that forced, statistically isotropic hydrodynamic turbulence develops a 'thermal equilibrium' spectrum, $\mathcal{E}(k) \propto k^2$, at large scales. This behaviour presents a puzzle, as it appears to imply the growth of a non-zero Saffman integral, which would require the development of long-range correlations in the velocity field. However, the Saffman integral is an invariant of decaying turbulence precisely because non-local interactions (i.e., interactions via exchange of pressure waves) are too weak to generate correlations of the required strength. Subject to certain restrictions on the nature of the forcing, we argue in Chapter 4 that the same should be true for forced turbulence. We show that long-range correlations and a k^2 spectrum arise as a result of the turbulent diffusion of linear momentum, and extend only up to a maximum scale that grows slowly with time. This picture has a number of interesting

consequences. First, if the forcing generates eddies with significant linear momentum, a thermal spectrum is not reached—instead, a shallower spectrum develops. Secondly, the energy of turbulence that is forced for a while and then allowed to decay generically obeys Saffman's decay laws (1.5) in the late-time limit.

1.6 Magnetoelasticity

Chapter 5 of this thesis represents a first effort to model the *dynamical* effect of a statistically homogeneous and isotropic stochastic magnetic field on the medium that hosts it. We explore the possibility that a magnetic field tangled at small length scales might resist large-scale shear in an elastic way (the collective result of small-scale magnetic-tension forces), much as a ball of tangled elastic strings responds elastically to an impulse. If so, tangled fields would support the propagation of 'magnetoelastic waves', the isotropic analogue of Alfvén waves on a straight magnetic field. In Chapter 5, we study magnetoelasticity under the idealised model of an equilibrium tangled field configuration. Our treatment differs from previous ones (Moffatt, 1986; Gruzinov & Diamond, 1996) in that we explicitly account for intermittency of the Maxwell stress, and show that this intermittency necessarily decreases the frequency of magnetoelastic waves in a stable field configuration. We develop a mean-field formalism to describe magnetoelastic behaviour, retaining leading-order corrections due to the coupling of large- and small-scale motions, and solve the initial-value problem for viscous fluids subjected to a large-scale shear, showing that the development of small-scale motions results in anomalous viscous damping of large-scale waves. Finally, we test these analytic predictions with (to the best of our knowledge) the first numerical simulations of magnetoelastic waves in tangled, linear force-free magnetic-field equilibria.

Chapter 2

The decay of magnetohydrodynamic turbulence

*This chapter is adapted from Hosking & Schekochihin, 2021, Phys. Rev. X **11**, 041005.*

2.1 Introduction

An outline of this chapter is as follows. In Section 2.2, we consider the decay of helical MHD turbulence from a magnetically dominated state. Since magnetic helicity is better conserved than magnetic energy in the limit of vanishing resistivity, helicity is precisely a quantity that can control the MHD evolution in the same way as the Loitsyansky (1.1) and Saffman (1.4) integrals do for hydrodynamics. Applying a Kolmogorov-style argument to helicity conservation for a decay occuring on the ideal timescale, L/B, yields a power law of $t^{-2/3}$ for both the magnetic and kinetic energies (Hatori, 1984; Biskamp & Müller, 1999; Son, 1999). This decay law is not well-supported by numerics, where a shallower decay law for magnetic energy, and a steeper decay law for kinetic energy are typically observed (Biskamp & Müller, 1999; Müller & Biskamp, 2000; Christensson *et al.*, 2001; Banerjee & Jedamzik, 2004; Frick & Stepanov, 2010; Berera & Linkmann, 2014; Brandenburg & Kahniashvili, 2017; Brandenburg *et al.*, 2019). We show that both of these results are expected for a decay occurring via magnetic reconnection in the Sweet-Parker regime. In particular, we show that the magnetic energy should decay as $t^{-4/7}$, with $t^{-2/3}$ only achieved by fast reconnection. We also find that, provided the

dominant flows are contained within Sweet-Parker sheets, the faster decay of kinetic energy, as $t^{-5/7}$, is a natural consequence of their changing aspect ratio.

In Section 2.3, we consider the decay of non-helical MHD turbulence from a magnetically dominated state. The mechanism controlling this type of decay has so far remained unknown: because the mean helicity density vanishes, its conservation cannot be used to derive a scaling relation relating B, the characteristic magnetic field, to its characteristic length scale L. Numerically, decay laws for both the magnetic and kinetic energies of close to t^{-1} have been observed (Zrake, 2014; Brandenburg *et al.*, 2015; Brandenburg & Kahniashvili, 2017; Reppin & Banerjee, 2017; Bhat *et al.*, 2021), though there is no definitive theoretical explanation for this behaviour. An influential idea is that in the absence of an integral invariant, the decay might satisfy the well-known scaling symmetry of the MHD equations (Olesen, 1997), including dissipative terms. Such a decay would have a t^{-1} power law for the magnetic energy (Orszag, 1977; Hossain *et al.*, 1995; Matthaeus *et al.*, 1996; Campanelli, 2004). Another suggestion is that the non-helical decay is effectively two-dimensional. In this case, it is the conservation of 'anastrophy', or the square of the magnetic vector potential, that should control the decay (Matthaeus & Montgomery, 1980; Ting *et al.*, 1986). A Kolmogorov-style argument then leads to a t^{-1} power law independently of whether the decay occurs on the ideal (Hatori, 1984; Biskamp & Welter, 1989; Brandenburg *et al.*, 2015; Brandenburg & Kahniashvili, 2017), or the Sweet-Parker (Zhou *et al.*, 2019, 2020; Bhat *et al.*, 2021) timescale (see Appendix 2.A). That both treatments predict the same power law is a coincidence related to the fact that anastrophy conservation implies constant Lundquist number (Zhou *et al.*, 2019) (the scaling argument is essentially this same point with the direction of implication reversed). However, it is not clear why fully three-dimensional, isotropic turbulence should two-dimensionalise in this way, nor why any special significance should be given to constant Lundquist number. Indeed, we show in Section 2.3 that both are inconsistent with numerical evidence.

Instead, we propose a treatment of the non-helical decay controlled by the conservation of fluctuations in magnetic helicity. The key point is that the vanishing of the total magnetic helicity does not necessarily imply that any given magnetic field structure is non-helical. Indeed, non-helical magnetic structures generally relax on ideal

timescales to zero magnetic energy, assuming they are not constrained by higher-order topological invariants. We therefore expect that the natural state of the turbulence will be to contain a collection of helical structures, though there will be equal abundances of positive- and negative-helicity structures so that the zero-overall-helicity constraint is satisfied. For such a turbulence, we identify a new integral invariant whose relation to magnetic helicity is precisely analogous to that of the Saffman and Loitsyansky integrals to linear and angular momentum. This invariant is the already-introduced 'Saffman helicity invariant' (1.6), denoted I_H and named for the close analogy between it and the Saffman integral, and also between our arguments and the arguments usually associated with the Saffman invariant and its various anisotropic generalisations (Davidson *et al.*, 2012; Davidson, 2013). As we will show, the conservation of I_H implies the scaling $B^4L^5 \sim$ const. This scaling implies a magnetic-energy-decay power law of $t^{-20/17}$ if reconnection occurs on the Sweet-Parker timescale, or $t^{-10/9}$ if reconnection is fast. These power laws are different from t^{-1}, but are still in excellent agreement with published numerical results, and with our own numerical results presented below. We also find that, for non-helical magnetic fields, the rate at which the aspect ratio of the current sheets changes is much smaller than in the helical case, explaining why a faster decay of kinetic energy is not observed for a non-helical decay from initial states that have small kinetic energy.

Finally, in Section 2.4, we discuss the behaviour of systems with fractional helicity, which we show will ultimately always transition to the fully helical regime as long as the system size is sufficiently large. We also discuss possible applications of the Saffman formalism to wider classes of turbulent decays. As an example, we suggest the existence of a Saffman-type cross-helicity invariant that may control the critically balanced decay of MHD turbulence in the presence of a mean magnetic field, recently studied in Zhou *et al.* (2020). We also conjecture that the simultaneous conservation of both the Saffman-type cross-helicity invariant and the magnetic helicity might govern the initial period of decay of an MHD state starting with $U \sim B$.

2.2 Decay of helical turbulence

We first consider the decay of MHD turbulence from an initial state where magnetic energy dominates kinetic ($B \gg U$), and the magnetic field is helical, i.e., the volume-averaged magnetic-helicity density,

$$\langle h \rangle = \lim_{V\to\infty} \frac{1}{V} H_V = \lim_{V\to\infty} \frac{1}{V} \int_V \mathrm{d}^3\boldsymbol{r}\, \boldsymbol{A}\cdot\boldsymbol{B}, \tag{2.1}$$

is maximal, $\sim B^2 L$. The case of initial parity between the two energies ($U \sim B$) will be discussed in Section 2.4.5. Magnetic helicity is a topological invariant — the total magnetic helicity of a collection of flux tubes is equal to the amount of (signed) flux linked by these tubes. As such, its conservation is related to Alfvén's theorem, which states that for $\eta_n = 0$, the magnetic field is frozen into fluid motions, ensuring that all topological invariants are precisely conserved. The special significance of magnetic helicity is that, unlike other topological invariants, it remains approximately conserved (i.e., better conserved than energy) for small but non-vanishing η_n (Ruzmaikin & Akhmetiev, 1994). This statement is true independently of the reconnection regime. A proof, adapted from Berger (1984), is as follows.

2.2.1 Helicity is conserved by (hyper-resistive) reconnection

In hyper-dissipative MHD, the evolution of the magnetic helicity in a closed volume whose surface is everywhere normal to $\boldsymbol{B}$ satisfies

$$\left|\frac{\mathrm{d}H}{\mathrm{d}t}\right| = 2\eta_n \left|\int \mathrm{d}^3\boldsymbol{r}\, (\nabla^n \boldsymbol{A})\cdot\boldsymbol{B}\right|. \tag{2.2}$$

Note that setting $n = 2$ here yields the familiar expression in terms of the current helicity. After integrating the integral on the right-hand side by parts, applying the Cauchy-Schwarz inequality, and then integrating by parts again, one obtains

$$\left|\frac{\mathrm{d}H}{\mathrm{d}t}\right|^2 \le 4 \left|\frac{\mathrm{d}E_M}{\mathrm{d}t}\, \eta_n \int \mathrm{d}^3\boldsymbol{r}\, \boldsymbol{A}\cdot(\nabla^n \boldsymbol{A})\right|, \tag{2.3}$$

where $\mathrm{d}E_M/\mathrm{d}t = \eta_n \int \mathrm{d}^3\boldsymbol{r}\, \boldsymbol{B}\cdot(\nabla^n \boldsymbol{B})$ is the rate of magnetic-energy decay due to Ohmic heating. For $n = 2$, the other integral in (2.3) is just twice the magnetic energy (Berger,

1984). More generally, we can write

$$\eta_n \left| \int \mathrm{d}^3\boldsymbol{r}\, \boldsymbol{A} \cdot (\nabla^n \boldsymbol{A}) \right| = \eta_n \left| \int \mathrm{d}^3\boldsymbol{r}\, \boldsymbol{B} \cdot (\nabla^{n-2} \boldsymbol{B}) \right| \sim \frac{\mathrm{d}E_M}{\mathrm{d}t}\, {\delta_\eta}^2, \tag{2.4}$$

where δ_η is the resistive dissipation scale. Equation (2.3) then implies

$$\frac{\mathrm{d}\log H}{\mathrm{d}t} \sim \frac{\delta_\eta}{L} \frac{\mathrm{d}\log E_M}{\mathrm{d}t}. \tag{2.5}$$

Eq. (2.5) states that the rate of change of magnetic helicity is smaller than the rate of the energy decay due to Ohmic heating (which will be even smaller than the true magnetic-energy-decay rate, because magnetic energy can also be converted to the kinetic energy of reconnection outflows) by a factor equal to the ratio of the integral scale to the resistive dissipation length scale, which becomes arbitrarily small as $\eta_n \to 0^+$. *Q.E.D.*

It may appear counter-intuitive that reconnection, a process that, by definition, changes the topology of magnetic field lines, can conserve helicity, a topological invariant. The resolution of this apparent paradox is that self-linkages, i.e., twists of the magnetic flux tube are also associated with helicity. For example, during the unlinking of two linked tori by reconnection to form a single torus, the resulting torus ends up twisted, and the total helicity of the configuration is conserved (Ruzmaikin & Akhmetiev, 1994).

2.2.2 Theory of helical decay

The conservation of the volume-averaged magnetic helicity, (2.1), implies the scaling

$$B^2 L \sim \text{const.} \tag{2.6}$$

The remaining ingredient required to compute the magnetic-energy decay law is the decay timescale, as a function of U, B and L. The simplest possible treatment is to assume Alfvénic dynamics, with $U \sim B$, similarity between the integral scales of the magnetic and kinetic energies, L, and, therefore, a decay timescale $L/B \sim L/U$. For

future reference, we compute the expected decay power law under such an assumption for a scaling more general than (2.6), *viz.*,

$$B^\alpha L \sim \text{const.} \tag{2.7}$$

Eq. (1.2) becomes (with B measured in velocity units)

$$\frac{\mathrm{d}}{\mathrm{d}t}\frac{1}{2}B^2 \sim -\frac{B^3}{L} \propto -B^{3+\alpha}, \tag{2.8}$$

with solution

$$B^2 \sim t^{-2/(1+\alpha)}. \tag{2.9}$$

Now setting $\alpha = 2$ for helicity conservation, the canonical $t^{-2/3}$ power law is recovered (Hatori, 1984). However, this prediction has proved to be in poor agreement with numerics, which have found a decay of the magnetic energy closer to $t^{-1/2}$, and, unexpectedly, a decay of the kinetic energy faster than $t^{-2/3}$ (Biskamp & Müller, 1999; Müller & Biskamp, 2000; Christensson *et al.*, 2001; Banerjee & Jedamzik, 2004; Frick & Stepanov, 2010; Berera & Linkmann, 2014; Brandenburg & Kahniashvili, 2017; Brandenburg *et al.*, 2019).

These discrepancies are readily resolved by assuming the decay to occur on the reconnection, rather than ideal, timescale. Naturally, the reconnection timescale depends on the reconnection regime, i.e., on whether the reconnection is slow (Sweet-Parker) or fast [plasmoid-dominated (Uzdensky *et al.*, 2010) or stochastic (Lazarian *et al.*, 2020)]. Fast reconnection, by definition, occurs on dynamical timescales, so will again produce a $t^{-2/3}$ decay. However, as explained in Chapter 1, extant numerical simulations of decaying MHD turbulence mostly probe the slow regime, owing to the large Lundquist numbers and hence large resolutions required for fast reconnection to take place. In this case, the reconnection timescale is

$$\tau_{\mathrm{rec}} \sim S_n^{1/n}\,\frac{L}{B}, \tag{2.10}$$

where $S_n = BL^{n-1}/\eta_n$ is the hyper-Lundquist number. Using (2.10) for the decay timescale, (2.8) becomes

$$\frac{\mathrm{d}}{\mathrm{d}t}\frac{1}{2}B^2 \sim -\frac{B^3}{L}B^{-1/n}L^{(1-n)/n} \propto -B^{(2\alpha n+3n-\alpha-1)/n}, \tag{2.11}$$

the solution of which is

$$B^2 \sim t^{-2n/(2\alpha n+n-\alpha-1)}. \tag{2.12}$$

Again, for a helicity-conserving decay, we set $\alpha = 2$ to obtain a power law of

$$B^2 \sim t^{-2n/(5n-3)}. \tag{2.13}$$

For $n = 2$ (Laplacian dissipation), the power law is

$$E_M \sim t^{-p_M}, \quad p_M = \frac{4}{7} \simeq 0.57, \tag{2.14}$$

which is indeed shallower than $p_M = 2/3$. Indeed, some recent studies at large resolution have reported $p_M \simeq 0.58$, in remarkable agreement with this prediction (Brandenburg & Kahniashvili, 2017; Brandenburg *et al.*, 2019). However, we caution against direct comparison with those simulations, because they employed time-dependent dissipation coefficients. For numerical studies using $n = 4$ hyper-dissipation (Biskamp & Müller, 1999), (2.12) predicts an even slower magnetic-energy-decay exponent of $p_M = 8/17 \simeq 0.47$. This is in excellent agreement with the $p_M \simeq 0.5$ found numerically by Biskamp & Müller (1999).

It may appear counter-intuitive that reconnection can result in a faster decay of kinetic energy than magnetic energy, as reconnection outflows are typically Alfvénic, i.e., the outflow velocity is approximately equal to the upstream Alfvén speed of the magnetic field prior to reconnection — a condition that is hard-wired into the Sweet-Parker scalings. However, the current sheets, where reconnection occurs, are not volume-filling. Denoting the current sheet width by δ, the volume occupied by the current sheet formed when two structures of volume L^3 reconnect and merge is $L^2\delta$. Therefore, we expect

$$E_K \sim \frac{\delta}{L} E_M \tag{2.15}$$

for Alfvénic outflows, where E_K and E_M should be understood as the total kinetic and magnetic energies in the system, respectively. This result allows for the possibility of different decay rates for the kinetic and magnetic energy, because the ratio δ/L need not be constant in time. For example, with hyper-dissipative Sweet-Parker sheets,

$\delta/L \sim S_n^{-1/n} \sim (BL^{n-1})^{-1/n}$. For $B^2 L \sim$ const [Eq. (2.6)], we find $\delta/L \sim E_M^{1-3/2n}$, which, via (2.15), translates to

$$E_K \sim E_M^{2-3/2n}. \tag{2.16}$$

Thus, kinetic energy is indeed expected to decay more quickly than magnetic energy, simply due to the changing aspect ratio of the Sweet-Parker sheets. For $n = 2$, this effect is relatively modest: the kinetic-energy decay exponent is 5/4 times greater than the magnetic one, so the decay exponents for E_M and E_K are $p_M = 4/7 \simeq 0.57$ and $p_K = 5/7 \simeq 0.71$, respectively. For $n = 4$, though, the kinetic-energy decay exponent is 13/8 times greater than the magnetic one, so these decay exponents become $p_M = 8/17 \simeq 0.47$ and $p_K = 13/17 \simeq 0.76$.

We note that the validity of (2.15) requires the initial kinetic energy to be much smaller than the magnetic energy, by a factor $\lesssim \delta/L$, as otherwise the kinetic energy contained in outflows may be subdominant to the rest. This condition will be true for our simulations, which are initialised with $U = 0$, but may not be true in all situations of interest. However, as we shall discuss in Section 2.4.5, there is reason to believe that decaying helical MHD turbulence should be driven towards (2.15), even if E_K is larger than $(\delta/L)E_M$ initially.

2.2.3 Numerical results

In this section, we compare the theoretical predictions of the previous section with numerical simulations of MHD turbulence, initialised as a Gaussian random magnetic field with characteristic scale $\simeq 1/33$ of the box size. These simulations employ the incompressible, spectral MHD code Snoopy (Lesur, 2015), with Prandtl number $\mathrm{Pm} \equiv \nu_n/\eta_n = 1$. We provide further information about Snoopy and describe the details of our numerical setup in Appendix 2.D.

In simulations with $n = 2$ dissipation, resolution constraints prevent the use of Lundquist numbers that are sufficiently large to achieve good conservation of the magnetic helicity. Nonetheless, supposing that helicity decays as $H(t) \sim t^{-p_H}$, while $E_M(t) \sim t^{-p_M}$, we expect $B^{2(1-p_H/p_M)}L \sim$ const. For small but non-vanishing η_n,

therefore, we expect to find an α somewhat smaller than 2 such that $B^\alpha L \sim$ const. We can determine this value of α numerically by measuring $E_M(t)$ and

$$L = \frac{2\pi}{E_M} \int \mathrm{d}k \, \frac{\mathcal{E}_M(k)}{k}, \tag{2.17}$$

where $\mathcal{E}_M(k)$ is the spectral magnetic-energy density.

As long as η_n is not too large, the decay should still occur on the Sweet-Parker timescale. We can then use (2.12) to determine the expected magnetic-energy decay exponent based on the empirically determined value of α, and compare it with the value measured in our simulations. While we do not expect that this procedure should yield exact agreement between the predicted and empirical decay exponents, as it neglects the role of Ohmic diffusion (which, when S_n is small, will ultimately become more important to the decay than reconnection), we expect approximate agreement that becomes better as S_n increases and α, therefore, becomes closer to 2.

In Fig. 2.1, we present the results of such a comparison, plotting the empirically measured values of p_M against those of α, for simulations with $n = 2$ and $n = 4$ (how the error bars are determined is explained in Appendix 2.D). This figure shows remarkable agreement between our simulations and the Sweet-Parker decay curves (coloured), despite the fact that we do not reach the asymptotic value of $\alpha = 2$ with $n = 2$ dissipation. For $n = 4$, we also find excellent agreement, and do reach $\alpha = 2$. As other authors have noted (Biskamp & Müller, 1999), this asymptotic scaling is reached much more rapidly in the hyper-dissipative case, and indeed we were forced to choose relatively small values of $S_n^{1/n}$ in order to populate the part of Fig. 2.1 with $\alpha < 2$. To illustrate this point further, we plot two simulations with $n = 6$ hyper-dissipation, which also exhibit the $\alpha = 2$ scaling (and are almost coincident in Fig. 2.1). The faster attainment of the correct asymptotic scaling with hyper-dissipation will be important in establishing the correct value of α for non-helical turbulence, previously unknown, in the next section.

Interestingly, we note that for $\alpha \simeq 2$, the decay exponent p_M is consistently somewhat larger than our theoretical prediction based on Sweet-Parker reconnection. This suggests these simulations may be at the start of the transition to the fast-reconnection

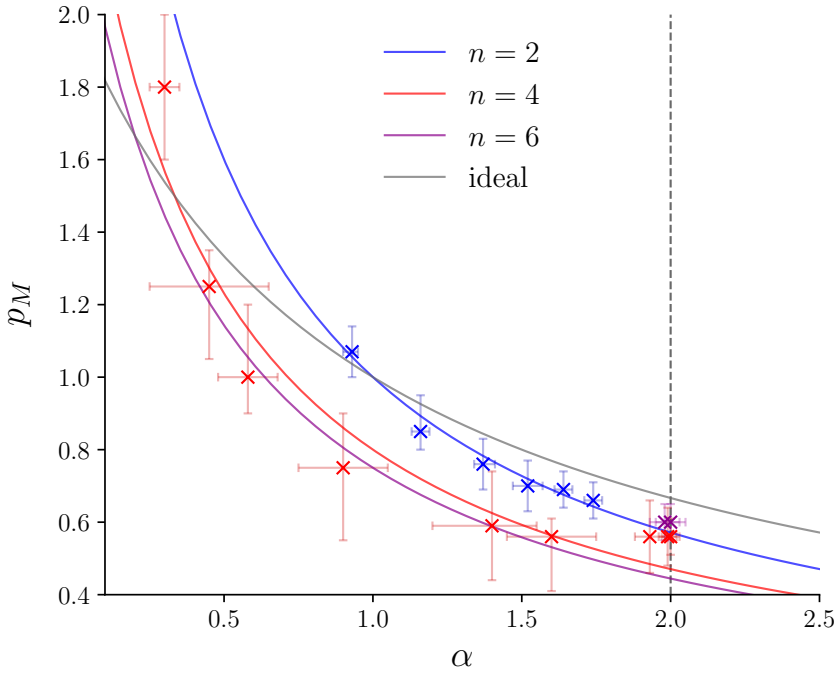

Figure 2.1: Relation between the empirically obtained magnetic-energy-decay power-law exponent, p_M, and the value of α for which $B^\alpha L \sim$ const. Solid curves show the expected relationship, (2.12), for decays occurring on the Sweet-Parker timescale, with $n = 2$, $n = 4$ and $n = 6$ shown in blue, red, and magenta, respectively. The grey solid curve depicts the 'ideal' scaling given by (2.9). Simulation results are in excellent agreement with the coloured curves, and not with the grey curve. This confirms that the decay takes place on the Sweet-Parker, rather than ideal, timescale. The full set of decay curves from which this plot was derived can be found in Appendix 2.D.

regime. We do not find the same transition in two-dimensional simulations (see Appendix 2.A), despite employing even larger Lundquist numbers, which is consistent with the intuitive expectation that fast reconnection should 'turn on' more quickly in three dimensions, due to turbulence in the reconnection region.

For the decay of the kinetic energy also, we find that the predictions of the previous section are in good agreement with our simulations, as shown in Fig. 2.2. The upper panel shows the evolution of the magnetic- and kinetic-energy spectra for a run with $n = 4$, $\eta_4 = 2 \times 10^{-8}$, confirming that at any given time, kinetic energy is contained at much smaller scales than the magnetic energy, consistent with the expectation that reconnection outflows should have a width $\delta \ll L$. The inset shows the relative sizes of the total magnetic and kinetic energies in the same run, which are in excellent agreement with (2.15). The lower panel shows the kinetic-energy decay exponents, p_K, plotted against the corresponding exponents for the magnetic energy, p_M, confirming that a faster decay of kinetic energy is realised in our simulations, in reasonably good agreement with our theoretical prediction, (2.16).

We note that, while we do observe faster decay of kinetic energy than magnetic in our simulations, the difference is not as stark as in the numerical study by Biskamp & Müller (1999), who found $E_K \propto E_M^2$. As we will discuss in Section 2.4, this discrepancy may arise because the initial state in their study was one with equipartition between the magnetic and kinetic energies, $U \sim B$, unlike the $U \ll B$ we have employed here. We will argue that when $U \sim B$, the conservation of cross-helicity, even though the latter is a sign-indefinite quantity, might play an important role in governing the decay. Simultaneously conserving magnetic helicity and *fluctuations* in the cross-helicity, under the same formalism as we are about to propose for helicity conservation in non-helical turbulence, does imply the scaling $E_K \propto E_M^2$ conjectured by Biskamp & Müller (1999).

To conclude, the results of this section represent what we consider compelling evidence that helical, magnetically dominated MHD turbulence relaxes by the self-similar coalescence of magnetic structures via magnetic reconnection, as was suggested by J.B. Taylor (Taylor, 1986). Physically, this implies that the correct way to think about the system is as consisting of a collection of magnetic structures that are unable to relax

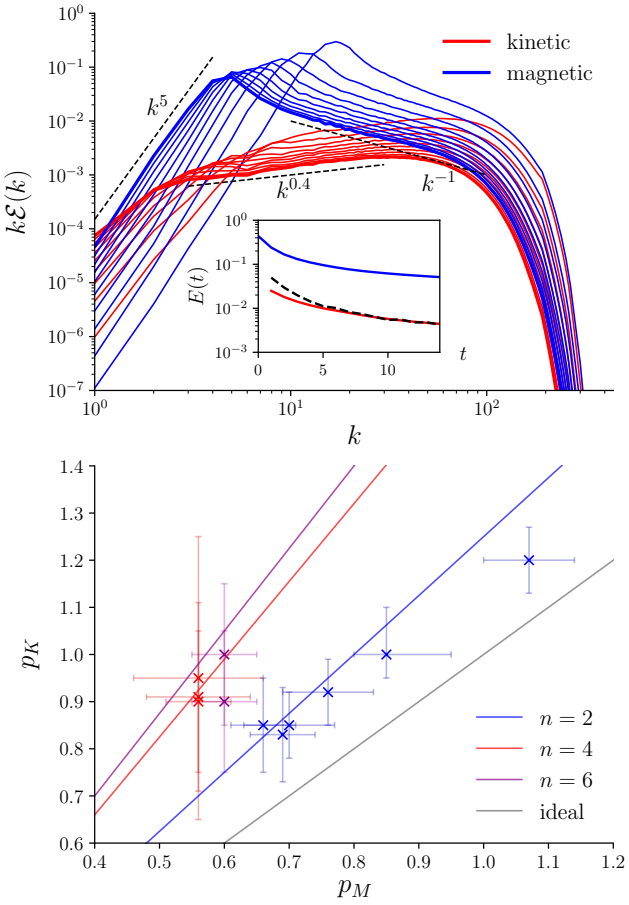

Figure 2.2: Top panel: Evolution of $k\mathcal{E}(k)$, where $\mathcal{E}(k)$ is the spectral energy density, for the magnetic (blue) and kinetic (red) energies. These plots are obtained from a helical simulation with $n = 4$, $\eta_4 = 2 \times 10^{-8}$. Each plot of $k\mathcal{E}(k)$ is separated by a time interval of 1.0 between $t = 1.0$ to $t = 10.0$ ($t = 10.0$ in bold), where time is in code units based on normalising the box size and initial mean-square magnetic field to 2π and 1, respectively, so that 1 time unit is approximately the initial Alfvén crossing time of the box. The peak of the magnetic energy is at much larger scales (smaller k) than the peak of the kinetic energy, consistent with the expectation that the kinetic energy should be contained within the Sweet-Parker sheets. Inset: decay of the total magnetic and kinetic energies. The total kinetic energy curve is much below the magnetic energy curve, and coincides with $(\delta/L)E_M$ (black), in agreement with (2.15), with δ/L computed as the ratio of the wavenumbers at which $k\mathcal{E}_M(k)$ and $k\mathcal{E}_K(k)$ peak. Bottom panel: Plot of the kinetic-energy decay exponent, p_M, against the magnetic-energy decay exponent, p_K, as measured in simulations with $S_{n,0}^{1/n} > 9.0$. Results are in reasonable agreement with the theoretical prediction, (2.16) (coloured lines), and are inconsistent with $E_K \propto E_M$ (grey line).

under ideal dynamics due to the topological constraints imposed by the flux freezing, and, therefore, relax via coalescence on a timescale at which these constraints can be broken, i.e., on the reconnection timescale.

2.3 Decay of non-helical turbulence

Having established a theory of the reconnection-controlled decay of helical turbulence from a magnetically dominated state, we now consider the case of non-helical turbulence, i.e., turbulence for which the volume-averaged magnetic-helicity density [Eq. (2.1)] vanishes. Here, as in Section 2.2, we consider the decay from an initial state with predominant magnetic energy ($B \gg U$), postponing the discussion of the case with $U \sim B$ until Section 2.4.5. As we have already noted, the mechanisms controlling the evolution of such turbulence are not well understood. Numerically, a power law close to t^{-1} has been measured (Zrake, 2014; Brandenburg *et al.*, 2015; Brandenburg & Kahniashvili, 2017; Reppin & Banerjee, 2017; Bhat *et al.*, 2021), prompting comparisons with the two-dimensional decay (Hatori, 1984; Biskamp & Welter, 1989; Zhou *et al.*, 2019), which conserves 'anastrophy', or the square of the magnetic vector potential (see Appendix 2.A), resulting in a t^{-1} decay law independently of the reconnection regime. The evidence that has been presented for this picture in three dimensions relies on demonstrating that the mean-square magnetic vector potential (defined according to some particular, necessarily non-unique gauge choice) changes more slowly with time than does the magnetic energy (Bhat *et al.*, 2021). However, this will be true for any decay satisfying $B^\alpha L \sim$ const for any $\alpha > 0$. Here, we propose a different theory of non-helical decay.

2.3.1 Qualitative theory of non-helical decay

The key point, already made in Section 2.1, is that a vanishing mean helicity density does not imply that individual magnetic structures are non-helical, because helicity is not a sign-definite quantity. Moreover, if not constrained by higher-order topological invariants, non-helical magnetic structures will relax to zero energy on the ideal timescale [as required by J.B. Taylor relaxation (Taylor, 1974, 1986)]. For example,

consider a toroidal structure without a twist — such a structure will shrink under the magnetic tension force (driving outflows along its axis) to zero magnetic energy. In contrast, for a toroidal structure with a net twist relative to the poloidal axis, such a relaxation is topologically impossible. Thus, we expect a collection of helical structures of different signs to be the natural state of non-helical MHD turbulence. Indeed, visualisations of our simulations do appear to support this intuition, see Fig. 2.3.

To motivate the more formal approach to follow, we first present an informal 'cartoon' of the expected dynamics (Fig. 2.4). Consider a volume filled with helical magnetic structures, which we shall refer to as 'blobs', as we wish to remain agnostic about their precise morphology. As in the helical case, we expect that topological constraints will hinder their relaxation on ideal timescales, and that instead the blobs will evolve via coalescences with other blobs on the prevailing reconnection timescale.

For simplicity, suppose that all blobs have helicity $\sim H$, and for the moment, that they all have the same sign of helicity. When any two blobs merge, the resulting structure will have helicity $H' = 2H$, implying that the characteristic magnetic field and length scale, B and L, will satisfy $B'^2 L'^4 \sim 2B^2 L^4$. If every blob in the system undergoes such a pairwise merger, then the total number of blobs, N, will decrease by a factor of 2: $N' = N/2$. Assuming the blobs fill all space, their characteristic size must then increase as $L' = 2^{1/3} L$. Together, these relations imply $B^2 L \sim$ const, which, of course, is precisely the condition obtained from the conservation of the volume-averaged helicity density, (2.6).

In contrast, for a system with vanishing total helicity, there will be equal numbers of blobs with helicities $-H$ and $+H$. When two blobs with opposite helicities merge, the resulting structure will be non-helical and, assuming that no higher-order topological invariants constrain its subsequent evolution, it will relax to zero magnetic energy on the ideal timescale [1]. In other words, when blobs of opposite helicity merge, they mutually 'annihilate'. Otherwise, the signs of the helicities of the blobs should not modify the dynamics, so the system will have no preference between like-helicity and

[1] Even if the Lundquist number is very large and reconnection is plasmoid dominated and fast, there will still be a separation of timescales between the ideal timescale and the reconnection one, the latter being a factor of 10^2 longer (Uzdensky *et al.*, 2010).

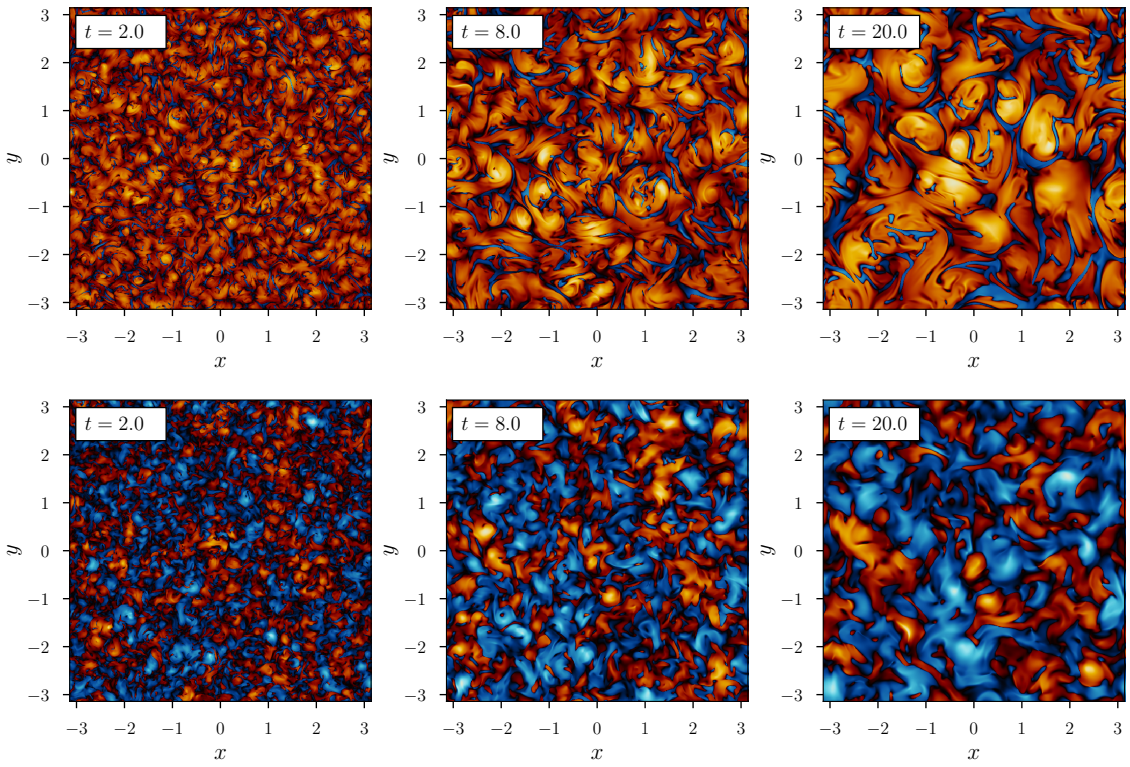

Figure 2.3: Slices of $\boldsymbol{B} \cdot \hat{\boldsymbol{J}}$, the projection of the magnetic field onto the direction of the electric current ($\hat{\boldsymbol{J}}$ is the unit vector in this direction), for three different times during helical (above) and non-helical (below) simulations with $n = 2$, $\eta_2 = 2 \times 10^{-4}$ (time is in code units, as explained in the caption to Fig. 2.2). Positive values are shown in red, negative values in blue. $\boldsymbol{B} \cdot \hat{\boldsymbol{J}}$ is a local measure of the twist of the magnetic field lines, with different signs indicating different directions of the twist. It is also related to the magnetic helicity, because the sign of $\boldsymbol{B} \cdot \hat{\boldsymbol{J}}$ is equal to the sign of the magnetic helicity for a fully relaxed helical magnetic structure, according to the J.B. Taylor relaxation theory (Taylor, 1974, 1986). Indeed, our helical simulations do feature a super-abundance of blobs with positive $\boldsymbol{B} \cdot \hat{\boldsymbol{J}}$, while in our non-helical simulations, blobs with both signs of $\boldsymbol{B} \cdot \hat{\boldsymbol{J}}$ have approximately equal representation.

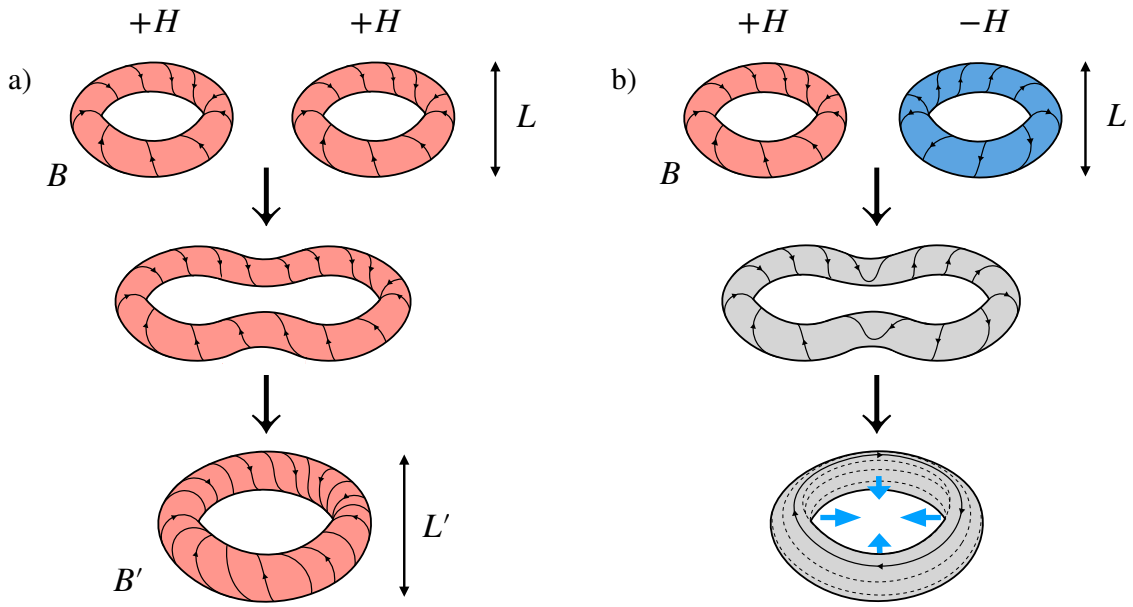

Figure 2.4: (a) Cartoon of a typical merger of two helical structures ('blobs'). As explained in the main text, $B'^2L' = B^2L$ for helical turbulence in which this is the only allowed process. (b) This additional 'annihilation' process is also possible in non-helical turbulence, and should occur equally frequently. The presence of this process modifies the previous scaling to $B'^4L'^5 = B^4L^5$.

opposite-helicity mergers. This implies that, after one merger timescale, we will have $N' = N/4$, because of any four randomly chosen blobs, on average, two will annihilate, and two will merge to form a single blob. Again, assuming blobs fill all space, we have $L' = 2^{2/3}L$, which, together with $B'^2L'^4 \sim 2B^2L^4$, implies

$$B^4L^5 \sim \text{const.} \tag{2.18}$$

This new scaling is the non-helical analogue of (2.6).

This picture, while conceptually simple, does rely on significant assumptions about the nature of the dynamics that are not obviously justifiable, e.g., that all structures have the same length scale and helicity, that the only dynamical process is mergers (rather than, say, fragmentation due to MHD instabilities) and that all mergers are pairwise processes. We now discuss how to formalise it.

2.3.2 Invariant-based theory of non-helical decay

2.3.2.1 The Saffman helicity invariant

We propose that the general evolution of a collection of localised structures of mixed magnetic helicity should conserve the integral

$$I_H = \int \mathrm{d}^3\boldsymbol{r} \langle h(\boldsymbol{x})h(\boldsymbol{x}+\boldsymbol{r})\rangle, \tag{2.19}$$

where, as before, $h = \boldsymbol{A}\cdot\boldsymbol{B}$ is the helicity density, and angle brackets denote an ensemble average. The form of this integral is immediately reminiscent of the Loitsyansky integral $I_{\boldsymbol{L}}$ (1.1) and the Saffman integral $I_{\boldsymbol{P}}$ (1.4) which govern hydrodynamic decay. It is because of this analogy, of which we shall make further profitable use in Section 2.4, that we refer to I_H as the 'Saffman helicity invariant'. We proceed by establishing the claims that, in non-helical turbulence, I_H is gauge invariant, finite, and conserved. These arguments are in most respects analogous to those originally made by Saffman (1967) for $I_{\boldsymbol{P}}$ (see Davidson (2013) for a review).

1. I_H is gauge-invariant.

Assuming that volume and ensemble averages are the same,

$$I_H = \lim_{V\to\infty} \frac{1}{V} \left[\int_V \mathrm{d}^3\boldsymbol{x}\, h(\boldsymbol{x}) \right]^2 = \lim_{V\to\infty} \frac{1}{V} \langle H_V^2 \rangle, \tag{2.20}$$

so I_H is the density of magnetic helicity squared. Gauge invariance is then guaranteed in the same manner as for the magnetic helicity, by arranging that the surface of the volume V is always normal to the magnetic-field direction. This can always be achieved because of our assumption that the magnetic field forms localised structures, which are arbitrarily small compared to V in the limit $V \to \infty$.

2. I_H is finite.

Returning to the definition of I_H, (2.19), and assuming that the system has no preference for accumulation of like- or opposite-helicity structures, $\langle h(\boldsymbol{x}) h(\boldsymbol{x}+\boldsymbol{r}) \rangle$ is zero if $\boldsymbol{r}$ extends beyond the characteristic size of a helical structure, L, and of size $\sim \langle h^2 \rangle \sim B^4 L^2$ otherwise. Integrating over $\boldsymbol{r}$ then gives $I_H \sim B^4 L^5$. Formally, this requires the two-point magnetic-helicity-density correlation function to decay faster than r^{-3} as $r \to \infty$. This is the condition for the magnetic structures to be 'localised'.

Another way to obtain this scaling is to consider the volume integral in (2.20) as a random walk in the net helicity contained within the volume V — the number of 'steps' is V/L^3, so

$$H_V = \int_V \mathrm{d}^3\boldsymbol{x}\, h(\boldsymbol{x}) \sim \left(\frac{V}{L^3} \right)^{1/2} B^2 L^4. \tag{2.21}$$

Then there is cancellation of V in (2.20), and the scaling $I_H \sim B^4 L^5$ is recovered.

3. I_H is conserved.

According to (2.21), the expectation value of the square helicity in a large volume of non-helical turbulence is $\langle H_V^2 \rangle \propto V$. As $\eta \to 0^+$, the magnetic helicity is conserved during all processes that occur locally inside the volume V, so $\langle H_V^2 \rangle \propto V$ can only be changed by processes occurring at the surface of V, $S = \partial V$. These are fluxes of helicity in or out of the volume, or else reconnection with magnetic structures not contained within the volume. However, both are random processes and hence the net rate of

change of square helicity associated with them scales as $\sim S \sim V^{2/3}$. Ultimately, then, we find that

$$\frac{1}{\langle H_V^2 \rangle} \frac{\mathrm{d}\langle H_V^2 \rangle}{\mathrm{d}t} \propto V^{-1/3}, \tag{2.22}$$

with the result that in the limit $V \to \infty$, $\langle H_V^2 \rangle$ is a conserved quantity. Therefore, so is I_H.

An alternative proof of the invariance of I_H, which follows directly from the MHD induction equation under the assumption of sufficiently rapid decay of long-range correlations, is detailed in Appendix 2.B.

The invariance of I_H implies precisely the same scaling as we found from our qualitative theory, (2.18). The argument based on I_H is much more general, however: while it requires that helical structures be localised (i.e., that correlations decay sufficiently quickly with distance), and that there be no preference for accumulation of like-helicity or opposite-helicity structures, it does not require that all structures be of the same size or magnitude of helicity at any given instant, and neither does it require that the only relevant dynamics be pairwise mergers. The cartoon presented in Section 2.3.1, should, therefore, be considered as a particular example of dynamics that would conserve I_H, and that, therefore, must produce the correct scaling, but not as the only dynamics allowed in the system, or required to be prevalent in order for the scaling (2.18) to hold.

2.3.2.2 Permanence and impermanence of the large scales

We now discuss some important consequences of the invariance of I_H for the small-k asymptotics of the spectra. In particular, we shall find that the phenomenon of 'inverse transfer' of magnetic energy (Brandenburg *et al.*, 2015; Reppin & Banerjee, 2017), whose explanation has so far been unclear, follows naturally from the conservation of I_H. We shall also find that the invariance of I_H implies an invariant small-k asymptotic of the helicity-variance spectrum, a fact that we shall utilise in Section 2.3.4 to provide a numerical test of our theory.

As is well known, the Saffman and Loitsyansky integrals are, respectively, proportional to the coefficients of k^2 and k^4 in the small-k asymptotic expansion of the kinetic-energy spectrum. To see why, note that if correlations between distant points

decay sufficiently quickly, *viz.*, if $\langle \boldsymbol{u}(\boldsymbol{x}) \cdot \boldsymbol{u}(\boldsymbol{x}+\boldsymbol{r}) \rangle < O(r^{-5})$ as $r \to \infty$, then the kinetic-energy spectrum,

$$\mathcal{E}_K(k) = \frac{k^2}{4\pi^2} \int \mathrm{d}^3\boldsymbol{r}\, \langle \boldsymbol{u}(\boldsymbol{x}) \cdot \boldsymbol{u}(\boldsymbol{x}+\boldsymbol{r}) \rangle e^{-i\boldsymbol{k}\cdot\boldsymbol{r}}, \tag{2.23}$$

may be Taylor-expanded in $kL \ll 1$, which yields (under the assumptions of statistical isotropy and homogeneity),

$$\mathcal{E}(k \to 0) = \frac{I_{\boldsymbol{P}} k^2}{4\pi^2} + \frac{I_{\boldsymbol{L}} k^4}{24\pi^2} + O(k^5). \tag{2.24}$$

Thus, Saffman turbulence, with $I_{\boldsymbol{P}} \neq 0$, has $\mathcal{E}(k \to 0) \propto k^2$ (Saffman, 1967), while Batchelor turbulence, with $I_{\boldsymbol{P}} = 0$, has $\mathcal{E}(k \to 0) \propto k^4$ instead (Batchelor & Proudman, 1956). Owing to the invariance of $I_{\boldsymbol{P}}$ and $I_{\boldsymbol{L}}$, (2.24) leads to a phenomenon known as the 'permanence of the large-scale eddies' or the 'selective decay of small-scale structure' — as hydrodynamic turbulence decays, the small-k part of its energy spectrum remains unchanged. In particular, this means that non-helical hydrodynamic turbulence supports no inverse energy transfer. This is unlike non-helical MHD, which, if initialised with $\mathcal{E}(k \to 0) \propto k^4$ (or steeper, like in our simulations — see Appendix 2.D), has been found in simulations to increase its energy content at large scales (Brandenburg *et al.*, 2015; Reppin & Banerjee, 2017). This may be interpreted as a consequence of the non-invariance of the magnetic equivalent of the Loitsyansky integral,

$$I_{\boldsymbol{L}_M} \equiv -\int \mathrm{d}^3\boldsymbol{r}\, r^2 \langle \boldsymbol{B}(\boldsymbol{x}) \cdot \boldsymbol{B}(\boldsymbol{x}+\boldsymbol{r}) \rangle, \tag{2.25}$$

which is related to the magnetic energy spectrum via the expansion analogous to (2.24),

$$\mathcal{E}_M(k \to 0) = \frac{I_{\boldsymbol{B}} k^2}{4\pi^2} + \frac{I_{\boldsymbol{L}_M} k^4}{24\pi^2} + O(k^5), \tag{2.26}$$

where $I_{\boldsymbol{B}}$ will be defined and discussed in Section 2.4.3, but for now can be assumed to be zero.

Of course, there was no reason to suspect that $I_{\boldsymbol{L}_M}$ should have been a dynamical invariant, as angular momentum does not have a magnetic equivalent — $\boldsymbol{L}_M \equiv \boldsymbol{r} \times \boldsymbol{B}$ is not a conserved quantity in MHD. In fact, the growth of $I_{\boldsymbol{L}_M}$, and hence the inverse

transfer, can be recovered immediately from the conservation of the Saffman helicity invariant, as

$$I_{\boldsymbol{L}_M} \sim B^2 L^5 \sim \frac{I_H}{B^2}, \tag{2.27}$$

so if I_H is conserved while B^2 decays, $I_{\boldsymbol{L}_M}$ must grow.

Owing to the presence of the inverse transfer, it would appear that there is no 'permanence of the large scales' principle for non-helical MHD. However, a modified version of this principle may be obtained by noting that I_H is proportional to the coefficient of k^2 in the small-k expansion of the helicity-variance spectrum,

$$\Theta(k) = \frac{k^2}{2\pi^2} \int \mathrm{d}^3\boldsymbol{r}\, \langle h(\boldsymbol{x})\, h(\boldsymbol{x}+\boldsymbol{r})\rangle e^{-i\boldsymbol{k}\cdot\boldsymbol{r}}. \tag{2.28}$$

Namely, at small k,

$$\Theta(k \to 0) = \frac{I_H k^2}{2\pi^2} + O(k^3), \tag{2.29}$$

provided that $\langle h(\boldsymbol{x})\, h(\boldsymbol{x}+\boldsymbol{r})\rangle < O(r^{-3})$ as $r \to \infty$. Thus, non-helical MHD does have a kind of 'permanence of the large scales' phenomenon, though it manifests itself in the helicity-variance spectrum, not in the energy spectrum. Detecting this phenomenon numerically will be a useful test of our theory and a way of confirming the conservation of I_H (see Section 2.3.4).

2.3.3 Decay laws

Let us now compute the decay laws associated with the conservation of I_H. Equation (2.12) with $\alpha = 4/5$, as demanded by (2.18), implies a magnetic-energy decay

$$E_M \propto t^{-20/17} \simeq t^{-1.18}, \tag{2.30}$$

if the dynamics occur on the Sweet-Parker timescale (with Laplacian viscosity), or (2.9) gives

$$E_M \propto t^{-10/9} \simeq t^{-1.11}, \tag{2.31}$$

if reconnection is fast, i.e., either stochastic or plasmoid-dominated. These exponents are both close to -1, so are consistent with previous numerical results that have reported a power law decay $\propto t^{-1}$ (Zrake, 2014; Brandenburg *et al.*, 2015; Brandenburg & Kahniashvili, 2017; Reppin & Banerjee, 2017; Bhat *et al.*, 2021).

For the kinetic energy, we again expect (2.15) to hold, provided the kinetic energy is dominated by reconnection outflows. Under the Sweet-Parker scalings and $B^4L^5 \sim$ const, this becomes

$$E_K \sim E_M^{(14n-9)/10n}. \tag{2.32}$$

For $n = 2$ and $n = 4$, this gives $E_K \sim E_M^{19/20}$ and $E_K \sim E_M^{47/40}$, respectively. The closeness of these exponents to 1 indicates that the current-sheet aspect ratio changes more slowly in the non-helical case than the helical case, and explains why no significant difference in the kinetic- and magnetic-energy decay laws has been reported in the previous numerical studies cited above.

2.3.4 Numerical results

To test the theory proposed in Sections 2.3.2 and 2.3.3, we now present results from simulations of decaying non-helical turbulence, analogous to those presented for helical fields in Section 2.2.3.

We first address the question of the scaling and conservation of I_H in our simulations. In a periodic box, rather than infinite space, one should interpret the limit $V \to \infty$ in (2.20) as requiring V to be large compared to the energy-containing scales, but small compared to the box size, where the assumption of isotropy fails, as does the random-walk scaling of magnetic helicity, (2.21), if the total helicity in the box is constrained to be exactly zero by the initial condition. Fig. 2.5 shows plots of $\langle H_V^2 \rangle / V$ vs. R, where V is a cube of width $2R$, and we take an ensemble average over many different cube positions in the simulation box (employing the Coulomb gauge, $\nabla \cdot \boldsymbol{A} = 0$, for numerical convenience). As $R \to 0$, $\langle H_V^2 \rangle / V \propto V \to 0$, because $\langle H_V^2 \rangle$ is dominated by individual structures. Similarly, $\langle H_V^2 \rangle / V$ vanishes as $R \to \pi$, because then V is the entire periodic simulation domain, which has zero magnetic helicity by construction. However, for intermediate values of R, $\langle H_V^2 \rangle / V$ turns out to be independent of V, confirming the random-walk scaling, (2.21).

The value of I_H is $\langle H_V^2 \rangle / V$ in this flat region. Computing it as the average of $\langle H_V^2 \rangle / V$ between the two dashed lines in Fig. 2.5 as a function of time, we find that I_H decays approximately as $t^{-0.1}$ (see the inset to Fig. 2.5). Considering the strong scaling

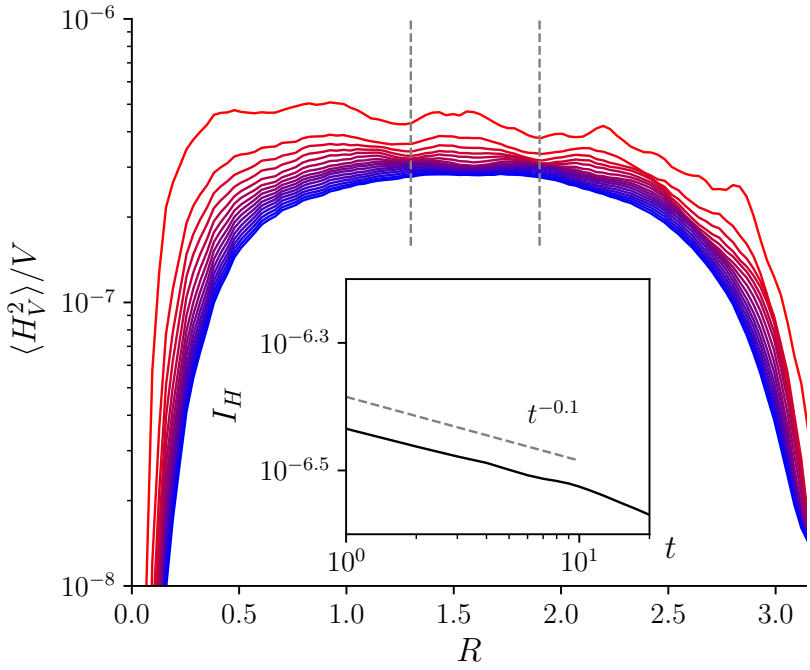

Figure 2.5: Confirmation of the expected scaling of $\langle H_V^2 \rangle / V$ with volume, $V = (2R)^3$, for a simulation with $n = 6$, $\eta_6 = 1.42 \times 10^{-12}$. Flat parts of the curves correspond to the volume-independent limit, as expected by (2.21). Curves are plotted with a constant interval of 1.0 between $t = 0.0$ (red) and $t = 15.0$ (blue), where time is in code units, as explained in the caption to Fig. 2.2. The inset shows the evolution of I_H, computed as the mean value of $\langle H_V^2 \rangle / V$ between $R = 1.3$ and $R = 1.9$.

of I_H with B and L — $I_H \sim B^4 L^5$ — this decay is very slow, i.e., (2.18) holds well. For comparison, if anastrophy were conserved, as in two dimensions, then, according to the robust Sweet-Parker scaling for $n = 4$, viz., $BL \sim$ const, $B^2 \sim t^{-3/4}$ (see Appendix 2.A), I_H would *grow*: $B^4 L^5 \sim t^{3/8}$ (and, indeed, even faster growth should be expected under the often-assumed $B^2 \sim t^{-1}$, $L \sim t^{1/2}$, since then $B^4 L^5 \sim t^{1/2}$). Thus, the distinction between our theory of non-helical decay and the conjecture of quasi-two-dimensional dynamics (Bhat *et al.*, 2021; Brandenburg *et al.*, 2015; Brandenburg & Kahniashvili, 2017) is measurable in numerical simulations, and there is strong evidence in support of the former over the latter.

The conservation of I_H may also be demonstrated from the invariance of the small-k part of the helicity-variance spectrum, $\Theta(k)$, as explained in Section 2.3.2.2. The evolution of this spectrum is shown in Fig. 2.6. The small-k part exhibits a k^2 power law, indicating that the expansion (2.29) is valid, and that I_H is finite. As the turbulence decays, the small-k part is preserved to good approximation, though there is a small amount of decay, owing to the finite scale separation between the box scale [close to which, $\Theta(k) \propto k^2$ should fail] and the energy-containing scales. Nonetheless, the behaviour is once again markedly different from what should be expected under the often-assumed $B^2 \sim t^{-1}$, $L \sim t^{1/2}$ laws. In that case, an inverse transfer of helicity variance should be expected, with the small-k part of $\Theta(k)$ growing like $B^4 L^5 \sim t^{1/2}$.

Turning to the measured decay laws, we note that, as in the helical case, the asymptotic scaling $B^4 L^5 \sim$ const will not necessarily be satisfied for a decay at finite η_n. Nevertheless, we can still measure a value of α for which $B^\alpha L \sim$ const is satisfied, and compare the measured value of the magnetic-energy decay exponent, p_M, with the one expected for a decay on Sweet-Parker or ideal timescales. The results of this comparison are shown in Fig. 2.7. While agreement with the Sweet-Parker curves (coloured) for $\alpha < 4/5$ is not quite as good as in the helical case, we still observe (*i*) a clear preference for the Sweet-Parker prediction over the prediction of a decay on ideal timescales (grey), and (*ii*) convergence to $B^{4/5} L \sim$ const for the hyper-dissipative simulations.

Finally, we describe the decay of kinetic energy. Fig. 2.8 again shows that, like in the helical case, the kinetic energy is peaked at smaller scales than the magnetic energy

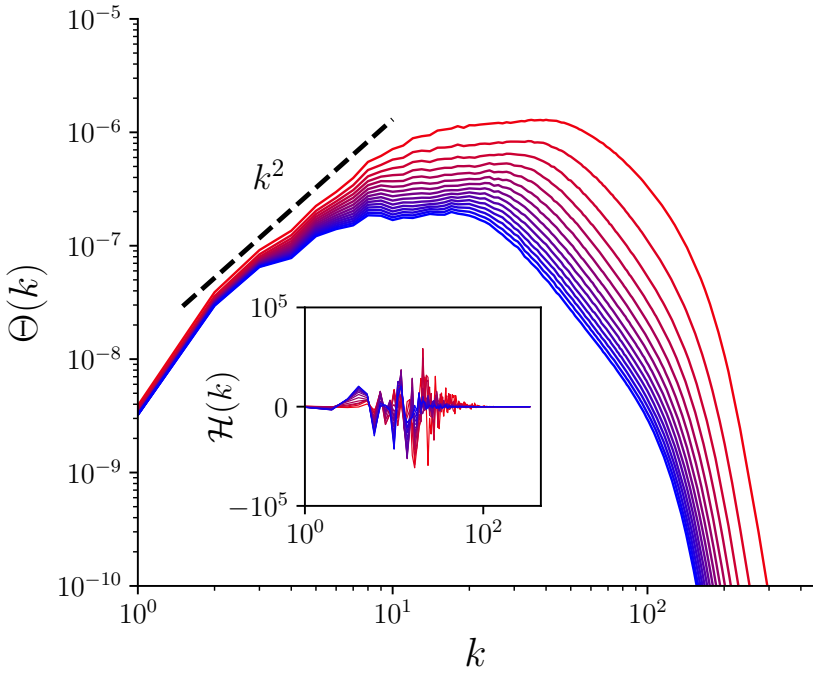

Figure 2.6: The evolution of the helicity-variance spectrum, (2.28), plotted for the same non-helical simulation and at the same times as Fig. 2.5. An invariant small-k asymptotic $\Theta(k) \propto k^2$ indicates finiteness and conservation of I_H, as explained in Section 2.3.2.2. Inset: The helicity spectrum, plotted at the same times, for reference (with linear vertical axis). While small fluctuations are present, there is no strong net helicity of either sign at any scale.

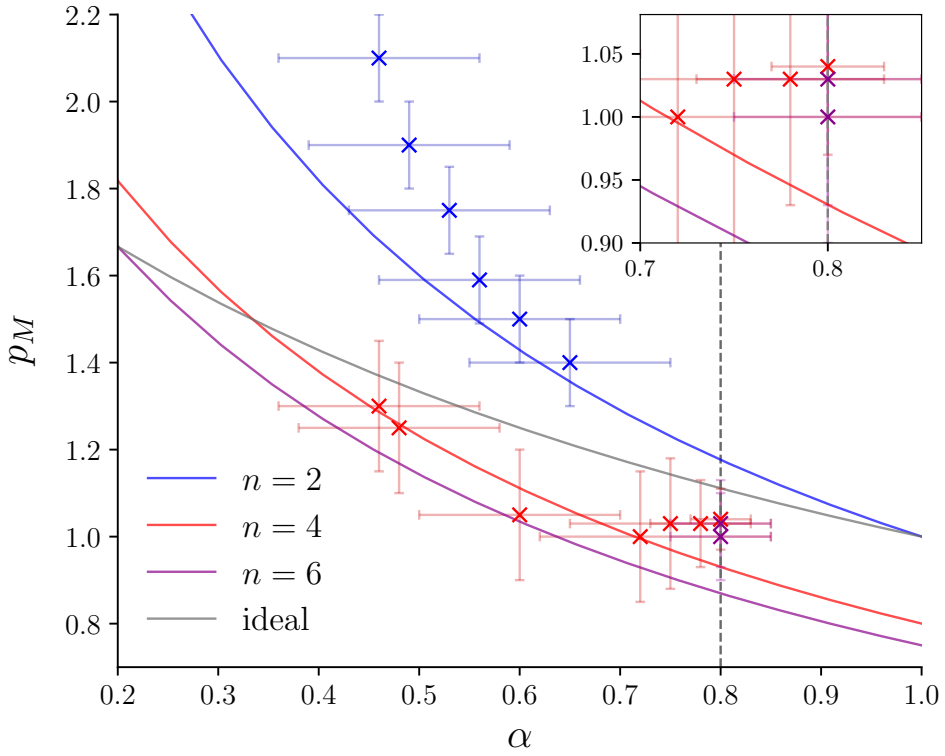

Figure 2.7: Relation between the empirically obtained magnetic-energy-decay power-law exponent, p_M, and the value of α for which $B^\alpha L \sim$ const for the non-helical simulations. As in Fig. 2.1, solid curves show the expected relationship, (2.12), for decays occurring on the Sweet-Parker timescale, with $n = 2$, $n = 4$ and $n = 6$ shown in blue, red, and magenta respectively. The grey solid curve depicts the scaling given by (2.9). Simulation results are in good agreement with the coloured curves, with better agreement as α increases towards the limiting value of 4/5. As in the helical case, simulations at the largest Lundquist numbers appear to be on the brink of the transition to the fast-reconnection regime. The full set of decay curves from which this plot was derived can be found in Appendix 2.D.

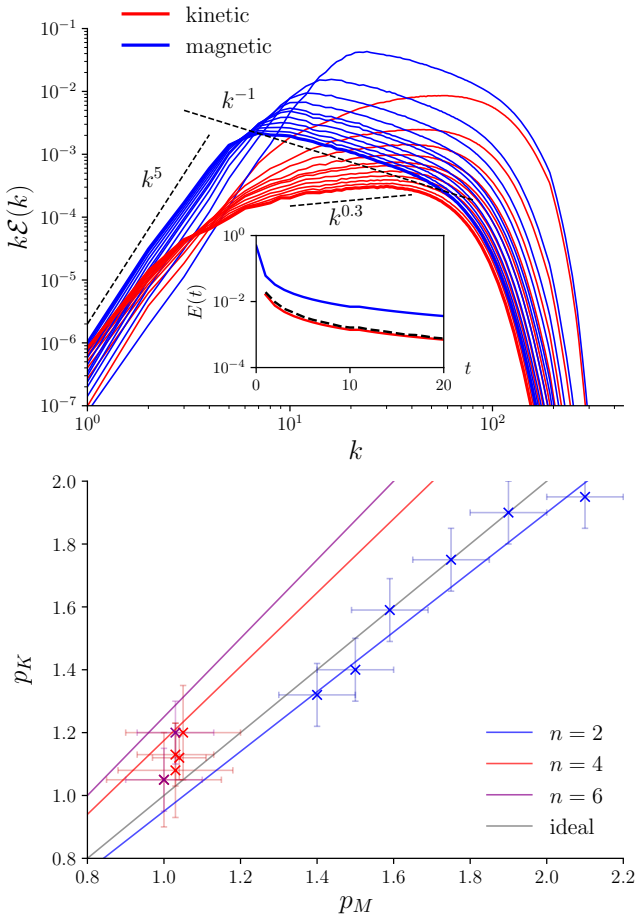

Figure 2.8: Top panel: Evolution of $k\mathcal{E}(k)$, where $\mathcal{E}(k)$ is the spectral energy density, for the magnetic (blue) and kinetic (red) energies. These plots are obtained from the non-helical simulation with $n = 4$, $\eta_4 = 2 \times 10^{-8}$. Each plot of $k\mathcal{E}(k)$ is separated by a time interval of 2.0 between $t = 1.0$ to $t = 21.0$ ($t = 21.0$ in bold), where time is in code units, as explained in the caption to Fig. 2.2. As in the helical case (Fig. 2.2), the peak of the magnetic energy is at much larger scales (smaller k) than the peak of the kinetic-energy spectrum, consistent with the expectation that the kinetic energy should be contained within the Sweet-Parker sheets. Inset: decay of the total magnetic and kinetic energies. The total kinetic energy curve is much below the magnetic energy curve, and coincides with $(\delta/L)E_M$ (black), in agreement with (2.15). Here, we compute δ/L as the ratio of the wavenumbers at which $k\mathcal{E}_M(k)$ and $k\mathcal{E}_K(k)$ peak. Bottom panel: The kinetic-energy decay exponent, p_K, against the magnetic-energy decay exponent, p_M, as measured in simulations with $S_{n,0}^{1/n} > 9.0$. Results are in reasonable agreement with the theoretical prediction, (2.32) (coloured lines), though as noted in the main text, this prediction is very similar to $E_K \propto E_M$ (grey).

is, consistent with the expectation of Alfvénic outflows in current sheets. We also find that (2.15) is very well satisfied, and a reasonable agreement with (2.32), although the magnetic- and kinetic-energy decay exponents are very close to each other.

2.3.5 The behaviour of other invariants

To conclude the discussion of numerical results, we now address the evolution of the other, better known invariants during our simulations, namely, the cross-helicity, as well as the Loitsyansky and Saffman integrals.

First, we consider the cross-helicity,

$$H_c = \int \mathrm{d}^3\boldsymbol{r}\, \boldsymbol{u}\cdot\boldsymbol{B}, \tag{2.33}$$

which is an ideal invariant of the (incompressible) MHD equations, though we find that it is not conserved in our simulations any better than energy is. In Fig. 2.9(a), we plot the average value of the squared total cross-helicity contained in a cube of volume $V = (2R)^3$, in a manner analogous to Fig. 2.5 for the magnetic helicity. We find that $\langle H_{cV}^2\rangle \sim V$ for $R \lesssim \pi/2$, as is expected from the random-walk argument. For $R > \pi/2$, $\langle H_{cV}^2\rangle/V$ increases with R but not as fast as R^3, which indicates that there is no net cross-helicity in the box. Even so, one may consider the Saffman-type integral, I_{H_c}, that is associated with cross-helicity (see Sections 2.4.4 and 2.4.5). It is given by the value of $\langle H_{cV}^2\rangle/V$ in the flat region of Fig. 2.9(a), and, as we see, decays. The reason for this behaviour is that the cross-helicity's decay rate has the same scaling with the dissipation coefficients η_n (resistivity) and ν_n (viscosity) as the decay rate of the magnetic energy does (and as is inevitable, because cross-helicity and energy have the same physical dimensions).

Likewise, the Loitsyansky integral, which encodes the statistics of angular-momentum fluctuations (Landau & Lifshitz, 1959; Davidson, 2009), is not conserved in our simulations, as is clear from the small-k part of Fig. 2.8. In Fig. 2.9(b), we plot $\langle|\boldsymbol{L}_V|^2\rangle$ against R, where $\boldsymbol{L}_V$ is the total angular momentum contained in a spherical control volume V of radius R, calculated about its centre. Presumably, this is due to injection of angular-momentum fluctuations by the reconnection outflows. Intriguingly, we observe a shift in the scaling properties of $\langle|\boldsymbol{L}_V|^2\rangle$ vs. R — at early times, $\langle|\boldsymbol{L}_V|^2\rangle \sim R^4$,

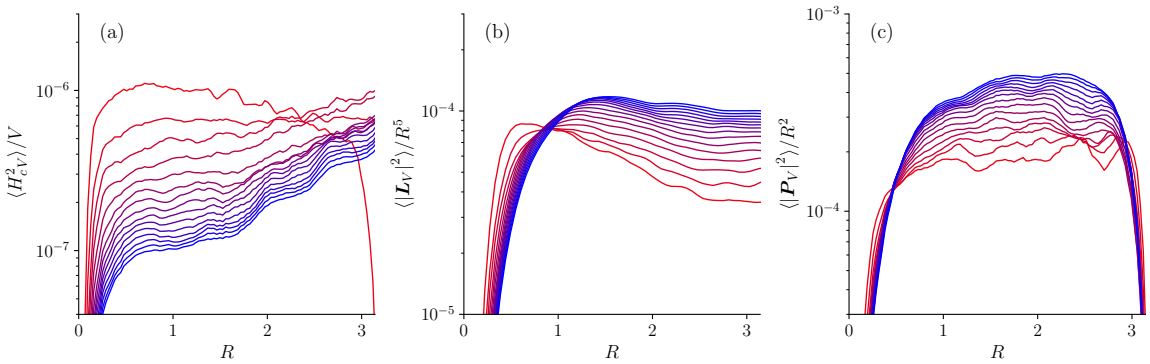

Figure 2.9: Evolution of Saffman-type invariants (other than the helicity invariant) in a non-helical simulation with $n = 6$, $\eta_6 = 1.42 \times 10^{-12}$. Curves are plotted with a constant interval of 1.0 between $t = 1.0$ (red) and $t = 15.0$ (blue), where time is in code units, as explained in the caption to Fig. 2.2. (a) $\langle H_{cV}^2 \rangle$, where H_{cV} is the cross-helicity contained in a cube with $V = (2R)^3$. While the expected random-walk scaling $\langle H_{cV}^2 \rangle \sim V$ is obeyed, $\langle H_{cV}^2 \rangle$ is not conserved. (b) $\langle |\boldsymbol{L}_V|^2 \rangle$, where $\boldsymbol{L}_V$ is the angular momentum contained in a *sphere* of radius R, about the centre of the sphere. We find $\langle |\boldsymbol{L}_V|^2 \rangle \sim R^5$, at late times, though the scaling is closer to R^4 initially. (c) $\langle |\boldsymbol{P}_V|^2 \rangle$, where $\boldsymbol{P}_V$ is the linear momentum contained in a cube with $V = (2R)^3$. We find $\langle |\boldsymbol{P}_V|^2 \rangle \sim R^2$, though the scaling appears to become somewhat stronger with time.

which is the expected scaling for 'Batchelor turbulence', i.e., when correlations between distant points are weak (Batchelor & Proudman, 1956; Davidson, 2013); subsequently, the system appears to evolve towards a state with $\langle |\boldsymbol{L}_V|^2 \rangle \sim R^5$. The latter is the 'Saffman-turbulence' scaling, and suggests strong long-range correlations in the velocity field (Davidson, 2013; Saffman, 1967). A corresponding shift in the analogous quantity for linear momentum, $\langle |\boldsymbol{P}_V|^2 \rangle$, vs. R is suggested by Fig. 2.9(c), which shows a stronger scaling than R^2 (the Batchelor scaling) for $R < \pi/2$ at later times, closer to the Saffman-turbulence scaling of R^3. This is also consistent with Figs. 2.2 and 2.8, which appear to show a decreasing slope in the large-scale kinetic-energy spectrum over time, perhaps towards $\mathcal{E}_K \propto k^2$, the hallmark of Saffman turbulence (Saffman, 1967; Davidson, 2013). This spectral behaviour has also been noted in studies by Brandenburg *et al.* (2015); Brandenburg & Kahniashvili (2017); Brandenburg *et al.* (2019), though it was considered an effect of compressibility, owing to the fact that the incompressible simulations of Berera & Linkmann (2014) appeared not to see it. However, this may just have been because there was not enough time for the k^2 velocity spectrum to establish itself before the outer scale of the turbulence reached the box size in that

study. While not present in decaying hydrodynamic turbulence (Davidson, 2013), we suggest the effect might be related to the 'thermalisation' phenomenon that is observed in forced, hydrodynamic turbulence (Dallas *et al.*, 2015; Cameron *et al.*, 2017; Alexakis & Biferale, 2018; Alexakis & Brachet, 2019). We shall address this topic specifically in Chapter 4 (Hosking & Schekochihin, 2022*b*).

Finally, for the reader concerned that the standard scalings for $\langle|\boldsymbol{L}_V|^2\rangle$ and $\langle|\boldsymbol{P}_V|^2\rangle$ referred to here are not the same as the $\propto R^3$ random-walk scalings assumed in Section 2.3.2, we show how these scalings may be obtained from the random-walk approach in Appendix 2.C. A more formal derivation of them may be found in Davidson (2013).

2.4 Discussion

2.4.1 Case of small, but non-zero, helicity

In Section 2.3, we proposed a way to impose the constraint of magnetic-helicity conservation on the decay laws of non-helical MHD turbulence, via the conservation of I_H. Of course, no real field configuration will have precisely zero helicity, and therefore it is important to consider the evolution of a field configuration with small, but non-zero, magnetic helicity. In such a case, the system will undergo a transient (though, perhaps, long) period of evolution according to the non-helical decay law $B^4L^5 \sim \text{const}$ [Eq. (2.18)], before ultimately entering the fully helical regime, with a corresponding change in the decay law to $B^2L \sim \text{const}$ [Eq. (2.6)].

This conclusion is an immediate consequence of the non-helical decay laws, as follows. Suppose that the system starts with some small helicity fraction $\sigma_0 \ll 1$, defined so that the total helicity is $H = \sigma_0 B_0^2 L_0 V$. At a later time, since helicity is conserved,

$$\sigma B^2 L = \sigma_0 B_0^2 L_0. \tag{2.34}$$

Because $\sigma_0 \ll 1$, the system is not controlled by its total helicity, at least initially. It therefore evolves according to $B^4L^5 \sim \text{const}$. Using this in (2.34), we find

$$\sigma \sim \sigma_0 \left(\frac{B}{B_0}\right)^{-6/5} \sim \sigma_0 \left(\frac{L}{L_0}\right)^{3/2}. \tag{2.35}$$

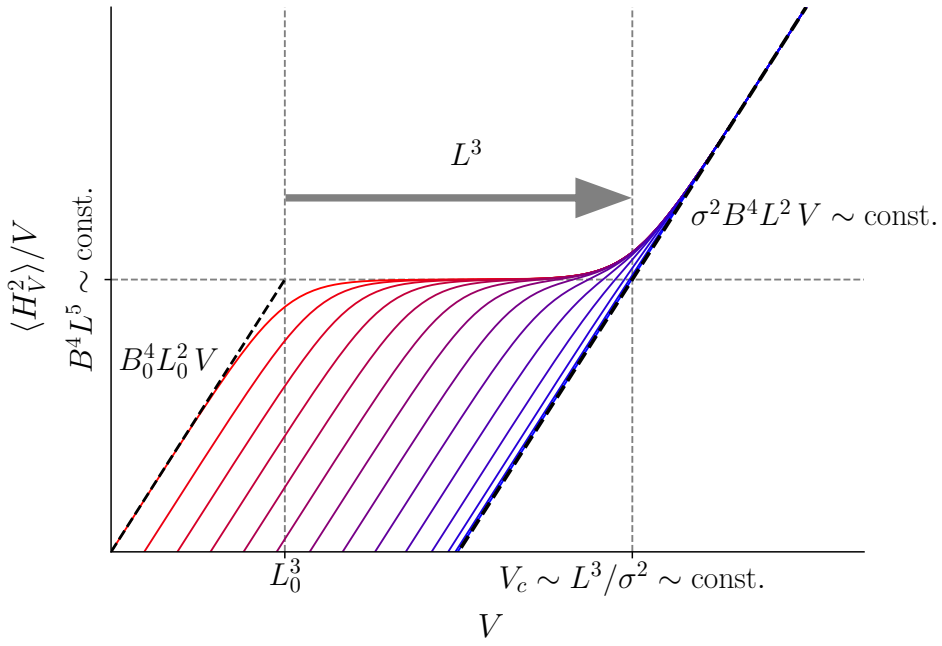

Figure 2.10: Schematic of $\langle H_V^2 \rangle / V$ as function of V, as a system with small initial fractional helicity, σ_0, transitions to the fully helical regime, as explained in the main text. The progression of time is shown by red $\rightarrow$ blue, with plots at logarithmically spaced time intervals. Note that both axes are plotted on logarithmic scales.

Thus, the helicity fraction σ will grow with time. This can continue until $\sigma \sim 1$, at which point the system enters the helical regime. This occurs when

$$B \sim B_0 \sigma_0^{5/6}, \quad L \sim L_0 \sigma_0^{-2/3}, \tag{2.36}$$

provided that the energy-containing scale L has not yet reached the system size.

This result is intuitive from the cartoon picture presented in Section 2.3: when blobs with one sign of helicity are more populous, the ultimate consequence of random mergers is for the less populous type to be used up (although this can take a long time, which scales with an appropriate negative power of σ_0, if the initial population imbalance is small).

The same conclusion can be reached from the consideration of the Saffman helicity invariant, (2.20), though some care should be taken, as I_H is formally infinite in the presence of any net helicity. However, if the helicity fraction σ is small, then we can interpret the limit $V \rightarrow \infty$ in (2.20) as requiring $L^3 \ll V \ll V_c$, where V_c is the critical volume at which H_V ceases to be dominated by the net helicity fluctuation owing to

its collection of helical structures of random signs, and instead is dominated by the helicity imbalance (see Fig. 2.10). This condition implies

$$\sigma\langle h^2\rangle^{1/2}\, V_c \sim \langle h^2\rangle^{1/2} L^3 \left(\frac{V_c}{L^3}\right)^{1/2} \implies V_c \sim \frac{L^3}{\sigma^2}. \tag{2.37}$$

For any V such that $L^3 \ll V \ll V_c$, the arguments presented in Section 2.3.2 in favour of the conservation of H_V remain valid and hence I_H still provides the dominant constraint on the decay of magnetic structures. Choosing instead $V > V_c$, $\langle H_V^2\rangle \sim \sigma^2 V B^4 L^2 \sim$ const, so we recover the evolution equation for σ, (2.34). However, when ultimately $\sigma \sim 1$, there is no longer any possibility of satisfying $L^3 \ll V \ll V_c$, because $V_c \sim L^3$. At this point, $\langle H_V^2\rangle \sim V B^4 L^2$ for any chosen volume, and we are back to the fully helical scaling, (2.6).

These arguments suggest that the non-helical decay is ultimately transient for any real system, and there will always eventually be a transition to the helical regime, provided that the growing, energy-containing scale does not reach the system size before this happens. The same conclusion was reached by Banerjee & Jedamzik (2004), although their argument was based on different non-helical decay laws than those that we have proposed. A numerical simulation demonstrating the expected transition between the two regimes would be highly desirable, but imposes considerable numerical cost, so is left for future work.

2.4.2 General decay principles

Let us now discuss how the principles that guided us in the above might be applied to other types of decaying turbulence. In any type of turbulence with an ideal invariant, $F = \int \mathrm{d}^3\boldsymbol{x}\, f(\boldsymbol{x})$, that is better conserved than the energy, the conservation of that invariant implies

$$\langle f\rangle = \lim_{V\to\infty} \frac{1}{V} \int_V \mathrm{d}^3\boldsymbol{x}\, f(\boldsymbol{x}) \sim \text{const}. \tag{2.38}$$

This is, in general form, is the 'selective decay' principle described by Taylor (1974); Montgomery *et al.* (1978); Matthaeus & Montgomery (1980); Riyopoulos *et al.* (1982); Matthaeus & Montgomery (1983); Taylor (1986); Ting *et al.* (1986).

If nonlinear structures (eddies, blobs) are necessarily in possession of F, so that the characteristic size of f can be related to the sizes and correlation scales of the dynamical fields, then (2.38) imposes a constraint on these fields that must be satisfied as the turbulence decays. In particular, if the sign of $f(\boldsymbol{x})$ within each structure is the same, either because it is sign-definite, or because the initial condition stipulates a predominance of structures of one particular sign, then $\langle f \rangle$ can be related to the characteristic sizes of dynamical fields and their correlation scales:

$$\langle f \rangle \sim \psi^a L_\psi^b \ldots, \tag{2.39}$$

where ψ is a representative dynamical field, L_ψ is its correlation scale, a and b are exponents determined by the functional form of f, and '...' denotes the possibility of other fields and scales. Together, (2.38) and (2.39) imply a constraint on the dynamical fields that must be satisfied during the decay,

$$\psi^a L_\psi^b \ldots \sim \text{const.} \tag{2.40}$$

Alternatively, for sign-indefinite f, there may be no strong predominance of structures associated with either sign of the invariant. In this case,

$$\langle f \rangle \sim \sigma \langle f^2 \rangle^{1/2} \sim \sigma \psi^a L_\psi^b \ldots, \tag{2.41}$$

where $\sigma \ll 1$ is the fractional imbalance in F, as in Section 2.4.1. While (2.38) still holds, its utility is reduced as σ is generally a function of time — the relationship

$$\sigma \langle f^2 \rangle^{1/2} \sim \sigma \psi^a L_\psi^b \cdots \sim \text{const}, \tag{2.42}$$

implied by (2.38) and (2.41), should be considered as an evolution equation for σ, rather than a constraint on ψ and L_ψ.

However, all is not lost. We propose that when $\sigma \ll 1$, conservation of *local fluctuations* in F imposes a constraint on the decay, through the associated Saffman-type integral

$$I_F = \int \mathrm{d}^3\boldsymbol{r}\, \langle f(\boldsymbol{x}) f(\boldsymbol{x}+\boldsymbol{r}) \rangle \sim \langle f^2 \rangle L_f^3 \sim \text{const}, \tag{2.43}$$

where L_f is the correlation scale of f. Again, if nonlinear structures are in possession of F, then $\langle f^2 \rangle L_f^3$ can be related to the characteristic sizes and correlation lengths of dynamical fields,

$$\langle f^2 \rangle L_f^3 \sim \psi^c L_\psi^d \ldots, \tag{2.44}$$

where c and d are different exponents than those in (2.39). Together with (2.43), this scaling leads to a different constraint on the decay,

$$\psi^c L_\psi^d \ldots \sim \text{const}, \tag{2.45}$$

which is independent of the fractional imbalance σ.

We note that an eventual transition from the balanced regime [Eqs. (2.42) and (2.45)] to the imbalanced regime [Eq. (2.40)] is a general consequence of these results, because, together, (2.42) and (2.43) imply

$$\sigma \propto L_f^{3/2}. \tag{2.46}$$

A necessary and sufficient condition for the fractional imbalance to grow is, therefore, that the scale L_f should increase with time. This tends to be the case for any realistic decay problem, even in the absence of inverse transfer of energy in k-space, because small-scale structures generally dissipate faster than large-scale ones.

The correspondence of Saffman-type invariants to the small-k asymptotics of spectra, as explained for I_H in Section 2.3.2, is also a general property: the invariant I_F is related to the spectrum of the variance of $f(\boldsymbol{x})$,

$$\Theta_F(k) \equiv \frac{k^2}{4\pi^2} \int \mathrm{d}^3\boldsymbol{r}\, \langle f(\boldsymbol{x})\, f(\boldsymbol{x}+\boldsymbol{r}) \rangle e^{-i\boldsymbol{k}\cdot\boldsymbol{r}}, \tag{2.47}$$

via

$$\Theta_F(k \to 0) = \frac{I_F k^2}{4\pi^2} + O(k^3), \tag{2.48}$$

provided that $\langle f(\boldsymbol{x})\, f(\boldsymbol{x}+\boldsymbol{r}) \rangle < O(r^{-3})$ as $r \to \infty$, and that the system is statistically isotropic (though this statement is easily reformulated for anisotropic systems). Therefore, systems that decay while respecting the conservation of a Saffman-type invariant generally have a 'permanence of large scales' principle that applies to the spectrum

of the variance of the relevant conserved quantity. This principle provides a convenient way to assess the existence and conservation of candidate invariants in numerical studies (as we did in Fig. 2.6).

To conclude this section, we note that our discussion has relied on two conditions: (*i*) that the invariant, F, is conserved, i.e., that its rate of change is smaller than the energy decay rate, and (*ii*) that it can always be considered the case that typical structures possess F, so that $\langle f \rangle$ and $\langle f^2 \rangle$ may be related to the sizes and correlation lengths of the dynamical fields, via (2.39), (2.41) and (2.44). Establishing whether (*i*) and (*ii*) holds for any given turbulent system requires some physical idea of the decay dynamics. For example, we found in Section 2.3.5 that the Saffman-type integral corresponding to cross-helicity was not conserved in our numerical simulations. Nonetheless, different dynamical processes can result in invariants being dissipated at different rates, and indeed there are plausible reasons to argue that cross-helicity (or its Saffman-type-invariant counterpart) might be conserved by the decaying turbulence of interacting nonlinear Alfvén waves, as we will explain in Section 2.4.4.

Dynamical processes may also govern whether structures possess the relevant invariants, condition (*ii*). For example, we have argued that in decaying MHD turbulence, non-helical magnetic structures tend to relax to zero energy [as is consistent with J.B. Taylor relaxation (Taylor, 1974, 1986)], so that at any given time, individual magnetic structures are maximally helical.

As a final general remark, we point out that it is possible for nonlinear structures to possess more than one invariant. If the constraints implied by the conservation of these invariants are not mutually exclusive, then they must be satisfied simultaneously. If, however, these conditions are contradictory, then it will be necessary for some of them to be broken. In that case, the decay cannot take place on the characteristic nonlinear timescale ("eddy-turnover time"), but must instead take place on the timescale on which the weaker constraint (in the sense of quality of conservation) can be broken. This is precisely the situation in magnetically dominated turbulence: magnetic helicity is not the only topological invariant associated with the magnetic field (Moffatt, 1985), and in principle all higher-order topological invariants might impose constraints on the decay. Conserving all topological invariants is not consistent with a decay in the

magnetic energy, however, because it implies $B \sim$ const. Therefore, the decay can only proceed on the timescale on which the higher-order topological constraints may be violated, i.e., the reconnection timescale. This is illustrative of a general rule that stronger, consistent constraints set the scalings between the integral scales and energies that control the decay, while inconsistent constraints set the decay timescale.

2.4.3 When the Saffman helicity invariant fails

Let us now apply the insights of Section 2.4.2 to determine the conditions under which the conservation of the Saffman helicity invariant does *not* impose a constraint on the decay of isotropic, non-helical MHD turbulence.

Naturally, this will be the case if it is zero, which is possible if each magnetic structure is *individually* non-helical, i.e., h is pointwise zero, so condition (ii) in Section 2.4.2 is violated. An example would be an ensemble of untwisted, unlinked magnetic tori, such as arise in the final stage of process (b) shown in Fig. (2.4) [2]. Such a configuration would not be prevented by the invariance of its magnetic topology from relaxing quickly under ideal dynamics, transferring magnetic energy to kinetic. The evolution should then be constrained by invariants pertaining to the velocity field, such as the Loitsyansky integral or cross-helicity — plausibly, the latter may be conserved in a net [cf. (2.38)] or fluctuating [cf. (2.43)] sense in turbulence with $U \sim B$ and similar integral scales for both fields, as we shall explain in Sections 2.4.4 and 2.4.5. In Appendix 3.C of Chapter 3, we shall present a numerical experiment initialised with unlinked magnetic tori that suggests the dynamo action of the decaying velocity field tends to restore magnetic helicity fluctuations (so $I_H \neq 0$) [also see Servidio *et al.* (2008) for a study of the tendency of MHD turbulence to form local helical patches], and thus ultimately turbulence initialised with $I_H = 0$ reorganises itself so as to decay with finite I_H according to the theory presented in Section 2.3.

While we thus acknowledge the possibility that I_H can be zero, we view such a field configuration as rather artificial. In any realistic physical scenario, it seems likely that some non-zero fraction of magnetic structures should possess helicity, whether due to twists or to linkages, so $I_H \neq 0$. Even if this fraction is not 1, we expect that

[2] We are grateful to K. Subramanian for pointing out this example to us.

individually non-helical structures should relax on ideal timescales (cf. Fig. 2.4), and the evolution of those that remain should then be constrained by conservation of I_H.

The other scenario in which the role of I_H is unclear is if the magnetic field has strong long-range correlations. If it does, then conservation of magnetic flux can also impose a constraint on the decay. For example, if (longitudinal) correlations in the magnetic field decay as r^{-3} as $r \to \infty$, the integral

$$I_{\boldsymbol{B}} \equiv \int \mathrm{d}^3\boldsymbol{r}\, \langle \boldsymbol{B}(\boldsymbol{x}) \cdot \boldsymbol{B}(\boldsymbol{x}+\boldsymbol{r}) \rangle \tag{2.49}$$

is non-zero. As we saw in (2.26), this situation corresponds to $\mathcal{E}_M(k \to 0) \propto k^2$. Because

$$I_{\boldsymbol{B}} = \lim_{V\to\infty} \frac{1}{V} \langle |\boldsymbol{\Phi}_V|^2 \rangle, \tag{2.50}$$

where $\boldsymbol{\Phi}_V = \int_V \mathrm{d}^3\boldsymbol{x}\, \boldsymbol{B}$ is the total flux contained within the control volume V, $I_{\boldsymbol{B}}$ is a Saffman-type invariant for magnetic flux [cf. Eq. (2.43)]. In light of (2.26), we note that its conservation suggests that non-helical turbulence with $\mathcal{E}_M(k \to 0) \propto k^2$ should not have an inverse energy transfer; its energy spectrum should instead obey a 'permanence of the large scales' principle. This prediction is consistent with the results of the extensive parameter study by Reppin & Banerjee (2017). On the other hand, we note that I_H and $I_{\boldsymbol{B}}$ appear to imply contradictory scaling relations for the decay: $B^4L^5 \sim$ const and $B^2L^3 \sim$ const respectively. We defer discussion of how this contradiction is resolved until Appendix 3.D of Chapter 3, where we shall argue that inverse transfer is not shut off when $I_{\boldsymbol{B}} \neq 0$, though it can only be observed over a finite range of wavenumbers. We shall find that the scaling relation $B^4L^5 \sim$ const implied by the conseration of I_H is the one that holds in the late-time limit.

2.4.4 Decay of MHD turbulence in the presence of strong mean field

In this chapter, we have so far restricted attention to the decay of isotropic MHD turbulence, i.e., MHD turbulence without a mean magnetic field. The case of turbulence with a strong mean field is fundamentally different, because then the magnetic helicity is not a conserved quantity. Formally, this is because the mean field 'sticks out' of any volume for which one might choose to compute the magnetic helicity. Intuitively, also,

this is a different situation compared to isotropic turbulence, because the constraints imposed by topology are reduced. For example, purely magnetic structures need not persist until they are able to reconnect with each other, instead they can relax by decomposing themselves into Alfvén waves travelling in opposite directions along the mean field.

Aside from energy, MHD turbulence with a strong mean field [described by the 'reduced MHD' equations (Strauss, 1976; Kadomtsev & Pogutse, 1974)] has only one conserved quantity related to the presence of the magnetic field, the cross-helicity,

$$H_c = \int \mathrm{d}^3\boldsymbol{r}\, \boldsymbol{u}_\perp \cdot \boldsymbol{b}_\perp, \tag{2.51}$$

where $\boldsymbol{u}_\perp$ is the fluid velocity perpendicular to the mean magnetic field, and $\boldsymbol{b}_\perp$ is the magnetic-field perturbation. Like magnetic helicity, the cross-helicity is sign-indefinite. In simulations of driven MHD turbulence with a strong mean field, a tendency to develop patches of strong local cross-helicity is observed, even in so-called balanced turbulence where the volume-averaged cross-helicity density is zero (Perez & Boldyrev, 2009; Stribling & Matthaeus, 1991; Ting *et al.*, 1986; Servidio *et al.*, 2008; Matthaeus *et al.*, 2008). The reason for this is that structures of large cross-helicity are also structures containing strong imbalance in the sizes of the two Elsässer fields, $\boldsymbol{Z}^\pm = \boldsymbol{u}_\perp \pm \boldsymbol{b}_\perp$. Importantly, individual Elsässer fields each represent exact nonlinear solutions to the MHD equations. Nonlinearity, and hence turbulent decay, can, therefore, only be present where both fields are present. Since $\boldsymbol{u}_\perp \cdot \boldsymbol{b}_\perp = (|\boldsymbol{Z}^+|^2 - |\boldsymbol{Z}^-|^2)/4$, a small cross-helicity density indicates balance between the Elsässer fields, and, therefore, large nonlinearity. Such structures are prone to turbulent decay. In contrast, structures with strong cross-helicity of either sign have reduced nonlinearity and, therefore, are more immune to turbulent decay.

Note, however, that these considerations need not apply to isotropic, magnetically dominated MHD turbulence decaying via reconnection, because the possession of cross-helicity does not afford immunity to reconnection. For balanced, Reduced-MHD turbulence, however, they motivate us to conjecture that the decay might be controlled by the 'Saffman cross-helicity invariant'

$$I_{H_c} = \int \mathrm{d}^3\boldsymbol{r} \langle h_c(\boldsymbol{x}) h_c(\boldsymbol{x}+\boldsymbol{r}) \rangle, \tag{2.52}$$

where $h_c = \boldsymbol{u}_\perp \cdot \boldsymbol{b}_\perp$.[3] We note that, like I_H, I_{H_c} is an example of an invariant that depends on a fourth-order correlation function. The relevance of fourth-order correlators to distinguishing between different species of decaying MHD turbulence has previously been suggested by Wan *et al.* (2012), inspired by the numerical results of Lee *et al.* (2010).

One might expect I_{H_c} to be finite and conserved by precisely the same arguments as we presented for I_H, the Saffman helicity invariant, in Section 2.3. By a random-walk-accumulation argument analogous to the one in Section 2.3.2, we have

$$I_{H_c} \sim b_\perp^2 u_\perp^2 l_\perp^2 l_\parallel, \tag{2.53}$$

where $l_\parallel$ and $l_\perp$ are the characteristic lengthscales parallel and perpendicular to the mean field, respectively. For Alfvénic motions, $b_\perp \sim u_\perp$. Note that this scaling is on much firmer ground in the mean-field case than the isotropic case, because of the absence of topological constraints associated with helicity conservation. The parallel and perpendicular length scales can be related to each other by the conjecture of critical balance (Zhou *et al.*, 2020), which states that $b_\perp/l_\perp \sim B_0/l_\parallel$, and is a cornerstone of the theory of strong MHD turbulence (Goldreich & Sridhar, 1995; Nazarenko & Schekochihin, 2011; Stawarz *et al.*, 2012). Critical balance is essentially a statement of causality: the characteristic parallel length scale of an eddy cannot be longer than the distance travelled by an Alfvén wave in one nonlinear timescale. It has been confirmed numerically to great precision in driven RMHD turbulence (Mallet *et al.*, 2015), and appears to be satisfied in decaying turbulence too (Zhou *et al.*, 2020).

Putting these scalings together, we find that $I_{H_c} \propto b_\perp^3 l_\perp^3$. If I_{H_c} is indeed conserved in decaying MHD turbulence, this implies

$$b_\perp l_\perp \sim \text{const.} \tag{2.54}$$

[3]MHD relaxation subject to net-cross-helicity conservation has been considered as part of the general selective-decay framework by Montgomery *et al.* (1978); Matthaeus & Montgomery (1980); Ting *et al.* (1986); Hossain *et al.* (1995); Wan *et al.* (2012), and has been termed 'dynamical alignment' [though this should not be confused with the use of the same term to describe the alignment of Elsässer fields in the inertial range of MHD turbulence (Perez & Boldyrev, 2009; Mallet *et al.*, 2015; Schekochihin, 2020)], owing to the tendency for a fractionally cross-helical state to reach the maximally cross-helical state (and hence, cease decaying) (Oughton *et al.*, 1994; Maron & Goldreich, 2001; Cho *et al.*, 2002; Chen *et al.*, 2011), which agrees with the general theory presented in Section 2.4.2. In the case of small or zero total cross-helicity, however, such conclusions do not apply, and one must consider the *Saffman* cross-helicity invariant, (2.52), as the relevant one.

Then, since the energies of the Elsässer fields are comparable in balanced turbulence, the turbulent decay would likely be governed by

$$\frac{\mathrm{d}E_{Z^\pm}}{\mathrm{d}t} \sim -\frac{Z^\mp E_{Z^\pm}}{l_\perp} \sim -E_{Z^\pm}^2. \tag{2.55}$$

This results in a decay of both magnetic and kinetic energy

$$E_M \sim E_K \sim t^{-1}. \tag{2.56}$$

Intriguingly, this decay law has indeed been observed in simulations of decaying, balanced RMHD turbulence, though was rationalised differently, by assuming local effective conservation of anastrophy, which also implies (2.56), as in two-dimensional MHD turbulence (Zhou *et al.*, 2020) (see Appendix 2.A).

If indeed the decay of MHD turbulence in the presence of a strong mean field conserves cross-helicity, any initial imbalance will eventually lead to a final state with maximal cross-helicity, i.e., a pure Elsässer state, according to the general argument presented in Section 2.4.2 [see (2.46)]. Such a state will not decay, since it is an exact solution of the non-linear RMHD equations. This result is consistent with the theoretical prediction of Dobrowolny *et al.* (1980), and has indeed been reported in numerical studies (Maron & Goldreich, 2001; Oughton *et al.*, 1994; Cho *et al.*, 2002; Chen *et al.*, 2011).

2.4.5 Decay of isotropic MHD turbulence from an initial state with $U \sim B$

Another problem to which the formalism developed here may be usefully applied is to the decay of isotropic MHD turbulence from an initial state with $U \sim B$, as opposed to the $B \gg U$ that we have so far considered in this chapter (apart from in Section 2.4.4). Such a state is the natural final state of the MHD dynamo [see, e.g., Rincon (2019); Schekochihin (2020) for reviews]. In such a case, we conjecture that the simultaneous conservation of magnetic helicity *and* cross-helicity might be respected by the decay, as the constraints they imply are not mutually exclusive. Such a prospect has been considered by Montgomery *et al.* (1978); Matthaeus & Montgomery (1980); Ting *et al.* (1986); Hossain *et al.* (1995); Wan *et al.* (2012) for net-cross-helical initial states — here,

however, we shall impose cross-helicity conservation via the Saffman-type-invariant formalism developed in Section 2.4.2, reflecting the fact that no strong net cross-helicity is generically present in MHD turbulence without a mean magnetic field. Naturally, checking the circumstances under which conservation of (2.52) (with $h_c = \boldsymbol{u} \cdot \boldsymbol{B}$ in the isotropic case) is valid will require a detailed numerical study, which is left for future work. However, the consequences of this conjecture merit discussion here, because they do appear to be consistent with already-existing numerical studies, and the argument demonstrates a general principle of simultaneous conservation of multiple invariants.

Let us consider a system that, as a result of dynamo or some other process, has reached equipartition between magnetic and kinetic energy, $U \sim B$, with the same integral scale L.

2.4.5.1 Helical magnetic field

First, let us assume that the magnetic field is helical, but that there is no predominance of either sign of cross-helicity. Then the conjecture of simulataneous conservation of magnetic helicity and cross-helicity (the latter as a Saffman-type invariant) implies $B^2 L \sim$ const [Eq. (2.6)] and $B^2 U^2 L^3 \sim$ const, respectively. Together, these conditions imply $U \sim B^2$, or

$$E_K \sim E_M^2 \tag{2.57}$$

precisely the condition found numerically by Biskamp & Müller (1999); Müller & Biskamp (2000), though without theoretical justification. They conjectured that the decay should take place on the timescale associated with the $\boldsymbol{u} \cdot \nabla \boldsymbol{u}$ nonlinearity in the MHD equations, i.e., L/U, which is consistent with the idea that the timescale associated with the magnetic nonlinearity $\boldsymbol{B} \cdot \nabla \boldsymbol{B}$ is effectively lengthened by topological constraints on the magnetic field. It is readily verified that such a decay leads to the power laws

$$E_K \sim t^{-1}, \quad E_M \sim t^{-1/2}, \tag{2.58}$$

as found numerically by Biskamp & Müller (1999); Müller & Biskamp (2000); Berera & Linkmann (2014).

The more rapid decay in kinetic energy will result in a state with $U \ll B$. The system should then decay in the strong-field regime described in Section 2.4.4. Denoting the small perturbations to the newly established strong magnetic field by $\delta B \sim U$, we should, according to (2.56), then have $\delta B^2 \sim U^2 \sim t^{-1}$, assuming the decay is critically balanced. Meanwhile, B^2 should decay according to the reconnection-controlled law, either $t^{-2/3}$ for fast reconnection, or $B^2 \sim t^{2n/(5n-3)}$ [Eq. (2.13)] for Sweet-Parker reconnection. For the $n = 4$ simulations employed by Biskamp & Müller (1999); Müller & Biskamp (2000), this implies

$$E_K \sim t^{-1}, \quad E_M \sim t^{-8/17}, \tag{2.59}$$

which will persist until the Sweet-Parker outflows dominate the kinetic energy, at which point the kinetic-energy law should change to the one given by (2.16), which, independently of the type of reconnection, is always slower than t^{-1}.

The decay laws given by (2.59) are very close to those of (2.58), and, therefore, either might explain the laws found numerically by Biskamp & Müller (1999); Müller & Biskamp (2000). Regardless, a more rapid decay of the kinetic than magnetic energy appears to be robust, as does the corresponding establishment of magnetically dominated state. Indeed, a magnetically dominated final state was observed in the simulations of Brandenburg *et al.* (2019), despite being initialised with $U \gg B$, with decay laws similar to (2.58) in the transient $U \sim B$ regime.

2.4.5.2 Non-helical magnetic field

Alternatively, let us consider the case of a non-helical magnetic field, initially in equipartition with the kinetic energy. Then, instead of the condition $B^2 L \sim$ const, we have $B^4 L^5 \sim$ const [Eq. (2.18)]. Together with the constraint implied by the conservation of the Saffman cross-helicity invariant, $B^2 U^2 L^3 \sim$ const, this implies $U \sim B^{1/5}$, or

$$E_K \sim E_M^{1/5}. \tag{2.60}$$

Unlike (2.57), (2.60) implies a much faster decay of the magnetic energy than the kinetic energy. However, this decay will be short lived, because the magnetic energy can be maintained at a small, but finite, fraction of the kinetic energy by dynamo. Nonetheless,

the magnetic field will always remain just below dynamical strength, because if it were to grow to dynamical levels, cross- and magnetic helicity conservation would force it to decay rapidly.

In the absence of a dynamical-strength magnetic field, the kinetic energy should decay according to the purely hydrodynamic Kolmogorov law, $E_K \sim t^{-10/7}$ [Eq. (1.3)]. Because the magnetic energy is tied to a finite fraction of the kinetic energy by the competing effects of dynamo and simultaneous cross- and magnetic-helicity conservation, it must also be the case that $E_M \propto t^{-10/7}$, i.e.,

$$E_M \propto (\text{but} <)\, E_K \sim t^{-10/7}. \tag{2.61}$$

Such a decay of E_M and E_K has indeed been observed in non-helical simulations (though initialised with $U \gg B$), by Bhat *et al.* (2021), together with evidence of dynamo action. We note, however, that it is possible that the reason E_M never grew to equipartition in these simulations was, rather, that the efficiency of the dynamo was reduced in the absence of the mean-field dynamo effect associated with helical velocity fields [see Rincon (2019) and references therein].

The arguments presented in this section, if correct, suggest a remarkable general principle: an initially helical velocity field will, due to its tendency to grow a helical magnetic field through mean-field dynamo action, eventually decay in a magnetically dominated state, with E_M, $E_K \propto t^{-2/3}$ (in the fast reconnection regime). In contrast, non-helical velocity fields will always remain in a kinetic-energy-dominated state, with E_M, $E_K \propto t^{-10/7}$.

Appendices

2.A Decay of two-dimensional turbulence

In this appendix, we review the problem of decaying two-dimensional MHD turbulence, which, like its three-dimensional counterpart, respects the conservation of an invariant associated with the topology of the magnetic field: the square of the magnetic vector potential, $\langle A^2\rangle = \langle A_z^2\rangle$ (Matthaeus & Montgomery, 1980; Hatori, 1984; Ting *et al.*, 1986; Biskamp & Welter, 1989), sometimes called 'anastrophy'. In two dimensions, anastrophy is well defined (i.e., not gauge dependent), and evolves according to

$$\begin{aligned}\left|\frac{\mathrm{d}}{\mathrm{d}t}\int_V \mathrm{d}^2\boldsymbol{r}A^2\right| &= 2\eta_n\left|\int_V \mathrm{d}^2\boldsymbol{r}\boldsymbol{A}\cdot\nabla^n\boldsymbol{A}\right| \\ &= 2\eta_n\left|\int_V \mathrm{d}^2\boldsymbol{r}\boldsymbol{B}\cdot\nabla^{n-2}\boldsymbol{B}\right| \\ &\sim \frac{\mathrm{d}E_M}{\mathrm{d}t}{\delta_\eta}^2. \end{aligned} \tag{2.62}$$

where $\mathrm{d}E_M/\mathrm{d}t = \eta_n\int \mathrm{d}^2\boldsymbol{r}\,\boldsymbol{B}\cdot\nabla^n\boldsymbol{B}$ is the rate of magnetic-energy decay due to Ohmic heating. Equation (2.62) implies that

$$\frac{\mathrm{d}\log\int_V \mathrm{d}^2\boldsymbol{r}\,A^2}{\mathrm{d}t} \sim \frac{{\delta_\eta}^2}{L^2}\frac{\mathrm{d}\log E_M}{\mathrm{d}t}, \tag{2.63}$$

which is an even slower rate of change than the one we found for the magnetic helicity in three dimensions, (2.5). Therefore, like helicity, anastrophy in two dimensions should be conserved as the turbulence decays, for $\eta_n \to 0^+$. Physically, anastrophy conservation is related to the conservation of in-plane magnetic flux (Zhou *et al.*, 2019). Unlike helicity, though, the anastrophy is manifestly positive definite, so there is only one decay regime, and no Saffman-type invariant.

The conservation of anastrophy implies

$$BL \sim \text{const}, \tag{2.64}$$

i.e., $\alpha = 1$ in (2.7). According to (2.9) and (2.12), this implies a power law decay of the magnetic energy

$$E_M \sim t^{-1}, \tag{2.65}$$

if the decay proceeds on the 'ideal' L/B timescale, and

$$E_M \sim t^{-2n/(3n-2)}, \tag{2.66}$$

for a decay proceeding on the Sweet-Parker timescale, $(L/B)\, S_n^{1/n}$. Coincidentally, these laws are the same for $n = 2$. Remarkably, the Sweet-Parker scaling for the kinetic-energy decay also turns out to be

$$E_K \sim \frac{\delta}{L} E_M \sim E_M^{(3n-2)/2n} \sim t^{-1}, \tag{2.67}$$

which is independent of n. These results mean that a decay on ideal timescales produces indistinguishable power laws ($E_K \sim E_M \sim t^{-1}$) to a decay on the $n = 2$ Sweet-Parker timescale. It is perhaps for this reason that over thirty years separates the derivation of the ideal decay law (Hatori, 1984; Biskamp & Welter, 1989) and the suggestion of a decay controlled by Sweet-Parker reconnection by Zhou *et al.* (2019). The picture presented by Zhou *et al.* (2019) is analogous to (and has inspired) the 'cartoon' model that we proposed in Section 2.3, although we observe that, as for the cartoon model in our study, the formulation based on the conservation of integral invariants, with decay proceeding on the reconnection timescale, is more general, as it does not require that pairwise mergers between structures of equal anastrophy (or helicity) be the only allowed dynamical process.

As a consequence of the degeneracy in power laws, it was confirmed by Zhou *et al.* (2019) that the Sweet-Parker timescale governed the decay in their simulations by showing that their evolution curves collapsed onto each other when time was renormalised by the initial Sweet-Parker reconnection timescale. An alternative method by which the Sweet-Parker-controlled decay can be established is via the use of hyperdissipation, in the same manner as we have done in the main part of this chapter, thanks

to hyper-dissipation lifting the power-law degeneracy. For example, from (2.66), the magnetic-energy-decay power laws are $t^{-4/5}$ and $t^{-3/4}$ for $n = 4$ and $n = 6$, respectively.

In Fig. 2.11(a-c), we show the evolution of the magnetic-energy decay rate in our two-dimensional simulations (see Table 2.1 in Appendix 2.D for details), normalised by the power of the energy to which it is proportional in the reconnection-based theory [i.e., the power of B^2 on the right-hand side of (2.11), with $\alpha = 1$]. As explained in Appendix 2.D [also, see Biskamp & Müller (1999)], such plots are preferable to more conventional plots of $\log E_M$ against $\log t$, because they give an unbiased estimate of the decay law. On these plots, horizontal curves indicate agreement with theoretical expectations. As the resistivity decreases, and hence the Lundquist number increases, Figs. 2.11(a-c) show increasingly horizontal curves, in agreement with (2.66). The insets to these figures show the scaling that would be expected if the decay proceeded via ideal motions (Hatori, 1984; Biskamp & Welter, 1989). In both cases, we find clearly decreasing curves for the largest Lundquist numbers tested, so these results are inconsistent with the 'ideal' law, (2.65).

In Fig. 2.11(d) we show E_M against $t/\tau_{\mathrm{rec},0}$, where $\tau_{\mathrm{rec},0}$ is the Sweet-Parker timescale $S^{1/2}L/B$ at the start of the self-similar decay period, which we take to occur at $t = 1$ in all cases for the purposes of this calculation. While such plots are not well-suited to an accurate determination of the decay law, they do show a clear difference in behaviour between the case of Laplacian dissipation ($n = 2$, blue) and hyper-dissipation ($n = 4$, red). As previously mentioned, the collapse of the decay curves onto each other under such a normalization was presented as evidence for a reconnection-controlled decay in two-dimensions by Zhou *et al.* (2019). Fig. 2.11(d) shows that the same behaviour occurs in the $n = 4$ hyper-dissipative case, and we find the same in the $n = 6$ case (not shown), so we agree entirely with Zhou *et al.* (2019) that the decay is controlled by reconnection.

The remaining panels of Fig. 2.11 show other relevant quantities besides the magnetic energy. In Fig. 2.11(e), we show the evolution of the hyper-Lundquist number, which is in excellent agreement with theoretical expectations based on (2.64) and (2.66). Interestingly, the hyper-Lundquist number is expected to grow when $n > 2$, so even if

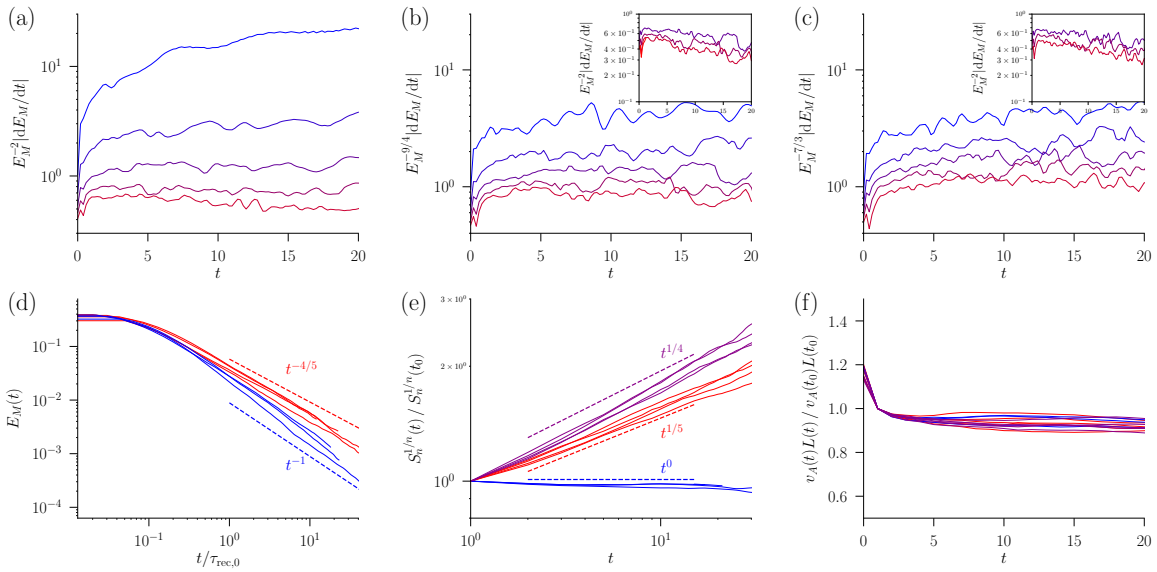

Figure 2.11: Evolution of average quantities during our two-dimensional simulations. (a) Normalised energy-decay rate for $n = 2$, (b) $n = 4$, (c) $n = 6$. In each case, a flat profile indicates agreement with the expected decay power laws, which are t^{-1}, $t^{-4/5}$ and $t^{-3/4}$, respectively [Eq. (2.66)]. Blue $\rightarrow$ red indicates increasing $S_n^{1/n}$. Insets show the scaling that would be expected if the ideal law $E_M \sim t^{-1}$ were satisfied [Eq. (2.65)]. (d) Magnetic energy evolution for $n = 2$ (blue) and $n = 4$ (red) plotted against time renormalised to the reconnection timescale at $t = 1$, as in Zhou *et al.* (2019). (e) Growth of the hyper-Lundquist number with time, for $n = 2$ (blue), $n = 4$ (red), and $n = 6$ (magenta) simulations. Dashed lines indicate the expected scalings. (f) Constancy of BL with time. N.B. the two $n = 2$ runs with smallest $S_n^{1/n}$ are not plotted in (d), (e), (f) as they do not exhibit constant BL (see Table 2.1).

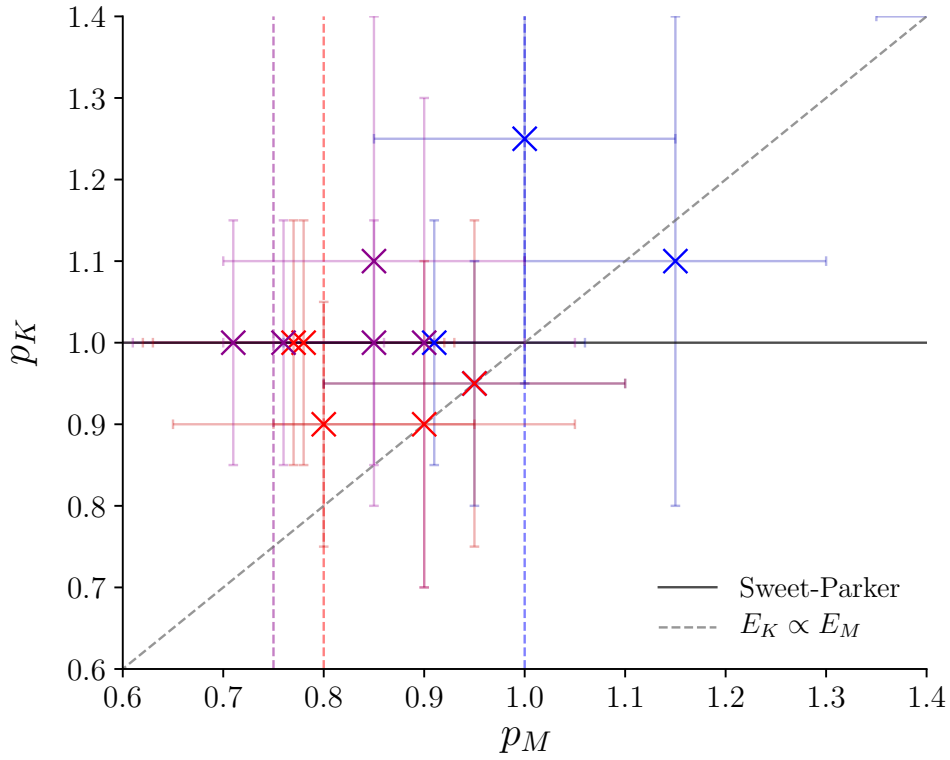

Figure 2.12: Relation between the measured magnetic- and kinetic-energy decay exponents in our two-dimensional simulations. Equation (2.67) predicts that all simulations should have $p_K = 1$, independently of p_M. While many of the simulations do fall close to this line, the evidence for $p_K = 1$ over $p_K = p_M$ is not very strong, owing to the closeness of all powers involved, and the large amount of noise in the two-dimensional simulations (see end of Appendix 2.A).

the simulation starts in the Sweet-Parker reconnection regime, it can ultimately transition to the plasmoid-dominated regime. We reiterate that in such a regime, which is formidable to simulate, the reconnection timescale becomes proportional to the ideal timescale [though longer by a factor of 10^2 (Uzdensky *et al.*, 2010)], and then we expect a transition to the 'ideal' t^{-1} decay [Eq. (2.65)]. Finally, Fig. 2.11(f) confirms that BL is indeed constant during the decay, as demanded by the conservation of anastrophy.

Consider now the decay of the kinetic energy. Fig. 2.12 shows plots of our best numerical estimates of p_K vs. p_M. While we note that most of our runs do fall close to the $p_K = 1$ line, as predicted by (2.67), the numerical evidence for $p_K = 1$ over $p_K = p_M$ is not very strong, due to the similarity between the decay laws involved. Another factor

that makes this comparison difficult is the high level of noise in the decay curves (see Fig. 2.15), which is not present in three dimensions, and arises because of the greatly reduced number of magnetic structures in the two-dimensional simulations. Because we initialise both types of simulation with the magnetic-spectral-energy density peaked at the same wavenumber, $k_p \simeq 33$ (see Appendix 2.D), there are initially ~ 33 times fewer structures in our two-dimensional runs.

2.B Alternative proof of the conservation of the Saffman helicity invariant

In this appendix, we present an alternative proof of the invariance of I_H, that follows directly from the MHD induction equation. As in Section 2.3.2, we shall rely on the assumption of rapidly decaying spatial correlations.

Restricting to the physical case of Laplacian ($n = 2$) dissipation, for simplicity, the MHD induction equation reads

$$\frac{\partial \boldsymbol{B}}{\partial t} = \boldsymbol{\nabla} \times (\boldsymbol{u} \times \boldsymbol{B} - \eta \boldsymbol{\nabla} \times \boldsymbol{B}). \tag{2.68}$$

Uncurling this equation, we have

$$\frac{\partial \boldsymbol{A}}{\partial t} = \boldsymbol{u} \times \boldsymbol{B} - \eta \boldsymbol{\nabla} \times \boldsymbol{B} + \boldsymbol{\nabla} \chi, \tag{2.69}$$

where χ is an arbitrary scalar function. From (2.68) and (2.69), it follows that

$$\frac{\partial h}{\partial t} + \boldsymbol{\nabla} \cdot \boldsymbol{F} = -2\eta \boldsymbol{B} \cdot (\boldsymbol{\nabla} \times \boldsymbol{B}) \tag{2.70}$$

where, as elsewhere, $h = \boldsymbol{A} \cdot \boldsymbol{B}$ is the magnetic helicity density, while

$$\boldsymbol{F} = \boldsymbol{u}(\boldsymbol{A} \cdot \boldsymbol{B}) - \boldsymbol{B}(\boldsymbol{A} \cdot \boldsymbol{u}) - \chi \boldsymbol{B} - \eta \boldsymbol{A} \times (\boldsymbol{\nabla} \times \boldsymbol{B}) \tag{2.71}$$

is the 'magnetic-helicity flux'. As argued in Section 2.2.1, the resistive helicity-dissipation term on the right-hand side of (2.70) is small — its size is $\eta B^2/\delta_\eta$, giving a helicity-dissipation timescale of $\sim L\delta_\eta/\eta$, which is long compared to the magnetic-energy dissipation timescale, δ_η^2/η. Dropping it, (2.70) is a continuity equation for magnetic helicity. Integrating over space, we obtain its conservation law.

Alternatively, we may use (2.70), applied at $\boldsymbol{x}$ and $\boldsymbol{x}+\boldsymbol{r}$, to compute the evolution of the two-point helicity correlation function. After taking an ensemble average, and using statistical isotropy and homogeneity, we have

$$\frac{\partial}{\partial t}\langle h(\boldsymbol{x})h(\boldsymbol{x}+\boldsymbol{r})\rangle + 2\frac{\partial}{\partial \boldsymbol{r}}\cdot\langle h(\boldsymbol{x})\boldsymbol{F}(\boldsymbol{x}+\boldsymbol{r})\rangle = 0. \tag{2.72}$$

Integrating over $\boldsymbol{r}$, assuming $\langle h(\boldsymbol{x})\boldsymbol{F}(\boldsymbol{x}+\boldsymbol{r})\rangle < O(r^{-3})$ as $r\to\infty$, (2.72) gives

$$\frac{\mathrm{d}I_H}{\mathrm{d}t} = 0. \tag{2.73}$$

The conservation of general Saffman-type invariants (see Section 2.4.2) may be shown from their corresponding continuity equations in precisely the same manner.

2.C Random-walk scalings for linear and angular momentum

In this appendix, we provide simple arguments for the scalings of $\langle|\boldsymbol{P}_V|^2\rangle$ and $\langle|\boldsymbol{L}_V|^2\rangle$ vs. R, based on the random-walk-accumulation argument employed in the main text. These are, respectively, the expectation values of the squared linear and angular momenta contained within a control volume $V\sim R^3$. In the latter case, we take V to be spherical, and compute the angular momentum about its centre. As noted in Section 2.3.5, these quantities do not necessarily scale with V as suggested by the naïve random-walk estimates employed in Section 2.3.2. However, the correct scalings may be obtained if one accounts for incompressibility, as we now demonstrate.

First, let us consider $\langle|\boldsymbol{P}_V|^2\rangle$ for a volume $V\sim R^3$. The random-walk argument put forward in Section 2.3.2 suggests that $\langle|\boldsymbol{P}_V|^2\rangle\propto R^3$. This is the correct scaling for Saffman turbulence, where the velocity field is initialised with long-range correlations and individual eddies can have non-vanishing linear momentum (Saffman, 1967; Davidson, 2013). For $\boldsymbol{u}$ initialised with a (longitudinal) correlation function that falls off with distance sufficiently rapidly (Batchelor turbulence), however, the correct scaling turns out to be $\langle|\boldsymbol{P}_V|^2\rangle\propto R^2$ (Saffman, 1967; Davidson, 2013). We can understand

this from the random-walk argument, taking into account incompressibility, as follows:

$$\langle|\boldsymbol{P}_V|^2\rangle = \left\langle \left[\int_V \mathrm{d}^3\boldsymbol{x}\,\boldsymbol{u}\right]^2 \right\rangle = \left\langle \left[\int_S \mathrm{d}\boldsymbol{S}\times\boldsymbol{\psi}\right]^2 \right\rangle$$
$$\sim L^4U^2R^2, \tag{2.74}$$

where $\boldsymbol{u}=\boldsymbol{\nabla}\times\boldsymbol{\psi}$, and we have assumed that $\int_S \mathrm{d}\boldsymbol{S}\times\boldsymbol{\psi}$ will sum as a random walk (an assumption that fails if the long-range correlations in $\boldsymbol{u}$ are strong). Therefore, the Saffman integral,

$$I_{\boldsymbol{P}} = \lim_{V\to\infty}\frac{1}{V}\langle|\boldsymbol{P}_V|^2\rangle \to 0 \tag{2.75}$$

for such turbulence. Note also that the linear-momentum fluctuation in V will not be conserved, because it is formally the same size, $\propto R$, as the net surface flux that can cause it to change. For the same reason, the conservation of the total magnetic flux $\int \mathrm{d}^3\boldsymbol{x}\,\boldsymbol{B}$ also does not provide a constraint on the decay of turbulence without strong long-range correlations in $\boldsymbol{B}$ (see Section 2.4.3 for a discussion of turbulence that does have such correlations).

Even if the Saffman integral vanishes, the local fluctuations in the linear momentum dominate $\langle|\boldsymbol{L}_V|^2\rangle$, over the local rotation of the eddies. The reason is that structures further from the origin will contribute more angular momentum than closer structures, leading to $\langle|\boldsymbol{L}_V|^2\rangle > O(R^3)$ (this effect also means that $\langle|\boldsymbol{L}_V|^2\rangle$ depends on the shape of V, which is why it was necessary to assume V to be spherical). In Saffman turbulence, where correlations are long-range and individual flow structures may have finite linear momentum, it turns out that $\langle|\boldsymbol{L}_V|^2\rangle \sim R^5$, owing to this effect (Davidson, 2013). This conclusion too can be obtained from a random-walk argument: the expected square angular momentum in a spherical shell of radius r and width δr satisfying $L \ll \delta r \ll r$, is

$$\delta\langle|\boldsymbol{L}|^2\rangle \sim r^2U_t^2L^6\,\frac{4\pi r^2\delta r}{L^3}, \tag{2.76}$$

where U_t is the typical size of the net translational velocity of a structure. Assuming any two shells are uncorrelated, the total square angular momentum is simply the sum over all shells of (2.76). Integrating over r, we get

$$\langle|\boldsymbol{L}_V|^2\rangle \sim U_t^2L^3R^5. \tag{2.77}$$

Like (2.74), the scaling (2.77) is also adjusted by incompressibility when correlations fall off quickly with distance. This is because

$$\boldsymbol{L}_V = \int_V \mathrm{d}^3\boldsymbol{r}\, \boldsymbol{r} \times \boldsymbol{u} = \int_V \mathrm{d}^3\boldsymbol{r}\, \boldsymbol{r} \times (\nabla \times \boldsymbol{\psi}). \tag{2.78}$$

Integrating by parts and expanding the double cross product gives

$$(\boldsymbol{L}_V)_i = -\int_{\partial V} \mathrm{d}S \left(\delta_{ij} - \frac{r_i r_j}{r^2}\right) r\psi_j + 2\int_V \mathrm{d}^3\boldsymbol{r}\, \psi_i, \tag{2.79}$$

where we have chosen V to be spherical. Since $\boldsymbol{\psi}$ is a random field, the first integral scales as R^2, so it dominates over the second, which scales as $R^{3/2}$. Therefore, (2.79) implies

$$\langle |\boldsymbol{L}_V|^2 \rangle \sim U_t^2 L^4 R^4. \tag{2.80}$$

As above, whether ultimately (2.77) or (2.80) provides the correct scaling depends on the strength of long-range correlations between eddies. A formal derivation of these statements may be found in (Davidson, 2013).

In either case, the scaling of $\langle |\boldsymbol{L}_V|^2 \rangle$ is different to the naïve expectation, $\langle |\boldsymbol{L}_V|^2 \rangle \sim R^3$, which assumes all eddies to have no translational motion. In that case, the angular momentum of an eddy at a distance r from the origin is $\sim [(r+L)U_r - (r-L)U_r]\, L^3 \sim U_r L^4$, where U_r is the typical rotational velocity of a structure. Then (2.76) becomes

$$\delta\langle |\boldsymbol{L}|^2 \rangle \sim U_r^2 L^8\, \frac{4\pi r^2 \delta r}{L^3}, \tag{2.81}$$

whence

$$\langle |\boldsymbol{L}_V|^2 \rangle \sim U_r^2 L^5 R^3. \tag{2.82}$$

In summary, while the scalings of $\langle |\boldsymbol{P}_V|^2 \rangle$ and $\langle |\boldsymbol{L}_V|^2 \rangle$ with R are modified from the naïve R^3, the correct application of the random-walk argument, taking into account incompressibility, and the greater contribution of more distant structures to $\langle |\boldsymbol{L}_V|^2 \rangle$, does result in the correct scalings. We therefore do not consider there to be an essential problem with the application of the random-walk argument in our treatment of the Saffman helicity invariant in Section 2.3.2, or in our discussion of general invariants in Section 2.4.2, though it should be understood that some of these scalings may have to be modified for particular conserved quantities that do not scale with R in the naïve way.

2.D Numerical setup and simulation details

The numerical simulations presented in this chapter were conducted with the spectral MHD code Snoopy (Lesur, 2015). The code solves the equations of incompressible MHD with hyper-viscosity and hyper-resistivity both of order n, viz.,

$$\frac{\partial \boldsymbol{u}}{\partial t} + \boldsymbol{u}\cdot\boldsymbol{\nabla}\boldsymbol{u} = -\boldsymbol{\nabla}p + (\boldsymbol{\nabla}\times\boldsymbol{B})\times\boldsymbol{B} + \nu_n\nabla^n\boldsymbol{u}, \tag{2.83}$$

$$\frac{\partial \boldsymbol{B}}{\partial t} = \boldsymbol{\nabla}\times(\boldsymbol{u}\times\boldsymbol{B}) + \eta_n\nabla^n\boldsymbol{B}, \tag{2.84}$$

where p, the thermal pressure, is determined via the incompressibility condition

$$\boldsymbol{\nabla}\cdot\boldsymbol{u} = 0. \tag{2.85}$$

In all our runs, $\mathrm{Pm} \equiv \nu_n/\eta_n = 1$. The code employs a pseudo-spectral algorithm in a periodic box of size 2π, with a 2/3 dealiasing rule. Snoopy performs time integration of non-dissipative terms using a low-storage, third-order, Runge-Kutta scheme, whereas dissipative terms are solved using an implicit method that preserves the overall third-order accuracy of the numerical scheme [comparisons between the results of Snoopy and other popular MHD codes for various nonlinear problems may be found in Fromang *et al.* (2007); Gong *et al.* (2020); Squire *et al.* (2020); also see Kunz & Lesur (2013) for a test of Snoopy's Hall-MHD module]. Units of time are chosen so that the initial magnetic energy is $E_M = 1/2$ (i.e., the unit of time is the initial Alfvén crossing time of the box).

We initialise the simulations with a magnetic field whose Fourier representation is

$$B_j(\boldsymbol{k}) = \left[i\epsilon_{jlm}\frac{k_m}{k} + sP_{jl}(\boldsymbol{k})\right]F(k)\,G_l(\boldsymbol{k}), \tag{2.86}$$

where $P_{ij}(\boldsymbol{k}) = \delta_{ij} - k_ik_j/k^2$ is the projection operator perpendicular to $\boldsymbol{k}$, $G_i(\boldsymbol{k})$ is the Fourier transform of a two- or three-dimensional Gaussian random field with zero correlation length. The parameter s controls the helicity — $s = 1$ for a helical field, $s = 0$ for a non-helical field — and is related to the fractional helicity, σ, discussed in Section 2.4.1 by $\sigma = 2s/(1+s^2)$ (Brandenburg *et al.*, 2019). The function $F(k)$ sets the initial spectrum of the field:

$$F(k) = A\begin{cases} k^{(a-D+1)/2}, & k < k_c, \\ k^{(a-D+1)/2}\exp(1-k^2/k_c^2), & k > k_c, \end{cases} \tag{2.87}$$

where $D = 2$, 3 is the number of spatial dimensions, a is the initial spectral exponent of the sub-inertial range (small k), and k_c sets the initial peak of the magnetic-energy spectrum, k_p, via $k_p = (7/4)^{1/2}\, k_c$. In all runs, we set $a = 7$, and $k_c = 25 \implies k_p \simeq 33$, so that the magnetic energy is initialised at scales $\simeq 1/33$ of the box size. We note that the initial k^7 sub-inertial-range spectrum is different from the k^4 spectrum (or k^3 in two dimensions) that the system quickly establishes in the subsequent evolution (see Figs. 2.2 and 2.8; see also Davidson (2013) for a discussion of the role of the large-scale spectrum in decaying hydrodynamic turbulence). Our choice to initialise the simulation with this spectrum was motivated by a finding in our exploratory runs that the transient period before the system entered a period of power-law decay was shorter when the large-scale slope was allowed to establish itself organically. Presumably, this is because even if the spectral exponent is the right one, the structure of the synthetic field, (2.86), is not, so it is better not to prejudice the system and let it decide for itself what structures to create at large scales ($k < k_p$).

We measure the decay exponents p_M and p_K by plotting $|{E_i}^{1+1/p_i} \mathrm{d}E_i/\mathrm{d}t|$ against time, selecting the parameter p_i ($i = M$, K) so as to obtain a flat curve. As noted by Biskamp & Müller (1999), plots of this type give an unbiased estimate of the decay laws, as compared to more conventional logarithmic plots of E against t. The reason for this is that, because the power-law behaviour is only established after a short time t_0 following the initialization of the simulation, a plot of $E \sim (t - t_0)^{-p}$ against t has a bias towards large energies, which decreases over time, giving the false impression of a steeper power law. Furthermore, a logarithmic t-axis exaggerates the importance of the initial times, during which the system has, in fact, not established a steady-state decay. In a similar way, we establish the value of α in (2.7) by plotting $E_M^{\alpha/2} L$ against time and selecting the value of α to give a flat curve. The power laws and values of α thus obtained are given for all our runs in Table 2.1, together with the resolution and initial Lundquist number for each run. For reference, the plots from which these results are obtained are shown in Figs. 2.13, 2.14 and 2.15. Also plotted there are the curves obtained using the values of p_M, p_K, and α at the extremes of the error bars in Figs. 2.1, 2.2(b), 2.7, 2.8(b) and 2.12, to give a sense of the precision with which these results hold.

Type	n	Resolution	$\eta_n = \nu_n$	$S_{n,0}^{1/n}$	α	p_M	p_K
H.	2	576^3	8.92×10^{-4}	14.59	0.93	1.07	1.20
H.	2	576^3	6.08×10^{-4}	17.68	1.16	0.85	1.00
H.	2	576^3	4.14×10^{-4}	21.42	1.37	0.76	0.92
H.	2	576^3	2.82×10^{-4}	25.93	1.52	0.70	0.85
H.	2	576^3	1.92×10^{-4}	31.44	1.64	0.69	0.83
H.	2	576^3	1.31×10^{-4}	38.09	1.74	0.66	0.85
H.	4	576^3	2.00×10^{-5}	4.30	0.30	1.80	1.15
H.	4	576^3	9.28×10^{-6}	5.21	0.45	1.25	1.20
H.	4	576^3	6.32×10^{-6}	5.74	0.58	1.00	1.15
H.	4	576^3	4.31×10^{-6}	6.32	0.90	0.75	0.97
H.	4	576^3	2.94×10^{-6}	6.95	1.40	0.59	0.76
H.	4	576^3	2.00×10^{-6}	7.65	1.60	0.56	0.95
H.	4	576^3	2.00×10^{-7}	13.61	1.93	0.56	0.95
H.	4	576^3	2.00×10^{-8}	24.20	1.99	0.56	0.91
H.	4	1152^3	2.00×10^{-9}	43.03	2.00	0.56	0.90
H.	6	576^3	4.48×10^{-11}	13.29	1.98	0.60	0.90
H.	6	576^3	1.42×10^{-12}	23.64	2.00	0.60	1.00
NH.	2	576^3	8.92×10^{-4}	14.59	0.46	2.10	1.95
NH.	2	576^3	6.08×10^{-4}	17.68	0.49	1.90	1.90
NH.	2	576^3	4.14×10^{-4}	21.42	0.53	1.75	1.75
NH.	2	576^3	2.82×10^{-4}	25.93	0.56	1.59	1.59
NH.	2	576^3	1.92×10^{-4}	31.44	0.60	1.50	1.40
NH.	2	576^3	1.31×10^{-4}	38.09	0.65	1.40	1.32
NH.	4	576^3	5.0×10^{-6}	6.09	0.48	1.25	1.30
NH.	4	576^3	2.0×10^{-6}	7.65	0.46	1.30	1.30
NH.	4	576^3	1.0×10^{-6}	9.10	0.60	1.05	1.20
NH.	4	576^3	5.0×10^{-7}	10.82	0.72	1.00	1.05
NH.	4	576^3	2.0×10^{-7}	13.61	0.75	1.03	1.08
NH.	4	576^3	2.0×10^{-8}	24.20	0.78	1.03	1.13
NH.	4	1152^3	2.0×10^{-9}	43.03	0.80	1.04	1.12
NH.	6	576^3	4.48×10^{-11}	13.29	0.80	1.00	1.05
NH.	6	576^3	1.42×10^{-12}	23.64	0.80	1.03	1.20
2D	2	1152^2	8.92×10^{-4}	14.59	0.55	1.50	1.40
2D	2	1152^2	2.82×10^{-4}	25.93	0.80	1.15	1.10
2D	2	2304^2	8.92×10^{-5}	46.15	0.98	1.00	1.25
2D	2	2304^2	2.82×10^{-5}	82.01	1.00	0.95	0.95
2D	2	4608^2	8.92×10^{-6}	145.94	0.97	0.91	1.00
2D	4	1152^2	2.0×10^{-7}	13.61	0.90	0.95	0.95
2D	4	1152^2	2.0×10^{-8}	24.20	1.00	0.90	0.90
2D	4	2304^2	2.0×10^{-9}	43.03	1.00	0.80	0.90
2D	4	2304^2	2.0×10^{-10}	76.52	0.95	0.77	1.00
2D	4	4608^2	2.0×10^{-11}	136.08	0.95	0.78	1.00
2D	6	1152^2	4.48×10^{-11}	13.29	0.98	0.90	1.00
2D	6	1152^2	1.42×10^{-12}	23.64	1.02	0.85	1.10
2D	6	2304^2	4.48×10^{-14}	42.04	1.00	0.85	1.00
2D	6	2304^2	1.42×10^{-15}	74.76	1.00	0.76	1.00
2D	6	4608^2	4.48×10^{-17}	132.95	0.97	0.71	1.00

Table 2.1: Details of all simulations, together with the measured decay exponents and the values of α such that $B^\alpha L \sim$ const.

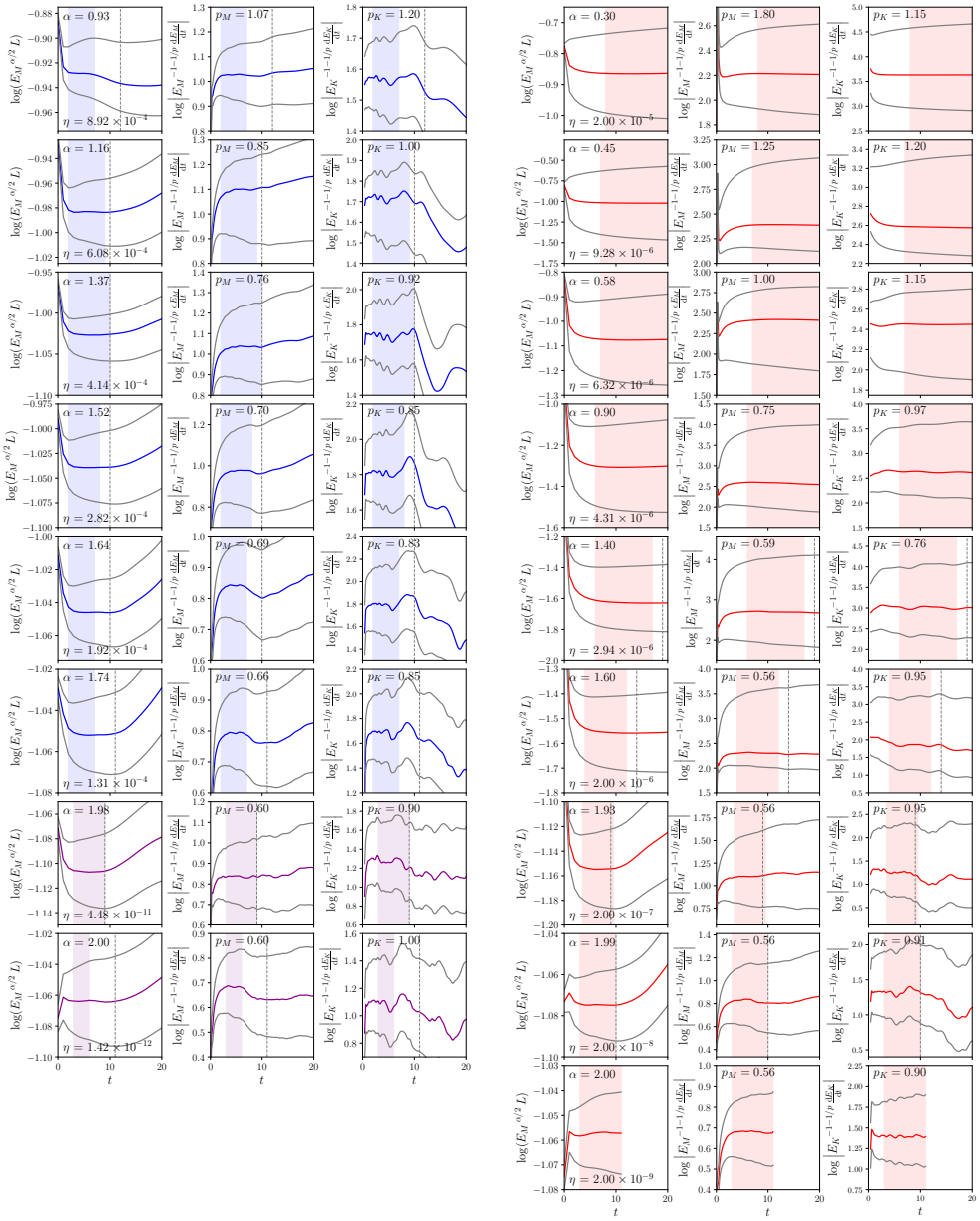

Figure 2.13: Plots used to obtain the parameters α (left), p_M (centre) and p_K (right), for each helical simulation. Simulations with $n = 2$, $n = 4$, and $n = 6$ hyper-dissipation are plotted in blue, red and magenta, respectively. In each case, a horizontal line indicates agreement with the stated value. The shaded region indicates the times at which the decay laws appear to be valid. Grey lines correspond to the values of α, p_M, and p_K at the extremes of the error bars shown in Figs. 2.7 and 2.8. Dashed lines show the time at which $L = 2\pi/5$, i.e., when magnetic structures have scale $1/5$ of the box size, which we find to be roughly the time at which finite-box-size effects begin to affect the decay laws.

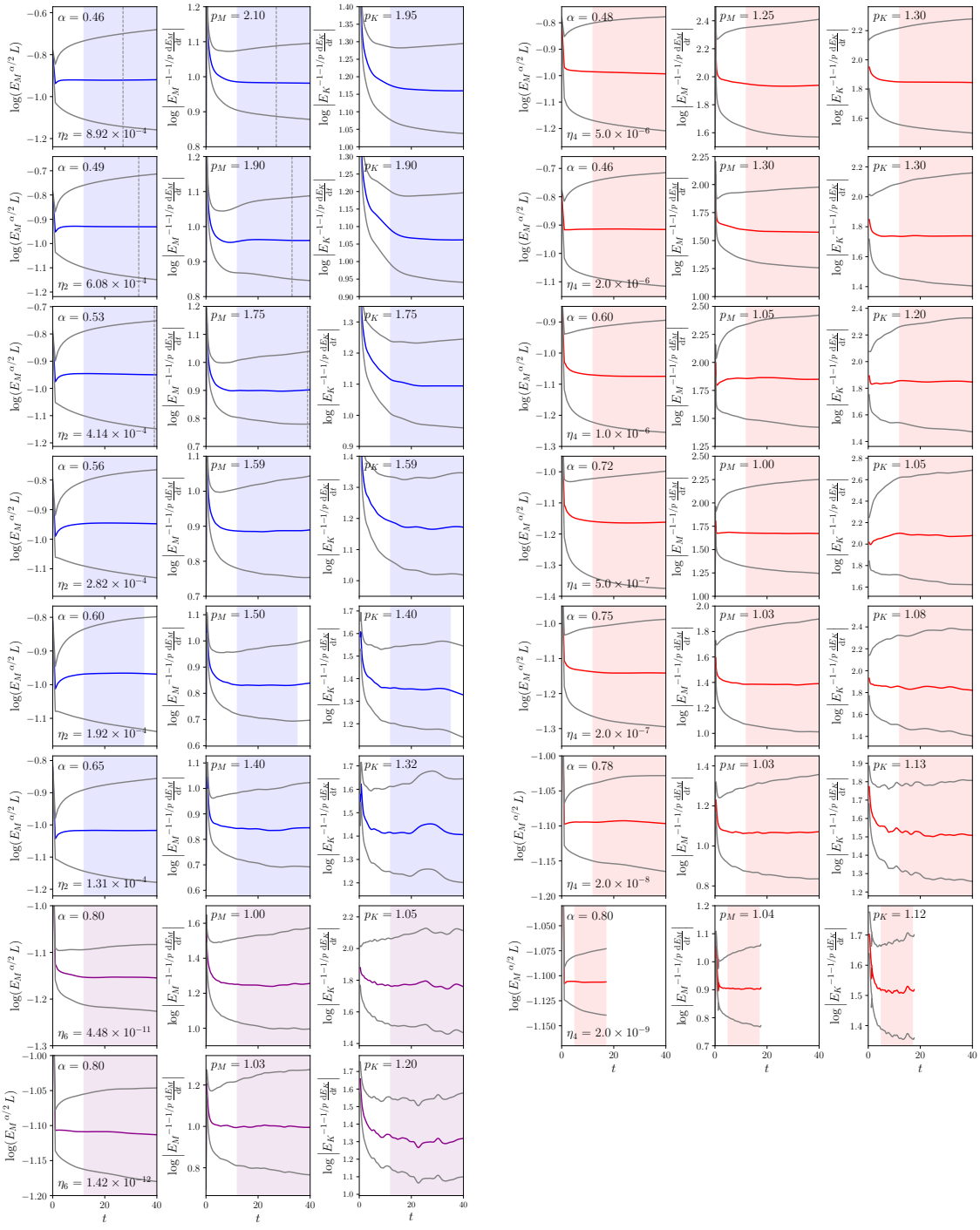

Figure 2.14: Same as Fig. 2.13, but for non-helical simulations.

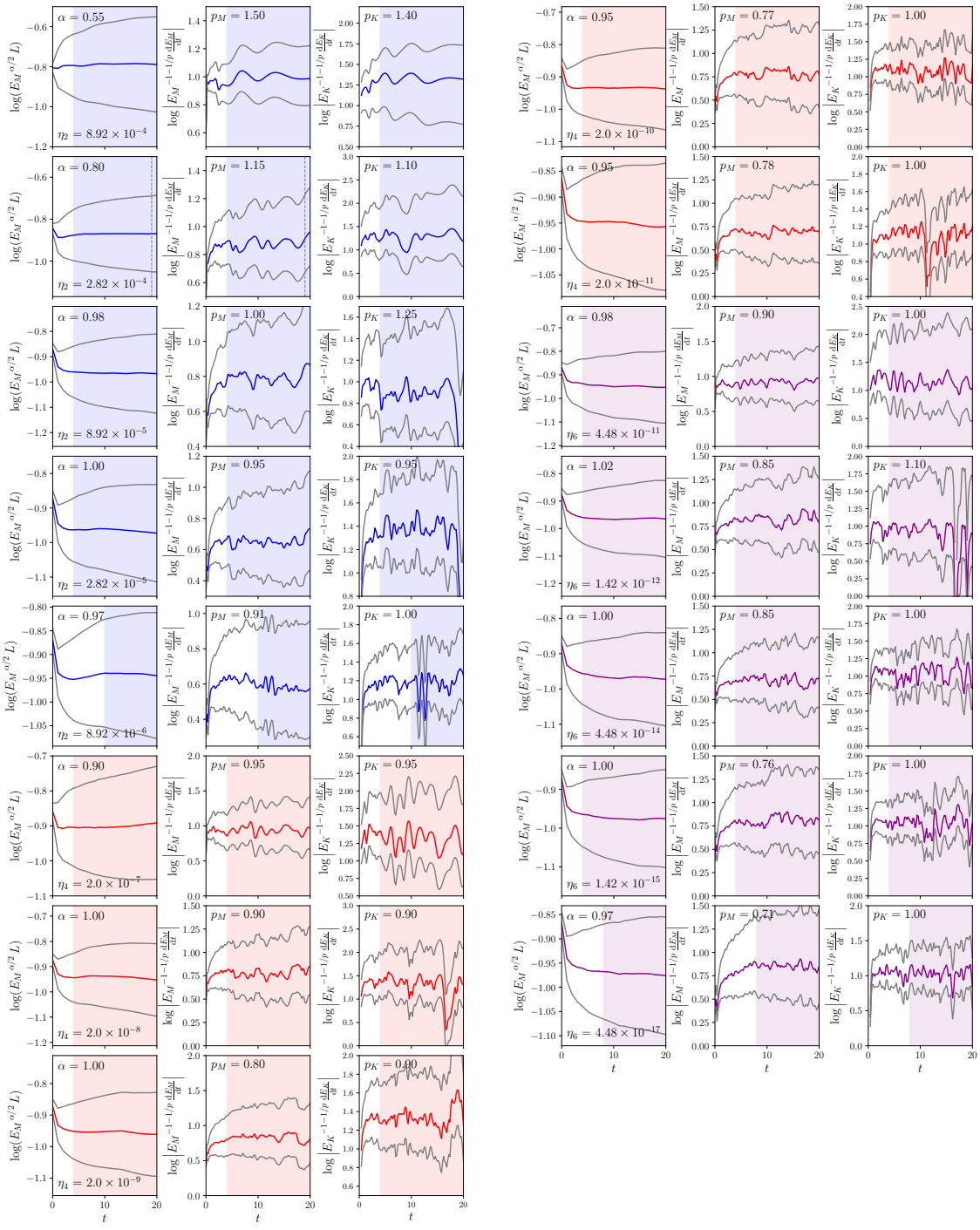

Figure 2.15: Same as Fig. 2.13, but for two-dimensional simulations.

Chapter 3

The primordial origin of void magnetic fields

This chapter is adapted from Hosking & Schekochihin (2022a), arxiv:2203.03573.

It has been suggested that the weak magnetic field hosted by the intergalactic medium (IGM) in voids could be a relic from the early Universe [see Durrer & Neronov (2013); Subramanian (2016); Vachaspati (2021) and references therein]. However, accepted models of turbulent magnetohydrodynamic (MHD) decay predict that the present-day strength of fields generated at the electroweak phase transition (EWPT) should be too low to explain the observed scattering of γ-rays from TeV blazars (Neronov & Vovk, 2010; Wagstaff & Banerjee, 2016; Taylor *et al.*, 2011). Here, we apply the theoretical developments of Chapter 2 — namely, the discovery of the Saffman helicity invariant (Hosking & Schekochihin, 2021) and of the role of magnetic reconnection in setting the decay rate (Hosking & Schekochihin, 2021; Zhou *et al.*, 2019, 2020; Bhat *et al.*, 2021) — to show that the accepted models greatly underpredict the present-day strength of relic fields. Our estimates restore the consistency of the EWPT-relic hypothesis with observational constraints; moreover, we find that efficient magnetogenesis at the EWPT could produce relics with the strength that is believed sufficient to resolve the Hubble tension (Jedamzik & Pogosian, 2020; Galli *et al.*, 2022) and explain galaxy-cluster magnetic fields without invoking dynamo amplification (Banerjee & Jedamzik, 2003).

Two essential quantities that parameterise the state of a stochastic, statistically isotropic magnetic field are its root-mean-square strength $B \equiv \langle \boldsymbol{B}^2 \rangle^{1/2}$ and its integral, or correlation, scale, which we shall now denote λ_B rather than L for consistency with the existing literature on primoridal magnetic fields. For extragalactic magnetic fields (EGMFs) in voids, B and λ_B are constrained by γ-ray observations [Neronov & Vovk (2010); see Durrer & Neronov (2013); Subramanian (2016); Vachaspati (2021) for reviews]: TeV γ-rays from blazars pair-produce high-energy electrons in voids, which emit secondary γ-rays in an electromagnetic cascade. EGMFs scatter these electrons, resulting in a reduction of the secondary γ-rays received at Earth. Using spectra measured by the *Fermi* telescope, Taylor *et al.* (2011) estimate that

$$B \gtrsim 10^{-17}\,\mathrm{G} \left(\frac{\lambda_B}{1\,\mathrm{Mpc}} \right)^{-1/2}, \tag{3.1}$$

where $10^{-17}\,\mathrm{G}$ turns into $10^{-15}\,\mathrm{G}$ if the possibility of certain photon-travel-time effects is excluded. Wagstaff & Banerjee (2016) argue that this lower bound on B is too high to be consistent with a primordial magnetic field (PMF) generated at the EWPT without magnetic helicity. Furthermore, they show that the amount of magnetic helicity required for consistency with (3.1) is greater than can be generated by baryon asymmetry at the EWPT, as estimated by Vachaspati (2001). In principle, other mechanisms of magnetic-helicity generation may have been present in the early Universe; one idea is *chiral MHD* [see Boyarsky *et al.* (2021) and references therein]. Whether enough net helicity can be generated via these mechanisms for PMFs to become maximally helical during their evolution remains an open question (for completeness, we present in Appendix 3.B some results for helical fields that are analogous to the ones presented in the main part of this chapter).

On the other hand, Wagstaff & Banerjee (2016) note that their conclusions could be subject to modification by the contemporaneous discovery of "inverse transfer" of magnetic energy in simulations of non-helical MHD turbulence (Zrake, 2014; Brandenburg *et al.*, 2015). Recently, this effect was explained as a consequence of *local fluctuations* in the magnetic helicity, which may be present even when the global helicity vanishes — see Section 2.3.2.2 of Chapter 2 (Hosking & Schekochihin, 2021). In this chapter, we demonstrate how this insight, together with the other key result of Chapter 2, and

of Zhou *et al.* (2019, 2020); Bhat *et al.* (2021), that the decay timescale is the one on which magnetic fields reconnect, restores consistency of the hypothesis of a non-helical EWPT-generated PMF with Eq. (3.1).

We consider a flat, expanding Universe with metric

$$\mathrm{d}s^2 = a^2(t)(-\mathrm{d}t^2 + \mathrm{d}x_i\,\mathrm{d}x^i), \tag{3.2}$$

where $a(t)$ is the scale factor, normalised to 1 at the present day, t is conformal time (related to cosmic time $\bar{t}$ by $a(t)\mathrm{d}t = \mathrm{d}\bar{t}$), and x_i are comoving coordinates. The expanding-Universe MHD equations can be transformed to those for a static Universe by a simple rescaling (Brandenburg *et al.*, 1996): the scaled variables

$$\begin{aligned} \tilde{\rho} = a^4\rho, \quad \tilde{p} = a^4 p, \quad \tilde{\boldsymbol{B}} = a^2\boldsymbol{B}, \quad \tilde{\boldsymbol{u}} = \boldsymbol{u}, \\ \tilde{\eta} = \eta/a, \quad \tilde{\nu} = \nu/a, \end{aligned} \tag{3.3}$$

[where ρ, p, $\boldsymbol{B}$, $\boldsymbol{u}$, η and ν are the physical values of the total (matter + radiation) density, pressure, magnetic field, velocity, magnetic diffusivity and kinematic viscosity, respectively] evolve according to the MHD equations in Minkowski spacetime. As in previous work [see Durrer & Neronov (2013); Subramanian (2016); Vachaspati (2021)], we consider the dynamics of the "tilded" variables in Minkowski spacetime and transform the result to the spacetime (3.2) of the expanding Universe via (3.3).

Previous treatments of PMF evolution have assumed that statistically isotropic MHD turbulence decays while preserving the small-k asymptotic of the magnetic-energy spectrum $\mathcal{E}_M(k)$ [see Durrer & Neronov (2013); Subramanian (2016) and references therein]. As was noted in Section 2.3.2.2 of Chapter 2, this idea (sometimes called "selective decay of small-scale structure") amounts to a statement of the invariance in time of the "magnetic Loitsyansky integral",

$$I_{\boldsymbol{L}_M} \equiv -\int \mathrm{d}^3\boldsymbol{r}\, r^2 \langle \tilde{\boldsymbol{B}}(\boldsymbol{x}) \cdot \tilde{\boldsymbol{B}}(\boldsymbol{x}+\boldsymbol{r})\rangle, \tag{3.4}$$

which, for isotropic turbulence without long-range spatial correlations, is related to $\mathcal{E}_M(k)$ by

$$\mathcal{E}_M(k \to 0) = \frac{I_{\boldsymbol{L}_M} k^4}{24\pi^2} + O(k^6). \tag{3.5}$$

Invariance of $I_{\boldsymbol{L}_M}$ implies

$$I_{\boldsymbol{L}_M} \sim \tilde{B}^2 \lambda_B^5 \sim \text{const}, \tag{3.6}$$

which can be translated into a decay law for magnetic energy by a suitable assumption about how the energy-decay timescale,

$$\tau\left(\tilde{B}, \lambda_B, t\right) \equiv -\left(\frac{\mathrm{d}\log \tilde{B}^2}{\mathrm{d}t}\right)^{-1}, \tag{3.7}$$

depends on $\tilde{B}$, λ_B and t. Regardless of this choice, (3.6) and (3.7) have the following important property. Suppose that, after some intermediate time t_c, $\tau(B, \lambda_B, t)$ can be approximated by some particular product of powers of its arguments. Then, for all $t \gg \tau(t_c)$, $\tilde{B}^2$ decays as a power law: $\tilde{B}^2 \propto t^{-p}$, where p is a number of order unity. Substituting this back into (3.7), one finds (Banerjee & Jedamzik, 2004)

$$\tau\left(\tilde{B}, \lambda_B, t\right) \sim t, \tag{3.8}$$

which is an implicit equation for $\tilde{B} = \tilde{B}(\lambda_B)$ that can be solved simultaneously with (3.6) for $\tilde{B}(t)$ and $\lambda_B(t)$. Note that doing so requires no knowledge of τ during the early stages of the decay; $\tilde{B}(t)$ and $\lambda_B(t)$ are independent of it.

Assuming that the decay satisfies (3.6) and that its timescale is Alfvénic, viz.,

$$\tau \sim \frac{\lambda_B}{\tilde{v}_A}, \quad \tilde{v}_A = \frac{\tilde{B}}{\sqrt{4\pi\tilde{\rho}_b}}, \tag{3.9}$$

when it terminates at the recombination time t_{recomb} (Subramanian, 2016) [Eq. (3.27) in Appendix 3.A], (3.8) implies (Banerjee & Jedamzik, 2004)

$$\tilde{B}(t_{\mathrm{recomb}}) \sim 10^{-8.5}\,\mathrm{G}\,\frac{\lambda_B(t_{\mathrm{recomb}})}{1\,\mathrm{Mpc}} \tag{3.10}$$

[see (3.31) in Appendix 3.A]. In (3.9), $\tilde{\rho}_b$ is the baryon density, which appears because photons do not contribute to the fluid inertia at scale λ_B at the time of recombination (Jedamzik & Saveliev, 2019) [see (3.29) in Appendix 3.A]. An approximate upper bound, $I_{\boldsymbol{L}_M,\,\mathrm{max}}$, on $I_{\boldsymbol{L}_M}$ follows from assuming that the magnetic-energy density $\tilde{\rho}_B \equiv \tilde{B}^2/8\pi$ and the electromagnetic-radiation density $\tilde{\rho}_\gamma$ were equal at the time t_* of the EWPT while $\lambda_B(t_*)$ was equal to the Hubble radius $r_H(t_*)$. This corresponds to $\tilde{B}(t_*) \sim 10^{-5.5}\,\mathrm{G}$ and $\lambda_B(t_*) \sim r_H(t_*) \sim 10^{-10}\,\mathrm{Mpc}$ (Durrer & Neronov, 2013;

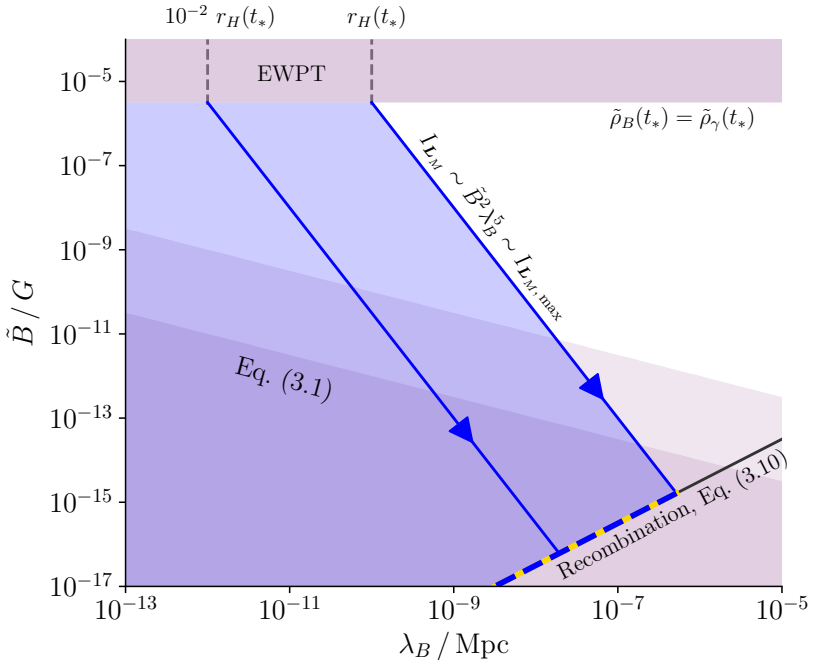

Figure 3.1: Inconsistency of the decay theory based on (3.6) and (3.9) with observational constraints for EWPT-generated PMFs. Purple regions denote values of $\tilde{B}$ and λ_B excluded on physical $[\tilde{\rho}_B(t) \lesssim \tilde{\rho}_\gamma(t_*)]$ or observational [the two forms of the constraint (3.1)] grounds. Under decays that conserve $I_{\boldsymbol{L}_M}$ [Eq. (3.4)], $\tilde{B}$ and λ_B evolve along lines parallel to the ones shown in blue. The predicted values of modern-day $\tilde{B}$ and λ_B are given by the intersection of these lines with (3.10). We see that even PMFs generated with $\tilde{\rho}_B(t_*) \sim \tilde{\rho}_\gamma(t_*)$ and $\lambda_B(t_*) \sim r_H(t_*)$ produce modern-day relics that are inconsistent with (3.1).

Wagstaff & Banerjee, 2016). As is shown in Fig. 3.1, these values and (3.10) together lead to values of $\tilde{B}$ and λ_B at t_{recomb} that violate the observational constraint (3.1). Note that $\lambda_B(t_*) \sim 10^{-2}\, r_H(t_*)$ is, in fact, a more popular estimate, corresponding to the typical coalescence size of "bubbles of new phase" that form at the phase transition (Turok, 1992); for this initial correlation scale, the predicted value of $\tilde{B}$ is separated from the allowed values by around three orders of magnitude. A similar calculation led Wagstaff & Banerjee (2016) to conclude that genesis of EGMFs at the EWPT was unlikely.

We now explain how this theory should be revised following the results of Chapter 2 (Hosking & Schekochihin, 2021). First, the idea of "selective decay of small-scale structure" is flawed. This is because the $k\lambda_B \ll 1$ tail of the magnetic-energy spectrum

$\mathcal{E}_M(k)$ corresponds not to physical structures (as in the Richardson-cascade picture of inertial-range hydrodynamic turbulence) but to cumulative statistical properties of the structures of size λ_B (Davidson, 2015). Absent a physical principle to support the invariance of $I_{\boldsymbol{L}_M}$ [such as angular-momentum conservation for its hydrodynamic equivalent (Landau & Lifshitz, 1959; Davidson, 2015)], there is therefore no reason to suppose that the small-k asymptotic of $\mathcal{E}_M(k)$ evolves on a longer timescale than the dynamical one of λ_B-scale structures [if this is long compared to the magnetic-diffusion timescale at scale λ_B, then selective decay *is* valid, as the simulations of Banerjee & Jedamzik (2004); Reppin & Banerjee (2017) confirm, but this is not the regime relevant to PMFs].

Instead, we argue that the decay of PMFs is controlled by the Saffman helicity invariant

$$I_H = \int \mathrm{d}^3\boldsymbol{r}\, \langle h(\boldsymbol{x})h(\boldsymbol{x}+\boldsymbol{r})\rangle, \tag{3.11}$$

introduced in Chapter 2 (Hosking & Schekochihin, 2021). Here, $h = \tilde{\boldsymbol{A}}\cdot\tilde{\boldsymbol{B}}$ is the comoving helicity density ($\tilde{\boldsymbol{B}} = \boldsymbol{\nabla}\times\tilde{\boldsymbol{A}}$). As explained in Section 2.3.2.1 of Chapter 2, (3.11) is equivalent to

$$I_H = \lim_{V\to\infty}\frac{1}{V}\left\langle\left[\int_V \mathrm{d}^3\boldsymbol{x}\, h(\boldsymbol{x})\right]^2\right\rangle = \lim_{V\to\infty}\frac{\langle H_V^2\rangle}{V}, \tag{3.12}$$

where H_V is the total magnetic helicity contained within the control volume V. The invariance of I_H can therefore be understood intuitively as expressing the conservation of the net mean square *fluctuation level* of magnetic helicity per unit volume that arises in any finite volume of MHD turbulence (see Fig. 3.2; we refer the reader concerned about the existence of such fluctuations to Appendix 3.C). From $I_H \sim$ const, we deduce

$$I_H \sim \tilde{B}^4\lambda_B^5 \sim \text{const}. \tag{3.13}$$

We reiterate briefly two additional points from Chapter 2. First, growth of $I_{\boldsymbol{L}_M}$, and, therefore, the inverse-transfer effect discovered by Zrake (2014) and Brandenburg *et al.* (2015), follows immediately from (3.13). This is because $I_{\boldsymbol{L}_M} \sim \tilde{B}^2\lambda_B^5 \sim I_H/\tilde{B}^2$ under self-similar evolution, so that $\mathcal{E}_M(k\to 0) \propto I_{\boldsymbol{L}_M}k^4$ [see (3.5)] grows while $\tilde{B}$

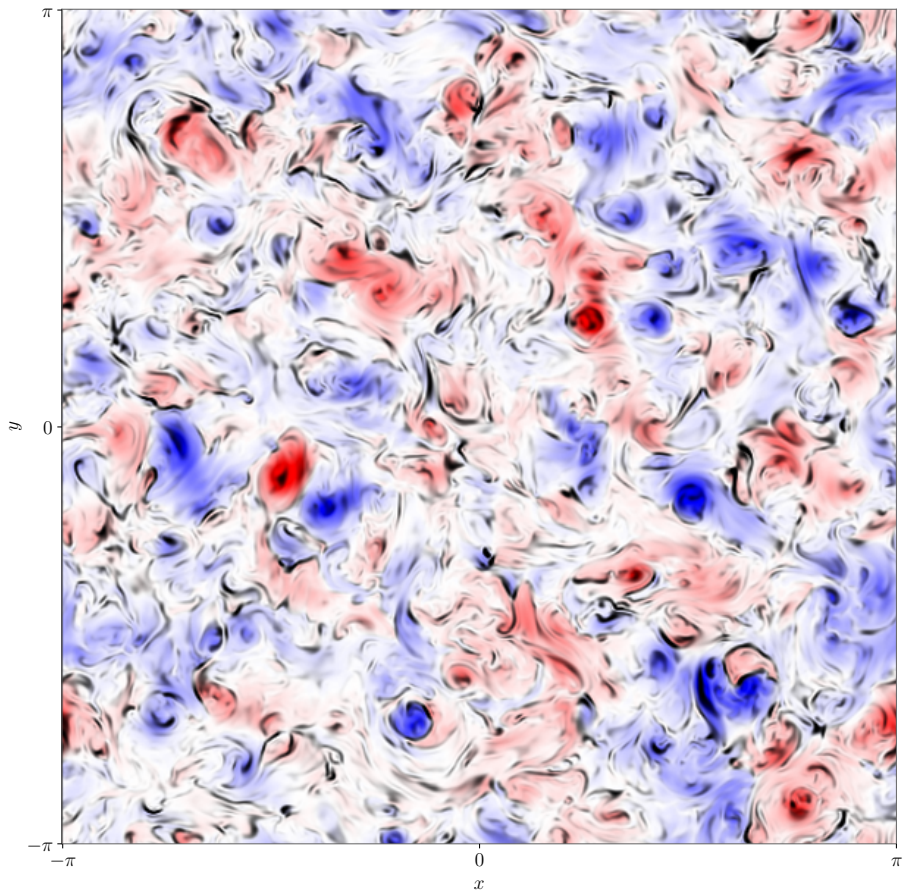

Figure 3.2: Slice of magnetic-helicity density from a simulation of decaying non-helical MHD turbulence. The turbulence breaks up into patches of positive and negative helicity h (computed in the Coulomb gauge; $\boldsymbol{\nabla} \cdot \tilde{\boldsymbol{A}} = 0$), shown in red and blue, respectively. The invariance of I_H (see main text) is a manifestation of the conservation of the net magnetic-helicity fluctuation level arising in large volumes. Because of the complex magnetic-field topology, the rate-setting process for the decay is magnetic reconnection: reconnection sites, indicated in the figure by patches of large current density $|\boldsymbol{\nabla} \times \tilde{\boldsymbol{B}}|$ (black; variable opacity scale), typically form between the helical structures. See Appendix 3.A for details of the numerical setup.

decays. Second, the value of the large-scale spectral exponent does not affect the late-time limit of the decay laws in our theory (see Appendix 3.D), unlike in the "selective-decay" paradigm.

The second revision to the existing theory required by the results of Chapter 2 is that the field's decay timescale τ should be identified not with the Alfvénic timescale (3.9), but with the magnetic-reconnection one. This is because relaxation of energetically dominant stochastic magnetic fields via the generation of Alfvénic motions is prohibited by topological constraints, which can only be broken by reconnection. Magnetically dominated conditions are relevant to the decay of PMFs because (i) the large neutrino and photon viscosities in the early Universe favour them, and (ii) once established, they are maintained, as reconnection is typically slow compared with the Alfvénic timescale. The identification of τ as the reconnection timescale implies that a number of different decay regimes are possible, as we now explain.

Under resistive-MHD theory, reconnecting structures in a fluid with large conductivity generate a hierarchy of current sheets at increasingly small scales via the plasmoid instability (Loureiro *et al.*, 2007). The global reconnection timescale is the one associated with the smallest of these sheets (the "critical sheet"), which is short enough to be marginally stable [Uzdensky *et al.* (2010); Bhattacharjee *et al.* (2009), see Schekochihin (2020) for a review]. This timescale is

$$\tau_{\rm rec} = (1+{\rm Pm})^{1/2} \min\left\{S^{1/2}, S_c^{1/2}\right\} \frac{\lambda_B}{\tilde{v}_A}, \tag{3.14}$$

where ${\rm Pm} = \tilde{\nu}/\tilde{\eta}$ is the magnetic Prandtl number, which appears because viscosity can suppress the outflows that advect reconnected field away from the reconnection site,

$$S = \frac{\tilde{v}_A \lambda_B}{\tilde{\eta}\,(1+{\rm Pm})^{1/2}} \tag{3.15}$$

is the Lundquist number based on the reconnection outflow and $S_c \sim 10^4$ is the critical value of S for the onset of the plasmoid instability. Pm is given by Spitzer's theory (Spitzer, 1956) [${\rm Pm_{Sp}} \sim 10^7$ at recombination, see (3.37) in Appendix 3.A] if the plasma is collisional, i.e., if the Larmor radius of protons $r_L = m_i c v_{{\rm th},i}/aeB$ is large compared to their mean free path, $\lambda_{\rm mfp}$ (m_i and $v_{{\rm th},i} \equiv \sqrt{2T/m_i}$ are the mass and thermal speed of protons respectively). If, on the other hand, $r_L < \lambda_{\rm mfp}$, which

happens if $B > B_{\rm iso} \equiv m_i c v_{{\rm th},i}/ea\lambda_{\rm mfp}$, then the components of the viscosity tensor perpendicular to the magnetic field are reduced by a factor $(r_L/\lambda_{\rm mfp})^2$, because protons' motions across $\tilde{\boldsymbol{B}}$ are inhibited by their Larmor gyration (Braginskii, 1965). These are the components that limit reconnection outflows because velocity gradients in reconnection sheets are perpendicular to the mean magnetic field. Therefore, ${\rm Pm} \to (r_L/\lambda_{\rm mfp})^2 {\rm Pm}_{\rm Sp} = (\tilde{B}_{\rm iso}/\tilde{B})^2 {\rm Pm}_{\rm Sp}$ in (3.14) if $\tilde{B} > \tilde{B}_{\rm iso} \equiv a^2 B_{\rm iso}$.

The validity of the resistive-MHD treatment that leads to (3.14) requires the fluid approximation to hold at the scale of the critical sheet: its width

$$\delta_c \sim \frac{S_c^{1/2}}{S}\lambda_B, \tag{3.16}$$

must be larger than either r_L or the ion inertial length $d_i = \sqrt{m_i c^2/4\pi e^2 n_i a^2}$ (n_i is the proton number density) (Uzdensky *et al.*, 2010; Ji *et al.*, 2022). If $\delta_c < r_L, d_i$, then the physics of the critical sheet is kinetic, not fluid, and the reconnection timescale is

$$\tau_{\rm rec} \sim 10\frac{\lambda_B}{\tilde{v}_A}, \tag{3.17}$$

rather than (3.14) [see (Comisso & Bhattacharjee, 2016) and (Cassak *et al.*, 2017) for reviews].

The decay timescale can also be limited by radiation drag due to photons (Banerjee & Jedamzik, 2004); this imparts a force $-\tilde{\alpha}\tilde{\boldsymbol{u}}$ per unit density of fluid [see (3.54) in Appendix 3.A]. The drag is subdominant to magnetic tension at sufficiently small scales (as it does not depend on gradients of $\tilde{\boldsymbol{u}}$), so does not contribute to Pm in (3.14). However, it can inhibit *inflows* to the reconnection layer. Balancing drag with magnetic tension at the integral scale λ_B, we find an inflow speed $\tilde{u} \sim \tilde{v}_A^2/\tilde{\alpha}\lambda_B$, so the timescale for magnetic flux to be processed by reconnection is

$$\tau_\alpha \equiv \frac{\tilde{\alpha}\lambda_B^2}{\tilde{v}_A^2}. \tag{3.18}$$

The timescale for energy decay depends on whether large-scale drag or small-scale reconnection physics is most restrictive:

$$\tau = \max\{\tau_{\rm rec}, \tau_\alpha\}. \tag{3.19}$$

The locus of possible PMF states for different values of $I_H \sim \tilde{B}^4\lambda_B^5$ under the theory that we have described is represented by the blue-gold line in Fig. 3.3. We denote the largest value of I_H consistent with EWPT magnetogenesis by $I_{H,\,\mathrm{max}}$; this corresponds to $\tilde{\rho}_B(t_*) = \tilde{\rho}_\gamma(t_*)$ and $\lambda_B(t_*) = r_H(t_*)$. For $I_H \lesssim 10^{-29} I_{H,\,\mathrm{max}}$, decays terminate on line (i) in Fig. 3.3 [Eq. (3.40) in Appendix 3.A], which represents (3.8) with $\tau = \tau_{\mathrm{rec}}$ given by (3.14) and $\mathrm{Pm} = \mathrm{Pm}_{\mathrm{Sp}}$. Use of (3.14) is valid here because $\delta_c \gtrsim r_L,\, d_i$ [see (3.41) and (3.42) in Appendix 3.A]. The Spitzer estimate of Pm is valid at recombination only if $\tilde{B} \lesssim \tilde{B}_{\mathrm{iso}} \sim 10^{-13}\,\mathrm{G}$ [Eq. (3.44) in Appendix 3.A], so decays with $I_H \gtrsim 10^{-29} I_{H,\,\mathrm{max}}$ have a shorter timescale at recombination — they terminate on line (ii) [Eq. (3.45) in Appendix 3.A], which represents (3.8) with $\tau = \tau_{\mathrm{rec}}$ given by (3.14) and $\mathrm{Pm} \sim (r_L/\lambda_{\mathrm{mfp}})^2 \mathrm{Pm}_{\mathrm{Sp}}$. For $I_H \gtrsim 10^{-2} I_{H,\,\mathrm{max}}$, the states on line (ii) have $\delta_c < d_i,\, r_L$ [see (3.46) and (3.47) in Appendix 3.A], so (3.14) is invalid for them. These decays pass through line (ii) at some time before recombination with timescale given by (3.17). However, they do access the domain of validity of (3.14) if, before t_{recomb}, $\tilde{B}$ becomes small enough for δ_c to be comparable with relevant kinetic scales. When that happens, their timescale becomes much larger than t_{recomb} so further decay is prohibited — these decays all terminate with $\tilde{B} \sim 10^{-11}\mathrm{G}$, which corresponds to $\delta_c \sim d_i$ at t_{recomb} [see (3.46) in Appendix 3.A]. Decays with $I_H \gtrsim 10^{8} I_{H,\,\mathrm{max}}$ are radiation-drag limited at recombination [line (iv); (3.55) in Appendix 3.A].

The EGMF parameters represented by the blue-gold line are consistent with (3.1) for $I_H \gtrsim 10^{-23} I_{H,\,\mathrm{max}}$, i.e.,

$$\left[\frac{\tilde{B}(t_*)}{10^{-5.5}\,\mathrm{G}}\right]^4 \left[\frac{\lambda_B(t_*)}{10^{-10}\,\mathrm{Mpc}}\right]^5 \gtrsim 10^{-23}. \tag{3.20}$$

The relic of a field with $\lambda_B(t_*) \sim 10^{-2}\, r_H(t_*) \sim 10^{-10}\,\mathrm{Mpc}$ at the EWPT would therefore be consistent with (3.1) if $\tilde{\rho}_B(t_*) \gtrsim 10^{-6.5}\tilde{\rho}_\gamma(t_*)$, confirming that void magnetic fields could feasibly be relics from the EWPT. Intriguingly, if instead $\tilde{\rho}_B(t_*) \sim \tilde{\rho}_\gamma(t_*)$ and $\lambda_B(t_*) \gtrsim 10^{-2} r_H(t_*)$, then we find $\tilde{B} \sim 10^{-11}\,\mathrm{G}$ at recombination. PMFs of this strength can explain the $\sim \mu$G magnetic fields in galaxy clusters without requiring dynamo amplification after structure formation (Banerjee & Jedamzik, 2003) and are also considered a promising candidate to resolve the Hubble tension (Jedamzik & Pogosian, 2020; Galli *et al.*, 2022).

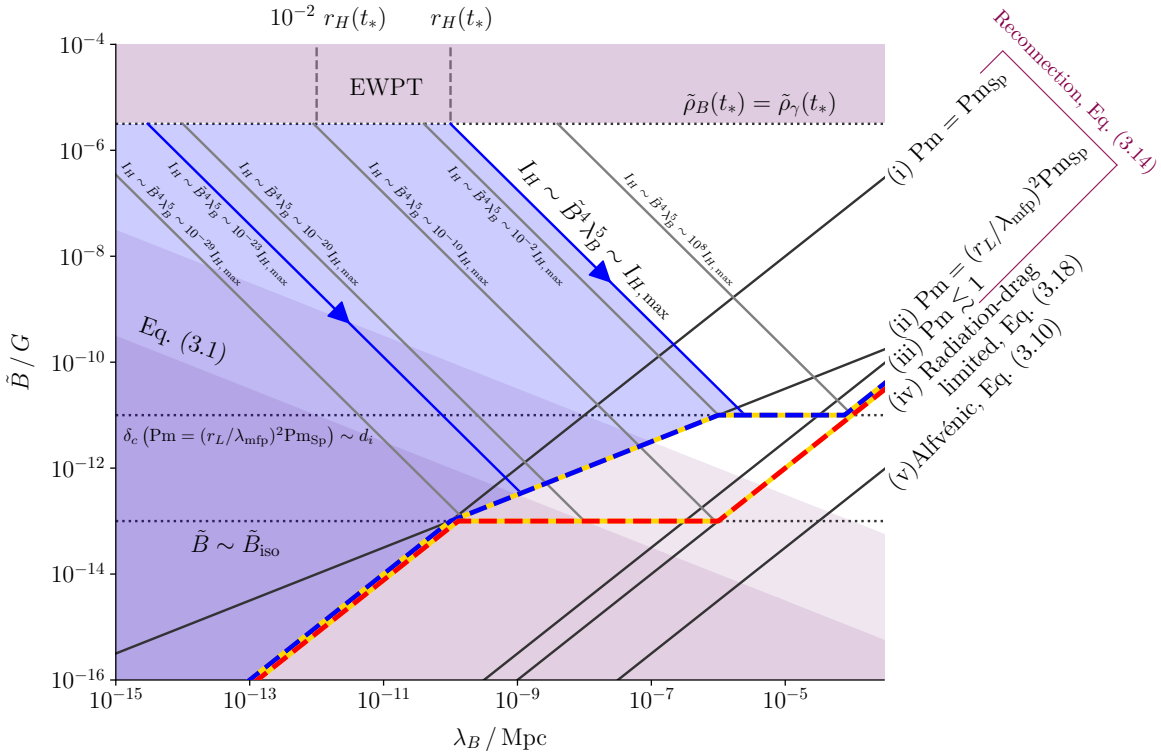

Figure 3.3: Reconnection-controlled decay of non-helical PMFs. As in Fig. 3.1, purple regions denote values of $\tilde{B}$ and λ_B excluded on physical or observational grounds [Eq. (3.1)]. Under decays that conserve I_H [Eq. (3.11)], $\tilde{B}$ and λ_B evolve along lines parallel to the ones shown in blue. The predicted values of modern-day $\tilde{B}$ and λ_B are given by the intersection of these lines with (3.8) evaluated at recombination [represented by lines (i-v), which are derived in Appendix 3.A], with τ the prevailing decay timescale. The blue-gold line shows the locus of possible present-day states resulting from reconnection-controlled decays on the timescales explained in the main text, assuming that the microscopic viscosity of the primordial plasma was controlled by collisions between protons. The effective value of Pm in (3.14) might have been heavily suppressed when $\tilde{B} > \tilde{B}_{\rm iso}$ if viscosity were then instead governed by plasma microinstabilities — the red-gold line shows the locus of modern-day states corresponding to the extreme choice of $\mathrm{Pm} \lesssim 1$ for $\tilde{B} > \tilde{B}_{\rm iso}$. In either case, we see that PMFs generated at the EWPT with a wide range of values of I_H produce modern-day relics that are consistent with (3.1), and even with the stronger version of this constraint [see text below (3.1)] which is indicated by the pale purple region.

Finally, we note that, for $\tilde{B} > \tilde{B}_{\rm iso}$, the effective values of $\tilde{\nu}$ and $\tilde{\eta}$ might be dictated by plasma "microinstabilities" rather than by collisions between protons (Schekochihin *et al.*, 2010) [this is conjectured to happen in galaxy clusters (Schekochihin *et al.*, 2005)]. In Appendix 3.A, we show that the decay of the integral-scale magnetic energy is too slow to excite the "firehose" instability important for clusters [see (3.60)]. Nonetheless, we cannot rule out the excitation of other microinstabilities, or local excitation of the firehose in reconnecting sheets. Doing so would require a numerical study of magnetic reconnection in a "microunstable" plasma — to our knowledge, no such study yet exists. The most dramatic effect that microinstabilities could plausibly have would be to reduce the effective value of Pm to $\lesssim 1$ [see St-Onge & Kunz (2018); Kunz *et al.* (2016)]. This corresponds to the red-gold line in Fig. 3.3, which remains consistent with (3.1) for $I_H \gtrsim 10^{-20} I_{H,\,\rm max}$. Compatibility between the EWPT-magnetogenesis scenario and the observational constraints on EGMFs therefore appears robust.

Appendices

3.A Technical aspects of the calculation in Chapter 3

Post-recombination evolution. In the matter-dominated Universe after recombination, the transformation that maps Minkowski-spacetime MHD onto its expanding-Universe equivalent is not Eq. (3.3), but (Banerjee & Jedamzik, 2004)

$$\tilde{\rho} = a^3\rho, \quad \tilde{p} = a^4 p, \quad \tilde{\boldsymbol{B}} = a^2\boldsymbol{B}, \quad \tilde{\boldsymbol{u}} = a^{1/2}\boldsymbol{u},$$
$$\tilde{\eta} = \eta/a^{1/2}, \quad \tilde{\nu} = \nu/a^{1/2}, \quad \mathrm{d}\tilde{t} = \mathrm{d}t/a^{1/2}. \tag{3.21}$$

As $a \propto t^2$ in the matter-dominated Universe, $\tilde{t} \propto \log t$, so a power-law decay in rescaled variables corresponds to only a logarithmic decay in comoving variables (Subramanian, 2016). Thus, in computing the expected present-day strength of EGMFs, one may assume the decay of $\tilde{B}$ to terminate at recombination with negligible error.

Derivation of (3.10)**.** In order to apply (3.8), we require an expression for the conformal time at recombination, t_{recomb}. From the Friedmann equation,

$$\frac{1}{a^4}\left(\frac{\mathrm{d}a}{\mathrm{d}t}\right)^2 = \frac{8\pi G\rho}{3}, \tag{3.22}$$

where G is the gravitational constant, the "entropy equation"

$$gT^3a^3 = \mathrm{const}, \tag{3.23}$$

where g is the number of degrees of freedom of the radiation field and T is the temperature, and Stefan's law for the radiation density

$$\rho = 3\chi g T^4, \tag{3.24}$$

where $\chi = \pi^2/90c^5\hbar^3$ (we work in "energy units" for temperature, with Boltzmann constant $k_B = 1$), it can be shown that

$$\left(\frac{\mathrm{d}T}{\mathrm{d}t}\right)^2 = 8\pi G g_0 \chi T^4 T_0^2 \left(\frac{g}{g_0}\right)^{1/3}, \tag{3.25}$$

where the subscript 0 refers to quantities evaluated at the present day. Because $(g/g_0)^{1/6} \simeq 1$, one may solve (3.25) to give an expression for the cosmic temperature as a function of conformal time,

$$T = \frac{1}{tT_0}\sqrt{\frac{1}{8\pi G g_0 \chi}}. \tag{3.26}$$

With $g_0 = 2$ (for the two photon-polarisation states), one obtains

$$t \sim 10^{16.5}\mathrm{s}\left(\frac{T}{0.3\,\mathrm{eV}}\right)^{-1}. \tag{3.27}$$

Therefore, (3.8) becomes

$$\tau \sim 10^{16.5}\mathrm{s}\left(\frac{T}{0.3\,\mathrm{eV}}\right)^{-1}. \tag{3.28}$$

Thus, $t_{\mathrm{recomb}} \sim 10^{16.5}$s. Equation (3.28) can be used to relate $\tilde{B}$ and λ_B under the assumption that the decay occurs on the Alfvénic timescale $\tau \sim \lambda_B/\tilde{v}_A$ [Eq. (3.9)]. As noted in the main text, $\tilde{v}_A$ should be computed using the baryon density $\tilde{\rho}_b$, because the photon mean free path (Durrer & Neronov, 2013)

$$\lambda_{\mathrm{mfp},\gamma} = \frac{1}{a\sigma_T n_e} \sim 1\mathrm{Mpc}\left(\frac{T}{0.3\,\mathrm{eV}}\right)^{-2} \tag{3.29}$$

(where σ_T is the Thompson-scattering cross-section) is large compared with λ_B at the time of recombination, indicating that photons are not strongly coupled to the fluid (Jedamzik & Saveliev, 2019). However, because $\tilde{\rho}_b \simeq \tilde{\rho}_\gamma$ at the time of recombination, the decoupling of photons does not affect (3.10). The Alfvén speed is

$$\tilde{v}_A = \frac{\tilde{B}}{\sqrt{4\pi\tilde{\rho}_b}} \simeq 10^{16}\mathrm{cm\,s^{-1}}\frac{\tilde{B}}{1G}\left(\frac{T}{0.3\,\mathrm{MeV}}\right)^{1/2}, \tag{3.30}$$

where we have used $\tilde{\rho}_b = a^4\rho_b \simeq a^4 m_i n_b$, with m_i the proton mass and n_b the WMAP value for the baryon number density $n_b \simeq 2.5 \times 10^{-7}\,\mathrm{cm}^{-3}a^{-3}$ (Bennett *et al.*, 2003),

and taken $a \simeq T_0/T$ [Eq. (3.23)]. Comparing (3.9) and (3.28), and substituting (3.30), we have

$$\tilde{B} \sim 10^{-8.5}\,\mathrm{G}\left(\frac{\lambda_B}{1\,\mathrm{Mpc}}\right)\left(\frac{T}{0.3\,\mathrm{eV}}\right)^{1/2}. \tag{3.31}$$

Evaluated at $T = T(t_{\mathrm{recomb}}) = 0.3\,\mathrm{eV}$, this is (3.10).

Derivation of line (i) of Fig. 3.3. Line (i) represents (3.14) evaluated at the time of recombination t_{recomb}, with $\mathrm{Pm} = \mathrm{Pm_{Sp}} \equiv \tilde{\nu}_{\mathrm{Sp}}/\tilde{\eta}_{\mathrm{Sp}}$, where $\tilde{\nu}_{\mathrm{Sp}}$ and $\tilde{\eta}_{\mathrm{Sp}}$ are the comoving Spitzer values of kinematic viscosity and magnetic diffusivity respectively (Spitzer, 1956). We first evaluate $\mathrm{Pm_{Sp}}$.

Under Spitzer theory, the dominant component of the plasma viscosity at the scale of the rate-determining current sheet is due to ion-ion (i.e., proton-proton) collisions. The collision frequency is (Spitzer, 1956)

$$\nu_{ii} \sim \frac{e^4 n_i \ln\Lambda_{ii}}{m_i^{1/2} T_i^{3/2}}, \tag{3.32}$$

where e is the elementary charge, n_i the ion number density, m_i the ion mass, T_i the ion temperature, and $\ln\Lambda_{ii}$ the Coulomb logarithm for ion-ion collisions. Neglecting any anisotropising effect of the magnetic field (see main text), the comoving isotropic kinematic viscosity is (Parra, 2019)

$$\tilde{\nu}_{\mathrm{Sp}} \sim \frac{v_{\mathrm{th},i}^2}{a\nu_{ii}} \sim \frac{T_i^{5/2}}{a m_i^{1/2} e^4 n_i \ln\Lambda_{ii}} \sim 10^{18}\mathrm{cm^2 s^{-1}}\left(\frac{T}{0.3\,\mathrm{eV}}\right)^{1/2}, \tag{3.33}$$

where $v_{\mathrm{th},i} = \sqrt{2T_i/m_i}$ is the thermal speed of ions, and we have assumed $T_i \simeq T$, used $a \simeq T_0/T$ [Eq. (3.23)], taken n_i to be equal to the WMAP value for the baryon number density $n_b \simeq 2.5 \times 10^{-7}\,\mathrm{cm^{-3}} a^{-3}$ (Bennett *et al.*, 2003), and estimated the Coulomb logarithm $\ln\Lambda_{ii}$ by

$$\ln\Lambda_{ii} \simeq \ln\frac{T_i^{3/2}}{e^3 n_i^{1/2}} \simeq 20. \tag{3.34}$$

Similarly, the electron-ion collision frequency is (Parra, 2019)

$$\nu_{ei} \sim \frac{e^4 n_e \ln\Lambda_{ei}}{m_e^{1/2} T_e^{3/2}}, \tag{3.35}$$

where $n_e \simeq n_i$ is the electron number density, T_e the electron temperature, and $\ln\Lambda_{ei}$ the Coulomb logarithm for electron-ion collisions. Equation (3.35) leads to the

Spitzer (Spitzer, 1956) value for the magnetic diffusivity

$$\tilde{\eta}_{\rm Sp} \sim \frac{\nu_{ei} m_e c^2}{4\pi n_e e^2 a} \sim 10^{10.5} {\rm cm}^2 {\rm s}^{-1} \left(\frac{T}{0.3\,{\rm eV}}\right)^{-1/2}, \tag{3.36}$$

where we have used $\ln \Lambda_{ei} \simeq \ln \Lambda_{ii} \simeq 20$, assumed the electron temperature $T_e \simeq T$, and again neglected any anisotropy resulting from the magnetic field. From (3.33) and (3.36), we have

$${\rm Pm}_{\rm Sp} = \frac{\tilde{\nu}_{\rm Sp}}{\tilde{\eta}_{\rm Sp}} \sim \frac{T^4}{m_e^{1/2} m_i^{1/2} e^6 n_i \ln \Lambda_{ii} \ln \Lambda_{ei}} \sim 10^7 \left(\frac{T}{0.3\,{\rm eV}}\right). \tag{3.37}$$

Let us now evaluate the Lundquist number, (3.15), in order to compare it with S_c, as (3.14) requires. Note that, as above, it is the Alfvén speed based on baryon inertia that appears in (3.15); photons are even more weakly coupled to the cosmic fluid at reconnection scales than at scale λ_B as the former are typically small compared with the latter. Using (3.13), (3.30), and (3.37), we find the Lundquist number

$$\begin{aligned} S &= \frac{1}{\sqrt{1+{\rm Pm}_{\rm Sp}}} \frac{\tilde{v}_A(t_*)\lambda_B(t_*)}{\tilde{\eta}} \left[\frac{\lambda_B(t_*)}{\lambda_B}\right]^{1/4} \\ &\sim 10^9 \left[\frac{\tilde{B}(t_*)}{10^{-5.5}\,{\rm G}}\right] \left[\frac{\lambda_B(t_*)}{10^{-12}\,{\rm Mpc}}\right] \left[\frac{T}{0.3\,{\rm eV}}\right]^{1/2} \left[\frac{\lambda_B(t_*)}{\lambda_B}\right]^{1/4}. \end{aligned} \tag{3.38}$$

Eq. (3.38) shows that $S \gg S_c \sim 10^4$ [unless $\tilde{B}(t_*)$ or $\lambda_B(t_*)$ are very small, in which case their evolution is inconsistent with the observational constraint (3.1), so we neglect this possibility for simplicity]. Substituting (3.37), we find that the decay timescale (3.14) is

$$\tau \sim 10^{5.5} \left(\frac{T}{0.3\,{\rm eV}}\right)^{1/2} \frac{\lambda_B}{\tilde{v}_A}. \tag{3.39}$$

Comparing (3.28) and (3.39), and again substituting (3.30), we find

$$\tilde{B} \sim 10^{-3} {\rm G} \left(\frac{\lambda_B}{1\,{\rm Mpc}}\right) \left(\frac{T}{0.3\,{\rm eV}}\right). \tag{3.40}$$

Evaluated at $T = T(t_{\rm recomb}) = 0.3\,{\rm eV}$, this is line (i) of Fig. 3.3.

Finally, we note that when reconnection occurs under large-Pm conditions with isotropic Spitzer viscosity, the ratio of δ_c [Eq. (3.16)] to r_L [defined below (3.15)] prior to recombination is independent of the magnetic-field strength, temperature and density:

$$\frac{\delta_c}{r_L} \sim S_c^{1/2} \left(\frac{m_e}{m_i}\right)^{1/4} \sim 10, \tag{3.41}$$

where we have used Eqs (3.36), (3.37) and (3.30). Thus, $\delta_c > r_L$ always. Furthermore, we find from (3.15), (3.16), (3.30), (3.36), (3.37) and the definition of d_i [see below (3.16)] that

$$\frac{\delta_c}{d_i} \sim S_c^{1/2} \left(\frac{m_e}{m_i}\right)^{1/4} \frac{v_{\mathrm{th},i}}{\tilde{v}_A} \sim \left(\frac{\tilde{B}}{10^{-9}\,\mathrm{G}}\right)^{-1}. \tag{3.42}$$

Therefore, $\delta_c > d_i, r_L$ at recombination for all relevant field strengths, so we are justified in using fluid theory to describe decays with $\tilde{B} < \tilde{B}_{\mathrm{iso}}$ [evaluated in (3.44)].

As described in the main text, (3.40) is valid when $\tilde{B}$ is small enough for the Larmor radius of ions r_L to be larger than their mean free path

$$\lambda_{\mathrm{mfp}} \sim \frac{v_{\mathrm{th},i}}{\nu_{ii} a} \sim 10^{12}\mathrm{cm}. \tag{3.43}$$

The critical magnetic field strength above which this condition is no longer satisfied is

$$\tilde{B}_{\mathrm{iso}} \sim \frac{m_i c \nu_{ii} a^2}{e} \sim 10^{-13}\,\mathrm{G} \left(\frac{T}{0.3\,\mathrm{eV}}\right)^{-1/2}. \tag{3.44}$$

Derivation of line (ii) of Fig. 3.3.

Line (ii) represents (3.14) evaluated at the time of recombination t_{recomb}, with magnetic Prandtl number $\mathrm{Pm} \sim (r_L/\lambda_{\mathrm{mfp}})^2 \mathrm{Pm}_{\mathrm{Sp}} = (\tilde{B}_{\mathrm{iso}}/\tilde{B})^2 \mathrm{Pm}_{\mathrm{Sp}}$. Note that this suppression of Pm relative to $\mathrm{Pm}_{\mathrm{Sp}}$ *increases* the value of S at any given $\tilde{v}_A$ and λ_B relative to the value (3.38) of S that corresponds to $\mathrm{Pm} = \mathrm{Pm}_{\mathrm{Sp}}$. We therefore expect this family of decays also to have $S \gg S_c \sim 10^4$.

The inclusion of the factor of $(\tilde{B}_{\mathrm{iso}}/\tilde{B})^2$ in Pm modifies (3.40) straightforwardly: it becomes

$$\tilde{B} \sim 10^{-3}\mathrm{G} \left(\frac{\tilde{B}_{\mathrm{iso}}}{\tilde{B}}\right) \left(\frac{\lambda_B}{1\,\mathrm{Mpc}}\right) \left(\frac{T}{0.3\,\mathrm{eV}}\right)$$
$$\implies \tilde{B} \sim 10^{-8}\mathrm{G} \left(\frac{\lambda_B}{1\,\mathrm{Mpc}}\right)^{1/2} \left(\frac{T}{0.3\,\mathrm{eV}}\right)^{1/4}. \tag{3.45}$$

Evaluated at $T = T(t_{\mathrm{recomb}}) = 0.3\,\mathrm{eV}$, this is line (iv) of Fig. 3.3.

The analogue of (3.42) for $\mathrm{Pm} \sim (\tilde{B}_{\mathrm{iso}}/\tilde{B})^2 \mathrm{Pm}_{\mathrm{Sp}}$ is

$$\frac{\delta_c}{d_i} \sim S_c^{1/2} \left(\frac{m_e}{m_i}\right)^{1/4} \frac{v_{\mathrm{th},i}}{\tilde{v}_A} \frac{\tilde{B}_{\mathrm{iso}}}{\tilde{B}} \sim \left\{ \tilde{B} \Big/ \left[10^{-11}\,\mathrm{G} \left(\frac{T}{0.3\,\mathrm{eV}}\right)^{-1/4} \right] \right\}^{-2}, \tag{3.46}$$

while the corresponding analogue of (3.41) is

$$\frac{\delta_c}{r_L} \sim S_c^{1/2} \left(\frac{m_e}{m_i}\right)^{1/4} \frac{\tilde{B}_{\rm iso}}{\tilde{B}} \sim \left\{ \tilde{B} \Big/ \left[10^{-12}\,{\rm G} \left(\frac{T}{0.3\,{\rm eV}}\right)^{-1/2} \right] \right\}^{-1}. \tag{3.47}$$

Eq. (3.46) shows that $\delta_c \gtrsim d_i$ at $t_{\rm recomb}$ if $\tilde{B} \lesssim 10^{-11}$G, while (3.47) indicates that $\delta_c \gtrsim r_L$ if $\tilde{B} \lesssim 10^{-12}$G. Following the prescription described by Uzdensky *et al.* (2010), we use the former condition on $\tilde{B}$ as the domain of validity of (3.14) in Fig. 3.3, though we note that our results do not depend strongly on this choice — the order-of-magnitude difference between the two critical values of $\tilde{B}$ is comparable to the degree of accuracy to which our scaling arguments are valid.

We also note that the temperature dependence of (3.46) means that a decaying field that developed $\delta_c \gtrsim d_i$ *before* recombination would have done so at a field strength $\tilde{B} < 10^{-11}$G; strictly, therefore, the decay of primordial fields should terminate somewhere below the horizontal part of the blue-gold curve in Fig. 3.3, not directly on it. However, the difference is order unity and thus negligible for the purposes of our order-of-magnitude estimates. This is because magnetic decay was strongly suppressed by radiative drag at early times [a consequence of the strong temperature dependence of (3.55)] — i.e., when temperatures exceeded around $10^2 \times 0.3\,{\rm eV}$. For all relevant values of I_H, the magnetic-field strength would therefore have greatly exceeded the critical value required for $\delta_c \sim d_i$ until the time that corresponds to this temperature, and by that time the critical field strength indicated by (3.46) was already within a small factor of its value at recombination.

Derivation of line (iii) of Fig. 3.3. Line (iii) represents (3.14) at the time of recombination $t_{\rm recomb}$, with ${\rm Pm} \lesssim 1$. With ${\rm Pm} \lesssim 1$, (3.38) should be replaced by

$$S \sim 10^{12.5} \left[\frac{\tilde{B}(t_*)}{10^{-5.5}\,{\rm G}}\right] \left[\frac{\lambda_B(t_*)}{10^{-12}\,{\rm Mpc}}\right] \left[\frac{T}{0.3\,{\rm eV}}\right] \left[\frac{\lambda_B(t_*)}{\lambda_B}\right]^{1/4}, \tag{3.48}$$

so that $S \gg S_c \sim 10^4$ for all decays of interest. The decay timescale (3.14) therefore becomes

$$\tau \simeq 10^2 \frac{\lambda_B}{\tilde{v}_A}. \tag{3.49}$$

Comparing (3.28) and (3.39), and substituting (3.30), we find

$$\tilde{B} \sim 10^{-6.5}\mathrm{G}\left(\frac{\lambda_B}{1\,\mathrm{Mpc}}\right)\left(\frac{T}{0.3\,\mathrm{eV}}\right)^{1/2}. \tag{3.50}$$

Evaluated at $T = T(t_{\mathrm{recomb}}) = 0.3\,\mathrm{eV}$, this is line (iii) of Fig. 3.3.

The analogues of (3.42) and (3.41) for $\mathrm{Pm} \lesssim 1$ (but $\tilde{\eta} \sim \tilde{\eta}_{\mathrm{Sp}}$) are

$$\frac{\delta_c}{r_L} \sim S_c^{1/2}\frac{c}{v_{\mathrm{th},e}}\frac{\ln\Lambda_{ei}}{\Lambda_{ii}} \sim 10^{-2.5}\left(\frac{T}{0.3\,\mathrm{eV}}\right)^{-1/2}, \tag{3.51}$$

and

$$\frac{\delta_c}{d_i} \sim S_c^{1/2}\frac{c}{\tilde{v}_A}\left(\frac{m_e}{m_i}\right)^{1/2}\frac{\ln\Lambda_{ei}}{\Lambda_{ii}} \sim \left\{\tilde{B}\Big/\left[10^{-13}\,\mathrm{G}\left(\frac{T}{0.3\,\mathrm{eV}}\right)^{-1/2}\right]\right\}^{-1}. \tag{3.52}$$

Note that the field strength at which $\delta_c \sim d_i$ is approximately equal to $\tilde{B}_{\mathrm{iso}}$ at recombination (both are $\sim 10^{-13}\,\mathrm{G}$), while $\delta_c \ll r_L$. The red-gold line in Fig. 3.3 therefore extends past line (iii) to line (iv) along the line $\tilde{B} \sim \tilde{B}_{\mathrm{iso}}$.

Radiation drag and the derivation of line (iv) of Fig. 3.3. As well as by viscosity arising from collisions between ions, the kinetic energy of primordial-plasma flows (after neutrino decoupling) can be dissipated by electron-photon collisions (Thompson scattering). Around the time of recombination, the comoving mean free path of photons, (3.29), is much larger than the anticipated correlation scale of the magnetic field (and, therefore, of any magnetically driven flows). Under these conditions, the effect of Thompson scattering is to induce a drag on electrons. Owing to the collisional coupling between ions and electrons, this drag can dissipate bulk plasma flows.

The comoving drag force on the fluid per unit baryon density is

$$\tilde{\boldsymbol{F}}_D = -\tilde{\alpha}\tilde{\boldsymbol{u}}, \tag{3.53}$$

where Banerjee & Jedamzik (2004)

$$\tilde{\alpha} \sim \frac{c}{\lambda_{\mathrm{mfp},\gamma}}\frac{\rho_\gamma}{\rho_b} \sim 10^{-13.5}\mathrm{s}^{-1}\left(\frac{T}{0.3\,\mathrm{eV}}\right)^3. \tag{3.54}$$

As explained in the main text, the effect of drag is most important at the scale λ_B (it becomes increasingly subdominant to magnetic tension at smaller scales) where it inhibits inflows to the reconnection layer. When the timescale $\tau_\alpha \equiv \tilde{\alpha}\lambda_B^2/\tilde{v}_A^2$ on

which flux can be delivered to the layer by strongly dragged inflows is larger than the reconnection timescale of the critical sheet $\tau_{\rm rec}$ [see (3.19)], τ_α gives the timescale for energy decay. Equation (3.28) with $\tau = \tau_\alpha$ yields, after substitution of (3.30) and (3.54)

$$\tilde{B} \sim 10^{-7}\mathrm{G}\left(\frac{\lambda_B}{1\,\mathrm{Mpc}}\right)\left(\frac{T}{0.3\,\mathrm{eV}}\right)^{3/2}. \tag{3.55}$$

Evaluated at $T = T(t_{\rm recomb}) = 0.3\,\mathrm{eV}$, this is line (iv) of Fig. 3.3.

Non-excitation of the firehose instability. Plasma with an anisotropic viscosity tensor can, in principle, be unstable to a variety of instabilities that develop at kinetic scales. For a decaying magnetic field, an instability of particular importance is the "firehose", which can generate the growth of small-scale magnetic fields in response to the decay of large-scale ones (Schekochihin *et al.*, 2010; Melville *et al.*, 2016). This happens if the size of the (negative) pressure anisotropy Δ exceeds a critical value:

$$\Delta \equiv \frac{p_\perp - p_\parallel}{p_\parallel} \leq -\frac{2}{\beta_i} \tag{3.56}$$

where $p_\parallel$ and $p_\perp$ are the thermal pressures parallel and perpendicular to the magnetic field, and

$$\beta_i \equiv \frac{p_\parallel}{B^2/8\pi} \tag{3.57}$$

is the "plasma beta". Δ can be estimated as (Schekochihin *et al.*, 2010)

$$\Delta \sim \frac{1}{\nu_{ii}}\frac{1}{B}\frac{\mathrm{d}B}{\mathrm{d}\bar{t}} \sim -\frac{1}{a\nu_{ii}\tau} \sim -10^{-11}\left(\frac{T}{0.3\,\mathrm{eV}}\right)^{1/2}, \tag{3.58}$$

where $\bar{t}$ is cosmic time [defined below (3.2)]. Naturally, the value of β_i at any given T depends on the evolution of the magnetic field. A lower bound on the value of $\tilde{B}$ at any given time for a given initial condition is the one that would develop from a decay on the kinetic reconnection timescale, $\tau \sim 10\lambda_B/\tilde{v}_A$ [Eq. (3.17)]. Solving (3.13), (3.17), (3.28) and (3.30) simultaneously, we find that this is

$$\tilde{B}(t) \sim 10^{-13}\,\mathrm{G}\left(\frac{T}{0.3\,\mathrm{eV}}\right)^{5/18}\left[\frac{\lambda_B(t_*)}{10^{-12}\,\mathrm{Mpc}}\right]^{5/9}\left[\frac{\tilde{B}(t_*)}{10^{-5.5}\,\mathrm{G}}\right]^{4/9}. \tag{3.59}$$

Using this lower bound on $\tilde{B}$, we can obtain an upper limit on $|\beta_i\Delta|$:

$$|\beta_i\Delta| \lesssim 10^{-6}\left(\frac{T}{0.3\,\mathrm{eV}}\right)^{-1/18}\left[\frac{\lambda_B(t_*)}{10^{-12}\,\mathrm{Mpc}}\right]^{-10/9}\left[\frac{\tilde{B}(t_*)}{10^{-5.5}\,\mathrm{G}}\right]^{-8/9}. \tag{3.60}$$

Eq. (3.60) suggests that the threshold for instability (3.56) is never met, unless $\lambda_B(t_*)$ and/or $\tilde{B}(t_*)$ are so small as to be inconsistent with the observational constraint (3.1).

Numerical simulation. The numerical simulations visualised in Fig. 3.2 and described in Appendix 3.C were conducted using the spectral MHD code Snoopy (Lesur, 2015). The code solves the equations of incompressible MHD in Minkowski spacetime with hyper-viscosity and hyper-resistivity both of order n, *viz.*,

$$\frac{\partial \boldsymbol{u}}{\partial t} + \boldsymbol{u}\cdot\boldsymbol{\nabla}\boldsymbol{u} = -\boldsymbol{\nabla}p + (\boldsymbol{\nabla}\times\boldsymbol{B})\times\boldsymbol{B} + \nu_n\nabla^n\boldsymbol{u}, \tag{3.61}$$

$$\frac{\partial \boldsymbol{B}}{\partial t} = \boldsymbol{\nabla}\times(\boldsymbol{u}\times\boldsymbol{B}) + \eta_n\nabla^n\boldsymbol{B}, \tag{3.62}$$

where p, the thermal pressure, is determined via the incompressibility condition

$$\boldsymbol{\nabla}\cdot\boldsymbol{u} = 0. \tag{3.63}$$

The code uses a pseudo-spectral algorithm in a periodic box of size 2π, with a 2/3 dealiasing rule. Snoopy performs time integration of non-dissipative terms using a low-storage, third-order, Runge-Kutta scheme, whereas dissipative terms are solved using an implicit method that preserves the overall third-order accuracy of the numerical scheme. In all runs presented here, we employ $\nu_n = \eta_n = 10^{-12}$, $n = 6$ and use a resolution of 512^3.

3.B Decay of helical PMFs

For completeness, here we provide the results for maximally helical fields that correspond to those presented in the main text for non-helical fields; these results are relevant for magnetogenesis mechanisms that are capable of parity violation. The decay of such fields conserves the net magnetic helicity, resulting in the self-similar scaling

$$\langle h\rangle = \tilde{B}^2\lambda_B \sim \text{const.} \tag{3.64}$$

As in the non-helical case, the decay proceeds on reconnection timescales — see Chapter 2 (Hosking & Schekochihin, 2021); the possible decay regimes are the same as those

described in the main text. Under (3.64), the PMF evolution in the $(\tilde{B}, \lambda_B)$ plane is parallel to (3.1) [see Fig. 3.4]. Thus, any field satisfying

$$\tilde{B}(t_*) \gtrsim 10^{-17}\,\mathrm{G}\,\left[\frac{\lambda_B(t_*)}{1\,\mathrm{Mpc}}\right]^{-1/2} \tag{3.65}$$

will satisfy the observational constraint (3.1) at recombination, as is well known [see, e.g., Durrer & Neronov (2013); Subramanian (2016)].

The locus of present-day PMF states for decays that occur on the reconnection timescales explained in the main text is shown by the blue-gold line in Fig. (3.4). Analogously to $I_{\boldsymbol{L},\,\mathrm{max}}$ and $I_{H,\,\mathrm{max}}$ in the main text, we denote the largest value of the mean magnetic-helicity density $\langle h \rangle$ that is consistent with EWPT magnetogenesis by $\langle h \rangle_{\mathrm{max}}$ [this corresponds to $\tilde{\rho}_B(t_*) = \tilde{\rho}_\gamma(t_*)$ and $\lambda_B(t_*) = r_H(t_*)$]. For $\langle h \rangle \lesssim 10^{-15}\langle h \rangle_{\mathrm{max}}$, the decay of PMFs terminates on line (i) in Fig. 3.4, which corresponds to (3.14) of the main text with $\mathrm{Pm} \sim \mathrm{Pm_{Sp}}$ [Eq. (3.37)]. For $10^{-15}\langle h \rangle_{\mathrm{max}} \lesssim \langle h \rangle \lesssim 10^{-11}\langle h \rangle_{\mathrm{max}}$, the decay of PMFs terminates on line (ii) [Eq. (3.45) in Appendix 3.A], which corresponds to (3.14) of the main text with $\mathrm{Pm} = (r_L/\lambda_{\mathrm{mfp}})^2\mathrm{Pm_{Sp}}$. For $10^{-7}\langle h \rangle_{\mathrm{max}} \lesssim \langle h \rangle \lesssim 10^{-5}\langle h \rangle_{\mathrm{max}}$, decays terminate at $\tilde{B} \sim 10^{-11}, \mathrm{G}$, which corresponds to $\delta_c \sim \lambda_{\mathrm{mfp}}$, as explained in the main text. Finally, decays are radiation-drag limited for $\langle h \rangle \gtrsim 10^{-5}\langle h \rangle_{\mathrm{max}}$, and therefore terminate on line (iv) [Eq. (3.55) in Appendix 3.A]. We note that, for $\langle h \rangle \lesssim 10^{-5}\langle h \rangle_{\mathrm{max}}$, the role of magnetic reconnection in determining the decay timescale implies significantly stronger relic fields than would be expected under the decay physics envisaged by Banerjee & Jedamzik (2004), i.e., Alfvénic [Eq. (3.9); line (v)] or radiation-drag-limited [line (iv)] decay.

As in the main text, we also indicate by a red-gold line the locus of present-day PMF states if $\mathrm{Pm} \lesssim 1$ (due to plasma microinstabilities) for $\tilde{B} \gtrsim \tilde{B}_{\mathrm{iso}}$.

3.C Decay of non-helical magnetic fields with $I_H = 0$

As explained in the main text, the invariance of I_H follows from the conservation of the fluctuation level of magnetic helicity. While we view fluctuations in magnetic helicity

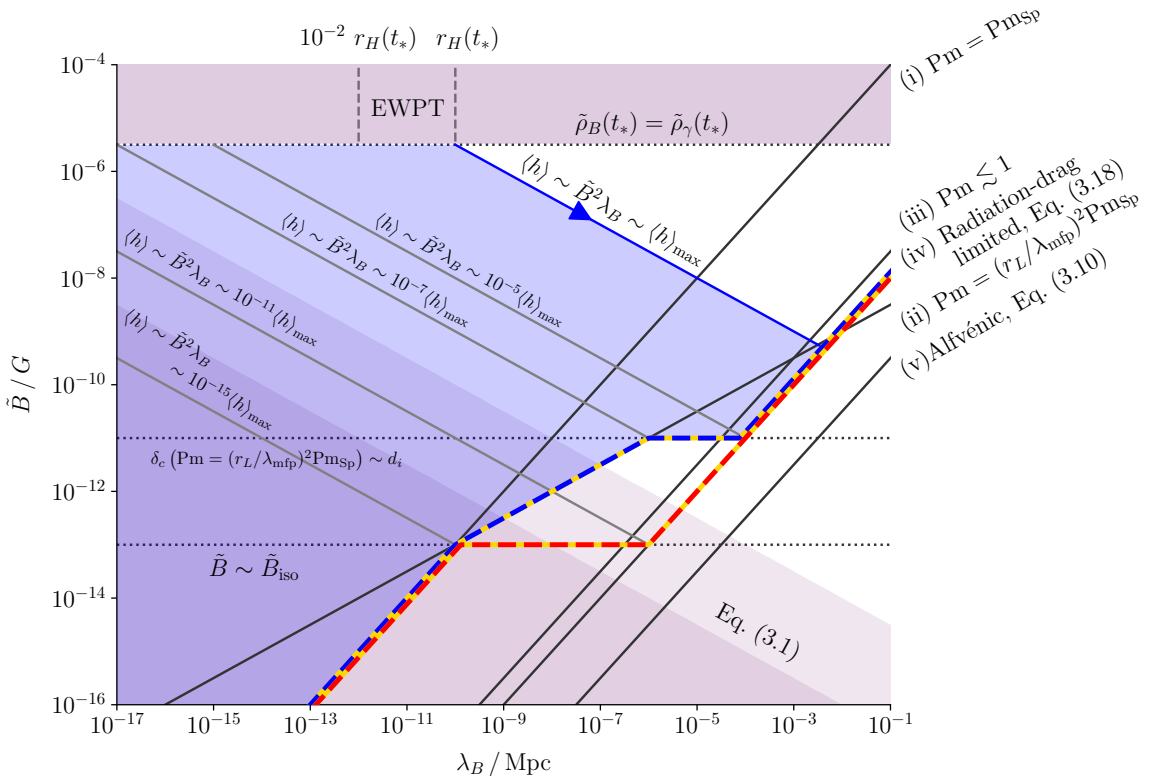

Figure 3.4: Analogue of Fig. 3.3, showing the decay of a maximally helical magnetic field generated at the EWPT.

to be a generic feature of real MHD turbulence[1], it is nonetheless possible to construct artificial field configurations for which the helicity of each magnetic structure vanishes — this will be the case if they have no twists and do not interlink. Strictly, therefore, the possibility that PMFs might have been generated without helicity fluctuations cannot be ruled out.

A priori, it appears that this kind of field might relax in a fundamentally different manner to the one described in the main text. In Chapter 2, we suggested that fields with $I_H = 0$ might decay subject to the conservation of invariants associated with the velocity, rather than the magnetic, field. This is because individually non-helical structures (unlike helical ones) can relax under entirely flux-frozen dynamics,

[1]It should also be noted that all extant numerical work on this subject (Biskamp & Müller, 1999; Müller & Biskamp, 2000; Christensson *et al.*, 2001; Banerjee & Jedamzik, 2004; Frick & Stepanov, 2010; Berera & Linkmann, 2014; Brandenburg *et al.*, 2015; Brandenburg & Kahniashvili, 2017; Reppin & Banerjee, 2017; Bhat *et al.*, 2021) has exclusively employed initial conditions *with* helicity fluctuations.

by driving flows with $\tilde{u} \sim \tilde{B}$ [a process sometimes called kinetic diffusion in the PMF literature (Durrer & Neronov, 2013)]. Plausibly, the decay of those flows would respect the invariance of the hydrodynamic Loitsyansky integral,

$$I_{\boldsymbol{L}} \equiv -\int \mathrm{d}^3\boldsymbol{r}\, r^2 \langle \tilde{\boldsymbol{u}}(\boldsymbol{x}) \cdot \tilde{\boldsymbol{u}}(\boldsymbol{x}+\boldsymbol{r}) \rangle, \tag{3.66}$$

which encodes the conservation of angular momentum $\boldsymbol{L} = \boldsymbol{x} \times \boldsymbol{u}$ (Landau & Lifshitz, 1959) [in the same fluctuating manner as I_H encodes helicity conservation].[2] Denoting the characteristic size and scale of the velocity field by $\tilde{u}$ and λ_u respectively, $I_{\boldsymbol{L}} \sim \tilde{u}^2 \lambda_u^5$. Conservation of $I_{\boldsymbol{L}}$ therefore implies $\tilde{u}^2 \lambda_u^5 \sim$ const. This suggests that $\tilde{B}^2 \lambda_B^5 \sim$ const also, if $\tilde{u} \sim \tilde{B}$ and $\lambda_B \sim \lambda_u$, which seems reasonable for, e.g., a magnetic field maintained by the dynamo effect. This returns us to Eq. (3.6), i.e., to the same prediction that was shown to be inconsistent with the observational constraints by Wagstaff & Banerjee (2016).

On the other hand, if the magnetic field *were* maintained by dynamo, then it seems unlikely that $I_H = 0$ would be maintained. This is because random helicity fluctuations could be generated freely at resistive scales (as the Lundquist number is order unity there), where dynamo primarily generates magnetic field [at least in its kinematic stage; Rincon (2019)]. Thus, I_H could become non-zero, although it would not need to be conserved if magnetic energy remained concentrated at the resistive scales. If, however, the dynamo-replenished magnetic fields later transferred to larger scales and saturated with $\lambda_B \sim \lambda_u$, as supposed above, while still having helicity fluctuations, then I_H would become invariant, because the integral scale of the magnetic field would be much larger than the resistive scale. This would push us back to the scaling $I_H \sim \tilde{B}^4 \lambda_B^5 \sim$ const [Eq. (3.13)]. Moreover, we conjecture that the size of the conserved product $\tilde{B}^4 \lambda_B^5$ would be of the same order as its value for the initial field with $I_H = 0$, because memory of its $\tilde{B}$ and λ_B would be retained by the velocity field.

In Fig. 3.5, we present results from a numerical simulation (Simulation A) designed to assess these arguments. We initialise a large number of untwisted, non-interlinking magnetic-flux loops (otherwise distributed in a random, statistically isotropic way) in

[2] $I_{\boldsymbol{L}}$ is related to the small-k asymptotic of the kinetic-energy spectrum, $\mathcal{E}_K(k)$, of isotropic turbulence without long-range spatial correlations by $\mathcal{E}_K(k \to 0) = I_{\boldsymbol{L}} k^4 / 24\pi^2 + O(k^6)$ (Davidson, 2015).

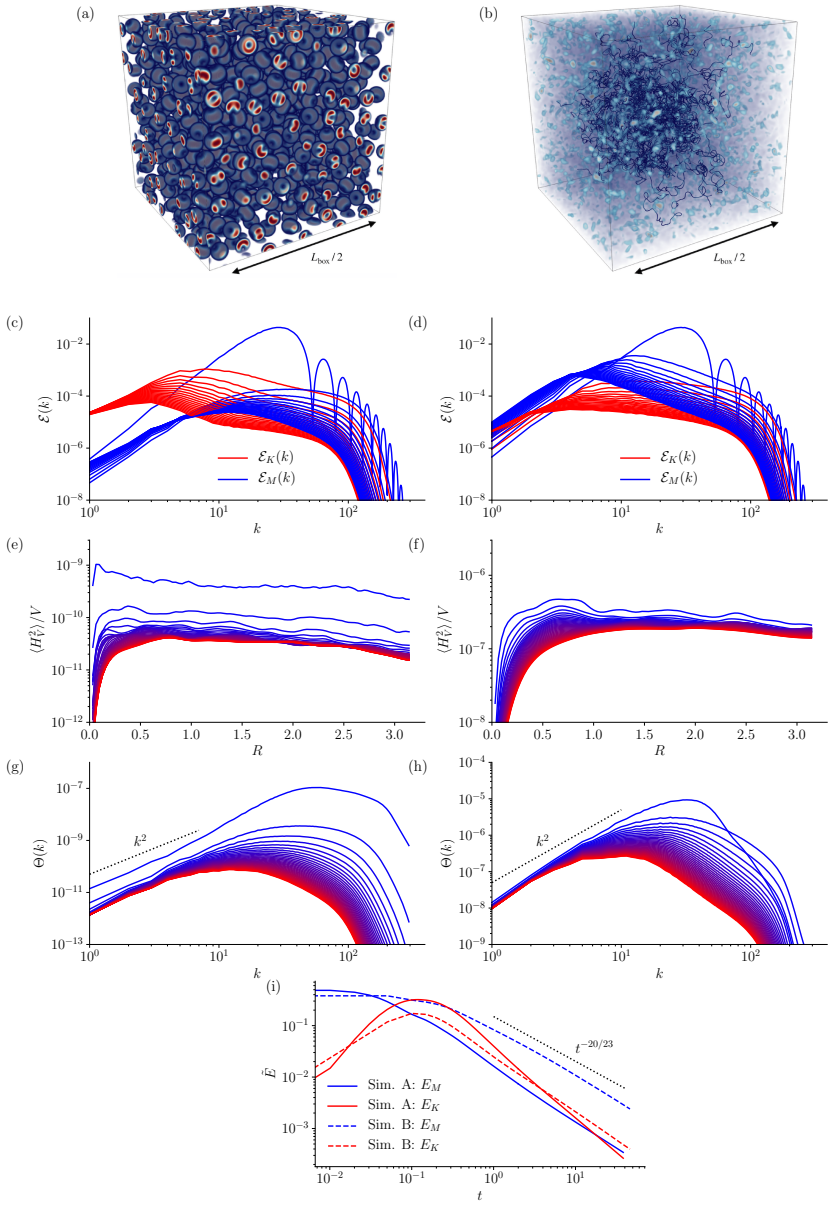

Figure 3.5: Simulations of MHD turbulence decaying from a magnetically dominated state. Left-hand plots are for Simulation A, which had $I_H = 0$ initially; right-hand plots are for Simulation B, which had $I_H \neq 0$ initially. Panels (a-b) show a 3D plot of the magnetic-energy distribution at the initial time, in a volume 1/8 the size of the simulation domain; panels (c-d) show energy spectra (kinetic in red, magnetic in blue), plotted at intervals of 2.0 between $t = 0$ and $t = 38.0$ (time is measured in code units based on normalising the box size and the mean-square magnetic field to 2π and 1, respectively, so that one time unit is equal to the initial Alfvén crossing time of the box); panels (e-f) show $\langle H_V^2\rangle/V$ (computed as an average over many spheres of radius R and volume V, distributed throughout the simulation domain) vs. R, plotted at intervals of 1.0 between $t = 0.25$ (blue) and $t = 38.25$ (red); panels (g-h) show the helicity-variance spectrum $\Theta(k)$, at the same times as for (e-f); panel (i) shows the evolution of magnetic energy E_M and kinetic energy E_K for each simulation as functions of time, with the theoretical prediction for the decay on the slow-reconnection timescale, $E_M \propto t^{-20/23}$, given for reference [this follows from (3.14), generalised appropriately for hyper-dissipation, with $S < S_c$ — see Hosking & Schekochihin (2021)].

a periodic simulation domain [see Fig. 3.5(a)]. At $t = 0$, $I_H = 0$ because the loops each have zero magnetic helicity. For the purpose of comparison, we also present a second simulation (Simulation B) with the same setup but without the non-interlinking condition, instead starting with many loops superimposed on top of each other. This field has complex initial topology, as Fig. 3.5(b) indicates, but no net helicity, in the sense that $\langle H_V \rangle / V \ll \tilde{B}^2 \lambda_B$ for all V. However, unlike the field in Simulation A, it has $I_H \neq 0$, because superimposing loops creates linkages in the magnetic field.

Figs. 3.5(c-d) show the evolution of energy spectra for the two simulations. In Simulation A, unlike in Simulation B, there is an immediate and rapid decay of the magnetic energy as the loops contract and drive flows. There is a corresponding decay of the large-scale (low-k) spectral tail, which demonstrates the non-invariance of $I_{\boldsymbol{L}_M}$. The newly generated kinetic energy is comparable in magnitude to the initial magnetic energy [see Fig. 3.5(i)], and its spectrum peaks close to the initial peak of the magnetic-energy spectrum.[3] On the other hand, the contraction of the loops leaves magnetic energy concentrated at small (resistive) scales, where it can be refuelled by the dynamo effect associated with the newly generated flows. As we anticipated above, this resistive-scale magnetic field has random fluctuations in magnetic helicity: this is shown explicitly in Fig. 3.5(e) where, for volumes V taken to be spheres of radius R, we plot $\langle H_V^2 \rangle / V$ vs. R at regular intervals in time (the average is taken over a large sample of spheres with centres throughout the simulation box). While $\langle H_V^2 \rangle \propto V^{2/3}$ at $t = 0$ (not shown) because H_V is dominated by random surface contributions at this time, this scaling is replaced by $\langle H_V^2 \rangle \propto V$ as soon as turbulence develops, indicating $I_H \neq 0$ [see (3.12) of the main text]. Though I_H, which is the value of $\langle H_V^2 \rangle / V$ in the flat part of the curves in Figs. 3.5(e-f), decays by around an order of magnitude during

[3] At larger scales, it exhibits a power law close to $\mathcal{E}(k) \propto k^2$, suggesting that it is a 'Saffman turbulence' — roughly speaking, eddies are translational rather than rotational (Davidson, 2015). However, we note that each flux tube must individually relax in a momentum-conserving manner, so it is unlikely that the relaxation could generate true Saffman turbulence, which has a stochastic momentum distribution. Instead, it is likely that the momentum distribution is "quasi-random", in the sense to be described in Chapter 4 (Hosking & Schekochihin, 2022*b*) — in an arbitrarily large simulation domain, one would find that the $\mathcal{E}_K(k) \propto k^2$ spectrum transitions to $\mathcal{E}_K(k) \propto k^4$ at sufficiently large scales. Similarly, the large-scale spectrum of the magnetic energy appears to be somewhat shallower than $\mathcal{E}_M(k) \propto k^4$ — we think that this too is an effect of the finite size of the simulation domain.

the first few eddy-turnover times, Fig. 3.5(e) shows that its decay ceases after that. This is consistent with our suggestion above that I_H should become constant when the dynamo saturates, due to migration of the helicity-containing scale towards the flow scale λ_u.[4] This interpretation is supported by the evolution of the helicity-variance spectrum $\Theta(k)$ [see Fig. 3.5(g)], which encodes the characteristic size of helicity fluctuations at each scale.[5] In Simulation A, $\Theta(k)$ is concentrated around the dissipation scale at early times (though after the decay of the magnetic loops), but later moves to larger scales. I_H [which is proportional to the coefficient of k^2 in the $\Theta(k \to 0) \propto k^2$ asymptotic — see Section 2.3.2.2 of Chapter 2] ceases to decay once the peak of $\Theta(k)$ is moderately separated from the dissipation scales.

The value of I_H ultimately attained by the magnetic field in Simulation A is smaller than the one in Simulation B by a factor of around 10^4. This appears to contradict our conjecture that dynamo should generate I_H of the same size as $\tilde{B}^4\lambda_B^5$ at the initial time. On the other hand, we note that (i) this factor may well be smaller for a simulation at larger resolution and larger Prandtl number [recent work has shown that extremely large resolutions are required to probe the asymptotic nature of the large-Pm dynamo (Galishnikova *et al.*, 2022)], and that (ii) the strong scaling of I_H with $\tilde{B}$ and λ_B means that even a factor-10^4 reduction in I_H corresponds only to a factor-10 reduction in $\tilde{B}$ or λ_B. This means that a PMF generated with $I_H = 0$ would migrate only a relatively short distance on the $(\tilde{B}, \lambda_B)$ plane (Fig. 3.3) before settling to decay with $\tilde{B}^4\lambda_B^5 \sim$ const.

To summarise, there appear to be both theoretical and numerical reasons to believe that a PMF generated with $I_H(t_*) = 0$ at the initial time t_* would, via an initial period of rapid decay and subsequent regeneration via dynamo, develop $I_H \sim \tilde{B}(t_*)^4\lambda_B(t_*)^5 \sim$ const. At later times, a magnetically dominated state would likely be re-established because the flows will drive Alfvénic turbulence, which cascades to small scales and

[4]We identify the migration as dynamo-induced because it occurs under conditions of dominant kinetic energy [see Fig. 3.5(i)]. An alternative explanation is that it occurs because of the non-helical inverse-transfer effect described in the main text. The connection between the two phenomena, and the role that the invariance of I_H might have in constraining the nonlinear dynamo's evolution, are topics to which we plan to return in future work.

[5]Note that $\Theta(k)$ is not the same as the helicity spectrum, which is close to zero for all k for both simulations, as the field is non-helical at all scales.

is dissipated by viscosity (which may be large, if associated with neutrinos or photons), while background "quasi-force-free" magnetic fields persist, decaying only on the magnetic-reconnection timescale, as described in the main text. There is some evidence of this in Fig. 3.5(i), which shows that magnetic energy becomes larger than kinetic in Simulation A at late times.

.

3.D The effect of the large-scale spectral slope: co-existence of flux and helicity invariants

In this chapter, we have contrasted our theory of I_H-conserving PMF decay with the previously accepted theory based on "selective decay of small-scale structure", i.e., the invariance of the large-scale asymptotic of the magnetic-energy spectrum. One success of our theory is that it explains the inverse-transfer effect observed in simulations of magnetic fields initialised with $\mathcal{E}_M(k \to 0) \propto k^4$ [Zrake (2014); Brandenburg *et al.* (2015); see main text]; this effect is manifestly not compatible with selective decay. On the other hand, Reppin & Banerjee (2017) observe that inverse transfer is *not* present in simulations that are initialised with sufficiently shallow large-scale spectra [namely, with $\mathcal{E}_M(k \to 0, t = 0) \propto k^n$, where $n < 3$]. Instead, they find that the $k \to 0$ asymptotic of $\mathcal{E}_M(k)$ is preserved. This result raises questions of whether a "selective-decay-like" principle might be at work in such decays, and what its effect might be on the laws for the decay of energy and growth of the integral scale. In this Section, we explain the invariance of this k^n asymptotic as a consequence of the conservation of magnetic flux, but also argue that, beyond an initial transient, flux conservation does not affect the decay laws if $n > 3/2$ (as is the case in all models of EWPT magnetogenesis of which we are aware). It is therefore not necessary to know the precise value of n to compute the present-day properties of EGMFs under the relic-field hypothesis — the theory presented in the main text is valid independently of it.

3.D.1 Invariance of the large-scale spectral asymptotic for $n \leq 3$

In general, the large-scale spectral asymptotic is frozen in time when the coefficient of k^n in $\mathcal{E}_M(k \to 0)$ is proportional to some statistical invariant. As explained in the main text of this chapter, this is not the case when correlations in $\boldsymbol{B}$ decay rapidly with distance, because then $\mathcal{E}_M(k \to 0) \propto I_{\boldsymbol{L}_M} k^4$ [Eq. (3.4)] where $I_{\boldsymbol{L}_M} \neq \text{const}$. However, for $n \leq 3$, it turns out that the coefficient of k^n is proportional to an invariant that is related to the conservation of magnetic flux. Physically, this invariant encodes the fact that, over sufficiently large volumes, local fluctuations in magnetic flux may sum to a non-zero net fluctuation level, which must be conserved as the field decays. Spatial correlations must be long (and hence spectra must be shallow) for the fluctuation level to be non-zero, because $\boldsymbol{\nabla} \cdot \boldsymbol{B} = 0$ means that magnetic structures without sufficiently strong far-field components have net zero flux. The relevant measure of correlation strength is the large-r asymptotic of the magnetic field's longitudinal correlation function, $\chi_B(r) \equiv \langle B_r(\boldsymbol{x}) B_r(\boldsymbol{x}+\boldsymbol{r})\rangle / \langle B_r^2 \rangle$, where $B_r = \boldsymbol{B} \cdot \boldsymbol{r}/r$. The argument is particularly transparent if $\chi_B(r \to \infty) \propto r^{-3}$ (as, for example, would be the case for a superposition of many randomly positioned and oriented magnetic dipoles), as then it can be shown that

$$\mathcal{E}_M(k \to 0) = \frac{I_{\boldsymbol{B}} k^2}{4\pi^2}, \tag{3.67}$$

where

$$I_{\boldsymbol{B}} \equiv \int \mathrm{d}^3\boldsymbol{r} \langle \tilde{\boldsymbol{B}}(\boldsymbol{x}) \cdot \tilde{\boldsymbol{B}}(\boldsymbol{x}+\boldsymbol{r})\rangle = \lim_{V\to\infty} \frac{1}{V} \left\langle \left(\int_V \mathrm{d}^3\boldsymbol{x}\, \tilde{\boldsymbol{B}} \right)^2 \right\rangle \equiv \lim_{V\to\infty} \frac{\langle \tilde{B}_V^2 \rangle}{V} \tag{3.68}$$

is the Saffman flux invariant introduced in Section 2.4.3 of Chapter 2. The invariance of $I_{\boldsymbol{B}}$ encodes conservation of the fluctuation level of magnetic flux in the same manner as the invariance of I_H does for magnetic helicity. More generally, if $\mathcal{E}_M(k \to 0) = Ck^n$ with $n > -1$, then it can be shown that χ_B satisfies

$$\chi_B(r \to \infty) \begin{cases} \leq O(r^{-1-n}) & \text{if } n = 2m,\ m = 2, 3, 4, \ldots; \\ = f_n C r^{-1-n} & \text{otherwise,} \end{cases} \tag{3.69}$$

where f_n is a numerical coefficient that depends only on n. Furthermore, it can also be shown that

$$\lim_{R\to\infty}\langle\tilde{B}_V^2\rangle\begin{cases}\propto R^2 & \text{if } n>3,\\ =g_nCR^2\ln R & \text{if } n=3,\\ =g_nCR^{5-n} & \text{if } -1<n<3,\end{cases} \tag{3.70}$$

where g_n is a different numerical coefficient dependent only on n, and R is the radius of a spherical control volume V. These results are straightforward analogues of ones that will derive for the kinetic-energy spectrum of hydrodynamic turbulence in Chapter 4 (Hosking & Schekochihin, 2022*b*). The rate of change of $\langle\tilde{B}_V^2\rangle$ due to the advection of flux through the surface of V scales as

$$\frac{\mathrm{d}}{\mathrm{d}t}\langle\tilde{B}_V^2\rangle\propto V^{2/3}\propto R^2 \implies \frac{\mathrm{d}}{\mathrm{d}t}\log\langle\tilde{B}_V^2\rangle\propto\begin{cases}1 & \text{if } n>3,\\ 1/\ln R & \text{if } n=3,\\ R^{n-3} & \text{if } -1<n<3,\end{cases} \tag{3.71}$$

so the timescale associated with changes in $\langle\tilde{B}_V^2\rangle$ is an increasing function of R for $n\le 3$. This means that the decay is constrained by the conservation of magnetic flux via

$$\lim_{R\to\infty}\frac{\langle\tilde{B}_V^2\rangle}{R^{5-n}}=\text{const}=g_nC. \tag{3.72}$$

Eq. (3.72) shows that $C=\text{const}$ for $n\le 3$, which explains the invariance of $\mathcal{E}_M(k\to 0)$ observed by Reppin & Banerjee (2017).

3.D.2 Conservation of magnetic flux does not affect the decay laws

We now turn to the effect that the need to satisfy the new constraint (3.72) has on the decay laws. A fully self-similar decay satisfying (3.72) would have

$$\lim_{R\to\infty}\frac{\langle\tilde{B}_V^2\rangle}{R^{5-n}}\sim\tilde{B}^2\lambda_B^{1+n}\sim\text{const}, \tag{3.73}$$

which is the selective-decay scaling considered by Banerjee & Jedamzik (2004). However, (3.73) cannot describe the true evolution as it is inconsistent with the invariance of I_H, as we now explain. While, in principle, I_H can be small compared to $\tilde{B}^4\lambda_B^5$

(see Appendix 3.C), it cannot be much larger than this: $I_H \sim \tilde{B}^4\lambda_B^5$ corresponds to magnetic fields that are locally maximally helical.[6] Therefore, adopting (3.73), we can write

$$I_H \lesssim B^4\lambda_B^5 \sim \tilde{B}^{2(2n-3)/(n+1)}. \tag{3.74}$$

Assuming that $n > 3/2$, (3.74) requires I_H to be smaller than a decreasing function of time, which contradicts its invariance.

On the other hand, the scaling $I_H \sim \tilde{B}^4\lambda_B^5 \sim$ const [Eq. (3.13) of the main text] is *not* incompatible with (3.72), as, under this scaling,

$$\lim_{R\to\infty} \frac{\langle \tilde{B}_V^2 \rangle}{R^{5-n}} \lesssim \tilde{B}^2\lambda_B^{1+n} \sim \tilde{B}^{2(3-2n)/5}. \tag{3.75}$$

Again assuming that $n > 3/2$, (3.75) only requires $\lim_{R\to\infty}\langle \tilde{B}_V^2\rangle/R^{5-n}$ to be smaller than an increasing function of time, which does not contradict its conservation. We conclude that while the selective-decay scaling (3.73) is ruled out by I_H conservation, the converse is not true: (3.13) is compatible with the conservation of the magnetic-flux fluctuation level, and thus with the invariance of the large-scale spectral asymptotic. We therefore expect (3.13) of the main text to hold regardless of the value of n (although for $n < 4$, some transient order-unity variation in $\tilde{B}^4\lambda_B^5$ should be expected as a result of departures from self-similarity; see below).

That conservation of I_H should provide the relevant constraint even in the presence of magnetic-flux fluctuations is also reasonable physically. Under (3.13) of the main text, (3.72) and (3.75) imply that the expectation value of the squared magnetic flux contained within the volume V decreases relative to its "maximal" value of $\tilde{B}^2\lambda_B^{1+n}R^{5-n}$. This makes sense: while there is a dynamical tendency for magnetic fields to favour locally maximally helical states (Taylor, 1974; Servidio *et al.*, 2008) (meaning

[6] We expect that $\langle H_V^2\rangle \propto R^3$ even in the presence of slowly decaying correlations in $\boldsymbol{B}$. This is because spatial correlations in the magnetic helicity decay faster than those in the magnetic field. To see why, it is convenient to imagine a turbulence consisting of a superposition of uncorrelated magnetic structures. For $n < 4$, the far-field component of $\boldsymbol{B}$ associated with any given structure must scale as r^{-1-n} [Eq. (3.69)], so the far-field component of the vector potential $\boldsymbol{A}$ due to that structure is proportional to r^{-n}, and hence the far-field component of h is proportional to r^{-2n-1}. I_H diverges only if the helicity correlation function $\langle h(\boldsymbol{x})h(\boldsymbol{x}+\boldsymbol{r})\rangle \geq O(r^{-3})$ as $r \to \infty$ [see (3.11) of the main text], which occurs if $n < 1$. Thus, $\langle H_V^2\rangle \propto R^3$ provided that $n > 1$. As explained in the main text, this scaling implies $I_H = \lim_{R\to\infty}\langle H_V^2\rangle/R^3 \sim \tilde{B}^4\lambda_B^5 \sim$ const.

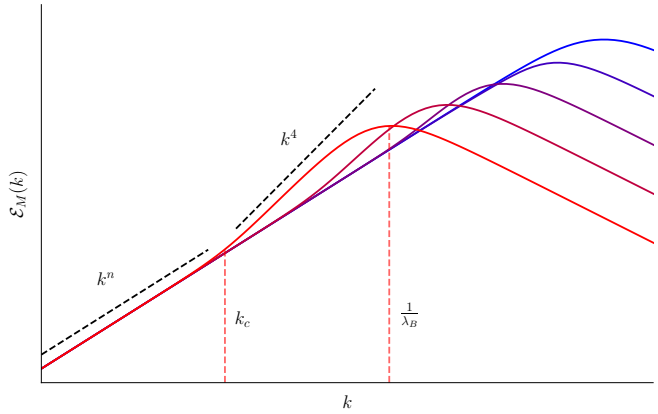

Figure 3.6: Schematic of the evolution of $\mathcal{E}_M(t,k)$ for $\mathcal{E}_M(t=0,k\to 0)\propto k^n$. For $n\leq 3$, the $k\to 0$ asymptotic of $\mathcal{E}_M(t,k)$ is preserved as the turbulence decays; this is a consequence of magnetic-flux conservation. Nonetheless, the inverse-transfer effect persists, though it only occurs for $k>k_c(t)$, where k_c is given by (3.77). The progression of time is from blue to red in this figure.

that we expect $I_H\sim\tilde{B}^4\lambda_B^5$), there is no physical reason that that they should maintain states of maximal magnetic flux (in the sense that $\lim_{R\to\infty}\langle\tilde{B}_V^2\rangle/R^{5-n}\sim\tilde{B}^2\lambda_B^{1+n}$).

A schematic of the evolution of the magnetic-energy spectrum decaying in a manner that satisfies both (3.72) and (3.13) of the main text is shown in Fig. 3.6. Under (3.13) of the main text, the spectral peak at $k\sim 1/\lambda_B$ grows relative to the position it would occupy under selective decay — i.e., there is an inverse transfer — nonetheless, the $k\to 0$ asymptotic is preserved. This leads to the development of a spectral knee at $k=k_c$, where k_c^{-1} is the minimal scale for the applicability of $\langle\tilde{B}_V^2\rangle\propto R^{5-n}$. Because coalescence of structures via magnetic reconnection is a local process, we argue that it should not generate correlations on scales much larger than λ_B. This means that the spectrum between k_c and λ_B^{-1} should be proportional to k^4 [cf. (3.5) of the main text; see Chapter 4 (Hosking & Schekochihin, 2022*b*) for discussion of the correspondence between long-range correlations and broken-power-law spectra].

The size of k_c can be estimated by equating the invariant asymptotic with the growing k^4 component of the spectrum, which on dimensional grounds is of size $\sim\tilde{B}^2\lambda_B^5k^4$:

$$\tilde{B}(0)^2\lambda_B(0)[k\lambda_B(0)]^n\sim\tilde{B}^2\lambda_B^5k^4. \tag{3.76}$$

From $\tilde{B}^4\lambda_B^5 \sim$ const, we have

$$k_c \sim \frac{1}{\lambda_B}\left[\frac{\lambda_B}{\lambda_B(0)}\right]^{-\frac{2n-3}{2(4-n)}} \sim \frac{1}{\lambda_B}\left[\frac{\tilde{B}}{\tilde{B}(0)}\right]^{\frac{2(2n-3)}{5(4-n)}}, \tag{3.77}$$

a decreasing function of time.

The evolution of the magnetic-energy spectrum depicted in Fig. 3.6 is manifestly non-self-similar. As a result, transient order-unity changes in $\tilde{B}^4\lambda_B^5$ and the decay timescale as a function of $\tilde{B}$ and λ_B should be expected at early times. On the other hand, the decay does become approximately self-similar at late times, when $k_c \ll 1/\lambda_B$, so any deviation from the theory proposed in the main text becomes small as t becomes large. Finally, we acknowledge that, while we expect the evolution depicted in Fig. 3.6 to be valid for any initial spectrum with $n > 3/2$, Reppin & Banerjee (2017) do not observe the formation of a "k^4 bulge" in their simulation with $n = 2$. We believe this to be a result of insufficient scale separation in that simulation: with $n = 2$, (3.77) implies $k_c\lambda_B \sim [\lambda_B/\lambda_B(0)]^{-1/4}$, so with $\lambda_B/\lambda_B(0) \simeq 10$ [see Fig. 16 of Ref. Reppin & Banerjee (2017)], $k_c\lambda_B \simeq 0.6$. It is therefore not surprising that these scales cannot be distinguished.

Chapter 4

Emergence of long-range correlations and thermal spectra in forced turbulence

This chapter is adapted from Hosking & Schekochihin (2022b), arXiv:2202.00462.

4.1 Introduction

Probably the best-known result in the theory of turbulence is Kolmogorov's law for the spectral energy density in the inertial range, $\mathcal{E}(k) \propto k^{-5/3}$. This law follows from the conjecture of a constant flux of energy in k-space, from the large scales at which it is injected, to the small scales at which it is dissipated by molecular viscosity (Kolmogorov, 1941*b*). However, a power-law spectrum can also be found at scales larger than the outer scale of the turbulence, if that scale is small compared to the system's size. Unlike the inertial-range spectrum, this small-k spectral tail does not correspond to large eddies with size k^{-1}—instead, it is controlled by statistical properties of the eddies at the outer scale (Davidson, 2015). As has been noted in the preceeding chapters, a purely kinematic calculation shows that, if the two-point velocity correlation function, $\langle \boldsymbol{u}(\boldsymbol{x}) \cdot \boldsymbol{u}(\boldsymbol{x}+\boldsymbol{r}) \rangle \equiv \langle \boldsymbol{u} \cdot \boldsymbol{u}' \rangle$, decays sufficiently quickly with distance, the energy spectrum of statistically isotropic and homogeneous turbulence satisfies

$$\mathcal{E}(k \to 0) = \frac{Lk^2}{4\pi^2} + \frac{Ik^4}{24\pi^2} + O(k^5), \tag{4.1}$$

where

$$L = \int \mathrm{d}^3\boldsymbol{r}\langle \boldsymbol{u}\cdot\boldsymbol{u}'\rangle, \tag{4.2}$$

and

$$I = -\int \mathrm{d}^3\boldsymbol{r} r^2\langle \boldsymbol{u}\cdot\boldsymbol{u}'\rangle, \tag{4.3}$$

are the already-introduced Saffman and Loitsyansky integrals (in this chapter, we denote these integrals by L and I in accordance with the conventions of the hydrodynamics literature). These integrals encode information about the distribution of linear and angular momentum in real space (Landau & Lifshitz, 1959; Saffman, 1967; Davidson, 2009). Owing to the conservation of these momenta, L and I are invariants of unforced, decaying turbulence[1], leading to a phenomenon often called the *'permanence of large-scale structure'*—as turbulence decays, the small-k part of the spectrum remains unchanged. As was explained in Chapter 1, this observation (together with the assumption of self-similarity) allows the decay of kinetic energy to be computed as a function of time (Saffman 1967; Batchelor & Proudman 1956; see Davidson 2015 for a review).

While these results are well established in the theory of decaying turbulence, the large-scale properties of *forced* turbulence, i.e., one into which energy is continually injected, are usually described in very different terms. In that context, the small-k part of the energy spectrum has received particular attention in recent years, owing to an attractive analogy with statistical mechanics. It has been shown in numerical simulations that there is no net k-space energy flux to these scales (Dallas *et al.*, 2015), as is to be expected on physical grounds. Accordingly, it has been argued that the largest scales of steady-state forced turbulence might constitute a subsystem in *thermal equilibrium* with the separate, non-equilibrium subsystem represented by the rest of the flow (Dallas *et al.*, 2015; Cameron *et al.*, 2017; Alexakis & Biferale, 2018; Alexakis & Brachet, 2019). This idea leads immediately to a prediction for the

[1]More precisely, I is related to a weighted integral of angular momentum density, and is invariant only if correlations decay sufficiently rapidly with distance (Davidson, 2009).

large-scale spectrum: energy should be equipartitioned between Fourier modes[2], so, in 3D,

$$\mathcal{E}(k^2) \propto k^2. \tag{4.4}$$

In reality, the large-scale modes do not constitute an isolated system, but, if their nonlinear interaction with the turbulent scales is weak, it may be expected that they should develop a close-to-equilibrium state (Alexakis & Brachet, 2019). Indeed, (4.4) is well supported by a number of numerical studies conducted in recent years (Dallas *et al.*, 2015; Cameron *et al.*, 2017; Alexakis & Biferale, 2018; Alexakis & Brachet, 2019). Furthermore, the validity of thermal-equilibrium spectra in more general types of turbulence has been demonstrated experimentally for capillary-wave turbulence by Michel *et al.* (2017). An experiment to study the large scales of hydrodynamic turbulence is also in development by the same group.

However, like any statistical-mechanics argument, the reasoning outlined above does not elucidate the mechanism by which the equilibrium spectrum is attained. Furthermore, it is unclear what relation (4.4) has to the expansion of $\mathcal{E}(k)$ in terms of the Saffman and Loitsyansky integrals, (4.1). Until now, it has been assumed that the connection between forced turbulence and the concept of decaying 'Saffman turbulence' (i.e., that with $L \neq 0$) is superficial, despite both having the same large-scale spectral power law. This is because (i) analysis of the former is mostly concerned with the statistical steady state, obtained by taking a long-time average, while decaying turbulence is, by definition, transient; and (ii) large scales in the former may interact with the forcing, which is absent from decaying turbulence (Alexakis & Brachet, 2019). Nonetheless, it should be noted that (4.1) is a purely kinematic result, and must, therefore, apply equally to the forced and decaying cases.

[2]If the large-scale Fourier modes of Navier-Stokes turbulence are taken to constitute a separate system to their smaller-scale forced and dissipating counterparts, then their thermal-equilibrium spectrum follows formally from the statistical mechanics of the truncated Euler equations, $\partial_t \boldsymbol{u} + \mathcal{P}_K\left[\boldsymbol{u}\cdot\boldsymbol{\nabla}\boldsymbol{u} + \boldsymbol{\nabla}p\right] = 0$, where $\boldsymbol{u}$ is the incompressible velocity field, p is the pressure, determined by $\boldsymbol{\nabla}\cdot\boldsymbol{u} = 0$, and $\mathcal{P}_K$ is a truncation operator that sets to zero all Fourier modes with $k > K$. This system satisfies a Liouville's theorem, and has an absolute equilibrium state that satisfies (4.4) in the absence of net kinetic helicity [Lee 1952; Orszag 1977; Kraichnan 1973, see Section 1 of Alexakis & Brachet 2019 for a review].

The central goal of this chapter is to reconcile the kinematic and statistical-mechanical points of view. This problem turns out to be non-trivial, because of the invariance of the Saffman integral. As we shall show in Section 4.2, this invariance is not restricted to decaying turbulence, but should also apply to forced turbulence, subject to certain reasonable conditions on the nature of the forcing. In particular, if the forcing is solenoidal and sufficiently local in real space (i.e., if its correlations decay sufficiently quickly), then non-local interactions via pressure waves are too weak to generate the long-range longitudinal velocity correlations, $\chi(r \to \infty) \propto r^{-3}$, required for a non-zero Saffman integral, as is the case in decaying turbulence (Saffman, 1967; Batchelor & Proudman, 1956; Davidson, 2015). Thus, the naïve conclusion that the equilibrium spectrum (4.4) simply corresponds to $L \neq 0$ cannot be correct. For consistency with (4.1), therefore, it must always be case that the equilibrium, $\propto k^2$, part of the spectrum terminates at some large cutoff scale, provided it is smaller than the system size. Above the cutoff scale, (4.1) demands that $\mathcal{E}(k \to 0) \propto k^4$.

In Section 4.3, we shall argue that the physical mechanism by which the equilibrium part of the spectrum develops is the stochasticisation of the distribution of linear momentum, an inevitable consequence of interactions between eddies, even if each of them individually has zero net momentum when it forms. We shall show that this process leads naturally to a split-power-law spectrum at the large scales, with (4.4) satisfied up to a cutoff scale that grows with time, corresponding to the largest scale at which eddies have been able to stochasticise their momentum distribution. The requirement of momentum conservation in these interactions means that different eddies become correlated, which generates the long-range correlations, $\chi(r) \propto r^{-3}$, required for $\mathcal{E}(k) \propto k^2$, though only up to the cutoff scale, above which correlations decay rapidly.

In Section 4.4, we propose a simple, though non-rigorous, model of this phenomenon, in which the large-scale momentum distribution of the flow evolves due to turbulent diffusion caused by flow-scale structures. Under this model, we find that the development of a k^2 spectrum is recovered for local, solenoidal forcing, with the cutoff scale growing like $t^{1/2}$. This prediction, along with a number of others, is borne out well in the numerical simulations that we present. Under the same model, we also consider

forcing that is local in real space, but not solenoidal—arguably, a more generic situation. Making use of a theorem due to Saffman (1967), we show that such turbulence need not equilibrate at large scales, on account of the long-range real-space correlations present in the solenoidal part of the forcing. Instead, the turbulent diffusion of injected momentum leads to a shallower spectrum than (4.4).

Finally, in Section 4.5, we investigate the implications of the equilibration phenomenon for decaying turbulence. We show that, regardless of the solenoidality of the forcing (i.e., its tendency to inject momentum fluctuations into the flow), the energy E of turbulence that is forced without long-range correlations for a long period and then allowed to decay obeys Saffman's law, $E \propto t^{-6/5}$ (Saffman, 1967), in the late-time limit. This is a result of continued stochasticisation of the momentum distribution during the period of decay.

Section 4.6 contains a short summary of our findings, followed by a discussion of their possible applications, implications and extensions in both hydrodynamical contexts and beyond—viz., in astrophysical MHD turbulence.

4.2 Long-range correlations and the invariance of Saffman's integral

Let us begin by reviewing an important kinematic result: turbulence with an energy spectrum satisfying $\mathcal{E}(k \to 0) \propto k^2$ necessarily has strong long-range correlations in real space (Batchelor & Proudman, 1956; Saffman, 1967; Davidson, 2015).

4.2.1 A k^2 spectrum requires strong long-range correlations

The energy spectrum is the Fourier transform of the two-point velocity correlation function, $\big\langle \boldsymbol{u}(\boldsymbol{x}) \cdot \boldsymbol{u}(\boldsymbol{x}+\boldsymbol{r}) \big\rangle \equiv \big\langle \boldsymbol{u} \cdot \boldsymbol{u}' \big\rangle$, where angle brackets indicate an ensemble average. For statistically homogeneous and isotropic turbulence, $\big\langle \boldsymbol{u} \cdot \boldsymbol{u}' \big\rangle$ is a function of $r = |\boldsymbol{r}|$ only, and then the energy spectrum is

$$\mathcal{E}(k) = \frac{k^2}{4\pi^2} \int \mathrm{d}^3\boldsymbol{r} \, \big\langle \boldsymbol{u} \cdot \boldsymbol{u}' \big\rangle e^{-i\boldsymbol{k}\cdot\boldsymbol{r}} = \frac{1}{\pi} \int_0^\infty \mathrm{d}r \big\langle \boldsymbol{u} \cdot \boldsymbol{u}' \big\rangle kr \sin(kr). \tag{4.5}$$

If correlations between points separated by distances much greater than the energy-containing scale of the turbulence, l, decay sufficiently quickly, then (4.5) may be Taylor-expanded for small k. Namely, if $\left\langle \boldsymbol{u} \cdot \boldsymbol{u}' \right\rangle < O(r^{-5})$ as $r \to \infty$, then (4.1) holds.

From (4.1), it would appear that the 'thermal' k^2 spectrum corresponds to $L \neq 0$. However, this conclusion is problematic, because L is an invariant. This fact is well known in the context of decaying turbulence, for which the conservation of L implies a meaningful distinction between turbulence with finite L, called 'Saffman turbulence', and that with $L = 0$, called 'Batchelor turbulence'. These two canonical types of turbulence have a number of differences, chief among them their laws for the decay of energy with time (see Davidson 2015 for a review). As we shall show in Section 4.2.2, conservation of L should also be expected in *forced* turbulence, provided that long-range correlations in the forcing function are sufficiently weak to prohibit injection of L. As a result, if $L = 0$ at $t = 0$, $L = 0$ at all subsequent times.

The relevance of correlations in the forcing function is that sufficiently strong long-range correlations in the velocity field are required for L to be non-zero. Statistical isotropy and homogeneity, together with incompressibility, restrict the allowed form of the two-point velocity correlation tensor $\langle u_i u_j' \rangle$ to

$$\langle u_i u_j' \rangle = \frac{u^2}{2r} \left[(r^2 \chi)' \delta_{ij} - \chi'(r) r_i r_j \right], \tag{4.6}$$

where $\chi(r) = \langle u_r(\boldsymbol{x}) u_r(\boldsymbol{x} + \boldsymbol{r}) \rangle / u^2$ is the longitudinal correlation function (see, e.g., Davidson, 2015; Landau & Lifshitz, 1959), and we follow the convention $u^2 \equiv \langle u_x^2 \rangle = \langle |\boldsymbol{u}|^2 \rangle / 3$. Equation (4.6) implies

$$\left\langle \boldsymbol{u} \cdot \boldsymbol{u}' \right\rangle = \frac{1}{r^2} \frac{\partial}{\partial r} (r^3 u^2 \chi). \tag{4.7}$$

Integrating (4.7) over all space, we find that the Saffman integral, (4.2), is

$$L = 4\pi u^2 \lim_{r \to \infty} r^3 \chi(r). \tag{4.8}$$

Thus, L is finite if and only if

$$\chi(r \to \infty) = O(r^{-3}). \tag{4.9}$$

Note that, somewhat counter-intuitively, (4.9) need not mean that $\left\langle \boldsymbol{u} \cdot \boldsymbol{u}' \right\rangle$ decays slowly with r, as may be shown by substituting (4.9) in (4.7). As a consequence, the

long-range correlations implied by (4.9) do not necessarily invalidate the expansion (4.1), which required $\langle \boldsymbol{u} \cdot \boldsymbol{u}' \rangle < O(r^{-5})$. An extreme example is a white-noise velocity field,

$$\langle \boldsymbol{u}(\boldsymbol{x}) \cdot \boldsymbol{u}(\boldsymbol{x}+\boldsymbol{r}) \rangle \propto \delta^3(\boldsymbol{r}) \implies \langle \boldsymbol{u} \cdot \boldsymbol{u}' \rangle(r) \propto \frac{\delta(r)}{r^2}. \tag{4.10}$$

It follows immediately from (4.2) and (4.10) that $L \neq 0$ for such a field (in this case, the k^2 spectrum extends to all scales). However, we see from (4.7) that $\chi(r) = 1/r^3$, and so, from (4.6), $\langle u_i u_j' \rangle = 3u^2 r_i r_j / 2r^5$ for $i \neq j$. This means that even a white-noise velocity field, if incompressible, must have long-range correlations hidden in the off-diagonal components of its spectral tensor.

4.2.2 Non-local fluid processes are insufficient to generate long-range correlations

Intuitively, no local (in real space) forcing mechanism can set up correlations between infinitely separated points, at least in the absence of non-local fluid processes. Of course, this need not be an obstacle to the development of a non-zero Saffman integral, and hence a thermal-equilibrium k^2 spectrum, because incompressible turbulence *is* subject to non-local interactions: physically, incompressibility is enforced via the action of pressure waves, which propagate at infinite velocity through the fluid. In this section, we show that these interactions are too weak to generate the long-range correlations required for $L \neq 0$.

The Navier-Stokes equations read

$$\frac{\partial \boldsymbol{u}}{\partial t} + \boldsymbol{u} \cdot \boldsymbol{\nabla} \boldsymbol{u} = -\boldsymbol{\nabla} p + \nu \nabla^2 \boldsymbol{u} + \boldsymbol{F}, \quad \boldsymbol{\nabla} \cdot \boldsymbol{u} = 0. \tag{4.11}$$

For the moment, let us assume that $\boldsymbol{F}$ is solenoidal, i.e., $\boldsymbol{\nabla} \cdot \boldsymbol{F} = 0$—we shall return to the case of $\boldsymbol{\nabla} \cdot \boldsymbol{F} \neq 0$ in Section 4.4.3.[3] Then,

$$\nabla^2 p(\boldsymbol{x}) = -\boldsymbol{\nabla} \cdot (\boldsymbol{u} \cdot \boldsymbol{\nabla} \boldsymbol{u}), \tag{4.12}$$

[3]The reader may wonder why this distinction is necessary. After all, only the solenoidal part of $\boldsymbol{F}$ is dynamically significant; the compressive part is negated by the pressure in an incompressible fluid. The problem is that when $\boldsymbol{\nabla} \cdot \boldsymbol{F} \neq 0$, the solenoidal part of $\boldsymbol{F}$ is not necessarily local in real space, even if $\boldsymbol{F}$ is. Remarkably, we shall find in Section 4.4.3 that when $\boldsymbol{\nabla} \cdot \boldsymbol{F} \neq 0$, locally forced turbulence does not generically tend to equilibrate towards $\mathcal{E}(k) \propto k^2$ at large scales.

so the pressure is always exactly what is required to negate the non-solenoidal part of the inertial force. We proceed following Batchelor & Proudman (1956), who analysed the strength of long-range correlations in decaying turbulence (see also Davidson 2015).

Let us consider the part of the pressure at coordinate $\boldsymbol{x}$ that results from the presence of a distant eddy located at the origin. Equation (4.12) may be inverted to give

$$p(\boldsymbol{x}) = \frac{1}{4\pi}\int \frac{\mathrm{d}^3\boldsymbol{x}'}{|\boldsymbol{x}'-\boldsymbol{x}|}\frac{\partial}{\partial x_i'}\frac{\partial}{\partial x_j'}u_i(\boldsymbol{x}')u_j(\boldsymbol{x}'). \tag{4.13}$$

Assuming the eddy is localised at scales that are much smaller than $|\boldsymbol{x}|$, we may Taylor-expand the Green's function $|\boldsymbol{x}'-\boldsymbol{x}|^{-1}$ in (4.13) in small $|\boldsymbol{x}'|$. Doing so, and employing $\boldsymbol{\nabla}\cdot\boldsymbol{u}=0$, we find

$$p(|\boldsymbol{x}|\to\infty) = \frac{1}{4\pi}\frac{\partial}{\partial x_i}\frac{\partial}{\partial x_j}\frac{1}{x}\int \mathrm{d}^3\boldsymbol{x}' u_i(\boldsymbol{x}')u_j(\boldsymbol{x}') + O(r^{-4}) = O(r^{-3}). \tag{4.14}$$

Thus, a localised eddy generates a pressure field that extends to arbitrarily large distances, falling off as r^{-3}. Through this pressure field, distant fluid elements are able to interact in a non-local manner, thereby generating long-range correlations in the velocity field.

The strength of these correlations may be estimated from the von Kármán-Howarth equation (von Kármán & Howarth, 1938), which follows from (4.11) under the assumptions of statistical isotropy and homogeneity:

$$\frac{\partial}{\partial t}\big\langle \boldsymbol{u}\cdot\boldsymbol{u}'\big\rangle = \frac{1}{r^2}\frac{\partial}{\partial r}\frac{1}{r}\frac{\partial}{\partial r}(r^4u^3K) + 2\nu\nabla^2\big\langle \boldsymbol{u}\cdot\boldsymbol{u}'\big\rangle + 2\big\langle \boldsymbol{u}\cdot\boldsymbol{F}'\big\rangle, \tag{4.15}$$

where $K(r) = \langle u_r(\boldsymbol{x})u_r(\boldsymbol{x})u_r(\boldsymbol{x}+\boldsymbol{r})\rangle/u^{3/2}$ is the longitudinal triple-correlation function. Notably, pressure does not appear in (4.15)—this is a consequence of isotropy, which demands that $\langle u_i p'\rangle = 0$. Instead, pressure enters implicitly via its coupling to higher-order correlators, i.e., to the term containing $K(r)$. The analogue of (4.15) for triple correlations is

$$\frac{\partial}{\partial t}\langle u_iu_ju_k'\rangle = \frac{\partial}{\partial r_l}\langle u_iu_ju_k'u_l\rangle - \frac{\partial}{\partial r_l}\langle u_iu_ju_k'u_l'\rangle - \left\langle u_iu_j\frac{\partial p'}{\partial x_k'}\right\rangle - \left\langle u_k'\left(u_i\frac{\partial p}{\partial x_j}+u_j\frac{\partial p}{\partial x_i}\right)\right\rangle$$
$$+\text{ viscous terms} + \langle u_iu_jf_k'\rangle + \langle (u_if_j+f_iu_j)u_k'\rangle, \tag{4.16}$$

where the terms involving p do not vanish. Because these terms depend on gradients of p only [as was inevitable, considering that only gradients of p enter (4.11)], they are $O(r^{-4})$ as $r \to \infty$, according to Batchelor's result (4.14) for the far-field pressure distribution generated by an eddy. This suggests that

$$K(r \to \infty) = O(r^{-4}). \tag{4.17}$$

On the other hand, just as long-range second-order correlations arise from the presence of triple correlators in (4.15), so also, in principle, can long-range triple correlations arise from the coupling of (4.16) to fourth-order correlators. The evolution equations for the latter in turn depend on gradients of pressure and fifth-order correlators, and so on *ad infinitum*. Denoting a general nth-order correlator of $\boldsymbol{u}$ by C_n, and suppressing primes, the nth-order analogue of (4.16) can be written schematically as

$$\frac{\partial C_n}{\partial t} = \frac{\partial C_{n+1}}{\partial r} + \left\langle u_{i_1} \dots u_{i_{n-1}} \frac{\partial p}{\partial x_{i_n}} \right\rangle + \dots \qquad (n \geq 3). \tag{4.18}$$

where $\partial C_{n+1}/\partial r$ represents gradients of various $(n+1)$th-order correlators, and '$\dots$' represents terms that are subdominant as $r \to \infty$. For each value of $n \geq 3$, the correlator in (4.18) that involves pressure is $O(r^{-4})$ as $r \to \infty$ (following Batchelor's result), which will tend to produce $C_n(r \to \infty) = O(r^{-4})$. Then, $\partial C_{n+1}/\partial r \leq O(r^{-5})$ as $r \to \infty$, which is small compared to the pressure correlator, so the large-r asymptotic behaviour of C_n is not affected. This means that the couplings to higher-order correlators are negligible for all $n \geq 3$, and, therefore,

$$C_n(r \to \infty) = O(r^{-4}) \qquad (n \geq 3). \tag{4.19}$$

In particular, $K(r \to \infty) = O(r^{-4})$ for $n = 3$, as anticipated above.

From (4.15), $K(r \to \infty) = O(r^{-4})$ produces $\langle \boldsymbol{u} \cdot \boldsymbol{u}' \rangle(r \to \infty) \leq O(r^{-5})$ [the von Kármán-Howarth equation is unique among the correlator-evolution equations in that it does not involve pressure, so there is no "source term" for $O(r^{-4})$ correlations]. This is too weak a correlation to permit $L \neq 0$: integrating (4.15) over all $\boldsymbol{r}$, we find

$$\frac{\mathrm{d}L}{\mathrm{d}t} = 4\pi \lim_{r \to \infty} \left[\frac{1}{r} \frac{\partial}{\partial r} (r^4 u^3 K) \right] + 2 \int \mathrm{d}^3 \boldsymbol{r} \langle \boldsymbol{u} \cdot \boldsymbol{F}' \rangle, \tag{4.20}$$

where the term involving K vanishes for $K(r \to \infty) = O(r^{-4})$.

4.2.3 Correlations generated directly by the forcing

The calculation in Section 4.2.2 shows that non-local interactions between fluid elements are too weak to allow the Saffman integral to change with time. Another possibility is that correlations in the forcing function itself decay sufficiently slowly with distance to permit development of $L \neq 0$; this effect is encoded in the second term on the right-hand side of (4.20). Let us examine how slowly these correlations need to decay for $\mathrm{d}L/\mathrm{d}t$ to be non-zero.

The formal solution for $\langle \boldsymbol{u} \cdot \boldsymbol{F}' \rangle$, obtained by integrating the Navier-Stokes equation in time, is

$$\langle \boldsymbol{u} \cdot \boldsymbol{F}' \rangle = \int_0^t \mathrm{d}s \left[\frac{\partial}{\partial r_j} \langle u_i(s) u_j(s) f_i'(t) \rangle - \frac{\partial}{\partial r_i} \langle p(s) f_i'(t) \rangle + \nu \nabla^2 \langle \boldsymbol{u}(s) \cdot \boldsymbol{F}'(t) \rangle + \langle \boldsymbol{F}(s) \cdot \boldsymbol{F}'(t) \rangle \right]. \tag{4.21}$$

Of the four terms in the right-hand side of (4.21), the first and third give rise to surface terms in (4.20) that vanish provided the far-field components of the body forces encoded in $\boldsymbol{F}$ fall off faster than r^{-2} and r^{-1}, respectively. The second term is identically zero by the solenoidality of $\boldsymbol{F}$. The fourth term is a two-point, two-time correlation function of $\boldsymbol{F}$, which, because $\boldsymbol{F}$ is a solenoidal, statistically isotropic vector field, satisfies [cf. (4.7)]

$$\int_0^t \mathrm{d}s \, \langle \boldsymbol{F}(s) \cdot \boldsymbol{F}'(t) \rangle = \frac{1}{r^2} \frac{\partial}{\partial r} \big[r^3 H(t, r) \big], \tag{4.22}$$

where $H(t, r)$ is the time-integrated longitudinal correlation function of $\boldsymbol{F}$. From (4.20), we find that the contribution of this term to the rate of change of the Saffman integral vanishes if

$$H(t, r) < O(r^{-3}), \tag{4.23}$$

which is unsurprising, given (4.9).

To conclude, if the forcing function is solenoidal and sufficiently localised, then correlations between infinitely separated points that are strong enough to change the Saffman integral cannot arise in finite time, even accounting for the non-local nature

of the pressure force.[4] Because the Saffman integral was zero at $t = 0$, when $\boldsymbol{u} = 0$, it remains zero at all times, and therefore, it might appear, the system is forbidden from developing a k^2 spectrum at $k \to 0$.

4.2.4 Long-range correlations as a cumulative effect of short-range interactions

How, then, does one explain the numerical evidence for a thermal-equilibrium k^2 spectrum in forced turbulence (Dallas *et al.*, 2015; Cameron *et al.*, 2017; Alexakis & Biferale, 2018; Alexakis & Brachet, 2019)? The answer is that the k^2 spectrum is established not by non-local processes (in real space), but by the cumulative effect of *local* ones. Then, while infinitely separated points can never be strongly correlated enough to induce a k^2 spectrum, points separated by a large but finite distance can be (as long as one is prepared to wait long enough), leading to a k^2 spectrum that spans a finite, time-dependent range of wavenumbers.

Let us now demonstrate that this is indeed the typical behaviour of forced turbulence, by means of a numerical simulation. We take the forcing function $\boldsymbol{F}$ to be a solenoidal, Gaussian random field, and to be delta-correlated in time, so the spectrum of energy injection is

$$F(k) \equiv \frac{k^2}{2\pi^2} \int_0^t \mathrm{d}s \int \mathrm{d}^3\boldsymbol{r}\, \langle \boldsymbol{F}(t) \cdot \boldsymbol{F}'(s) \rangle e^{-i\boldsymbol{k}\cdot\boldsymbol{r}} \propto k^4 \exp(-k^2/k_p^2), \tag{4.24}$$

where the peak wavenumber $k_p = 80$. The large-scale k^4 tail of $F(k)$ is consistent with the generic spectral tail of an isotropic field with short spatial correlations.[5] The algorithm that we employ to generate $\boldsymbol{F}$ is the same as the one described in Section 2.D

[4] The reader used to thinking of forcing whose properties are specified in spectral, rather than real, space, might wonder whether the condition of "sufficient localisation" is satisfied for the common choice of forcing in a finite spectral band. In Appendix 4.A, we show that a finite-band forcing with a smooth spectrum has very weak correlations at the largest scales (i.e., it decays faster with r than any power law), as is intuitive, given the absence of energy in large-scale modes. If the spectrum of $\boldsymbol{F}$ is not smooth, but instead has sharp discontinuities at the edge of the band, correlations are induced in $\langle \boldsymbol{u} \cdot \boldsymbol{u}' \rangle$ that oscillate in r at the wavenumbers of the edges, and decay in amplitude as r^{-3}. While these correlations may, in principle, propagate into all other correlators, we show in Appendix 4.A that any oscillatory component of $\langle \boldsymbol{u} \cdot \boldsymbol{u}' \rangle$ always has a negligible effect on $\mathcal{E}(k)$ at small k, so these oscillatory correlations are of little dynamical significance.

[5] An expansion of $F(k \to 0)$ analogous to (4.1) yields $F(k \to 0) \propto k^4$ if $\langle \boldsymbol{F} \cdot \boldsymbol{F}' \rangle$ decays rapidly with r. A faster decay of $F(k \to 0)$ would require the equivalent of the Loitsyansky integral (4.3) for $\boldsymbol{F}$, $I_{\boldsymbol{F}} \equiv -\int_0^t \mathrm{d}s \int \mathrm{d}^3\boldsymbol{r} r^2 \langle \boldsymbol{F}(t) \cdot \boldsymbol{F}'(s) \rangle$, to be zero, which is an artificial situation.

(Hosking & Schekochihin, 2021). With this choice, we solve the Navier-Stokes equations (4.11) in a periodic domain of size 2π using the pseudo-spectral code Snoopy (Lesur, 2015) with 512^3 resolution. We employ de-aliasing according to the 2/3-rule, and use eighth-order hyper-dissipation, i.e., $\nu\nabla^2$ is replaced by $\nu_8\nabla^8$ in (4.11), where $\nu_8 = 10^{-16}$. The use of hyper-dissipation ensures that the effect of viscosity on the development of the large-scale structure is negligible.

The results of this simulation are shown in Figure 4.1. We observe that $\boldsymbol{u}$ gradually develops a k^2 spectrum at large scales, with a spectral knee at a time-dependent wavenumber $k_c(t)$ separating the $\propto k^4$ and $\propto k^2$ parts, as anticipated. By fitting the numerical spectrum to a trial function of the form $k^2[1 - \exp(-k^2/k_c(t)^2)]$, we find that $k_c(t) \propto t^{-1/2}$ (see inset to Figure 4.1). At large enough times, the k^2 part of the spectrum extends all the way to the box size, which is the steady state. However, the ability of the system to reach this steady state hinges on the finite size of the simulation box—in an infinite system, $\mathcal{E}(k) \propto k^2$ would only ever be satisfied in an ever-broadening but finite band of wavenumbers.

To summarise our progress so far, we have seen that the law of conservation of the Saffman integral, ported from the theory of decaying turbulence, also holds for forced turbulence, and that this law prohibits the thermal equilibration of arbitrarily large scales in finite time. Nonetheless, thermal equilibration up to a large but finite scale is not prohibited, and indeed this is the behaviour that turbulence whose forcing is spatially decorrelated tends to adopt (as is shown by Figure 4.1). However, we still lack a physical mechanism for the development of the thermal spectrum. In the next section, and the one that follows it, we shall argue that this mechanism is turbulent diffusion of linear momentum.

4.3 The large-scale spectrum and linear momentum

Assuming the equivalence of volume and ensemble averages, the definition of the Saffman integral, (4.2), is equivalent to

$$L = \lim_{V\to\infty} \frac{1}{V} \left\langle \left[\int_V \mathrm{d}^3\boldsymbol{r}\, \boldsymbol{u} \right]^2 \right\rangle \equiv \lim_{V\to\infty} \frac{\left\langle \boldsymbol{P}_V^2 \right\rangle}{V}. \tag{4.25}$$

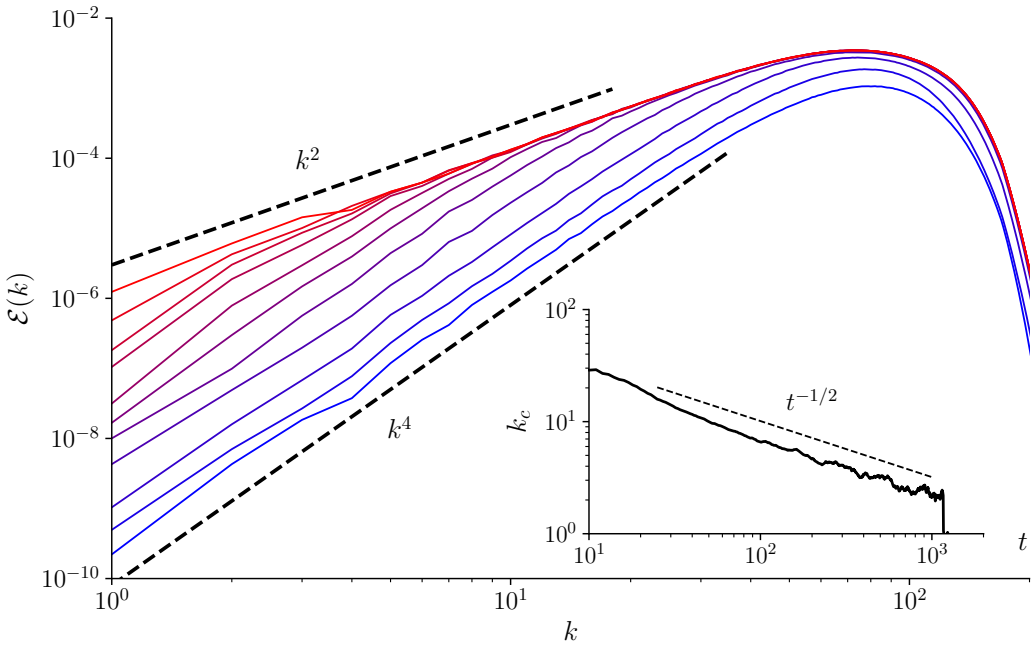

Figure 4.1: Saturation of the large scales in simulated Navier-Stokes turbulence forced by a delta-correlated, Gaussian random field with weak long-range spatial correlations [so that $F(k \to 0 \propto k^4)$, as explained in the text]. Displayed spectra are logarithmically spaced in time, with blue $\to$ red indicating earlier $\to$ later times. The inset shows the evolution of the knee wavenumber, $k_c(t)$, that separates the $\propto k^4$ and $\propto k^2$ parts of the spectrum. In the chosen units, the energy-injection rate is 0.7, and the r.m.s. velocity is $\simeq 0.5$.

The Saffman integral, therefore, is a measure of how much linear momentum $\boldsymbol{P}_V$ is contained in a large control volume V (Saffman, 1967; Davidson, 2015). For instance, in Saffman turbulence, where each eddy in V has non-zero, but random, linear momentum, $\left\langle \boldsymbol{P}_V^2 \right\rangle \propto V$ (accumulating as a random walk), so L is finite. If, instead, each eddy has vanishing total momentum, as in Batchelor turbulence, then (4.25) is dominated by the contributions of eddies at the surface of V. In that case, $\left\langle \boldsymbol{P}_V^2 \right\rangle \propto V^{2/3}$, and so $L = 0$.

This idea immediately provides a physical explanation for why long-range correlations (4.9) are required for a finite L. Consider an isolated turbulent eddy in an otherwise quiescent fluid. The linear momentum contained in a large sphere V of radius R, centred on the eddy, is

$$\boldsymbol{P}_{\text{eddy}} = \int_V \mathrm{d}^3\boldsymbol{r}\, \boldsymbol{u} = \int_{\partial V} \mathrm{d}\boldsymbol{S} \times \boldsymbol{A}, \tag{4.26}$$

where we have represented the solenoidal velocity field as $\boldsymbol{u} = \boldsymbol{\nabla} \times \boldsymbol{A}$. Clearly, $\boldsymbol{P}_{\text{eddy}}$ vanishes unless the average of $\boldsymbol{A}$ over ∂V scales as R^{-2} as $R \to \infty$, implying that the mean velocity on ∂V scales as R^{-3}. One can imagine building a synthetic $L \neq 0$ turbulence by superimposing such eddies with random positions and orientations; this velocity field will necessarily have long-range correlations, owing to the long tails of the component eddies.

In fact, there is a deep connection between the linear-momentum content of the turbulence and the large-scale spectrum, that goes beyond the finiteness of the Saffman integral and the Taylor expansion (4.1). Davidson (2015) has shown that, in incompressible, homogenenous and isotropic turbulence, $\langle \boldsymbol{P}_V^2 \rangle$ is a functional of $\chi(r)$: if V is a sphere of radius R,

$$\langle \boldsymbol{P}_V^2 \rangle = 4\pi^2 R^2 u^2 \int_0^{2R} \mathrm{d}r\, r^3 \chi(r) \left[1 - \left(\frac{r}{2R} \right)^2 \right]. \tag{4.27}$$

It is convenient to integrate this formula by parts, which gives

$$\langle \boldsymbol{P}_V^2 \rangle = 2\pi^2 u^2 \int_0^{2R} \mathrm{d}r r \int_0^r \mathrm{d}r' r'^3 \chi(r'), \tag{4.28}$$

boundary terms having vanished exactly. From (4.28), it is clear that $\langle \boldsymbol{P}_V^2 \rangle \propto R^3$ only if $\chi(r' \to \infty) \propto r'^{-3}$. If, instead, $\chi(r')$ decays quickly, viz., $\chi(r' \to \infty) < O(r'^{-4})$,

the r' integral in (4.28) is dominated by small r', and hence $\langle \boldsymbol{P}_V^2 \rangle \propto R^2$, which is the scaling $\langle \boldsymbol{P}_V^2 \rangle \propto V^{2/3}$ obtained above. Equation (4.28) is also readily inverted, to yield

$$u^2 \chi(2R) = \frac{1}{128\,\pi^2} \frac{1}{R^3} \frac{\partial}{\partial R} \frac{1}{R} \frac{\partial \langle \boldsymbol{P}_V^2 \rangle}{\partial R}. \tag{4.29}$$

Therefore, full knowledge of $\langle \boldsymbol{P}_V^2 \rangle$ as a function of R is equivalent to full knowledge of $\chi(r)$, and hence, via (4.5) and (4.7), of the energy spectrum. This observation suggests that one might seek the explanation of the growth of the thermal spectrum in Figure 4.1 as a consequence of the evolution of $\langle \boldsymbol{P}_V^2 \rangle$.

4.3.1 Broken-power-law spectra and their momentum content

The above discussion suggests that we might interpret the growth of a k^2 spectrum over a finite range of wavenumbers as indicating the development of random fluctuations in momentum that satisfy $\left\langle \boldsymbol{P}_V^2 \right\rangle \propto R^3$ over the corresponding range of scales. More precisely, these fluctuations would be quasi-random, in that the momenta of the eddies contained within V would cancel more precisely when R was large enough, so that $\left\langle \boldsymbol{P}_V^2 \right\rangle$ would be dominated by eddies at the surface of V, so that $\left\langle \boldsymbol{P}_V^2 \right\rangle \propto R^2$. Then, $\mathcal{E}(k \to 0) \propto k^4$. A schematic representation of the distribution of momentum of this "quasi-Saffman turbulence", similar to those presented by Davidson (2015) for the true Saffman and Batchelor turbulence, is shown in Figure 4.2.

Let us now check that these intuitive expectations hold up mathematically, i.e., that broken-power-law spectra do correspond to broken power laws in the dependence of $\langle \boldsymbol{P}_V^2 \rangle$ on R. From (4.7) and

$$\left\langle \boldsymbol{u} \cdot \boldsymbol{u}' \right\rangle = 2 \int_0^\infty \mathrm{d}k \mathcal{E}(k) \frac{\sin(kr)}{kr}, \tag{4.30}$$

which is the inverse of (4.5), it follows that

$$u^2 \chi(r) = 2 \int_0^\infty \mathrm{d}k\, \mathcal{E}(k)\, \frac{\sin(kr) - kr\cos(kr)}{(kr)^3}. \tag{4.31}$$

In Appendix 4.B, we present a formal asymptotic expansion of (4.31), assuming that $\mathcal{E}(k) \propto k^a$ for $k_1 \le k \le k_2$ with $k_2 \gg k_1$ [we remain agnostic about $\mathcal{E}(k)$ outside of

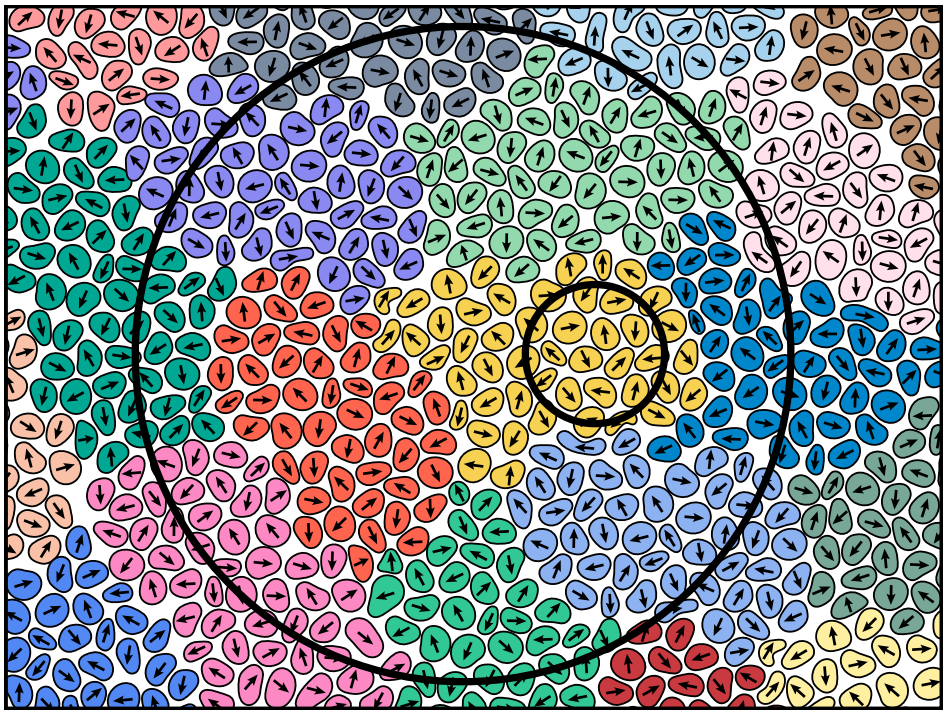

Figure 4.2: Schematic of a 'quasi-random' distribution of linear momentum, i.e., one that would result in a broken-power-law spectrum, as in Figure 4.1. Sufficiently large patches of turbulence have vanishing total momentum—a number of such patches (identified in a non-unique manner) are shown in different colours in the figure. For a control volume V that is larger than the outer scale of the turbulence but smaller than the characteristic scale of the net-zero-momentum patches (e.g., the smaller circle in the figure), $\langle \boldsymbol{P}^2 \rangle \propto R^3$ because the eddies contained by V (represented by individual blobs) have uncorrelated, random momenta (represented by arrows). On the other hand, $\langle \boldsymbol{P}^2 \rangle \propto R^2$ for V much larger than the zero-net-momentum patches, because then only patches at the surface of V contribute to the sum—in the figure, the central orange and yellow patches do not contribute to the total momentum contained within the larger circle.

this range]. This choice for $\mathcal{E}(k)$ models the broken-power-law spectrum shown in Figure 4.1. We show that, for $1/k_2 \ll r \ll 1/k_1$,

$$u^2\chi(r) \simeq \begin{cases} \text{constant} \sim \displaystyle\int_0^{k_1} \mathrm{d}k\mathcal{E}(k) & \text{if } a < -1; \\ \dfrac{1}{3}\dfrac{\ln(k_1 r)}{\ln(k_2/k_1)} \displaystyle\int_{k_1}^{k_2} \mathrm{d}k\mathcal{E}(k) & \text{if } a = -1; \\ \text{undetermined}, \ \lesssim (k_2 r)^{-1-a} \displaystyle\int_{k_1}^{k_2} \mathrm{d}k\mathcal{E}(k) & \text{if } a = 4, 6, 8 \ldots; \\ -\Gamma(a-2)(a^2-1)\sin\left(\dfrac{a\pi}{2}\right)(k_2 r)^{-1-a} \displaystyle\int_{k_1}^{k_2} \mathrm{d}k\mathcal{E}(k) & \text{otherwise.} \end{cases} \tag{4.32}$$

Let us explain qualitatively each case in turn.

If $a < -1$, $\chi(r) \sim$ const, which is intuitive: the energy contained in the band $\{k_1, k_2\}$ is dominated by the largest structures, while we are looking at correlations on scales much smaller than them ($r \ll k_1^{-1}$).

If $a = -1$, then every scale in the band $\{k_1, k_2\}$ contributes equally to the energy contained within it—this energy diverges in the limit $k_2/k_1 \to \infty$, explaining the factor of $\ln(k_2/k_1)$ in the denominator of (4.32). It turns out that the r dependence of $\chi(r)$ is logarithmic in this case.

If $a = 4, 6, 8 \ldots$, then although $\chi(r)$ must decay faster than r^{-1-a} in the range $1/k_2 \ll r \ll 1/k_1$, its behaviour is not uniquely determined by our assumption of a power-law scaling for $\mathcal{E}(k)$. This was to be expected, because even-power spectra are precisely the ones generated in the expansion (4.1), and no specific strength of long-range correlations in the velocity field is required for the coefficients of k^a with $a = 4, 6, 8 \ldots$ in this expansion to be non-zero (unlike for $a = 2$).

Finally, for all other cases, including that of $a = 2$, $\chi(r)$ decays like r^{-1-a} for $1/k_2 \ll r \ll 1/k_1$. In particular, note that (4.9) may be recovered from (4.32) for $a = 2$, as $\lim_{a\to 2} \Gamma(a-2)\sin(a\pi/2) = -\pi/2$.

Our motivation in deriving (4.32) was to obtain the dependence of $\langle \boldsymbol{P}_V^2 \rangle$ on R that is associated with a finite-extent large-scale power law in $\mathcal{E}(k)$. Let us consider scales $1/k_2 \ll R \ll 1/k_1$, where k_2 is now identified with the outer scale of the turbulence,

i.e., $k_2 \sim 1/l$, and k_1 is identified with the scale of the spectral knee k_c in Figure (4.1). Then, from (4.28),

$$\langle \boldsymbol{P}_V^2 \rangle = 2\pi^2 u^2 \int_0^{2R} \mathrm{d}r r \left[\int_0^{X/k_2} \mathrm{d}r' r'^3 \chi(r') + \int_{X/k_2}^{r} \mathrm{d}r' r'^3 \chi(r') \right], \tag{4.33}$$

where X is chosen so that $1 \ll X \ll k_2/k_1$, in which case (4.32) is applicable in the second integral appearing inside the brackets in (4.33). This integral dominates over the first one for $r \gg X/k_2$ as long as $r^3\chi(r) \geq O(1/r)$, which, according to (4.32), it will do if the spectrum follows a local power law with exponent $a \leq 3$. Otherwise, the first integral, which is independent of r, dominates. Thus, we have

$$\langle \boldsymbol{P}_V^2 \rangle \propto \begin{cases} R^2 & \text{if } a > 3, \\ R^2 \ln R & \text{if } a = 3, \\ R^{5-a} & \text{if } -1 < a < 3, \\ R^6 \ln R & \text{if } a = -1, \\ R^6 & \text{if } a < -1. \end{cases} \tag{4.34}$$

We note that the classical scalings (see Davidson 2015) are readily recoverable from (4.34): the intuitive "surface-term-dominated" $\langle \boldsymbol{P}_V^2 \rangle \propto R^2$ is recovered for steep spectral slopes, $a > 3$, corresponding to weak long-range correlations, while the Saffman scaling $\langle \boldsymbol{P}_V^2 \rangle \propto R^3$ is recovered for $a = 2$. The scaling $\langle \boldsymbol{P}_V^2 \rangle \propto R^6$ for $a < -1$ is also an intuitive one: such a spectrum is energetically dominated by structures with characteristic scale much larger than R, therefore control volumes $V \propto R^3$ will contain a total amount of momentum that is proportional to V. Though these results are familiar, (4.34) has the important new feature that it does not require the spectral power law to extend all the way to $k = 0$—it is sufficient for $\mathcal{E}(k) \propto k^a$ only for $k_1 \leq k \leq k_2$, as long as we restrict attention to volumes with $1/k_2 \ll R \ll 1/k_1$.[6]

[6] Aside from the generalisation of previous results to a finite-band power law in $\mathcal{E}(k)$, the other qualitatively new feature in (4.34) is that we have allowed for non-integer a. In this respect, (4.32) and (4.34) can be viewed as an extension of the results for $\chi(r \to \infty) \propto r^{-m}$ for integer m derived by Davidson (2011). While non-integer large-scale spectral power laws may be of limited applicability to real turbulence (though they can, of course, be manufactured numerically), they nonetheless have pedagogical value, particularly for $3 < a < 4$, when $\langle \boldsymbol{P}_V^2 \rangle \propto R^2$, implying that arguments for the invariance of the large-scale spectrum in decaying turbulence that are based on momentum conservation (Saffman 1967, Davidson 2011; also see Section 4.5) do not apply. If it is true that the large-scale

4.3.2 The development of "quasi-random" momentum fluctuations

Having confirmed that broken-power-law spectra, of the form shown in Figure 4.1, do correspond to $\langle \boldsymbol{P}_V^2 \rangle \propto R^3$ over a finite range of scales, we now turn to the question of the physical mechanism that is responsible for the development of such a scaling.

Intuitively, $\langle \boldsymbol{P}_V^2 \rangle \propto R^3$ can arise as a simple consequence of momentum transport by the flow. Consider a localised fluid motion that develops at $t = 0$ as a result of the forcing. While the total linear momentum associated with this structure will be zero, its momentum density will be transported under the action of the flow (i.e., the sum of the eddy's own motion and that of the rest of the flow), and therefore will become distributed over an ever-increasing volume as time advances. When this volume becomes large compared to the control volume V for which we are interested in computing the total square momentum, this structure will contribute to $\boldsymbol{P}_V$ as a "volume term", rather than as a surface one. The occurence of this process at all points in space will then lead to a "quasi-random" momentum distribution, of the form depicted in Figure 4.2.

In Figure 4.3, we present a simple toy model to illustrate this idea. In this model, turbulent eddies initialised by the forcing at $t = 0$ are represented by pairs of particles. Each particle in the pair is initialised with the same random position in 2D space, though they have opposite momenta – see panel (a). This means that at $t = 0$, $\langle \boldsymbol{P}_V^2 \rangle \propto R$, because only "eddies" at the boundary of V contribute, much as in a real forced turbulence that has just reached saturation at the forcing scale (note that, naturally, the surface-dominated and volume-dominated scalings are different in 2D). Subsequently, the particles move ballistically, i.e., without interacting, all at the same speed, u, but in random directions. At later times, the distribution of their momenta becomes quasi-random, in the sense described above. For $R \ll ut \equiv R_c(t)$, $\langle \boldsymbol{P}_V^2 \rangle \propto R^2$,

asymptotic of the energy spectrum is indeed invariant in decaying turbulence with $3 < a < 4$, then this must be a result of the conservation of some other quantity. The arguments presented in Davidson (2009, 2011) suggest that angular-momentum conservation, if it holds, would result in the invariance of this asymptotic; direct numerical simulations of turbulence with $3 < a < 4$ might therefore shed some light on the unsolved problem of angular-momentum conservation in turbulence in open domains. Interestingly, large-scale spectra with $3 < a < 4$ are not invariant under the EDQNM closure model, whereas those with $a < 3$ are (Eyink & Thomson, 2000; Lesieur *et al.*, 2005; Lesieur, 2008).

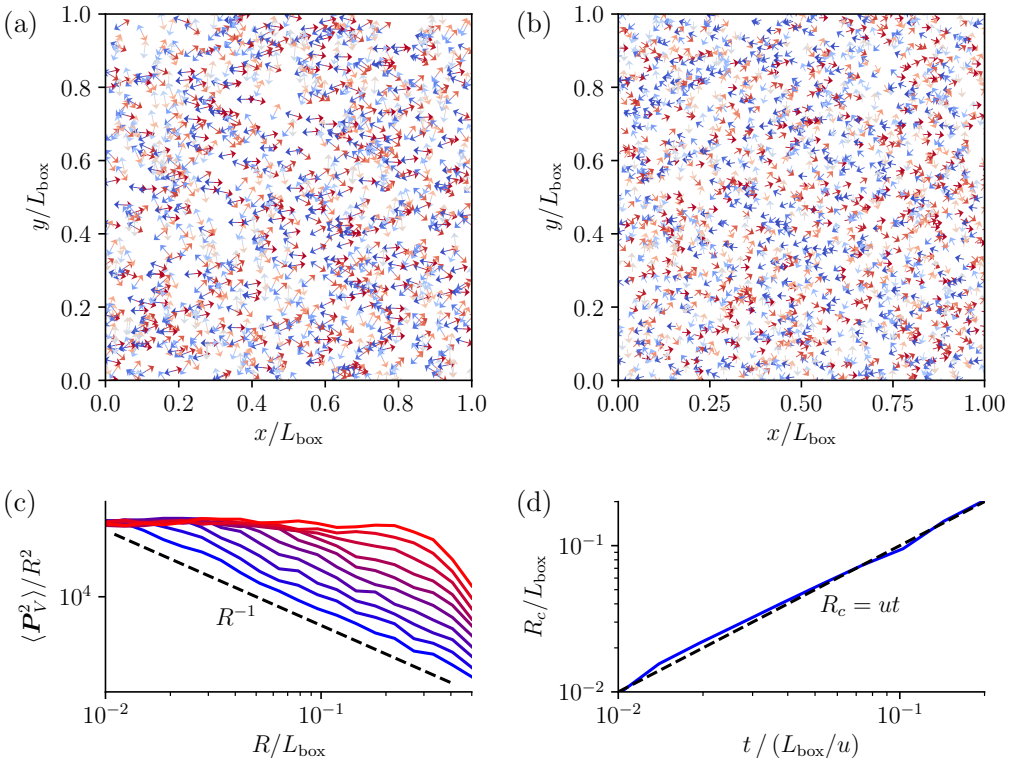

Figure 4.3: A toy model to illustrate quasi-randomisation of eddy momentum. Eddies are represented by pairs of particles that are initialised with equal and opposite momenta, but at the same position in space, shown as red and blue arrows in panel (a). Panel (b) shows the state of the system at $t = L_{\mathrm{box}}/5u$. Panel (c) shows the evolution of $\langle \boldsymbol{P}_V^2 \rangle$ with time (blue = early, red = late), demonstrating the development of the "stochastic" momentum scaling, $\langle \boldsymbol{P}_V^2 \rangle \propto R^2$, as explained in the text. Panel (d) shows that the position $R_c(t)$ of the "knee" in the scaling behaviour of $\langle \boldsymbol{P}_V^2 \rangle$, between $\propto R$ and $\propto R^2$, grows linearly with time, $R_c = ut$.

because the control volume V will only contain one particle from each pair. For $R \gtrsim R_c(t)$, $\left\langle \boldsymbol{P}_V^2 \right\rangle \propto R$, as the volume will contain both particles, whose contributions will cancel, unless they straddle the boundary.

While ballistic streaming is likely a poor model of the real motions of turbulent fluid structures, and while this toy model also neglects the effect of continuous forcing and energy dissipation, it captures the essential idea: transport of linear momentum means that highly ordered states where the total momentum of each flow structure vanishes cannot be maintained. Instead, it seems inevitable that the distrubution of momentum will become quasi-random, i.e., that $\left\langle \boldsymbol{P}_V^2 \right\rangle \propto R^3$ (in 3D) up to a finite $R = R_c(t)$, which will grow with time.

Intuitively, ballistic streaming represents the upper bound permitted by causality on the rate at which the distribution of momentum can become stochasticised in the absence of significant non-local interactions. In Appendix 4.C, we show how this causal bound, $R_c \sim ut$, can be recovered from the Navier-Stokes equation directly. In real turbulence, however, momentum is transported chaotically, rather than ballistically, so we should expect that $R_c \ll ut$. Owing to the long non-linear timescale associated with interactions between structures on the largest scales, it is reasonable to suppose that "momentum density" is transported *passively* by the turbulent diffusivity of the flow, at least insofar as the large scales are concerned. In that case, we expect a diffusive scaling $R_c \sim 1/k_c \propto t^{1/2}$, rather than the ballistic one, $R_c \propto t$. As we shall see in Section 4.4, the diffusive scaling is indeed in excellent agreement with direct numerical simulations.

4.3.3 $R_c \propto t^{1/2}$ due to linear growth of the Loitsyansky integral

Before we explore this topic further, however, let us pause to consider a tempting, if dangerous, argument that would appear to guarantee the scaling $R_c \sim 1/k_c \propto t^{1/2}$ without any further assumptions.

Let us accept, on the basis of the intuitive momentum-stochasticisation argument of Section 4.3.2, that a k^2 spectrum will develop in a limited range of k, as depicted in Figure 4.1.

It follows from integrating (4.15) over r that the Loitsyansky integral (4.3) grows according to

$$\frac{\mathrm{d}I}{\mathrm{d}t} = 8\pi u^3 \lim_{r\to\infty}\left[r^4 K(r)\right] - 12\nu L - 2\int \mathrm{d}^3\boldsymbol{r}\, r^2\left\langle \boldsymbol{u}\cdot\boldsymbol{F}'\right\rangle. \tag{4.35}$$

Because the system always has a vanishing Saffman integral, the second term on the right-hand side of (4.35) is zero. For simplicity, let us assume that the forcing has a short correlation time, in which case (4.35) becomes, after substitution of (4.21) and (4.22),

$$\frac{\mathrm{d}I}{\mathrm{d}t} = 8\pi u^3 \lim_{r\to\infty}\left[r^4 K(r)\right] + 8\pi\int \mathrm{d}r\, r^4 H(r). \tag{4.36}$$

It is often conjectured that I is conserved by an isotropic turbulence decaying from an initial state with a k^4 spectrum (Kolmogorov, 1941*a*; Landau & Lifshitz, 1959; Davidson, 2015; Ishida *et al.*, 2006). While this point is not universally accepted (e.g., I is not conserved under the popular EDQNM closure; see Lesieur 2008 and references therein), the evidence from direct numerical simulations appears to support the conservation of I, at least after an initial transient period (Ishida *et al.*, 2006). As may be seen from (4.36), the invariance of I in the absence of forcing requires that $K(r\to\infty) < O(r^{-4})$, i.e., long-range triple correlations must decay faster than the $K(r\to\infty) = O(r^{-4})$ that follows from considering long-range pressure-mediated interactions (Batchelor & Proudman 1956; Davidson 2015; see our Section 4.2.2). Supposing that a state with $K(r\to\infty) < O(r^{-4})$ can also arise in forced turbulence, (4.36) implies linear growth of I, whence, by (4.1),

$$\mathcal{E}(k\to 0) \propto k^4 t. \tag{4.37}$$

From our expectation that the system will saturate with a spectrum $\mathcal{E}(k)\propto k^2$, the wavenumber k_c that has just saturated at time t satisfies

$$k_c^4 t \propto k_c^2 \implies k_c \propto t^{-1/2}, \tag{4.38}$$

which is precisely the diffusive scaling suggested above.

However, this argument should be treated with caution, because it seems unlikely that $K(r\to\infty) < O(r^{-4})$ could be realised in forced turbulence. Numerical evidence

suggests that this condition is only satisfied in decaying turbulence after an initial transient period (Ishida *et al.*, 2006), during which the system loses memory of the initial conditions. Prior to this, growth of I is observed, which requires $K(r \to \infty) = O(r^{-4})$. Forced turbulence, of course, is essentially always in this 'transient' regime, as the system never loses memory of the statistical properties of the forcing. Indeed, it is clear that $K(r \to \infty) = O(r^{-4})$ from the fact that $\mathcal{E}(k) \propto k^4$ does develop at the largest scales in turbulence forced with $I_{\boldsymbol{F}} = 0$, which is the case, e.g., for forcing in a finite spectral band (see Section 4.4.1).

On the other hand, the diffusive scaling (4.38) may still be obtained if $\lim_{r\to\infty} r^4 K(r)$ is constant in time. Admittedly, it is not *a priori* clear that this should be the case, because the value of this limit can change as a result of the long-range, pressure-mediated interactions between eddies, whose statistical properties do, after all, change with time as a result of the stochasticisation of linear momentum. Nonetheless, in the next section, we show that a passive model of the large-scale dynamics reproduces the linear growth (4.37) of I, indicating that $\lim_{r\to\infty} r^4 K(r) = \text{const}$ may be a reasonable approximation in real forced turbulence.

4.4 A solvable model of passive momentum diffusion

In Section 4.3, we argued that the development of a thermal k^2 spectrum over a finite, but growing, large-scale band is a consequence of the quasi-randomisation of the linear momentum distribution. In this section, we consider a model of this process in which the momentum density is a *passive* quantity, in which case its randomisation can be understood as a consequence of turbulent diffusion.

To motivate the model, let us consider the evolution of a velocity field $\boldsymbol{w}$ under the Navier-Stokes equations. Let $\boldsymbol{w} = \overline{\boldsymbol{w}} + \widetilde{\boldsymbol{w}}$, where $\overline{\boldsymbol{w}}$ is the large-scale part of $\boldsymbol{w}$, formally defined as the result of applying a Fourier-space filter to $\boldsymbol{w}$ to isolate only those modes with $k < K$, for some K much smaller than the characteristic wavenumber of the forcing, while $\widetilde{\boldsymbol{w}}$ is the remaining smaller-scale part, consisting of modes with

$k > K$. Then the evolution of $\boldsymbol{w}$ proceeds according to

$$\frac{\partial \boldsymbol{w}}{\partial t} + \mathcal{P}\big[\overline{\boldsymbol{w}} \cdot \boldsymbol{\nabla}\overline{\boldsymbol{w}} + \overline{\boldsymbol{w}} \cdot \boldsymbol{\nabla}\widetilde{\boldsymbol{w}} + \widetilde{\boldsymbol{w}} \cdot \boldsymbol{\nabla}\overline{\boldsymbol{w}} + \widetilde{\boldsymbol{w}} \cdot \boldsymbol{\nabla}\widetilde{\boldsymbol{w}}\big] = \nu\nabla^2\boldsymbol{w} + \boldsymbol{F}, \tag{4.39}$$

where $\mathcal{P}$ is the Fourier-space projection operator that returns the solenoidal part of the field on which it operates: $[\mathcal{P}\boldsymbol{w}]_i \equiv (\delta_{ij} - k_i k_j/k^2)w_j$. Let us assume that, because the large-scale modes are energetically subdominant to the rest of the flow, advection by them is unimportant. Then we are left with

$$\frac{\partial \boldsymbol{w}}{\partial t} + \mathcal{P}\big[\widetilde{\boldsymbol{w}} \cdot \boldsymbol{\nabla}\boldsymbol{w}\big] = \nu\nabla^2\boldsymbol{w} + \boldsymbol{F}, \tag{4.40}$$

so the only important non-linearity is advection by the small-scale part of $\boldsymbol{w}$. The small-scale part of (4.40) is

$$\frac{\partial \widetilde{\boldsymbol{w}}}{\partial t} + \mathcal{P}\big[\widetilde{\widetilde{\boldsymbol{w}} \cdot \boldsymbol{\nabla}\widetilde{\boldsymbol{w}}} + \widetilde{\widetilde{\boldsymbol{w}} \cdot \boldsymbol{\nabla}\overline{\boldsymbol{w}}}\big] = \nu\nabla^2\widetilde{\boldsymbol{w}} + \widetilde{\boldsymbol{F}}. \tag{4.41}$$

Again, owing to the energetic subdominance of $\overline{\boldsymbol{w}}$ (and its small gradients), let us assume that the term involving $\overline{\boldsymbol{w}}$ is negligible compared to the other term inside the square brackets, so

$$\frac{\partial \widetilde{\boldsymbol{w}}}{\partial t} + \mathcal{P}\big[\widetilde{\widetilde{\boldsymbol{w}} \cdot \boldsymbol{\nabla}\widetilde{\boldsymbol{w}}}\big] = \nu\nabla^2\widetilde{\boldsymbol{w}} + \widetilde{\boldsymbol{F}}. \tag{4.42}$$

Equation (4.42) shows that, under the approximations outlined so far, the evolution of $\widetilde{\boldsymbol{w}}$ is entirely decoupled from that of $\overline{\boldsymbol{w}}$. Taking the large-scale part of (4.40), we find that $\overline{\boldsymbol{w}}$ satisfies

$$\frac{\partial \overline{\boldsymbol{w}}}{\partial t} + \mathcal{P}\big[\,\overline{\widetilde{\boldsymbol{w}} \cdot \boldsymbol{\nabla}\widetilde{\boldsymbol{w}}} + \overline{\widetilde{\boldsymbol{w}} \cdot \boldsymbol{\nabla}\overline{\boldsymbol{w}}}\,\big] = \nu\nabla^2\overline{\boldsymbol{w}} + \overline{\boldsymbol{F}}. \tag{4.43}$$

In a sense, therefore, $\overline{\boldsymbol{w}}$ is a passive field: although (4.43) shows that its evolution is affected by $\widetilde{\boldsymbol{w}}$, $\widetilde{\boldsymbol{w}}$ is not affected by $\overline{\boldsymbol{w}}$, according to (4.42).

Motivated by this property, we propose to replace $\widetilde{\boldsymbol{w}}$ with an artificial field, $\boldsymbol{u}$, wherever the former appears as an advecting field in (4.42) and (4.43). This model can be summarised by

$$\frac{\partial \boldsymbol{w}}{\partial t} + \mathcal{P}\big[\boldsymbol{u} \cdot \boldsymbol{\nabla}\boldsymbol{w}\big] = \nu\nabla^2\boldsymbol{w} + \boldsymbol{F}. \tag{4.44}$$

This equation is sometimes called the "linear pressure model" of the Navier-Stokes equation; a number of its properties have been studied by Benzi *et al.* (2001), Adzhemyan *et al.* (2001*a*,*b*), Antonov *et al.* (2003), and Arponen (2009). Physically, (4.44)

describes "eddies" of the field $\boldsymbol{w}$ interacting nonlinearly with eddies of the field $\boldsymbol{u}$, rather than other $\boldsymbol{w}$-eddies. The $\boldsymbol{w}$-eddies can receive momentum from their interaction with the $\boldsymbol{u}$-eddies, whereas the latter do not get anything back, as their motion is externally prescribed. Nonetheless, the receipt of momentum by $\boldsymbol{w}$-eddies still occurs in a way that locally conserves momentum, because $\int \mathrm{d}^3\boldsymbol{x}\,\boldsymbol{w}$ is an invariant of (4.44). Ultimately, then, the $\boldsymbol{w}$-eddies do have local interactions that satisfy net-momentum conservation, which is the key ingredient for the stochasticisation of their momentum distribution. If the field $\boldsymbol{u}$ is chosen so that its statistical properties are close to those of real turbulence, it may be hoped that the evolution of $\overline{\boldsymbol{w}}$ should mimic that of the large-scale part of a real velocity field (the same need not be true of $\widetilde{\boldsymbol{w}}$, though see Benzi *et al.* 2001 for some similarities in small-scale properties).

In Section 4.4.2, we shall present an analytic treatment of (4.44), taking $\boldsymbol{u}$ to be the so-called Kraichnan ensemble (Kraichnan, 1965, 1994). First, however, we present numerical simulations to demonstrate the validity of the model (4.44).

4.4.1 Assessing the passive-velocity model in simulated turbulence

In Figure 4.4, we present results of simulations with both "active" and "passive" velocity fields. Specifically, we plot the evolution of the energy spectra of the fields $\boldsymbol{v}$ and $\boldsymbol{w}$, denoted $\mathcal{E}_{\boldsymbol{v}}(k)$ and $\mathcal{E}_{\boldsymbol{w}}(k)$, respectively, where $\boldsymbol{v}$ is determined by the forced Navier-Stokes equation,

$$\frac{\partial \boldsymbol{v}}{\partial t} + \boldsymbol{v}\cdot\boldsymbol{\nabla}\boldsymbol{v} = -\boldsymbol{\nabla}p_{\boldsymbol{v}} + \nu\nabla^2\boldsymbol{v} + \boldsymbol{F}_{\boldsymbol{v}}, \tag{4.45}$$

while $\boldsymbol{w}$ is governed by the passive-velocity equation (4.44), viz.,

$$\frac{\partial \boldsymbol{w}}{\partial t} + \boldsymbol{u}\cdot\boldsymbol{\nabla}\boldsymbol{w} = -\boldsymbol{\nabla}p_{\boldsymbol{w}} + \nu\nabla^2\boldsymbol{w} + \boldsymbol{F}_{\boldsymbol{w}}, \tag{4.46}$$

where $\boldsymbol{u} = \mathcal{P}_K\boldsymbol{v}$, $\mathcal{P}_K$ is the truncation operator that removes all Fourier modes with $k < K = 40$, and $\boldsymbol{F}_{\boldsymbol{v}}$ and $\boldsymbol{F}_{\boldsymbol{w}}$ are forcing functions that are delta-correlated in time and inject an equal amount of energy into each Fourier mode in the band $40 < k < 80$ at every timestep (the box size is 2π). The other details of the simulations are as described in Section 4.2.3.

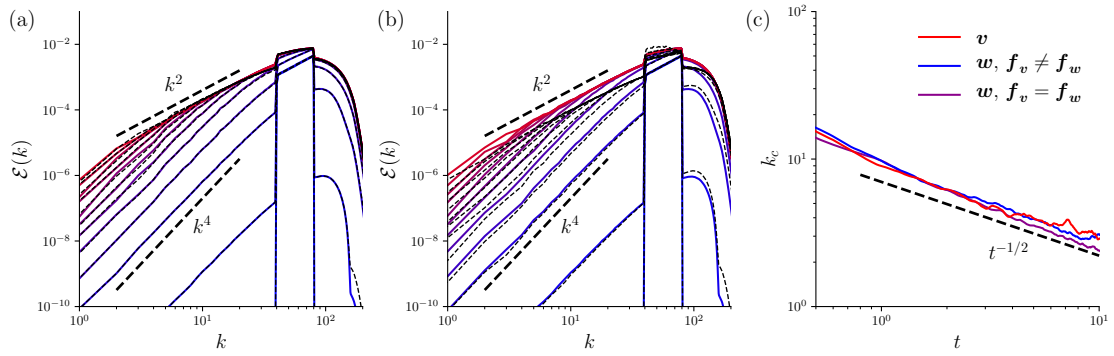

Figure 4.4: Development of the "thermal" k^2 spectrum by a Navier-Stokes velocity field, $\boldsymbol{v}$, described by (4.45), and a "passive velocity field", $\boldsymbol{w}$, described by (4.46). Panel (a) shows the case where $\boldsymbol{w}$ and $\boldsymbol{v}$ are forced by the same function, $\boldsymbol{F}_{\boldsymbol{v}} = \boldsymbol{F}_{\boldsymbol{w}}$, while panel (b) shows the case where $\boldsymbol{w}$ and $\boldsymbol{v}$ are forced independently. Spectra of $\boldsymbol{w}$, $\mathcal{E}_{\boldsymbol{w}}(k)$, are plotted with dashed black lines, while spectra of $\boldsymbol{v}$, $\mathcal{E}_{\boldsymbol{v}}(k)$, are plotted with solid coloured lines: blue $\rightarrow$ red indicates earlier $\rightarrow$ later times. Panel (c) shows the evolution of the knee wavenumber $k_c(t)$ between the k^4 and k^2 parts of the spectrum. In the chosen units, the energy injection rate into each of $\boldsymbol{v}$ and $\boldsymbol{w}$ is 2.5, and the r.m.s. values of all velocity fields are $\simeq 1.0$.

Panel (a) of Figure 4.4 shows the results of a simulation where $\boldsymbol{F}_{\boldsymbol{v}} = \boldsymbol{F}_{\boldsymbol{w}}$. The only difference between $\boldsymbol{v}$ and $\boldsymbol{w}$ in this case is that $\boldsymbol{w}$ evolves without being advected by the modes in the large-scale tail of the spectrum of $\boldsymbol{v}$. We see that both $\boldsymbol{v}$ and $\boldsymbol{w}$ develop k^2 spectra at large scales gradually, with a spectral knee separating the $\propto k^4$ and $\propto k^2$ parts, as we anticipated in Figure 4.1. The spectra $\mathcal{E}_{\boldsymbol{w}}(k)$ and $\mathcal{E}_{\boldsymbol{v}}(k)$ are almost the same at all scales and at all times. This finding demonstrates that the role of the large-scale structure of the turbulence in advecting itself and the small-scale flow is of negligible importance to the development of the thermal spectrum.

In panel (b), we plot the same spectra for a simulation where $\boldsymbol{F}_{\boldsymbol{v}}$ and $\boldsymbol{F}_{\boldsymbol{w}}$ are independent random variables. In this case, the small-scale field that advects $\boldsymbol{w}$ resembles $\boldsymbol{w}$'s small-scale part only in a statistical sense. Nonetheless, $\boldsymbol{w}$ develops a k^2 band at roughly the same rate as $\boldsymbol{v}$. We view this finding as numerical justification of the passive-velocity model.

Finally, panel (c) shows the wavenumbers of the spectral knees in $\mathcal{E}_{\boldsymbol{v}}(k)$ and $\mathcal{E}_{\boldsymbol{w}}(k)$ as functions of time, computed by fitting a trial function of the form $k^2[1-\exp(-k^2/k_c^2)]$ to the large-scale tail of the spectra. In all three cases, $k_c \propto t^{1/2}$, which is the dif-

fusive scaling anticipated in Section 4.3.2. In the next section, we shall derive this result (including the functional form of the knee) analytically from the passive-velocity equation (4.44).

4.4.2 Advection by a Kraichnan flow

In this section, we shall compute $\mathcal{E}_{\boldsymbol{w}}(k,t)$ from (4.44) analytically. The price we pay to do so is the need to make model assumptions about the advecting velocity field $\boldsymbol{u}$. First, as is common in solvable turbulence models, we assume that $\boldsymbol{u}$ has Gaussian statistics, allowing the use of the splitting property of Gaussian averages. Secondly, we ignore all finite-correlation-time effects and take both $\boldsymbol{u}$ and $\boldsymbol{F}_{\boldsymbol{w}}$ to be delta-correlated in time. Under this assumption, the $\boldsymbol{k}$-space correlation function of $\boldsymbol{u}$ is

$$\left\langle u_i(t,\boldsymbol{k})u_j(t',\boldsymbol{k}')\right\rangle = (2\pi)^3\delta(t-t')\delta(\boldsymbol{k}+\boldsymbol{k}')\kappa_{ij}(\boldsymbol{k}), \tag{4.47}$$

where the appearance of $\delta(\boldsymbol{k}+\boldsymbol{k}')$ in this expression is a consequence of statistical homogeneity. A similar expression is adopted for $\boldsymbol{F}_{\boldsymbol{w}}$ (see Appendix 4.D). Together, incompressibility and isotropy further imply that

$$\kappa_{ij}(\boldsymbol{k}) = \kappa(k)\mathcal{P}_{ij}(\boldsymbol{k}), \tag{4.48}$$

where $\mathcal{P}_{ij}(\boldsymbol{k}) = \delta_{ij} - k_ik_j/k^2$ is the usual $\boldsymbol{k}$-space projection operator. A synthetic velocity field satisfying (4.47) is often called the (incompressible) Kraichnan ensemble, after Kraichnan (1968, 1994), who proposed it as a model for studying the behaviour of a passive scalar advected by a turbulent flow. The same model was used independently by Kazantsev (1968) to study the growth of magnetic fields via the turbulent dynamo effect. In both of these applications, the model gave rise to a lively analytical following (see reviews by Falkovich *et al.* 2001 and Rincon 2019). The inertial-range statistics of the passive-velocity equation (4.44) with $\boldsymbol{u}$ the Kraichnan ensemble have also been studied in detail by Benzi *et al.* (2001), Adzhemyan *et al.* (2001*a*,*b*), and Arponen (2009). We note that, while the Gaussian property is artificial, the short-correlation-time approximation is a natural one for our problem, because the timescale on which large-scale structures diffuse is much longer than the correlation time of the outer-scale turbulence.

Finally, we assume further that

$$\kappa(k) = \kappa_0 \delta(k - k_f), \tag{4.49}$$

i.e., that the advecting field has a single wavenumber, k_f. While this assumption is not strictly required to produce a closed set of equations, it nonetheless greatly simplifies the calculation, and is not particularly limiting considering the simplifications already adopted. It should be noted that (4.49) does not restrict the applicability of the model to turbulence that is forced at a single scale, as $\boldsymbol{F}_{\boldsymbol{w}}$ can still be multi-scale. We also note that there is little to be gained by choosing $\boldsymbol{u}$ to have large-scale structure, because in any situation in which the large-scale structure of the advecting flow is important, the passive model of momentum diffusion will not be appropriate anyway.

We show in Appendix 4.D that under these assumptions, the spectrum $\mathcal{E}_{\boldsymbol{w}}(k)$ of the passive velocity field $\boldsymbol{w}$ satisfies the following mode-coupling equation

$$\partial_t \mathcal{E}_{\boldsymbol{w}}(k) + 2\left[\nu + \nu_T(k)\right] k^2 \mathcal{E}_{\boldsymbol{w}}(k) = \frac{\kappa_0 k_f}{(2\pi)^2} k \int_{|k-k_f|}^{k+k_f} \frac{\mathrm{d}k'}{k'} K(k', k) \mathcal{E}_{\boldsymbol{w}}(k') + F_{\boldsymbol{w}}(k), \tag{4.50}$$

where the spectrum of energy injection is

$$F_{\boldsymbol{w}}(k) = \frac{k^2}{2\pi^2} \int_0^t \mathrm{d}s \int \mathrm{d}^3\boldsymbol{r} \, \langle \boldsymbol{F}_{\boldsymbol{w}}(t) \cdot \boldsymbol{F}'_{\boldsymbol{w}}(s) \rangle e^{-i\boldsymbol{k}\cdot\boldsymbol{r}}. \tag{4.51}$$

The turbulent viscosity $\nu_T(k)$ and the kernel $K(k', k)$ that appears in the mode-coupling integral are both unwieldy functions whose precise forms are given in Appendix 4.D. However, because our interest is in wavenumbers $k \ll k_f$, we only need the small-k part of (4.50), and thus only the small-k limits of $\nu_T(k)$ and $K(k', k)$. These are

$$\lim_{k\to 0} \nu_T(k) = \frac{\kappa_0 k_f^2}{10\pi^2}, \quad \lim_{k,\, q\to 0} K(k' = k_f + q, k) = \frac{k^4 - q^4}{4k^2}. \tag{4.52}$$

Substituting (4.52) into (4.50) yields, for $k \ll k_f$,

$$\partial_t \mathcal{E}_{\boldsymbol{w}}(k) + \beta k_f^2 k^2 \mathcal{E}_{\boldsymbol{w}}(k) = \frac{5}{16} \frac{\beta}{k} \int_{-k}^{k} \mathrm{d}q (k^4 - q^4) \mathcal{E}_{\boldsymbol{w}}(k_f + q) + F_{\boldsymbol{w}}(k), \tag{4.53}$$

where we have defined $\beta = \kappa_0 / 5\pi^2$ and assumed that the turbulent viscosity dominates over the molecular one. Finally, if k is small compared to the wavenumber scale on which $\mathcal{E}_{\boldsymbol{w}}(k)$ varies in the vicinity of k_f, then we may take $\mathcal{E}_{\boldsymbol{w}}(k_f + q) \simeq \mathcal{E}_{\boldsymbol{w}}(k_f)$ in (4.53)

(we shall consider the effect of relaxing this assumption in Section 4.4.4). Then (4.53) becomes

$$\partial_t \mathcal{E}_{\boldsymbol{w}}(k) + \beta k_f^2 k^2 \mathcal{E}_{\boldsymbol{w}}(k) = \beta k^4 \mathcal{E}_{\boldsymbol{w}}(k_f) + C k^b, \tag{4.54}$$

where we have replaced $F_{\boldsymbol{w}}(k)$ by its small-k asymptotic form, taken to be a power law with exponent b (note that the case of finite-band forcing may be recovered by setting $C = 0$ in what follows).

Equation (4.54) is coupled to the forcing-scale modes via the appearance of $\mathcal{E}_{\boldsymbol{w}}(k_f)$. Therefore, in order to calculate the growth of $\mathcal{E}_{\boldsymbol{w}}(k \ll k_f)$ from an initial state with $\mathcal{E}_{\boldsymbol{w}}(k) = 0$, we should, strictly speaking, compute the evolution of $\mathcal{E}_{\boldsymbol{w}}(k_f)$ from (4.50) and substitute the result into (4.54). However, we expect the spectrum to saturate much more quickly at the forcing scale than at $k \to 0$, so we may, with negligible error, take $\mathcal{E}_{\boldsymbol{w}}(k_f)$ to be equal to its saturated value at all times. Then, solving (4.54) subject to $\mathcal{E}_{\boldsymbol{w}}(t = 0, k) = 0$ gives

$$\mathcal{E}_{\boldsymbol{w}}(k) = \left(1 - e^{-\beta k^2 k_f^2 t}\right) \frac{C k^b + \beta \mathcal{E}_{\boldsymbol{w}}(k_f) k^4}{\beta k^2 k_f^2}. \tag{4.55}$$

As anticipated, (4.55) exhibits a split power law. For any value of b, the critical wavenumber demarcating the two regimes is

$$k_c \sim \frac{1}{\sqrt{\beta k_f^2 t}} \sim \frac{1}{l} \sqrt{\frac{t_{\mathrm{nl}}}{t}}, \tag{4.56}$$

where $l \sim k_f^{-1}$ and $t_{\mathrm{nl}} \sim 1/\beta k_f^4$ is the characteristic nonlinear advection time at the injection scale. This is the diffusive scaling for the spectral knee anticipated at the end of Section 4.3.2.

For $k \ll k_c$, (4.55) reduces to

$$\mathcal{E}_{\boldsymbol{w}}(k) = \left[C k^b + \beta \mathcal{E}_{\boldsymbol{w}}(k_f) k^4\right] t. \tag{4.57}$$

Therefore, at small enough k (or early enough times), $\mathcal{E}_{\boldsymbol{w}}(k)$ has a k^b power law if $b \leq 4$, or a k^4 power law if $b > 4$. In the case of solenoidal forcing that is local in real space, which has been our focus so far, $b = 4$, so $\mathcal{E}_{\boldsymbol{w}}(k \to 0) \propto k^4$, consistent with the numerical results presented in figures 4.1 and 4.4. The development of a k^4 spectrum

in the case of $b > 4$ or $C = 0$ reflects the fact that turbulence with zero Loitsyansky integral is unsustainable: even if the forcing has $I_{\boldsymbol{F}} = 0$, the flow will develop $I \neq 0$ on a dynamical timescale, owing to interactions between eddies [cf. (4.36)]. We note that the linear dependence of the right-hand side of (4.57) on t indicates that our passive model of momentum diffusion corresponds to real turbulence with $\lim_{r\to\infty} r^4 K(r)$ constant in time [see Section 4.3.3].

In the opposite limit, $k \gg k_c$, (4.55) becomes

$$\mathcal{E}_{\boldsymbol{w}}(k) = \frac{Ck^b + \beta\mathcal{E}_{\boldsymbol{w}}(k_f)k^4}{\beta k^2 k_f^2}, \tag{4.58}$$

so $\mathcal{E}_{\boldsymbol{w}}(k) \propto k^2$ if $b \geq 4$. Thus, we recover the expected thermal spectrum for $b \geq 4$, i.e., for real-space correlations in the forcing function that satisfy $H_{\boldsymbol{w}}(r \to \infty) \leq O(r^{-5})$ (where $H_{\boldsymbol{w}}$ is the analogue of H for $\boldsymbol{F}_{\boldsymbol{w}}$).[7] As explained in Section 4.3.1, this corresponds to the development of a quasi-random momentum distribution, $\langle \boldsymbol{P}_V^2 \rangle \propto R^3$. If long-range correlations in the forcing are stronger, i.e., $b < 4$, then the thermal spectrum is not realised: instead, a shallower k^{b-2} spectrum develops.

According to (4.34), (4.57) and (4.58) correspond to

$$\langle \boldsymbol{P}_V^2 \rangle \propto \begin{cases} R^{7-b} & \text{if } l \ll R \ll R_c, \\ R^{5-b} & \text{if } R \gg R_c \;\&\; b < 3, \\ R^2 & \text{if } R \gg R_c \;\&\; 3 < b < 4, \end{cases} \tag{4.59}$$

where $R_c \equiv k_c^{-1}$. The $R \gg R_c$ scalings are easily interpreted: for large volumes for which there has not been enough time for momentum diffusion to act, the turbulence inherits the momentum scaling dictated by the forcing. The $\langle \boldsymbol{P}_V^2 \rangle \propto R^{7-b}$ scaling in the range $l \ll R \ll R_c$ is less intuitive. Interestingly, different values of b in the range $3 < b < 4$ tend to saturate with different power laws, even though all $\mathcal{E}_{\boldsymbol{w}} \propto k^a$ spectra with $3 < a < 4$ have $\langle \boldsymbol{P}_V^2 \rangle \propto R^2$, as (4.34) shows. To understand the origins of these scalings, it is convenient to consider the momentum-diffusion process as the net result of a series of instances of a decaying passive vector field. While the characteristic scale of the diffusing momentum grows like $t^{1/2}$ in all cases, the energy of the diffusing field

[7] This statement follows from a calculation directly analogous to the one that showed that $\mathcal{E}(k \to 0) \propto k^a \iff \chi(r \to \infty) \leq O(r^5)$ for $a \geq 4$; see (4.32).

decays at a rate that depends on the exponent b, and therefore the contribution of each instance of forcing to $\langle \boldsymbol{P}_V^2 \rangle \propto R^2$ depends on b, even when $3 < b < 4$. In Appendix 4.E, we show how the scalings (4.59) can be derived directly by thinking about the diffusion of momentum in such terms.

4.4.3 Local, non-solenoidal forcing

While forcing with $b \leq 4$ is easy to implement in numerical simulations, where complete control of the forcing spectrum is possible, such forcing is rather artificial, as $b < 4$ corresponds to long-range correlations that decay with distance in a very particular way [see (4.32)]. An important exception to this statement is the case of $b = 2$. An expansion of $F_{\boldsymbol{w}}(k \to 0)$ analogous to (4.1) yields

$$F_{\boldsymbol{w}}(k \to 0) = \frac{L_{\boldsymbol{F}_{\boldsymbol{w}}} k^2}{2\pi^2} + \dots , \tag{4.60}$$

so $b = 2$ corresponds to a finite value of

$$L_{\boldsymbol{F}_{\boldsymbol{w}}} \equiv \int_0^t \mathrm{d}s \int \mathrm{d}^3\boldsymbol{r} \langle \boldsymbol{F}_{\boldsymbol{w}}(t) \cdot \boldsymbol{F}'_{\boldsymbol{w}}(s) \rangle, \tag{4.61}$$

which is the analogue of the Saffman integral for $\boldsymbol{F}_{\boldsymbol{w}}$. If the forcing is solenoidal, then strong long-range correlations in $\boldsymbol{F}_{\boldsymbol{w}}$ are required for $L_{\boldsymbol{F}_{\boldsymbol{w}}}$ to be finite, because then (4.22) yields

$$L_{\boldsymbol{F}_{\boldsymbol{w}}} = 4\pi \lim_{r \to \infty} r^3 H_{\boldsymbol{w}}(r), \tag{4.62}$$

so $L_{\boldsymbol{F}_{\boldsymbol{w}}} \neq 0$ requires $H_{\boldsymbol{w}}(r \to \infty) = O(r^{-3})$. However, these long-range correlations need not be present if the forcing is non-solenoidal, as it turns out that they are generated naturally when the non-solenoidal part of $\boldsymbol{F}$ is removed by the action of the projection operator $\mathcal{P}$—this effect is illustrated in Figure 4.5. Physically, the correlations arise because non-solenoidal forcing generates pressure gradients that decay slowly with distance from the point at which an impulse is applied (these gradients are established instantaneously in an incompressible fluid). This result is due to Saffman (1967), who used it to argue that naturally occurring decaying turbulence need not have $\mathcal{E}(k \to 0) \propto k^4$, as had been supposed by Batchelor & Proudman (1956). A proof (closely following the one presented by Saffman 1967) and some further comments are given in Appendix 4.F.

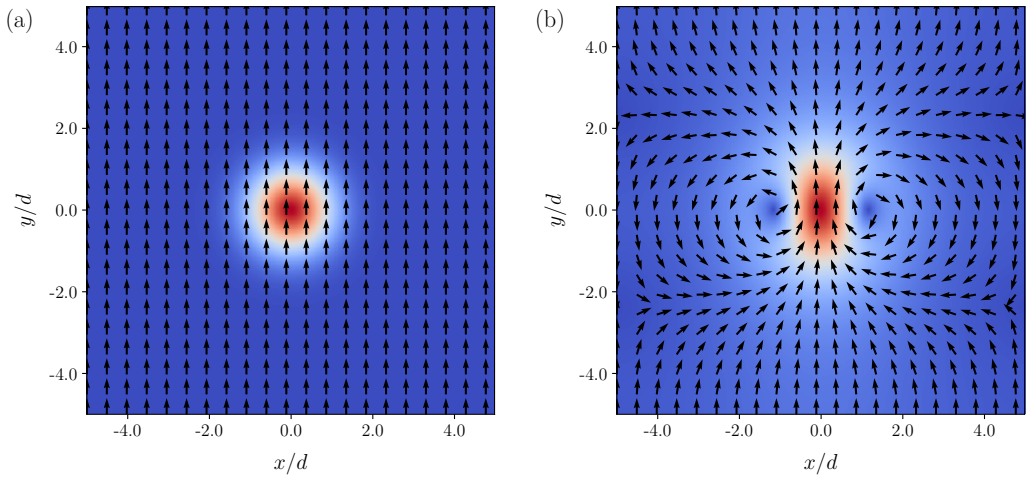

Figure 4.5: The effect of Fourier-space projection of a non-solenoidal forcing. Panel (a) shows a uniformly directed 2D impulse that decays exponentially with distance from the origin. Panel (b) shows the result of removing the non-solenoidal part of this impulse by application of the Fourier-space operator $\mathcal{P}_{ij} = \delta_{ij} - k_i k_j / k^2$; the impulse now falls off much more slowly with distance from the origin.

In summary, there are two values of b that are relevant to turbulence that is forced locally in real space. If the forcing is solenoidal (or non-solenoidal but with $L_{\boldsymbol{F_w}} = 0$), $b = 4$, in which case our passive diffusion model predicts saturation with a thermal k^2 spectrum. If the forcing is non-solenoidal and has $L_{\boldsymbol{F}} \neq 0$, then $b = 2$, and (4.55) predicts saturation with a flat spectrum: from (4.55), with $C = L_{\boldsymbol{F_w}}/2\pi^2$,

$$\mathcal{E}_{\boldsymbol{w}}(k) \simeq (1 - e^{-\beta k^2 k_f^2 t}) \frac{L_{\boldsymbol{F_w}}}{2\pi^2 \beta k_f^2}. \tag{4.63}$$

As we show in Figure 4.6, these predictions hold up reasonably well in our numerical simulations of Navier-Stokes turbulence, as do the corresponding scalings for linear momentum. For the $b = 4$ case, panel (a) shows that a finite-band k^2 spectrum develops over a wavenumber interval that widens over time, in close agreement with (4.56) and (4.58) [panel (a) is the same as Figure 4.1, and is presented again here to facilitate comparison]. Panel (b) shows the corresponding development of $\langle \boldsymbol{P}_V^2 \rangle \propto R^3$, although the split-power-law structure in $\langle \boldsymbol{P}_V^2 \rangle$, between $\propto R^2$ and $\propto R^3$, is somewhat less pronounced than in the spectrum. For $b = 2$, panel (c) shows that the saturation spectrum is somewhat steeper than k^0, instead appearing closer to $k^{1/2}$. Likewise, the decrease in k_c with time is somewhat faster than (4.56) predicts: the inset to panel (c)

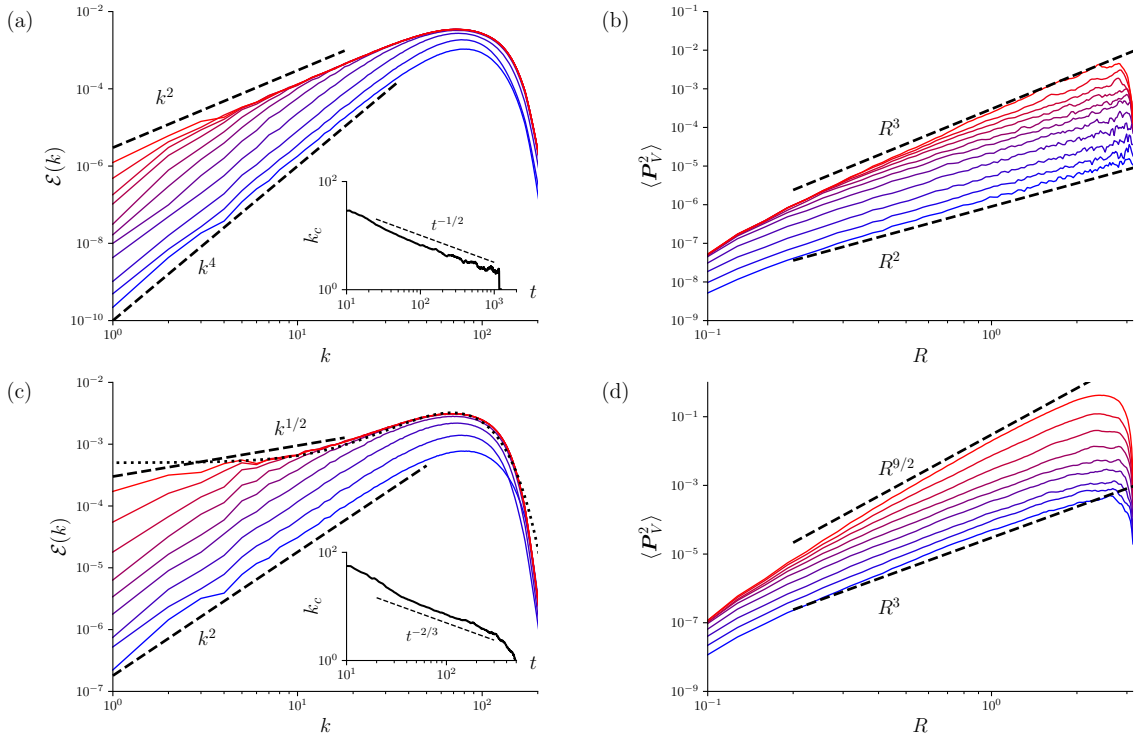

Figure 4.6: Saturation of the large scales in Navier-Stokes turbulence with a delta-correlated Gaussian random forcing. Panel (a) (the same as Figure 4.1) shows the evolution of the energy spectrum, while (b) shows the evolution of the mean square momentum $\langle \boldsymbol{P}_V^2 \rangle$, here computed for cubic subvolumes of the box with side length $2R$. Simulations shown in Panels (a) and (b) had the forcing spectrum $F(k) \propto k^4 \exp(-k^2/k_p^2)$. Panels (c) and (d) show the same quantities for $F(k) \propto k^2 \exp(-k^2/2k_p^2)$. In both cases, the peak of $F(k)$ is at $k_p = 80$. In panel (c), a numerical fit of the data to $(Ak^2/k_p^2 + B)\exp(-Ck^2)$, as explained in the text, is plotted as a dotted line. Insets to panels (a) and (c) show the evolution of the spectral knee $k_c(t)$. In the chosen units, the energy injection rate is 0.7 in both cases, and the r.m.s. velocities are $\simeq 0.5$. The plotted curves are logarathmically spaced in time, with blue $\rightarrow$ red indicating earlier $\rightarrow$ later times. Details of the numerical setup are described in Section 4.4.1 and Section 4.2.4.

indicates $k_c \propto t^{-2/3}$, which is consistent with $\mathcal{E}(k)$ growing as $k^2 t$ before saturating with $\mathcal{E}(k) \propto k^{1/2}$. It is plausible that this $k^{1/2}$ spectrum is a consequence of the scale separation between the forcing scale and the scale of the simulation box being insufficient to observe the true k^0 large-scale asymptotic: when $b = 2$, unlike when $b = 4$, (4.58) only reduces to the asymptotic behaviour $\mathcal{E}(k) \propto k^{b-2}$ when

$$\frac{k}{k_f} \ll \sqrt{\frac{L_{\boldsymbol{F}_{\boldsymbol{w}}}}{2\pi^2 \beta k_f^2 \mathcal{E}_{\boldsymbol{w}}(k_f)}}. \tag{4.64}$$

If the right-hand side of (4.64) happened to be a moderately small number, then the k^0 and k^2 terms in (4.58) would be comparable over a range of $k \lesssim k_f$, giving the appearance of a steeper spectrum than k^0. To illustrate this possibility, we show in panel (c) of Figure 4.6 a numerical fit of the function $(Ak^2/k_p^2 + B)\exp(-Ck^2)$, where $k_p = 80$ is the peak forcing wavenumber, and A, B, C are fitting parameters, to the final data curve. The result reproduces the data well with $A/B \simeq 20$. Alternatively, the discrepancy with the prediction of the passive-velocity model might be a result of the neglected effect of advection by large-scale modes, which do possess a significant proportion of the total energy for a close-to-flat spectrum. Panel (d) shows that $\langle \boldsymbol{P}_V^2 \rangle$ follows a scaling close to $R^{9/2}$ at late times, which is consistent with a $k^{1/2}$ spectrum at large scales, according to (4.34). We note that, for a forcing with $b = 2$, running the simulation to later times than those shown in Figure 4.6 tends to produce a build-up of energy in the largest-scale modes, making the large-scale asymptotic difficult to measure; a similar effect was found in some of the simulations of Alexakis & Brachet (2019). Here, we ended our runs before this effect became significant.

4.4.4 Narrow-band forcing

Finally, we discuss the case of forcing in a narrow spectral band, which is artificial, but a common choice for numerical simulations (see, e.g., Alexakis & Brachet 2019). As noted above, the prediction of the passive model for forcing in a finite band may be obtained by setting $C = 0$ in (4.55). This is valid when k is much smaller than any other characteristic wavenumber associated with $F_{\boldsymbol{w}}(k)$, including the inverse characteristic

width of the forcing spectrum. This assumption entered when we used

$$k \ll \left[\frac{1}{\mathcal{E}_{\boldsymbol{w}}(k)}\frac{\mathrm{d}\mathcal{E}_{\boldsymbol{w}}(k)}{\mathrm{d}k}\right]^{-1}_{k=k_f}, \tag{4.65}$$

in order to justify setting $\mathcal{E}_{\boldsymbol{w}}(k_f+q) \simeq \mathcal{E}_{\boldsymbol{w}}(k_f)$ in the q integral in (4.53). Of course, (4.65) is always justified if one takes $k \to 0$. However, if the forcing is concentrated in a narrow range of wavenumbers of width Δk, as is often the case in numerical simulations of forced turbulence, then it is possible that the energy contained within the forced band will greatly exceed the energy contained by the nearby unforced modes. In that case, there will be an extended range of k for which

$$\left[\frac{1}{\mathcal{E}_{\boldsymbol{w}}(k)}\frac{\mathrm{d}\mathcal{E}_{\boldsymbol{w}}(k)}{\mathrm{d}k}\right]^{-1}_{k=k_f} \sim \Delta k \ll k \ll k_f. \tag{4.66}$$

For k in this range, (4.55) does not apply. Taking

$$\mathcal{E}_{\boldsymbol{w}}(k_f+q) \simeq \begin{cases} \dfrac{C'}{\Delta k}, & \text{if } |q-k_f| < \Delta k/2, \\ 0, & \text{otherwise,} \end{cases} \tag{4.67}$$

where C' is a constant, modifies the injection term on the right-hand side of (4.54) to be $\propto k^3$ rather than $\propto k^4$, viz.,

$$\partial_t \mathcal{E}_{\boldsymbol{w}}(k) + \beta k_f^2 k^2 \mathcal{E}_{\boldsymbol{w}}(k) = \frac{5}{8}\beta C' k^3. \tag{4.68}$$

The saturated spectrum for $\Delta k \ll k \ll k_f$ is then readily obtained from (4.68) with $\partial_t \to 0$:

$$\mathcal{E}_{\boldsymbol{w}}(k) \simeq \frac{5}{8}\frac{C'k}{k_f^2}, \tag{4.69}$$

i.e., $\mathcal{E}_{\boldsymbol{w}}(k) \propto k$, *not* k^2, in this range.

How should we interpret this behaviour? These scalings are reminiscent of two-dimensional turbulence—in 2D, the expansion (4.1) of $\mathcal{E}_{\boldsymbol{w}}(k \to 0)$ becomes

$$\mathcal{E}(k) = \frac{L_{\mathrm{2D}}k}{4\pi} + \frac{I_{\mathrm{2D}}k^3}{16\pi} + \ldots \tag{4.70}$$

where L_{2D} and I_{2D} are the two-dimensional analogues of the Saffman and Loitsyansky integrals. In the absence of the inverse cascade, therefore, the two-dimensional forced-turbulence spectrum would consist of a growing k^3 part at the largest scales, changing

to a growing k^1 band at $k_c \propto t^{1/2}$, precisely as we have found for a narrow spectral band in three dimensions. While the latter system is not two-dimensional in real space, the same scalings are obtained because the Fourier modes that dominate the mode-coupling integral in (4.54) are confined to the $k = k_f$ surface in Fourier space.

In practice, saturation precisely according to (4.69) is unlikely, because the energy in forced modes usually does not greatly exceed the total energy at the flow scale at saturation. Nonetheless, there can still be some deviation from a precise k^2 spectrum, as reported by Alexakis & Brachet (2019).

4.5 Decay of initially forced turbulence

In this section, we consider how forced turbulence decays after the forcing is removed. This situation is somewhat different to the one usually considered in theoretical treatments of decaying turbulence (see Davidson 2015 for a review), where it is common to consider an initial condition that was generated effectively instantaneously (physically, over a period $\lesssim$ the initial eddy turnover time). For an initial condition generated in this way, the decay is usually believed to be governed by the principle of the 'permanence of the large-scale spectrum': while the energy contained at the flow scale cascades to small scales and is dissipated, the large-scale power law is preserved, i.e., $\mathcal{E}(k \ll l(t)^{-1}) \simeq \text{const}$. This is illustrated in panel (a) of Figure 4.7. Here, we investigate how this picture is altered by diffusion of momentum (and its associated modification of the large-scale spectrum) during the period of forcing, if the latter is long compared to the turnover time of the largest eddies.

4.5.1 Saffman-like forcing

The large-scale part of the energy spectrum of turbulence that was generated instantaneously typically follows an unbroken power law, i.e., $\mathcal{E}(k \ll l^{-1}) \propto k^a$; $a = 2$ and $a = 4$ are the "classical" scalings, both of which can arise from initial impulses that do not have long-range spatial correlations [cf. (4.1)], although it is also possible to consider other, non-classical, values for a. For $a \leq 3$, the principle of the permanence

of the large-scale spectrum that we outlined above is a consequence of the conservation of linear momentum (Saffman, 1967; Davidson, 2015). From (4.34), we have that $a \leq 3$ corresponds to $\langle \boldsymbol{P}_V^2 \rangle > O(R^2)$ as $R \to \infty$, indicating that eddies throughout the volume V, not just those at its surface, contribute to $\langle \boldsymbol{P}_V^2 \rangle$. On the other hand, $\mathrm{d}\langle \boldsymbol{P}_V^2 \rangle / \mathrm{d}t = O(R^2)$ because $\langle \boldsymbol{P}_V^2 \rangle$ only changes as a result of random fluxes through the surface of V [this assumes $K(r \to \infty) < O(r^{-3})$; see (4.121) and Davidson (2015)]. Therefore,

$$\lim_{V \to \infty} \frac{\mathrm{d} \log \langle \boldsymbol{P}_V^2 \rangle}{\mathrm{d}t} = 0, \tag{4.71}$$

so the large-R scaling of $\langle \boldsymbol{P}_V^2 \rangle$ vs. R is preserved and hence so is the large-scale spectral power law. In the classical case of $a = 2$ considered by Saffman (1967), which can result from a non-solenoidal initial forcing without long-range correlations (see Section 4.4.3), preservation of the large-scale part of the energy spectrum requires $u^2 l^3 \sim$ const [this follows from the expansion (4.1) and the form of the Saffman integral (4.2)]. Assuming that the decay is self-similar and occurs on the turnover time l/u of the largest eddies, it follows that

$$\frac{\mathrm{d}u^2}{\mathrm{d}t} \sim -\frac{u^3}{l} \propto u^{11/3} \implies u^2 \propto t^{-6/5}, \quad l \propto t^{2/5}, \tag{4.72}$$

which are Saffman's laws for decaying turbulence (Saffman, 1967).

For initially forced turbulence with a forcing spectrum $\propto k^2$, the situation is somewhat more complex, because $\mathcal{E}(k < l^{-1})$ is initially a split power law. If the forcing is maintained for a period $t_0 \gg t_{\mathrm{nl},0} \equiv l(t_0)/u(t_0)$, the passive model of momentum diffusion presented in Section 4.4 indicates that $\mathcal{E}(k < k_c) \propto k^2$, while $\mathcal{E}(k > k_c) \propto k^0$, where $k_c \sim (t_0/t_{\mathrm{nl},0})^{-1/2} l(t_0)^{-1}$. As the turbulence decays, the $k > k_c$ part of the spectrum will be preserved [see Figure 4.7(b)], because the argument leading to (4.71) is still valid for volumes V that are large but finite, viz., $l \ll V^{1/3} \ll k_c^{-1}$. This requires $u^2 l \sim$ const, which corresponds to

$$\frac{\mathrm{d}u^2}{\mathrm{d}t} \sim -\frac{u^3}{l} \propto u^5 \implies u^2 \propto t^{-2/3}, \quad l \propto t^{2/3}. \tag{4.73}$$

These laws hold until $l(t) \sim k_c^{-1}$ (because both the k^0 and k^2 parts of the spectrum are preserved during the decay, the wavenumber k_c of their intersection is also constant in time). This happens at the time denoted t_c on Figure 4.7(b), which is $(t_0/t_{\mathrm{nl},0})^{-1/4} t_0 \ll t_0$ after forcing ceases. For $t > t_c$, the decay obeys Saffman's laws (4.72).

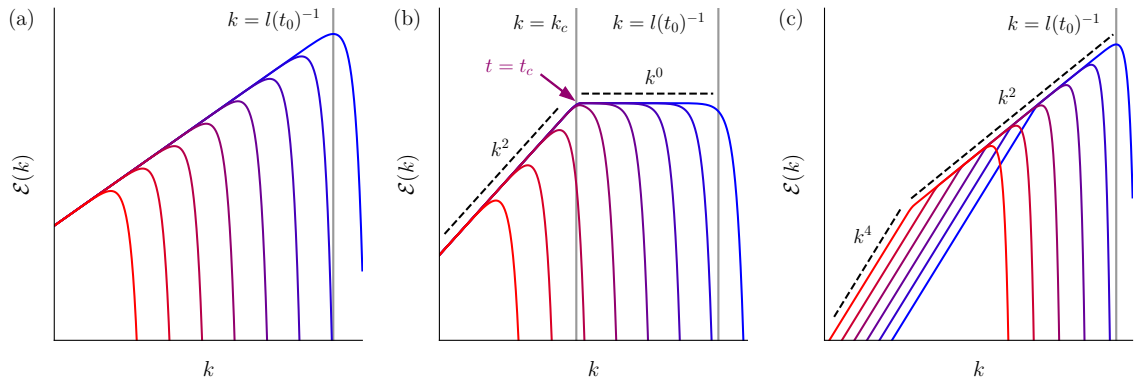

Figure 4.7: Schematic diagrams of the evolution of the energy spectrum of decaying isotropic turbulence initially forced for a period t_0, where (a) $t_0 \lesssim$ the initial eddy-turnover time, (b) $t_0 \gg$ the initial eddy-turnover time and the forcing spectrum was $\propto k^2$, and (c) $t_0 \gg$ the initial eddy-turnover time and the forcing spectrum was $\propto k^4$. Blue $\rightarrow$ red indicates earlier $\rightarrow$ later times.

4.5.2 Batchelor-like forcing

The other classical case, with $a = 4$, would, for example, be generated by a solenoidal forcing function without long-range correlations. A turbulence with $\mathcal{E}(k \rightarrow 0) \propto k^4$ has $\langle \boldsymbol{P}_V^2 \rangle = O(R^2)$ as $R \rightarrow \infty$ [see (4.34)], and therefore the permanence of the k^4 asymptotic is not guaranteed by momentum conservation. Nonetheless, it is often conjectured that the principle of permanence of the large-scale spectrum still applies (Davidson, 2015); if it does, $u^2 l^5 \sim$ const, and hence

$$\frac{\mathrm{d}u^2}{\mathrm{d}t} \sim -\frac{u^3}{l} \propto u^{17/5} \implies u^2 \propto t^{-10/7}, \quad l \propto t^{2/7}, \tag{4.74}$$

which are Kolmogorov's laws for decaying turbulence (Kolmogorov, 1941*a*). As noted in Section 4.3.3, permanence of the large-scale spectrum in decaying turbulence with $\mathcal{E}(k \rightarrow 0) \propto k^4$ requires the triple-correlation function $K(r)$ to fall off with distance faster than r^{-4} [this is the condition for the conservation of the Loitsyansky integral I; see (4.35)]. There currently exists no analytic theory to explain why (or whether) this should happen [see the discussion in Davidson (2013)], although numerical studies of instantaneously generated, decaying turbulence do offer some support for the invariance of I after an initial period of transient growth (Ishida *et al.*, 2006). We now present a simple argument based on our passive model of momentum diffusion that suggests that growth of I should persist indefinitely in decaying k^4 turbulence that was initially

forced for a long time, and therefore that Kolmogorov's laws (4.74) are never realised in such a turbulence.

According to the passive-velocity model of Section 4.4, turbulence forced with $F(k) \propto k^4$ develops a broken-power-law spectrum with $\mathcal{E}(k < k_c) \propto k^4$, and $\mathcal{E}(k > k_c) \propto k^2$, where again $k_c(t_0) \sim (t_0/t_{\mathrm{nl},0})^{-1/2} l(t_0)^{-1}$. As for the turbulence considered in Section 4.5.1, momentum conservation demands that the k^2 part of the spectrum be preserved while the turbulence decays, so Saffman's laws (4.72) should be satisfied while $l(t) \lesssim k_c^{-1}$. However, unlike in Section 4.5.1, k_c need not be constant in time, as the k^4 part of the spectrum need not be invariant. Let us employ our passive model of the large scales to determine how $k_c(t)$ evolves. Assuming $\mathcal{E}(k \to 0) \propto k^4$, (4.54) predicts

$$\frac{\partial \mathcal{E}(k \to 0)}{\partial t} \sim \beta k^4 \mathcal{E}(l^{-1}) \implies \mathcal{E}(k \to 0) \propto t^{4/5} k^4, \tag{4.75}$$

where we have used (4.72) to find that $\mathcal{E}(l^{-1}) \sim u^2 l \propto t^{-4/5}$ and $\beta \sim u l^3 \propto t^{3/5}$. On physical grounds, we expect the growth of $\mathcal{E}(k)$ predicted by (4.75) to terminate when $\mathcal{E}(k) \sim u^2 l^3 k^2$, as this corresponds to a stochastic distribution of the linear momentum [it is readily checked that this is the steady-state solution of (4.54) under the assumed time dependences of $\mathcal{E}(l^{-1})$ and β]. Equation (4.75) indicates that this saturation happens when $t^{4/5} k^4 \sim u^2 l^3 k^2$, so the scale k_c^{-1} that has just saturated at time t is $k_c \propto t^{-2/5}$. Comparing this with (4.72), we find that the scales l and k_c^{-1} grow at the same rate as the turbulence decays. Thus, a state with $l > k_c^{-1}$ is never reached—the Saffman decay laws (4.72) are satisfied at all times.

Together with the result of Section 4.5.1, this conclusion indicates that decay according to the Saffman laws (4.72) is the generic late-time behaviour for decaying turbulence that was initially generated by a long period of forcing. A numerical study to test this prediction would be extremely valuable, although it would incur significant numerical cost—it would be necessary to resolve two scale separations, first between the box size and $k_c(t_0)^{-1}$, and second between $k_c(t_0)^{-1}$ and $l(t_0)$ (and to run the forced part of the simulation for long enough for the latter scale separation to be reached), while furthermore also ensuring that the Reynolds number at the integral scale were always large enough for the Saffman decay laws (4.72) to be valid. We therefore defer such a numerical study to future work (or invite the reader to undertake it).

4.6 Conclusion

In this chapter, we have addressed the apparent disconnect between the "decaying-turbulence view" of the large-scale structure of turbulence, i.e., the notion that it is determined kinematically by the values of certain invariants that describe statistical properties of the flow field, and the increasingly popular idea that the large-scale spectral tail might (in some cases) constitute an isolated subsystem in thermal equilibrium. If the latter were true, equipartition of energy between Fourier modes would imply $\mathcal{E}(k \to 0) \propto k^2$, which corresponds to a non-zero Saffman integral, L [see (4.1)]. However, as we found in Section 4.2, L is an invariant not only of decaying turbulence, but also of forced turbulence, provided that the forcing is solenoidal and sufficiently localised in real space. This invariance is a manifestation of the conservation of linear momentum: solenoidal, localised forcing can only generate eddies with vanishing total momentum, so the total momentum contained within a sufficiently large volume of the turbulence must always vanish (in the sense that only surface contributions matter to the total), in which case $L = 0$ [see (4.25)].

Nonetheless, the total momentum contained within a *finite* volume of turbulence need not vanish, provided that one waits long enough for the momentum distribution to become stochastic on the relevant scale. As explained in Section 4.3, this scale-dependent stochasticisation is the net result of the momentum-conserving interactions between eddies, and leads to a broken-power-law spectrum at large scales. The "knee" wavenumber that separates the developing k^2 spectrum from the "Batchelor" asymptotic $\mathcal{E}(k \to 0) \propto k^4$ is a decreasing function of time: numerically, we have found it to decrease like $k_c \propto t^{-1/2}$, as would be expected for a turbulently diffusing field (of which a good solvable model can be constructed using the Kraichnan flow: see Section 4.4). In a finite system, such as a numerically simulated turbulence in a periodic box, the spectral knee eventually reaches the box scale, at which point the turbulence is essentially identical in character to a finite-system-size approximation of "Saffman turbulence", i.e., turbulence with $L \neq 0$. In particular, $\mathcal{E}(k) \propto k^2$ at all resolved scales larger than the forcing scale. However, in an infinite domain, the spectral knee grows indefinitely, and increasingly slowly, as increasingly distant points become correlated.

We anticipate that there may be a number of applications of the ideas developed in this chapter to more complex variants of fluid turbulence—in particular, to naturally occurring astrophysical turbulence. One such astrophysical application might be to the evolution of primordial magnetic fields in the early Universe, the subject of Chapter 3. It is usually assumed that these magnetic fields have a magnetic-energy spectrum that is $\propto k^4$ at large scales, because it is usually thought that long-range correlations in the magnetic field, of the sort required for a shallower spectrum, are excluded by causality constraints imposed by cosmological inflation models (Durrer & Caprini, 2003; Brandenburg *et al.*, 2015; Brandenburg & Kahniashvili, 2017; Reppin & Banerjee, 2017). In the statistically isotropic case, their decay then proceeds via reconnection of magnetic-field lines, conserving magnetic helicity, either in a "net" (Hatori, 1984; Biskamp & Müller, 1999; Brandenburg & Kahniashvili, 2017; Hosking & Schekochihin, 2021) or "fluctuating" sense (Hosking & Schekochihin, 2021)—see Chapter 2. However, intuitively, it seems likely that a process akin to the one described in this chapter may be able to induce a magnetic-energy spectrum $\propto k^2$ over a finite range of scales, if the magnetic energy is maintained by an effective "forcing" from the velocity field (i.e., magnetic dynamo). In this case, the process of momentum diffusion would be replaced by "flux diffusion", which presumably can occur due to magnetic reconnection. While a dedicated study would be necessary for a complete understanding of this effect, we note that numerical simulations of the MHD fluctuation dynamo that have scale separation between the box size and forcing scale do indeed appear to saturate with a magnetic-energy spectrum $\propto k^2$ at large scales (Maron & Blackman, 2002). This would motivate consideration of a k^2 large-scale spectrum in the primordial magnetic field. In the process of decay of such a field, the "Saffman flux invariant",

$$L_{\boldsymbol{B}} = \int \mathrm{d}^3\boldsymbol{r}\,\langle \boldsymbol{B}(\boldsymbol{x})\cdot\boldsymbol{B}(\boldsymbol{x}+\boldsymbol{r})\rangle, \tag{4.76}$$

which is the analogue of the Saffman integral (4.2) but for magnetic flux, should be conserved—the interested reader will find a discussion of the effect of $L_{\boldsymbol{B}}$ on MHD decay laws in Section 3.D (Hosking & Schekochihin, 2022*a*). We also note that momentum and flux diffusion, in the sense described here, provides a mechanism for the transfer of some energy to large spatial scales. It might therefore be useful to consider this effect in

the context of the fluctuation (non-helical) dynamo, whose saturated energy spectrum is an outstanding theoretical problem (see, e.g., Galishnikova *et al.* 2022, Rincon 2019, and references therein).

Another application of the ideas presented here to MHD turbulence concerns the 2D spectra of the latter in the presence of a strong mean field, in which case the idea of thermalisation turns out to have some traction in treating the scales perpendicular to the mean field that lie in the inertial range but are larger than the "critical-balance" scale—an intrigued reader will find the details in Appendix B of Schekochihin (2020). Such 2D spectral scalings turn out to be of some consequence also in the theory of phase-space turbulence in kinetic plasmas (Schekochihin *et al.*, 2016).

Returning to hydrodynamics, one intriguing finding of this study is that turbulence does *not* develop a thermal large-scale spectrum when the forcing generates eddies with non-zero linear momentum directly. This can occur even with a spatially localised forcing, provided it is non-solenoidal. In that case, long-range correlations can be generated when the non-solenoidal part is removed, an idea that underpins the realisability of decaying Saffman turbulence (Saffman, 1967). The measurement of a flatter-than-k^2 large-scale spectrum in a forced-turbulence experiment, such as the one under construction at ENS Paris, would therefore represent a neat direct demonstration of the physics underlying Saffman's theory of decaying turbulence, as would direct measurement of the Saffman decay laws (4.72) in turbulence forced locally and solenoidally until a large-scale thermal spectrum developed, and then allowed to decay. From the statistical-mechanics perspective, the thermodynamical motivation for an equilibrium spectrum (see Section 4.1) relies on weak interaction between the forcing scales and the much larger ones. This condition is satisfied when the forcing is solenoidal, because then the fluid response is essentially local in real space (see Section 4.2.2), but it is violated when the forcing is non-solenoidal, because then long-range interactions between distant points via exchange of pressure waves become an important feature of the dynamics, even though the forcing itself might be local in real space.

In light of this observation, we suggest that an interesting topic for further study would be the large-scale structure of compressible turbulence, in which pressure (sound)

waves propagate with finite velocity. In the large-Mach-number limit of highly supersonic motions, turbulent diffusion should be the dominant mechanism of momentum transport, so equilibration of the large scales should be possible. At finite Mach number, however, sound waves may correlate distant points before the turbulent diffusion of momentum can, owing to the fact that sound waves propagate ballistically, rather than diffusively. Whether this precludes thermalisation of the large scales in forced compressible turbulence is an intriguing question.

Appendices

4.A Long-range correlations induced by finite-band forcing

In Section 4.2, we approached the problem of the conservation of the Saffman integral [i.e., the coefficient of k^2 in the expansion (4.1) of $\mathcal{E}(k)$ as $k \to 0$] in terms of the strength of real-space correlations possessed by the forcing function. This is natural for turbulence occurring in nature or in a laboratory, where the spatial profile of the forcing may be measured, or prescribed. However, in numerical studies, forcing is commonly implemented in spectral space—in particular, it is common to force in a finite band of wavenumbers. Here, we examine the strength of correlations in real space induced by such a forcing.

As we have seen, the strongest long-range correlations in $\langle \boldsymbol{u} \cdot \boldsymbol{F}' \rangle$ are typically induced by the last term on the right-hand side of (4.21), so that, according to (4.22),

$$\lim_{r\to\infty} \langle \boldsymbol{u} \cdot \boldsymbol{F}' \rangle = \lim_{r\to\infty} \int_0^t \mathrm{d}s \langle \boldsymbol{F}(s) \cdot \boldsymbol{F}'(t) \rangle = \lim_{r\to\infty} \frac{1}{r^2} \frac{\partial}{\partial r} \big[r^3 H(t,r) \big]. \tag{4.77}$$

The function $H(t,r)$ is related to the spectral function $F(k)$ by a Fourier transform: dropping explicit dependence on time,

$$\frac{1}{r^2} \frac{\partial}{\partial r} \big[r^3 H(r) \big] = 2 \int_0^\infty \mathrm{d}k F(k) \frac{\sin(kr)}{kr}, \tag{4.78}$$

whence it follows that

$$H(r) = 2 \int_0^\infty \mathrm{d}k \, F(k) \, \frac{\sin(kr) - kr\cos(kr)}{(kr)^3}. \tag{4.79}$$

Let us now suppose that $F(k)$ is non-zero only for $k_1 \le k \le k_2$. Under the assumption that F is smooth, it is possible to show that $H(r)$ decays arbitrarily quickly

(i.e., more quickly than any power law) at large r. This is intuitive, given the absence of any non-zero large-scale Fourier modes of $\boldsymbol{F}$. A proof is as follows.

Integrating (4.79) by parts, we have

$$H(r) = \frac{2}{r^3}\int_0^\infty \mathrm{d}k \frac{1}{k}\left(\frac{\partial}{\partial k}\frac{F}{k}\right)\sin(kr) = \frac{2}{r^3}\mathrm{Im}\left[\int_0^\infty \mathrm{d}k \frac{1}{k}\left(\frac{\partial}{\partial k}\frac{F}{k}\right)e^{ikr}\right], \tag{4.80}$$

where the boundary terms vanish because F and all its derivatives vanish at 0 and ∞. If we integrate by parts a further n times, boundary terms continue to vanish, leaving

$$H(r) = \frac{2}{r^{3+n}}\mathrm{Im}\left[i^n\int_0^\infty \mathrm{d}k \left(\frac{\partial^n}{\partial k^n}\frac{1}{k}\frac{\partial}{\partial k}\frac{F}{k}\right)e^{ikr}\right], \tag{4.81}$$

so that

$$|H(r)| = \frac{2}{r^{3+n}}\left|\int_0^\infty \mathrm{d}k \left(\frac{\partial^n}{\partial k^n}\frac{1}{k}\frac{\partial}{\partial k}\frac{F}{k}\right)e^{ikr}\right| < \frac{2}{r^{3+n}}\int_0^\infty \mathrm{d}k\left|\frac{\partial^n}{\partial k^n}\frac{1}{k}\frac{\partial}{\partial k}\frac{F}{k}\right| = \frac{C_n}{r^{3+n}}, \tag{4.82}$$

where C_n is a finite constant. Thus, as $r \to \infty$, $|H(r)| \leq \text{const} \times r^{-m}$, for any m. *Q.E.D.*

However, $F(k)$ is not typically chosen to be smooth in numerical studies. Instead, $F(k)$ is often discontinuous at k_1 and k_2, with $F(k < k_1) = F(k > k_2) = 0$. In this case, (4.79) becomes, after integrating by parts,

$$H(r) = \frac{2}{r^3}\left[\frac{F(k_1)\sin(k_1 r)}{k_1^2} - \frac{F(k_2)\sin(k_2 r)}{k_2^2}\right] + \frac{2}{r^3}\int_{k_1}^{k_2}\mathrm{d}k\frac{1}{k}\left(\frac{\partial}{\partial k}\frac{F}{k}\right)\sin(kr). \tag{4.83}$$

The boundary term that has arisen in (4.83) is dominant over the integral, in the limit $r \gg 1/k_1,\ 1/k_2$, by the Riemann-Lebesgue lemma. Subdominant terms in the expansion may be computed by continuing to integrate by parts: at every order, the resulting terms will be of the form (oscillating part at frequency k_1 or k_2) $\times\, r^{-n}$. Thus, the effect of the discontinuity in $F(k)$ at k_1 and k_2 is to induce correlations that, at large distances, oscillate about zero with component wavenumbers k_1 and k_2, and an amplitude decreasing as a power law in r.

While a forcing of this sort will not inject energy into large-scale modes directly [i.e., via (4.77)], oscillatory behaviour will inevitably propagate into other correlators via the von Kármán-Howarth equation (4.15) and its higher-order analogues (4.18). It may then be the case that the oscillatory correlations induced in $\chi(r)$ decay more

slowly with distance than the monotonically decaying ones implied by (4.83). However, this should not affect the properties of the small-k part of the energy spectrum, as it turns out that oscillatory behaviour in $\chi(r \to \infty)$, with the amplitude of oscillations decaying as a power law, always has negligible effect on $\mathcal{E}(k \to 0)$, independently of the power-law exponent.

To see why, let us suppose that

$$\left\langle \boldsymbol{u} \cdot \boldsymbol{u}' \right\rangle (r \geq r_0) = A \left[\frac{\sin(k_f r)}{r^n} + \frac{1}{r_0^n} \left(\frac{r_0}{r} \right)^m \right], \tag{4.84}$$

i.e., that the behaviour of $\left\langle \boldsymbol{u} \cdot \boldsymbol{u}' \right\rangle$ at r larger than some r_0 is the sum of an oscillation with frequency $k_f \gg 1/r_0$, with an amplitude that decays as r^{-n}, and a monotonically decaying part that decays as r^{-m}, where m and n are both larger than 1 for finite $\mathcal{E}(k)$ as $k \to 0$. According to (4.5), the contribution of the oscillating part of $\left\langle \boldsymbol{u} \cdot \boldsymbol{u}' \right\rangle$ to the energy spectrum at small k is

$$\frac{Ak}{\pi} \int_{r_0}^{\infty} \mathrm{d}r \frac{1}{r^{n-1}} \sin(k_f r) \sin(kr) = \frac{Ak^2}{\pi k_f r_0^{n-2}} \cos(k_f r_0) \left[1 + O\left(\frac{1}{k_f r_0} \right) \right], \tag{4.85}$$

where we have integrated $\sin(k_f r)$ by parts and applied the Riemann-Lebesgue lemma. Meanwhile, the contribution of the monotonically decaying part is

$$\frac{Akr_0^{m-n}}{\pi} \int_{r_0}^{\infty} \mathrm{d}r \frac{1}{r^{m-1}} \sin(kr) = \frac{AF_m}{\pi k r_0^n} (kr_0)^{\min[m,\,3]} \left[1 + O\left(kr_0 \right) \right], \tag{4.86}$$

where F_m is a positive number that depends on m. The equality in (4.86) is non-trivial: it is proven by direct application of asympototic methods to the integral, with a case distinction for $m < 3$ and $m \geq 3$, or else via evalutation of the integral directly (resulting in a hypergeometric function), and taking the limit of small kr_0.

The right-hand side of (4.86) is always large compared to that of (4.85); for $m > 3$, which is likely the only case of physical significance, the difference is $k_f r_0 \gg 1$. This confirms our assertion that decaying oscillatory behaviour in $\chi(r \to \infty)$ has negligible effect on $\mathcal{E}(k \to 0)$: the latter is always dominated by any part of $\chi(r \to \infty)$ that decays monotonically. In conclusion, therefore, while forcing with a discontinuous spectrum does induce long-range correlations (as it must, owing to the sharp features induced in the spectrum of $\boldsymbol{u}$), these are likely of little significance to the dynamics of the large scales.

4.B Asymptotic form of $\chi(r)$ for turbulence with a power-law energy spectrum

In this appendix, we present a derivation of (4.32), which gives the longitudinal correlation function, $\chi(r)$, corresponding to turbulence with spectrum

$$\mathcal{E}(k) = Ck^a \tag{4.87}$$

at scales $k_1 \leq k \leq k_2$, for values of r satisfying $k_2^{-1} \ll r \ll k_1^{-1}$. The constant C may be expressed in terms of the total energy contained at scales $k_1 \leq k \leq k_2$: since

$$\int_{k_1}^{k_2} \mathrm{d}k\, \mathcal{E}(k) \simeq \begin{cases} Ck_1^{a+1}/|1+a| & \text{if } a < -1, \\ C\ln(k_2/k_1) & \text{if } a = -1, \\ Ck_2^{a+1}/(1+a) & \text{if } a > -1, \end{cases} \tag{4.88}$$

we have

$$C = \int_{k_1}^{k_2} \mathrm{d}k\, \mathcal{E}(k) \times \begin{cases} |1+a|k_1^{-1-a} & \text{if } a < -1, \\ 1/\ln(k_2/k_1) & \text{if } a = -1, \\ (1+a)k_2^{-1-a} & \text{if } a > -1. \end{cases} \tag{4.89}$$

Let us start from (4.31),

$$u^2\chi(r) = 2\int_0^\infty \mathrm{d}k\, \mathcal{E}(k)\, \frac{\sin(kr) - kr\cos(kr)}{(kr)^3}, \tag{4.90}$$

and consider first the part of the integral with $k < k_1$, which we denote J_1. A straightforward Taylor expansion in $kr \ll 1$ yields

$$J_1 \equiv 2\int_0^{k_1} \mathrm{d}k\mathcal{E}(k)\frac{\sin(kr) - kr\cos(kr)}{(kr)^3} = \frac{2}{3}\int_0^{k_1} \mathrm{d}k\, \mathcal{E}(k) + O\left[(k_1 r)^3\right]. \tag{4.91}$$

Then (4.90) becomes

$$u^2\chi(r) = \frac{2}{3}\int_0^{k_1} \mathrm{d}k\, \mathcal{E}(k) + J_2 + J_3 + O\left[(k_1 r)^3\right], \tag{4.92}$$

where J_2 and J_3 are integrals that correspond to the parts of (4.90) with $k_1 < k < k_2$ and $k > k_2$, respectively, so that

$$J_2 + J_3 = 2\int_{k_1}^\infty \mathrm{d}k\mathcal{E}(k)\frac{\sin(kr) - kr\cos(kr)}{(kr)^3}. \tag{4.93}$$

Depending on the particular value of a, it can be convenient to integrate (4.93) by parts before choosing precise definitions for J_2 and J_3. This allows the boundary term at $k = k_2$ to be redistributed between J_2 and J_3. For some values of a in (4.87), it will then be possible to show that J_2 is the dominant contribution to (4.92), allowing the dominant part of $\chi(r)$ to be computed despite our incomplete knowledge of $\mathcal{E}(k)$. We proceed by considering different ranges of a in turn, defining and computing J_2 and J_3 for each case. The final asymptotic expressions for $\chi(r)$ will be assembled using (4.92) at the end of this appendix.

4.B.1 Case of $a < 2$

4.B.1.1 Calculation of J_2

In this case, it is unnecessary to integrate by parts. We define

$$J_2 \equiv 2\int_{k_1}^{k_2} \mathrm{d}k \mathcal{E}(k) \frac{\sin(kr) - kr\cos(kr)}{(kr)^3} = 2Cr^{-a-1}\int_{k_1 r}^{k_2 r} \mathrm{d}x x^a \frac{\sin(x) - x\cos(x)}{x^3}. \tag{4.94}$$

For $-1 < a < 2$, (4.94) is convergent for $k_1 r \to 0$, $k_2 r \to \infty$: to leading order in $k_1 r$ and $1/k_2 r$,

$$J_2 = -2Cr^{-a-1}(a-1)\Gamma(a-2)\sin\frac{a\pi}{2}, \qquad -1 < a < 2. \tag{4.95}$$

Therefore, J_2 is large compared to $J_1 \sim Ck_1^{1+a}$ by a factor of $(k_1 r)^{-1-a} \gg 1$.

For $a < -1$, the integral in (4.94) is divergent at the lower limit. Its leading-order asymptotic as $k_1 r \to 0$ is

$$J_2 = \frac{2Ck_1^{1+a}}{3|1+a|}\left\{1 + O\left[(k_1 r)^2\right]\right\}, \qquad a < -1, \tag{4.96}$$

which is the same size as $J_1 \sim Ck_1^{1+a}$, and is independent of r.

In the particular case of $a = -1$, taking the leading-order asymptotic of (4.94), we have

$$J_2 = \frac{2C}{3}\left[\ln(k_1 r) + O(1)\right], \qquad a = -1. \tag{4.97}$$

Despite appearances, J_2 does not blow up as $k_1 r \to 0$, because $C \to 0$ as $k_1 r \to 0$ in order for the total energy to be finite, as (4.89) shows. Nonetheless, J_2 dominates over $J_1 \sim C$ in (4.92), by a factor of $\ln(k_1 r)$.

4.B.1.2 Calculation of J_3

In J_3, we define $x = k/k_2$ and integrate by parts:

$$\begin{aligned} J_3 &\equiv 2\int_{k_2}^{\infty} \mathrm{d}k \mathcal{E}(k) \frac{\sin(kr) - kr\cos(kr)}{(kr)^3} \\ &= -2k_2 \left[\mathcal{E}(k_2 x) \frac{\cos(k_2 r x) + k_2 r x \sin(k_2 r x)}{(k_2 r x)^4} \right]_1^{\infty} \\ &\quad + 2k_2 \int_1^{\infty} \mathrm{d}x \left[\frac{\partial}{\partial x} \frac{\mathcal{E}(k_2 x)}{(k_2 r x)^3} \right] \frac{\cos(k_2 r x) + k_2 r x \sin(k_2 r x)}{k_2 r x}. \end{aligned} \tag{4.98}$$

The boundary term at ∞ is exponentially small, by assumption, while the remaining integral is small compared to the boundary term by a factor of $(k_2 r)^{-1} \ll 1$, by the Riemann-Lebesgue lemma. This leaves

$$J_3 = 2k_2 \mathcal{E}(k_2) \frac{\cos(k_2 r) + k_2 r \sin(k_2 r)}{(k_2 r)^4} + O\left[(k_2 r)^{-1}\right] \tag{4.99}$$

$$= 2C r^{-a-1} (k_2 r)^{a-3} \left[\cos(k_2 r) + k_2 r \sin(k_2 r)\right] + O\left[(k_2 r)^{-1}\right], \tag{4.100}$$

which is manifestly small compared to J_2 for all $a < 2$.

4.B.2 Case of $2 \leq a \leq 3$

In this range of a, it is more convenient to use integration by parts in (4.93) before splitting the integration domain. We have

$$2\int_{k_1}^{\infty} \mathrm{d}k \mathcal{E}(k) \frac{\sin(kr) - kr\cos(kr)}{(kr)^3} = 2C(k_1 r)^{a-1} r^{-1-a} + 2\int_{k_1}^{\infty} \mathrm{d}k \left[\frac{\partial}{\partial k} \frac{\mathcal{E}(k)}{kr} \right] \frac{\sin(kr)}{kr^2}, \tag{4.101}$$

where the boundary term at ∞ vanishes by assumption.

4.B.2.1 Calculation of J_2

We take

$$\begin{aligned} J_2 &\equiv 2C(k_1 r)^{a-1} r^{-1-a} + 2\int_{k_1}^{k_2} \mathrm{d}k \left[\frac{\partial}{\partial k} \frac{\mathcal{E}(k)}{kr} \right] \frac{\sin(kr)}{kr^2} \\ &= 2C(k_1 r)^{a-1} r^{-1-a} + 2C r^{-1-a} (a-1) \int_{k_1 r}^{k_2 r} dx x^{a-3} \sin x. \end{aligned} \tag{4.102}$$

When $2 \leq a < 3$, the integral is convergent for $k_1 r \to 0$, $k_2 r \to \infty$, so

$$J_2 = -2C r^{-a-1} (a-1)\Gamma(a-2) \sin\frac{a\pi}{2} \tag{4.103}$$

to leading order, the boundary term being small by a factor of $(k_1 r)^{a-1} \ll 1$. As before, J_2 is large compared to $J_1 \sim C k_1^{1+a}$ by a factor of $(k_1 r)^{-1-a} \gg 1$.

If $a = 3$, then (4.102) does not converge as $k_2 r \to \infty$. Instead, we have

$$J_2 = 4Cr^{-4} \left[1 - \cos(k_2 r)\right], \tag{4.104}$$

to leading order in $k_1 r \ll 1$.

4.B.2.2 Calculation of J_3

Taking J_3 to be the part of (4.101) not included in J_2 as defined in (4.102), integrating by parts and applying the Riemann-Lebesgue lemma as in (4.98) gives

$$\begin{aligned} J_3 &\equiv 2 \int_{k_2}^{\infty} \mathrm{d}k \left[\frac{\partial}{\partial k} \frac{\mathcal{E}(k)}{kr}\right] \frac{\sin(kr)}{kr^2} \\ &= 2(a-1) C r^{-1-a} (k_2 r)^{a-3} \cos(k_2 r) + O\left[(k_2 r)^{-1}\right]. \end{aligned} \tag{4.105}$$

Comparison with (4.103) shows that J_3 is small compared to J_2 for $a < 3$. If $a = 3$, then the leading-order part of J_3 cancels with the term proportional to $\cos(k_2 r)$ in (4.104). The remaining term in (4.104) is precisely (4.103) with $a = 3$, therefore we conclude that (4.103) is valid for $2 \leq a \leq 3$, and provides the leading order part of (4.92) in this range.

4.B.3 Case of $a > 3$

The procedure for $a > 3$ is similar to the one followed in Section 4.B.2: we continue to integrate (4.101) by parts, split the resulting integral into pieces with $k < k_2$ and $k > k_2$, and use the Riemann-Lebesgue lemma to infer that the $k > k_2$ piece is subdominant. While a different number of integrations by parts will be required depending on the particular value of a, let us treat them all simultaneously, and integrate the integral appearing in (4.101) by parts n times. Using the complex representation of

trigonometric terms for convenience, we have

$$2\int_{k_1}^{\infty}\mathrm{d}k\left[\frac{\partial}{\partial k}\frac{\mathcal{E}(k)}{kr}\right]\frac{\sin(kr)}{kr^2}=\frac{2}{r^3}\mathrm{Im}\Bigg\{\sum_{m=1}^{n}(-1)^{m-1}\left[\frac{e^{ikr}}{(ir)^m}\frac{\partial^{m-1}}{\partial k^{m-1}}\frac{1}{k}\frac{\partial}{\partial k}\frac{\mathcal{E}(k)}{k}\right]_{k_1}^{\infty}$$
$$+(-1)^n\int_{k_1}^{\infty}\mathrm{d}k\frac{e^{ikr}}{(ir^n)}\frac{\partial^n}{\partial k^n}\frac{1}{k}\frac{\partial}{\partial k}\frac{\mathcal{E}(k)}{k}\Bigg\} \tag{4.106}$$

$$=2\mathrm{Im}\Bigg[\sum_{m=1}^{n}i^m e^{ik_1r}\frac{\Gamma(a-2)}{\Gamma(a-m-1)}(k_1r)^{a-m-2}Cr^{-a-1}$$
$$+\frac{(-1)^n}{r^3}\int_{k_1}^{\infty}\mathrm{d}k\frac{e^{ikr}}{(ir)^n}\frac{\partial^n}{\partial k^n}\frac{1}{k}\frac{\partial}{\partial k}\frac{\mathcal{E}(k)}{k}\Bigg]. \tag{4.107}$$

The last expression was obtained by simplifying the boundary term using the fact that $\mathcal{E}(k)=Ck^a$ around $k=k_1$.

4.B.3.1 Calculation of J_2

As before, we split (4.101) into two components, J_2 and J_3. Formally, J_2 should be defined to include the $k=k_1$ boundary terms in (4.101) and (4.107). However, these are all small compared to Cr^{-a-1} as long as we choose $n<a-2$. Doing so, we have

$$J_2=2\mathrm{Im}\left[\frac{(-1)^n}{r^3}\int_{k_1}^{k_2}\mathrm{d}k\frac{e^{ikr}}{(ir)^n}\frac{\partial^n}{\partial k^n}\frac{1}{k}\frac{\partial}{\partial k}\frac{\mathcal{E}(k)}{k}\right]\left\{1+O\left[(k_1r)^{a-n-2}\right]\right\}$$
$$\simeq 2\frac{\Gamma(a-2)}{\Gamma(a-n-2)}(a-1)Cr^{-1-a}\mathrm{Im}\left(i^n\int_{k_1r}^{k_2r}\mathrm{d}x e^{ix}x^{a-n-3}\right). \tag{4.108}$$

Now, if $-1<a-n-3<0$ (which is consistent with our earlier choice of $n<a-2$), the integral in (4.108) is convergent as we take $k_1r\to 0$, $k_2r\to\infty$. In that case, (4.108) becomes the now-familiar

$$J_2=-2Cr^{-a-1}(a-1)\Gamma(a-2)\sin\frac{a\pi}{2}. \tag{4.109}$$

It follows that (4.109) is valid for all non-integer $a>3$, since then it is always possible to choose n such that $-1<a-n-3<0$.

If a is an integer, we choose $n=a-3$ instead. In this case, (4.108) becomes

$$J_2=2(a-1)\Gamma(a-2)Cr^{-1-a}\,\mathrm{Im}\left\{i^a\left[e^{ik_2r}-1+O(k_1r)\right]\right\}. \tag{4.110}$$

4.B.3.2 Calculation of J_3

Taking J_3 to be the part of (4.101) not included in J_2 and using (4.107), we have

$$\begin{aligned} J_3 &\equiv 2\mathrm{Im}\left[\frac{(-1)^n}{r^3}\int_{k_2}^{\infty}\mathrm{d}k\frac{e^{ikr}}{(ir)^n}\frac{\partial^n}{\partial k^n}\frac{1}{k}\frac{\partial}{\partial k}\frac{\mathcal{E}(k)}{k}\right] \\ &= 2\mathrm{Im}\left(i^{n+1}e^{ik_2r}\right)\frac{\Gamma(a-2)}{\Gamma(a-n-2)}(a-1)Cr^{-1-a}(k_2r)^{a-n-3} \\ &\quad + 2\mathrm{Im}\left[\frac{i^{n+1}}{r^3}\int_{k_2}^{\infty}\mathrm{d}k\frac{e^{ikr}}{r^{n+1}}\frac{\partial^{n+1}}{\partial k^{n+1}}\frac{1}{k}\frac{\partial}{\partial k}\frac{\mathcal{E}(k)}{k}\right]. \end{aligned} \tag{4.111}$$

In the case of non-integer a, our choice of $a-n-3<0$ ensures the boundary term in (4.111) is small compared to J_2, while the integral is lower order still, by the Riemann-Lebesgue lemma. For integer a, our choice of $n=a-3$ means that the boundary term in (4.111) cancels with the term that is proportional to $\mathrm{Im}(i^a e^{ik_2r})$ in (4.110). The remaining term in (4.110) is precisely the right-hand side of (4.109), which dominates over the remaining integral in (4.111) (by the Riemann-Lebesgue lemma), provided that a is odd.

However, special care must be taken when a is an even integer greater than 3. After the term proportional to $\mathrm{Im}(i^a e^{ik_2r})$ in (4.110) cancels with its partner in (4.111), the other term in (4.110) is proportional to $\mathrm{Im}(i^a)$, which vanishes if a is even. This means that $J_2 = Cr^{-1-a}\times O(k_1r)$. The leading-order non-vanishing term in the asymptotic expansion in $k_2r \gg 1$ is contained within the integral in (4.111). However, unlike for other values of a, this term cannot be extracted from (4.111) by any number of integrations by parts, as the boundary terms so generated always vanish. This is because the desired leading-order contribution to $\chi(r)$ comes from the part of $\mathcal{E}(k)$ with $k>k_2$, where the form of $\mathcal{E}(k)$ is unknown. At best, we can constrain the dependence on r by noting that, for $n=a-3$,

$$\left|2\mathrm{Im}\left[\frac{i^{n+1}}{r^3}\int_{k_2}^{\infty}\mathrm{d}k\frac{e^{ikr}}{r^{n+1}}\frac{\partial^{n+1}}{\partial k^{n+1}}\frac{1}{k}\frac{\partial}{\partial k}\frac{\mathcal{E}(k)}{k}\right]\right| < 2r^{-1-a}\int_{k_2}^{\infty}\mathrm{d}k\left|\frac{\partial^{a-2}}{\partial k^{a-2}}\frac{1}{k}\frac{\partial}{\partial k}\frac{\mathcal{E}(k)}{k}\right|. \tag{4.112}$$

The integral on the right-hand side of (4.112) is independent of r. It has the same dimensions as C, and typically will be $\sim C$, in which case the integral in (4.111) can be large compared to the $O(k_1r)$ part of J_2, and therefore it provides the dominant

contribution to $\chi(r)$ in (4.92). Thus, for even integer $a > 3$, we are only able to conclude that $\chi(r)$ decays as Cr^{-1-a} or faster as $r \to \infty$.

4.B.4 The leading-order correction in $k_1 r \ll 1$

The conclusion that $\chi(r \to \infty) \leq O(Cr^{-1-a})$ may fail if the contribution to $\chi(r)$ from $\mathcal{E}(k > k_2)$ is much smaller than the upper limit enforced by (4.112), with the result that the strongest long-range correlations are instead determined by the $k < k_1$ part of the spectrum. An example of this is the superposition of a small-scale velocity field with exponentially decaying correlations and a second velocity field at much larger scales. On scales longer than those of the former field, correlations are dominated by the latter, so $\chi(r) \sim$ const if r is small compared to the characteristic scale of the large-scale field.

A convenient way to obtain this result formally, without the need to keep track of higher-order terms in the expansion in $k_1 r$ above, is to define an auxiliary spectrum

$$\mathscr{E}(k) = \begin{cases} Ck^a & \text{if } k < k_1, \\ \mathcal{E}(k) & \text{otherwise,} \end{cases} \tag{4.113}$$

i.e., $\mathscr{E}(k)$ is the spectrum obtained by extending the power-law behaviour of $\mathcal{E}(k)$ at $k_1 < k < k_2$ to $k < k_1$. Let us denote by $\chi_{\mathscr{E}}(r)$ the function obtained by replacing $\mathcal{E}(k)$ by $\mathscr{E}(k)$ in (4.90) while retaining the definition of u^2. In this notation, $\chi(r) = \chi_{\mathcal{E}}(k)$ is the correlation function that we have been concerned with thus far. Then, $\chi_{\mathscr{E}}$ may be computed by simply setting $k_1 = 0$ in the calculation presented above:

$$\chi_{\mathscr{E}}(r) = \chi_{\mathcal{E}}(r)\big|_{k_1=0}. \tag{4.114}$$

Now we define $\Delta(k) = \mathcal{E}(k) - \mathscr{E}(k)$ to be the spectrum of the "excess energy" contained at large scales (which can be negative). Owing to the linearity of (4.90) in $\mathcal{E}$, we have

$$\chi_{\mathcal{E}}(r) = \chi_{\mathscr{E}+\Delta}(r) = \chi_{\mathscr{E}}(r) + \chi_{\Delta}(r) = \chi_{\mathcal{E}}(r)\big|_{k_1=0} + \chi_{\Delta}(r). \tag{4.115}$$

Thus, the finite-$k_1 r$ correction to the correlation function corresponding to $\mathcal{E}(k)$ is exactly the function obtained by replacing $\mathcal{E}(k)$ by $\Delta(k)$ in (4.90) (again, while retaining

the definition of u^2). This is easily computed to leading order in $k_1 r$: since $\Delta(k > k_1) = 0$,

$$u^2 \chi_\Delta(r) \equiv 2 \int_0^{k_1} \mathrm{d}k\, \Delta(k)\, \frac{\sin(kr) - kr\cos(kr)}{(kr)^3} = \frac{2}{3} \int_0^{k_1} \mathrm{d}k\, \Delta(k) + O\left[(k_1 r)^3\right]. \quad (4.116)$$

As anticipated above, the leading-order correction is $\chi_\Delta(r) \sim$ const. The size of the correction depends on the amount of "excess energy" contained at $k < k_1$, i.e., on the difference between the actual energy and the energy that would be present if the power law $\mathcal{E}(k) \propto Ck^a$ extended to $k < k_1$. We note that this excess energy can be negative, in which case $\chi_\Delta(r)$ will also be negative, resulting in a tendency to introduce anti-correlations.

It should, however, be noted that this discussion is largely academic: while it is formally possible that the leading-order term in the $k_1 r$ expansion, (4.116), will dominate $\chi(r)$, this is an artificial situation, because correlations do not fall off exponentially quickly in real turbulence (Batchelor & Proudman, 1956). Instead, $\chi(r)$ typically decays as r^{-6} in isotropic Batchelor turbulence (see Davidson 2013 for a discussion). In the general case, it should therefore be expected that the integral in (4.111) provides the dominant part of $\chi(r)$.

4.B.5 Final expression

Assembling all the results derived in this appendix, and using (4.89) to eliminate C, (4.92) becomes (4.32) [in the case of $a = 2, 4, 6, \ldots$, we assume that the dominant correlations come from the part of $\mathcal{E}(k)$ with $k > k_2$; see the discussion in Section 4.B.4].

4.C Evolution of mean square momentum in forced turbulence

In this appendix, we examine the evolution of $\left\langle \boldsymbol{P}_V^2 \right\rangle$ under the forced Navier-Stokes equation, as Davidson (2015) did for decaying turbulence.

Ignoring viscous forces, the evolution of the total momentum contained within a volume V is given by

$$\frac{\mathrm{d}\boldsymbol{P}_V}{\mathrm{d}t} = -\int_{\partial V} \boldsymbol{u}(\boldsymbol{u} \cdot \mathrm{d}\boldsymbol{S}) - \int_{\partial V} p \mathrm{d}\boldsymbol{S} + \int_V \mathrm{d}^3\boldsymbol{x}\boldsymbol{F}. \quad (4.117)$$

The three terms appearing on the right-hand side are identified straightforwardly as the advection of momentum out of V, the net pressure force on V, and the net external forcing. Therefore,

$$\frac{\mathrm{d}\boldsymbol{P}_V^2}{\mathrm{d}t} = 2\int_V \mathrm{d}^3\boldsymbol{x}'\boldsymbol{u}' \cdot \left[-\int_{\partial V} \boldsymbol{u}(\boldsymbol{u}\cdot\mathrm{d}\boldsymbol{S}) - \int_{\partial V} p\mathrm{d}\boldsymbol{S} + \int_V \mathrm{d}^3\boldsymbol{x}\boldsymbol{F}\right]. \tag{4.118}$$

For simplicity, we shall assume that the correlation time of the forcing is short compared to the eddy-turnover time. In that case, (4.21) and (4.22) give

$$\left\langle \boldsymbol{u}\cdot\boldsymbol{F}'\right\rangle = \frac{1}{r^2}\frac{\partial}{\partial r}\left[r^3 H(t,r)\right], \tag{4.119}$$

while isotropy also demands [cf. (4.6)]

$$\langle u_i f_j'\rangle = \frac{1}{2r}\left[(r^2H)'\delta_{ij} - H'(r)r_i r_j\right]. \tag{4.120}$$

Taking an ensemble average of (4.118), using (4.119) and (4.120), and restricting attention to spherical V with radius R, one can show that

$$\frac{\mathrm{d}\langle \boldsymbol{P}_V^2\rangle}{\mathrm{d}t} = 4\pi^2R^2u^3\int_0^{2R}\mathrm{d}r\left[1-\left(\frac{r}{2R}\right)^2\right]\frac{1}{r}\frac{\partial}{\partial r}(r^4K) + 8\pi^2R^2\int_0^{2R}\mathrm{d}r\left[1-\left(\frac{r}{2R}\right)^2\right]r^3H. \tag{4.121}$$

The derivation of this equation is closely analogous to the one presented in Davidson (2015) for $\mathrm{d}\langle\boldsymbol{P}_V^2\rangle/\mathrm{d}t$ in decaying turbulence, to which we refer the reader for details.

Equation (4.121) shows that there are two relevant processes that can change the expectation value of the squared linear momentum contained in a volume of size V. The first, represented by the first term on the right-hand side, encodes the effect of the advection of momentum by the flow, the second the injection of momentum by the forcing. Both terms are at most $O(R^2)$ as $R\to\infty$, as long as $K(r\to\infty) < O(r^{-3})$ and $H(r\to\infty) < O(r^{-3})$. This makes sense, given that both effects are surface processes (as long as long-range correlations in the forcing are weak). This means that neither term can spontaneously generate $\left\langle \boldsymbol{P}_V^2\right\rangle \propto R^3$ for arbitrarily large R, as is consistent with the conclusion of Section 4.2.

In fact, the net effect of the two terms on the right-hand side of (4.121) may be a scaling of $\mathrm{d}\left\langle \boldsymbol{P}_V^2\right\rangle/\mathrm{d}t$ vs. R even weaker than R^2, because there can be partial

cancellation between them, or else because $\partial(r^4 K)/\partial r$ may change sign at some r. Of course, some cancellation between the two terms is inevitable: the forcing cannot perpetually increase $\langle \boldsymbol{P}_V^2 \rangle$ unchecked, because, even if turbulence could maintain very short-range correlations and so not grow a k^2 spectrum, there would still be a cascade of energy to smaller scales (encoded in the first term) resulting in the destruction of the local structures. Nonetheless, it appears robustly the case that the net size of the right-hand side of (4.121) must scale at most as R^2 for large R.

Let us then consider some $R \gg l$, and suppose that, indeed, the aggregate of the terms on the right-hand side of (4.121) scales as R^2. In that case, on dimensional grounds,

$$\frac{\mathrm{d}\langle \boldsymbol{P}_V^2 \rangle}{\mathrm{d}t} \sim u^3 R^2 l^3. \tag{4.122}$$

Suppose, roughly, that $\langle \boldsymbol{P}_V^2 \rangle$ increases according to (4.122) until it saturates. Saturation occurs when $\langle \boldsymbol{P}_V^2 \rangle \sim u^2 R^3 l^3$—this must be the case on dimensional grounds, because the R dependence is fixed by (4.34) with $a = 2$. We then find that the time taken for saturation at scale R is $t_{\mathrm{sat}} \sim R/u$. Equivalently, the scale R_c at which the growth of $\langle \boldsymbol{P}_V^2 \rangle$ has just saturated at time t is given by

$$R_c \sim ut. \tag{4.123}$$

That this should be the strongest-allowed scaling of R_c vs. t is intuitive: (4.123) simply represents the limit on the growth of R_c imposed by causality. At distances greater than $R_c \sim ut$, two points in the flow cannot have exchanged momentum, because there has not been enough time for local processes, namely, advection at speed u (or else the cumulative effect of local forces acting on scales $\sim l$ with timescales $\sim l/u$), to act.

4.D Derivation of the passive-momentum equations

In this appendix, we show how the mode-coupling equation (4.50) is obtained under the assumptions explained in Section 4.4.2. Our goal is to compute the evolution of the spectrum $\mathcal{E}_{\boldsymbol{w}}(t,k)$ of the passive vector field $\boldsymbol{w}$ satisfying (4.44). To do this, we shall derive an evolution equation for the correlation function $\langle w_i(t,\boldsymbol{k}) w_j(t,\boldsymbol{k}') \rangle$.

4.D.1 Homogeneous and isotropic forms of relevant correlators

Let us first note the restrictions imposed by symmetries on the various correlators involved. Due to statistical homogeneity of $\boldsymbol{w}$, this function is restricted to satisfy

$$\left\langle w_i(t,\boldsymbol{k})w_j(t,\boldsymbol{k}')\right\rangle = (2\pi)^3\delta(\boldsymbol{k}+\boldsymbol{k}')\Psi_{ij}(t,\boldsymbol{k}). \tag{4.124}$$

The form of the tensor $\Psi_{ij}(t,\boldsymbol{k})$ is further restricted by isotropy and incompressibility:

$$\Psi_{ij}(t,\boldsymbol{k}) = \frac{1}{2}\Psi(t,k)\mathcal{P}_{ij}(\boldsymbol{k}), \tag{4.125}$$

where

$$\mathcal{P}_{ij}(\boldsymbol{k}) = \delta_{ij} - \frac{k_i k_j}{k^2} \tag{4.126}$$

is the usual projection operator onto the plane perpendicular to $\boldsymbol{k}$, and the isotropic function $\Psi(t,k)$ is related to $\mathcal{E}_{\boldsymbol{w}}(t,k)$ via

$$\Psi(t,k) = 2\pi^2\frac{\mathcal{E}_{\boldsymbol{w}}(t,k)}{k^2}. \tag{4.127}$$

In order to compute (4.124), we require similar correlation functions for $\boldsymbol{u}$ and $\boldsymbol{F}_{\boldsymbol{w}}$. In particular, we shall need $\left\langle u_i(t,\boldsymbol{k})u_j(t',\boldsymbol{k}')\right\rangle$, whose general form is also restricted by homogeneity and statistical invariance of $\boldsymbol{u}$ in time:

$$\left\langle u_i(t,\boldsymbol{k})u_j(t',\boldsymbol{k}')\right\rangle = (2\pi)^3\delta(\boldsymbol{k}+\boldsymbol{k}')\kappa_{ij}(\boldsymbol{k},t-t'). \tag{4.128}$$

As explained in Section 4.4.2, we shall take $\boldsymbol{u}$ to have zero correlation time:

$$\kappa_{ij}(\boldsymbol{k},t-t') = \kappa_{ij}(\boldsymbol{k})\delta(t-t'). \tag{4.129}$$

Together, incompressibility and isotropy further imply

$$\kappa_{ij}(\boldsymbol{k}) = \kappa(k)\mathcal{P}_{ij}(\boldsymbol{k}). \tag{4.130}$$

As explained in Section 4.4.2, we shall assume $\boldsymbol{u}$ to have a single scale, so that the isotropic function $\kappa(k)$ is

$$\kappa(k) = \kappa_0\delta(k-k_f), \tag{4.131}$$

Finally, we shall require $\left\langle f_i(t,\boldsymbol{k})f_j(t',\boldsymbol{k}')\right\rangle$, which satisfies

$$\left\langle f_i(t,\boldsymbol{k})f_j(t',\boldsymbol{k}')\right\rangle = \frac{1}{2}(2\pi)^3\delta(\boldsymbol{k}+\boldsymbol{k}')\delta(t-t')\Phi(k)\mathcal{P}_{ij}(\boldsymbol{k}) \tag{4.132}$$

for the same reasons as the other two correlation functions.

4.D.2 Derivation of the mode-coupling equation

Equation (4.44) reads, after dropping the subscript $\boldsymbol{w}$ from $p_{\boldsymbol{w}}$ and $\boldsymbol{F}_{\boldsymbol{w}}$ (there can be no confusion with the corresponding fields for $\boldsymbol{u}$, as $\boldsymbol{u}$ is now prescribed artificially),

$$\partial_t w_i = -\partial_j(u_j w_i) - \partial_i p + \nu\nabla^2 w_i + f_i. \tag{4.133}$$

In Fourier space, this is

$$\partial_t w_i(\boldsymbol{k}) + \nu k^2 w_i(\boldsymbol{k}) = -ik_l \mathcal{P}_{ip}(\boldsymbol{k}) \int \frac{\mathrm{d}^3\boldsymbol{k}'}{(2\pi)^3} u_l(\boldsymbol{k}') w_p(\boldsymbol{k}-\boldsymbol{k}') + f_i(\boldsymbol{k}), \tag{4.134}$$

where we have taken $\boldsymbol{F}$ to be solenoidal—there is no loss of generality here, as if one is interested in a non-solenoidal forcing, one can interpret $\boldsymbol{F}$ to be its solenoidal part. Then,

$$\begin{aligned}
&\partial_t \big\langle w_i(\boldsymbol{k}) w_j(\boldsymbol{k}')\big\rangle + \nu\left(k^2 + k'^2\right)\big\langle w_i(\boldsymbol{k}) w_j(\boldsymbol{k}')\big\rangle \\
&= -i\int \frac{\mathrm{d}^3\boldsymbol{k}''}{(2\pi)^3}\Big[k_l \mathcal{P}_{ip}(\boldsymbol{k})\big\langle u_l(\boldsymbol{k}'') w_p(\boldsymbol{k}-\boldsymbol{k}'') w_j(\boldsymbol{k}')\big\rangle + k'_l \mathcal{P}_{jp}(\boldsymbol{k}')\big\langle u_l(\boldsymbol{k}'') w_p(\boldsymbol{k}'-\boldsymbol{k}'') w_i(\boldsymbol{k})\big\rangle\Big] \\
&\qquad + \langle f_i(\boldsymbol{k}) w_j(\boldsymbol{k}')\rangle + \langle f_j(\boldsymbol{k}') w_i(\boldsymbol{k})\rangle.
\end{aligned} \tag{4.135}$$

In order to simplify the correlators appearing on the right-hand side of (4.135), we can make use of the zero-correlation-time assumption for $\boldsymbol{u}$ and $\boldsymbol{F}$. In the latter case, we note that integrating (4.134) over time, multiplying by $f_j(\boldsymbol{k}', t)$ and ensemble-averaging yields

$$\begin{aligned}
\langle w_i(\boldsymbol{k}) f_j(\boldsymbol{k}')\rangle &= \int^t \mathrm{d}t' \Bigg[-\nu k^2 \langle w_i(\boldsymbol{k}, t') f_j(\boldsymbol{k}', t)\rangle \\
&\qquad - ik_l \mathcal{P}_{ip}(\boldsymbol{k}) \int \frac{\mathrm{d}^3\boldsymbol{k}'}{(2\pi)^3} \langle u_l(\boldsymbol{k}', t') w_p(\boldsymbol{k}-\boldsymbol{k}', t') f_j(\boldsymbol{k}', t)\rangle + \langle f_i(\boldsymbol{k}, t') f_j(\boldsymbol{k}', t)\rangle\Bigg] \\
&= \frac{1}{2}(2\pi)^3 \delta(\boldsymbol{k}+\boldsymbol{k}')\Phi(k)\mathcal{P}_{ij}(\boldsymbol{k}),
\end{aligned} \tag{4.136}$$

where, in the second equality, we have taken the contributions of the first two correlators inside the t' integral to vanish, as demanded by causality, and used (4.132) to express the final correlator in terms of $\Phi(k)$.

A similar strategy may be employed to treat the triple correlations appearing in (4.135). Owing to our assumption of Gaussian statistics for $\boldsymbol{u}$, they can be computed using the Furutsu-Novikov (Gaussian-integration) formula:

$$\begin{aligned}\big\langle w_i(t,\boldsymbol{k}_1)w_j(t,\boldsymbol{k}_2)u_l(t,\boldsymbol{k}_3)\big\rangle &= \int^t \mathrm{d}t' \int \mathrm{d}^3\boldsymbol{k}' \big\langle u_l(t,\boldsymbol{k}_3)u_n(t',\boldsymbol{k}')\big\rangle \left\langle \frac{\delta\left[w_i(t,\boldsymbol{k}_1)w_j(t,\boldsymbol{k}_2))\right]}{\delta u_n(t',\boldsymbol{k}')}\right\rangle \\ &= \frac{1}{2}(2\pi)^3\kappa_{ln}(\boldsymbol{k}_3)\left\langle \frac{\delta\left[w_i(t,\boldsymbol{k}_1)w_j(t,\boldsymbol{k}_2))\right]}{\delta u_n(t,-\boldsymbol{k}_3)}\right\rangle, \end{aligned} \tag{4.137}$$

where we have used (4.128) in the second equality. The averaged same-time response function that appears in (4.137) can be computed by taking functional derivatives of the formal solution of the unaveraged version of (4.135), which is

$$\begin{aligned} w_i(\boldsymbol{k})w_j(\boldsymbol{k}') = \int^t \mathrm{d}t' \Bigg\{ &-\nu\left(k^2+k'^2\right) w_i(\boldsymbol{k},t')w_j(\boldsymbol{k}',t') \\ &- i\int \frac{\mathrm{d}^3\boldsymbol{k}''}{(2\pi)^3}\Big[k_l\mathcal{P}_{ip}(\boldsymbol{k})u_l(\boldsymbol{k}'',t')w_p(\boldsymbol{k}-\boldsymbol{k}'',t')w_j(\boldsymbol{k}',t') \\ &\quad + k'_l\mathcal{P}_{jp}(\boldsymbol{k}')u_l(\boldsymbol{k}'',t')w_p(\boldsymbol{k}'-\boldsymbol{k}'',t')w_i(\boldsymbol{k},t')\Big] \\ &\quad + f_i(\boldsymbol{k},t')w_j(\boldsymbol{k}',t') + f_j(\boldsymbol{k}',t')w_i(\boldsymbol{k},t')\Bigg\}. \end{aligned} \tag{4.138}$$

Since $\boldsymbol{F}$ is independent of $\boldsymbol{u}$, the functional differentiation gives

$$\begin{aligned}\left\langle \frac{\delta\left[w_i(t,\boldsymbol{k}_1)w_j(t,\boldsymbol{k}_2))\right]}{\delta u_n(t,-\boldsymbol{k}_3)}\right\rangle &= -ik_{1n}\mathcal{P}_{iq}(\boldsymbol{k}_1)\Psi_{qj}(\boldsymbol{k}_1+\boldsymbol{k}_3)\delta(\boldsymbol{k}_1+\boldsymbol{k}_2+\boldsymbol{k}_3) \\ &\quad -ik_{2n}\mathcal{P}_{jq}(\boldsymbol{k}_2)\Psi_{iq}(\boldsymbol{k}_2+\boldsymbol{k}_3)\delta(\boldsymbol{k}_1+\boldsymbol{k}_2+\boldsymbol{k}_3). \end{aligned} \tag{4.139}$$

Using (4.136), (4.137), and (4.139), (4.135) becomes

$$\begin{aligned} \partial_t\big\langle w_i(\boldsymbol{k})w_j(\boldsymbol{k}')\big\rangle + \nu\left(k^2+k'^2\right)\big\langle w_i(\boldsymbol{k})w_j(\boldsymbol{k}')\big\rangle = -\frac{1}{2}\int \mathrm{d}^3\boldsymbol{k}''\kappa_{ln}(\boldsymbol{k}'')\delta(\boldsymbol{k}+\boldsymbol{k}')\times \\ \Big\{k_l\mathcal{P}_{ip}(\boldsymbol{k})\Big[(k_n-k''_n)\mathcal{P}_{pq}(\boldsymbol{k}-\boldsymbol{k}'')\Psi_{qj}(\boldsymbol{k}) + k'_n\mathcal{P}_{jq}(\boldsymbol{k}')\Psi_{pq}(\boldsymbol{k}'+\boldsymbol{k}'')\Big] \\ + k'_l\mathcal{P}_{jp}(\boldsymbol{k}')\Big[k_n\mathcal{P}_{iq}(\boldsymbol{k})\Psi_{qp}(\boldsymbol{k}+\boldsymbol{k}'') + (k'_n-k''_n)\mathcal{P}_{pq}(\boldsymbol{k}'-\boldsymbol{k}'')\Psi_{iq}(\boldsymbol{k}')\Big]\Big\} \\ + (2\pi)^3\delta(\boldsymbol{k}+\boldsymbol{k}')\Phi(k)\mathcal{P}_{ij}(\boldsymbol{k}). \end{aligned} \tag{4.140}$$

Integrating (4.140) over $\boldsymbol{k}'$, and taking the trace (i.e., setting $i=j$ and summing over

i), we obtain, after a small amount of algebra,

$$\begin{aligned}
&\partial_t \Psi(k) + 2\nu k^2 \Psi(k) \\
&= -\frac{1}{2}\int \frac{\mathrm{d}^3\boldsymbol{k}''}{(2\pi)^3}\kappa_{ln}(\boldsymbol{k}'')k_l k_n \mathcal{P}_{pq}(\boldsymbol{k})\mathcal{P}_{pq}(\boldsymbol{k}+\boldsymbol{k}'')\left[\Psi(k) - \Psi(|\boldsymbol{k}+\boldsymbol{k}''|)\right] + 2\Phi(k), \quad (4.141)
\end{aligned}$$

where a useful step in the simplification of the integrand was noting that $\kappa_{ln}(\boldsymbol{k}'')k_n'' \propto \mathcal{P}_{ln}(\boldsymbol{k}'')k_n'' = 0$.

Now, $\Psi(k)$ may be brought outside the first integral in (4.141), giving rise to a turbulent-viscosity term, $-\nu_T(k)k^2\Psi(k)$, where

$$\begin{aligned}
2\nu_T(k) &\equiv \frac{1}{2}\int \frac{\mathrm{d}^3\boldsymbol{k}''}{(2\pi)^3}\kappa_{ln}(\boldsymbol{k}'')\frac{k_l k_n}{k^2}\mathcal{P}_{pq}(\boldsymbol{k})\mathcal{P}_{pq}(\boldsymbol{k}+\boldsymbol{k}'') \\
&= \frac{1}{(2\pi)^3}\int_0^\infty \mathrm{d}k'' k''^2 \kappa(k'')\int \mathrm{d}^2\Omega''\left[1 - \frac{(\boldsymbol{k}\cdot\boldsymbol{k}'')^2}{k^2 k''^2}\right]\left[1 - \frac{(\boldsymbol{k}\times\boldsymbol{k}'')^2}{2k^2(\boldsymbol{k}+\boldsymbol{k}'')^2}\right] \\
&\equiv \frac{1}{(2\pi)^2}\int_0^\infty \mathrm{d}k''\, k''^2\kappa(k'')G\left(\frac{k''}{k}\right). \quad (4.142)
\end{aligned}$$

The function $G(x)$ may be obtained by choosing a spherical coordinate system about $\boldsymbol{k}$. Computing the angle integral then yields

$$G(x) = \frac{1}{96x^3}\left[2x(3+53x^2-11x^4+3x^6) - 3(1-x^2)^4\log\left|\frac{1+x}{1-x}\right|\right]. \quad (4.143)$$

Finally, substituting $\kappa(k'') = \kappa_0(k''-k_f)$, we get

$$2\nu_T(k) = \frac{1}{(2\pi)^2}\kappa_0 k_f^2\, G\left(\frac{k_f}{k}\right). \quad (4.144)$$

The other term inside the integral in (4.141), containing $\Psi(|\boldsymbol{k}+\boldsymbol{k}''|)$, is handled in the following manner:

$$\begin{aligned}
&\frac{1}{2}\int \frac{\mathrm{d}^3\boldsymbol{k}''}{(2\pi)^3}\kappa_{ln}(\boldsymbol{k}'')k_l k_n \mathcal{P}_{pq}(\boldsymbol{k})\mathcal{P}_{pq}(\boldsymbol{k}+\boldsymbol{k}'')\Psi(\left|\boldsymbol{k}+\boldsymbol{k}''\right|) \\
&= \frac{1}{2}\frac{1}{(2\pi)^3}\int_0^\infty \mathrm{d}k'' k''^2\kappa(k'')\int \mathrm{d}^2\Omega'' k_l k_n \mathcal{P}_{ln}(\boldsymbol{k}'')\mathcal{P}_{pq}(\boldsymbol{k})\mathcal{P}_{pq}(\boldsymbol{k}+\boldsymbol{k}'')\Psi(\left|\boldsymbol{k}+\boldsymbol{k}''\right|) \\
&= \frac{1}{2}\frac{1}{(2\pi)^3}\int_0^\infty \mathrm{d}k'' k''\kappa(k'')\int_0^{2\pi}\mathrm{d}\varphi''\int_{|k-k''|}^{k+k''}\mathrm{d}k'\frac{k'}{k}k_l k_n \mathcal{P}_{ln}(\boldsymbol{k}'')\mathcal{P}_{pq}(\boldsymbol{k})\mathcal{P}_{pq}(\boldsymbol{k}')\Psi(k') \\
&= \frac{1}{(2\pi)^2}\int_0^\infty \mathrm{d}k'' k''\kappa(k'')\int_{|k-k''|}^{k+k''}\mathrm{d}k'\frac{k'}{k}K(k'',k',k)\Psi(k'), \quad (4.145)
\end{aligned}$$

where, in the second equality, we set $\boldsymbol{k}' = \boldsymbol{k}+\boldsymbol{k}''$, chose the polar axis to be along $\boldsymbol{k}$, and changed variables from the polar angle θ'' to $k' = |\boldsymbol{k}'|$, noting that $k'\mathrm{d}k' =$

$-kk''\sin\theta''\mathrm{d}\theta''$. In the final equality, we have used $\boldsymbol{k}\cdot\boldsymbol{k}'' = (k'^2 - k^2 - k''^2)/2$ and $\boldsymbol{k}\cdot\boldsymbol{k}' = (k'^2 + k^2 - k''^2)/2$ to write the intergration kernel $K(k'', k', k)$ in terms of the magnitudes of k, k' and k'' only. Explicitly, it is

$$K(k'',k',k) = -\frac{(k^2-k''^2)^4}{32k^2k''^2}\frac{1}{k'^2} - \frac{(k^2-k''^2)^3}{8k^2k''^2} + \frac{(5k^4+6k^2k''^2-3k''^4)}{16k^2k''^2}k'^2 - \frac{k^2-k''^2}{8k^2k''^2}k'^4 - \frac{1}{32k^2k''^2}k'^6. \quad (4.146)$$

Finally, taking $\kappa(k'') = \kappa_0(k''-k_f)$ and integrating over k'', we find

$$\frac{1}{2}\int\frac{\mathrm{d}^3\boldsymbol{k}''}{(2\pi)^3}\kappa_{ln}(\boldsymbol{k}'')k_lk_n\mathcal{P}_{pq}(\boldsymbol{k})\mathcal{P}_{pq}(\boldsymbol{k}+\boldsymbol{k}'')\Psi(\left|\boldsymbol{k}+\boldsymbol{k}''\right|) = \frac{\kappa_0}{(2\pi)^2}k_f\int_{|k-k_f|}^{k+k_f}\mathrm{d}k'\frac{k'}{k}K(k_f,k',k)\Psi(k'). \quad (4.147)$$

Using (4.142) and (4.147), (4.141) becomes

$$\partial_t\Psi(k) + 2\left[\nu+\nu_T(k)\right]k^2\Psi(k) = \frac{\kappa_0}{(2\pi)^2}k_f\int_{|k-k_f|}^{k+k_f}\mathrm{d}k'\frac{k'}{k}K(k',k)\Psi(k') + 2\Phi(k), \quad (4.148)$$

where we have suppressed the explicit dependence of $K(k_f, k', k)$ on k_f. Using $\mathcal{E}(k) = k^2\Psi(k)/2\pi^2$, and identifying $F = k^2\Phi(k)/\pi^2$ as the spectrum of the energy injection, the evolution equation for the spectrum of the passive vector becomes

$$\partial_t\mathcal{E}(k) + 2\left[\nu+\nu_T(k)\right]k^2\mathcal{E}(k) = \frac{\kappa_0k_f}{(2\pi)^2}k\int_{|k-k_f|}^{k+k_f}\frac{\mathrm{d}k'}{k'}K(k',k)\mathcal{E}(k') + F(k), \quad (4.149)$$

which is (4.50), as promised. This is the analogue for the passive vector field $\boldsymbol{w}$ of the similar mode-coupling equations for the magnetic field (Kulsrud & Anderson, 1992) and the passive scalar (Schekochihin *et al.*, 2004).

4.D.3 Small-k limit of the mode-coupling equation

In the present study, we require only the limit of (4.149) with $k \ll k_f$. Noting that $\lim_{x\to\infty}G(x) = 4/5$, and

$$\lim_{k,\,q\to0}K(k' = k_f+q, k) = \frac{k^4-q^4}{4k^2}, \quad (4.150)$$

we find that (4.149) becomes

$$\partial_t\mathcal{E}(k) + \beta k_f^2k^2\mathcal{E}(k) = \frac{5}{16}\frac{\beta}{k}\int_{-k}^{k}\mathrm{d}q(k^4-q^4)\mathcal{E}(k_f+q) + F(k), \quad (4.151)$$

where $\beta = \kappa_0/5\pi^2$ and we have assumed that $\nu_T \gg \nu$. This is (4.53).

4.E Alternative derivation of the scaling of $\langle \boldsymbol{P}_V^2 \rangle$ vs. R in turbulence forced with long-range correlations

In this appendix, we show how the scalings (4.59), viz.,

$$\langle \boldsymbol{P}_V^2 \rangle \propto \begin{cases} R^{7-b} & \text{if } l \ll R \ll R_c, \\ R^{5-b} & \text{if } R \gg R_c \ \& \ b < 3, \\ R^2 & \text{if } R \gg R_c \ \& \ 3 < b < 4, \end{cases} \tag{4.152}$$

which were derived in Section 4.4.2 from the spectral evolution equation (4.54) for the passive vector field, can be obtained by instead considering momentum diffusion as the sum of many instances of a decaying passive vector field.

Between the times t_{inj} and $t_{\text{inj}} + \mathrm{d}t_{\text{inj}}$, the forcing causes the spectral energy density to increase by $\mathrm{d}\mathcal{E}_{\boldsymbol{w}} = Ck^b \mathrm{d}t_{\text{inj}}$. As (4.54) is linear, we may consider the evolution of the spectral-energy-density increment $\mathrm{d}\mathcal{E}_{\boldsymbol{w}}$ in isolation from the rest of $\mathcal{E}_{\boldsymbol{w}}$. Assuming that $k \ll k_f$ and $b < 4$, (4.54) implies that $\mathrm{d}\mathcal{E}_{\boldsymbol{w}}$ decays with time t according to

$$\mathrm{d}\mathcal{E}_{\boldsymbol{w}}(k,t) = Ck^b \, \mathrm{d}t_{\text{inj}} \, \exp(-\beta k_f^2 k^2 \Delta t), \tag{4.153}$$

where $\Delta t = t - t_{\text{inj}} > 0$. The energy-containing scale and total energy associated with $\mathrm{d}\mathcal{E}_{\boldsymbol{w}}$ are respectively $\lambda \sim (\beta k_f^2 \Delta t)^{1/2}$ (note that λ is not the same as l, the latter being the energy-containing scale associated with the full field $\boldsymbol{w}$, rather than solely the increment generated at t_{inj}) and

$$\mathrm{d}E = C \, \mathrm{d}t_{\text{inj}} \int_0^\infty \mathrm{d}k \, k^b \exp(-\beta k_f^2 k^2 \Delta t) = \frac{1}{2}\Gamma\left(\frac{1+b}{2}\right) C \mathrm{d}t_{\text{inj}} \, (\beta k_f^2 \Delta t)^{-(1+b)/2}. \tag{4.154}$$

Let us now determine the contribution of $\mathrm{d}\mathcal{E}_{\boldsymbol{w}}(k,t)$ to the mean square momentum $\mathrm{d}\langle \boldsymbol{P}_V^2 \rangle$ contained within a spherical control volume V with radius R. There are three different cases to consider:

1. If $R \ll \lambda$, then (4.34) gives $\mathrm{d}\langle \boldsymbol{P}_V^2 \rangle \propto R^6 \, \mathrm{d}E \propto R^6 (\Delta t)^{-(1+b)/2} \mathrm{d}t_{\text{inj}}$, as the decaying field has reached scales much larger than R, so there is little variation of $\boldsymbol{w}$ within V.

2. If $R \gg \lambda$ and $b < 3$, then (4.34) gives $\mathrm{d}\langle \boldsymbol{P}_V^2 \rangle \propto R^{5-b} \mathrm{d}t_{\mathrm{inj}}$, with no time dependence, owing to the fact that the momentum scaling is set by the power-law part of (4.153) [see (4.33) and surrounding discussion], which is constant in time, a consequence of momentum conservation.

3. If $R \gg \lambda$ and $3 < b < 4$, then (4.34) gives $\mathrm{d}\langle \boldsymbol{P}_V^2 \rangle \propto R^2\, c(\Delta t) \mathrm{d}t_{\mathrm{inj}}$. An as-yet undetermined function $c(\Delta t)$ appears here because the integral (4.33) is dominated by the evolving contribution from the energy-containing scales, rather than from the invariant k^b tail of (4.153). In principle, we can determine $c(\Delta t)$ by substituting (4.153) into our equation for $\chi(r)$ in terms of $\mathcal{E}(k)$, (4.31), and then evaluating the integral (4.28) exactly. However, some effort can be spared by using the self-similar form of (4.153). Substituting $\mathcal{E}(k) = k^b g(k^2 \Delta t)$ in (4.31), and changing the integration variable to $x = kr$, we have

$$u^2 \chi(r) = \frac{2}{r^{1+b}} \int_0^\infty \mathrm{d}x x^b g\left(\frac{x^2 t}{r^2}\right) \frac{\sin x - x \cos x}{x} \equiv \frac{2}{r^{1+b}} G\left(\frac{\Delta t}{r^2}\right). \tag{4.155}$$

Then, with a change of variables to $y = r'/\sqrt{\Delta t}$, (4.28) becomes

$$\langle \boldsymbol{P}_V^2 \rangle = 4\pi^2 u^2 (\Delta t)^{(3-b)/2} \int_0^{2R} \mathrm{d}r\, r \int_0^{r/\sqrt{\Delta t}} \mathrm{d}y\, y^{2-b}\, G\left(\frac{1}{y}\right). \tag{4.156}$$

For $b > 3$, (4.34) demands that $\langle \boldsymbol{P}_V^2 \rangle \propto R^2$ at any fixed time, so the integral over y in (4.156) must be independent of its upper limit. In this case, the result of the double integration is time independent, so we deduce $c(\Delta t) = (\Delta t)^{(3-b)/2}$.

To summarise these results, we have established that:

$$\mathrm{d}\langle \boldsymbol{P}_V^2 \rangle \propto \mathrm{d}t_{\mathrm{inj}} \begin{cases} R^6\, (\Delta t)^{-(1+b)/2} & \text{if } R \ll \lambda \sim (\beta k_f^2 \Delta t)^{1/2}, \\ R^{5-b} & \text{if } R \gg \lambda \sim (\beta k_f^2 \Delta t)^{1/2} \ \&\ b < 3, \\ R^2\, (\Delta t)^{(3-b)/2} & \text{if } R \gg \lambda \sim (\beta k_f^2 \Delta t)^{1/2} \ \&\ 3 < b < 4. \end{cases} \tag{4.157}$$

Under the passive-field assumption, and owing to the fact that the forcing at any given time is uncorrelated with the forcing at any other time, the total squared momentum contained within a volume of continually forced turbulence may be obtained as the sum of contributions from passive decays initialised continuously and uniformly in time. Let us consider a fixed sphere of radius R and let $t_c = R^2/\beta k_f^2$ be the time

at which the energy-containing scale of the decaying field initialised at $t_{\rm inj} = 0$ reaches the scale R. Then, for $t < t_c$, each part of the sum comes from the $R \gg \lambda$ part of (4.157), so

$$\langle \boldsymbol{P}_V^2 \rangle = \int \mathrm{d}\langle \boldsymbol{P}_V^2 \rangle = \int_0^t \mathrm{d}t_{\rm inj} \frac{\mathrm{d}\langle \boldsymbol{P}_V^2 \rangle}{\mathrm{d}t_{\rm inj}} \propto \begin{cases} R^{5-b} t & \text{if } b < 3, \\ R^2 t^{(5-b)/2} & \text{if } 3 < b < 4. \end{cases} \tag{4.158}$$

If, instead, $t > t_c$, then

$$\langle \boldsymbol{P}_V^2 \rangle = \int \mathrm{d}\langle \boldsymbol{P}_V^2 \rangle = \int_{t-t_c}^t \mathrm{d}t_{\rm inj} \frac{\mathrm{d}\langle \boldsymbol{P}_V^2 \rangle}{\mathrm{d}t_{\rm inj}} + \int_0^{t-t_c} \mathrm{d}t_{\rm inj} \frac{\mathrm{d}\langle \boldsymbol{P}_V^2 \rangle}{\mathrm{d}t_{\rm inj}}. \tag{4.159}$$

The first integral encodes all the decays that have not yet reached the scale R, as $t - t_{\rm inj} < t_c$ for them. Therefore, we may again substitute for $\mathrm{d}\langle \boldsymbol{P}_V^2 \rangle$ using the $R \gg \lambda$ part of (4.157), giving

$$\begin{aligned} \int_{t-t_c}^t \mathrm{d}t_{\rm inj} \frac{\mathrm{d}\langle \boldsymbol{P}_V^2 \rangle}{\mathrm{d}t_{\rm inj}} &\propto \begin{cases} R^{5-b} t_c & \text{if } b < 3, \\ R^2 t_c^{(5-b)/2} & \text{if } 3 < b < 4, \end{cases} \\ &\propto R^{7-b}. \end{aligned} \tag{4.160}$$

The second integral in (4.159) encodes all the decays that were initialised at $t_{\rm inj} < t - t_c$, so have reached a scale larger than R at time t. It is

$$\int_{t_c}^t \mathrm{d}t_{\rm inj} \frac{\mathrm{d}\langle \boldsymbol{P}_V^2 \rangle}{\mathrm{d}t_{\rm inj}} \propto R^6 \int_0^{t-t_c} \mathrm{d}t_{\rm inj} (t - t_{\rm inj})^{-(1+b)/2} \propto R^6 \, t_c^{(1-b)/2} \propto R^{7-b}. \tag{4.161}$$

Thus, decays that have reached $\lambda > R$ and ones with $\lambda < R$ both contribute a term $\propto R^{7-b}$ to $\langle \boldsymbol{P}_V^2 \rangle$, explaining the scaling found in (4.59). In particular, this calculation explains why forcing with different values of $3 < b < 4$ results in saturation with different scalings for $\langle \boldsymbol{P}_V^2 \rangle$, despite both having $\langle \boldsymbol{P}_V^2 \rangle \propto R^2$ at $R > R_c$: the total energy contained within an initally more diffuse blob of momentum decays more slowly than an initally less diffuse one (i.e., one with smaller b), even though the energy-containing scales of both grow at the same rate.

As an aside, we note that the saturated spectrum is also derivable directly from the ensemble of decaying states, (4.153):

$$\mathcal{E}_{\boldsymbol{w}}(k,t) = \int \mathrm{d}\mathcal{E}_{\boldsymbol{w}}(k,t) = \int_0^t \mathrm{d}t_{\rm inj} C k^b \exp(-\beta k_f^2 k^2 (t - t_{\rm inj})) = \left[1 - e^{-\beta k^2 k_f^2 t}\right] \frac{C k^{b-2}}{\beta k_f^2}, \tag{4.162}$$

which is (4.55) [with the $\beta \mathcal{E}_{\boldsymbol{w}}(k_f) k^4$ term neglected].

4.F Non-solenoidal forcing

In this appendix, we formalise the discussion of non-solendoidal forcing in Section 4.4.3. The essential result is due to Saffman (1967), which may be stated in the notation of present study as follows:

Theorem (Saffman)**.** *Let $\boldsymbol{F}(\boldsymbol{x})$ be a random function of $\boldsymbol{x}$ that is statistically isotropic and homogeneous, and that has an analytic spectral tensor,*

$$M_{\alpha\beta}(\boldsymbol{k},t,t') \equiv \int \mathrm{d}^3\boldsymbol{r}\langle f_\alpha(t,\boldsymbol{x})f_\beta(t',\boldsymbol{x}+\boldsymbol{r})\rangle e^{-i\boldsymbol{k}\cdot\boldsymbol{r}}. \tag{4.163}$$

Let $\boldsymbol{F}^{(\mathrm{s})}$ be the solenoidal part of $\boldsymbol{F}$, with spectral tensor $M^{(\mathrm{s})}_{\alpha\beta}(\boldsymbol{k},t,t')$. Then, the "Saffman integrals" associated with $\boldsymbol{F}$ and $\boldsymbol{F}^{(\mathrm{s})}$, given by $L_{\boldsymbol{F}} = \int^t \mathrm{d}t'\, M_{\alpha\alpha}(0,t,t')$ and $L_{\boldsymbol{F}^{(\mathrm{s})}} = \int^t \mathrm{d}t'\, M^{(\mathrm{s})}_{\alpha\alpha}(0,t,t')$, respectively [cf. (4.61)], satisfy

$$L_{\boldsymbol{F}^{(\mathrm{s})}} = \frac{2}{3}L_{\boldsymbol{F}}. \tag{4.164}$$

For completeness, we present in Section 4.F.1 a proof (which is adapted from Saffman 1967) of this theorem. First, we make a number of remarks.

1. The utility of Saffman's theorem for forced turbulence is as follows. Equations (4.20) and (4.21) together imply that

$$\frac{\mathrm{d}L}{\mathrm{d}t} = 4\pi \lim_{r\to\infty}\left(\frac{1}{r}\frac{\partial}{\partial r}r^4u^3K\right) + L_{\boldsymbol{F}^{(\mathrm{s})}} \tag{4.165}$$

   for a turbulence forced by a series of realisations of $\boldsymbol{F}$ that are delta-correlated in time. According to the argument presented in Section 4.2.2, the term involving $K(r)$ vanishes.[8] Thus, according to (4.164),

$$\frac{\mathrm{d}L}{\mathrm{d}t} = \frac{2}{3}L_{\boldsymbol{F}}, \tag{4.166}$$

   so the rate of growth of L in forced turbulence is finite, and proportional to $L_{\boldsymbol{F}}$.

[8] Note that, if $L_{\boldsymbol{F}^{(\mathrm{s})}} \neq 0$, $K(r) = O(r^{-3})$ as $r\to\infty$, not $O(r^{-4})$ [as in (4.17)]. This is because long-range correlations in $\boldsymbol{F}$ can propagate into K via the correlators of $\boldsymbol{u}$ and $\boldsymbol{F}$ that are present in (4.16). Nonetheless, such a decay of $K(r\to\infty)$ is still sufficiently rapid for the term containing $K(r)$ in (4.165) to be negligible.

2. Saffman's theorem requires that $M_{\alpha\beta}$ be analytic. This condition is guaranteed by choosing $\boldsymbol{F}$ so that $\langle f_i(\boldsymbol{x}) f_j(\boldsymbol{x}+\boldsymbol{r})\rangle$ decays rapidly with distance – for example, we might take $\boldsymbol{F}$ to consist of an ensemble of local patches of uniformly directed force, whose magnitude decays exponentially away from their centre. However, it should be emphasised that Saffman's result does fail if $\langle f_i(\boldsymbol{x}) f_j(\boldsymbol{x}+\boldsymbol{r})\rangle$ decays slowly. An immediate example of this is the case where $\boldsymbol{F}$ is itself solenoidal, so $\boldsymbol{F} = \boldsymbol{F}^{(\mathrm{s})}$. In that case, (4.164) appears to suggest $L_{\boldsymbol{F}} = 0$. However, this does not imply that $L_{\boldsymbol{F}} = 0$ in general for solenoidal forcing, as the argument applies only to functions $\boldsymbol{F}(\boldsymbol{x})$ with an analytic spectral tensor. Long-range correlations in $\boldsymbol{F}^{(s)}(\boldsymbol{x})$ are necessary for $L_{\boldsymbol{F}^{(s)}} \neq 0$, so the spectral tensor is not analytic (Saffman, 1967).

3. Saffman's theorem does not imply that *any* incompressible forcing with an analytic spectral tensor will have $L_{\boldsymbol{F}^{(\mathrm{s})}} \neq 0$, and so induce a flow with $\mathcal{E}(k \to 0) \propto k^2$. This is because it remains possible that $L_{\boldsymbol{F}} = 0$. An example of this would be a ensemble of *pairs* of oppositely directed, local instantaneous impulses, separated by a small distance [cf. Section 4.3.2]. Another example, pertinent to numerical studies of forced turbulence, is forcing in a finite spectral band. As shown in Appendix 4.A, long-range correlations decay arbitrarily rapidly for such a forcing, meaning that $M_{\alpha\beta}$ is analytic—nonetheless, $L_{\boldsymbol{F}}$ is manifestly zero for such a $\boldsymbol{F}$, and, therefore, so is $L_{\boldsymbol{F}^{(\mathrm{s})}}$.

4.F.1 Proof of Saffman's theorem

A proof of Saffman's theorem, adapted from Saffman (1967), is as follows. Let us denote the "vorticity" of $\boldsymbol{F}$ by $\boldsymbol{\omega}$, so that $\boldsymbol{\omega} = \boldsymbol{\nabla} \times \boldsymbol{F} = \boldsymbol{\nabla} \times \boldsymbol{F}^{(\mathrm{s})}$. Then the two-point vorticity correlation function is

$$\begin{aligned} \langle \omega_i(\boldsymbol{x}) \omega_j(\boldsymbol{x}+\boldsymbol{r})\rangle &= -\epsilon_{im\alpha}\epsilon_{jl\beta} \frac{\partial}{\partial r_m}\frac{\partial}{\partial r_l}\langle f_\alpha(\boldsymbol{x}) f_\beta(\boldsymbol{x}+\boldsymbol{r})\rangle \\ &= -\epsilon_{im\alpha}\epsilon_{jl\beta} \frac{\partial}{\partial r_m}\frac{\partial}{\partial r_l}\langle f^{(\mathrm{s})}_\alpha(\boldsymbol{x}) f^{(\mathrm{s})}_\beta(\boldsymbol{x}+\boldsymbol{r})\rangle. \end{aligned} \tag{4.167}$$

Taking the Fourier transform, we find the corresponding spectral tensor to be

$$\begin{aligned}\Omega_{ij} &\equiv \frac{1}{8\pi^3}\int \mathrm{d}^3\boldsymbol{r}\langle\omega_i(\boldsymbol{x})\omega_j(\boldsymbol{x}+\boldsymbol{r})\rangle e^{-i\boldsymbol{k}\cdot\boldsymbol{r}} \\ &= \epsilon_{im\alpha}\epsilon_{jl\beta}k_m k_l M_{\alpha\beta} = \epsilon_{im\alpha}\epsilon_{jl\beta}k_m k_l M^{(\mathrm{s})}_{\alpha\beta}. \end{aligned} \tag{4.168}$$

Taking the trace of (4.168) and using $k_i M^{(\mathrm{s})}_{ij} = 0$, we obtain

$$M^{(\mathrm{s})}_{\gamma\gamma}(\boldsymbol{k}) = \epsilon_{im\alpha}\epsilon_{il\beta}\frac{k_m k_l}{k^2}M_{\alpha\beta}(\boldsymbol{k}). \tag{4.169}$$

Finally, we take the limit of small $k = |\boldsymbol{k}|$. Analyticity of $M_{\alpha\beta}$ implies that

$$M_{\alpha\beta}(k) = M_{\alpha\beta}(0) + O(k) = \frac{1}{3}M_{\gamma\gamma}(0)\delta_{\alpha\beta} + O(k), \tag{4.170}$$

where the second equality follows from isotropy. Substituting this into (4.169), we obtain

$$M^{(\mathrm{s})}_{\gamma\gamma}(0) = \frac{2}{3}M_{\gamma\gamma}(0), \tag{4.171}$$

which is equivalent to (4.164). *Q.E.D.*

Chapter 5

Elasticity of tangled magnetic fields

This chapter is adapted from Hosking et al.*, 2020, J. Plasma Phys.* ***86****, 905860511.*

5.1 Introduction

Tangled magnetic fields are ubiquitous in astrophysical systems, expected to develop in stellar interiors, accretion discs, galaxies and clusters of galaxies (Zel'dovich *et al.*, 1983). Their ubiquity results from the freezing of magnetic flux into fluid motions in ideal magnetohydrodynamics (MHD): initially straight field lines are quickly tangled by the random stretching motions of a turbulent flow, typically at spatial scales smaller than those associated with the global flow (see, e.g., Rincon, 2019).

If such turbulence is driven sporadically in time and the subsequent relaxation is slow — as in the decay of primordial magnetic fields on the large-Pm-suppressed reconnection timescale described in Chapter 3, for example — or if the system relaxes to some quasi-stable steady state, then there may be periods of time when dynamical-strength magnetic field tangled at small scales threads relatively quiescent fluid. The large-scale dynamic properties of such a fluid may be highly relevant for questions of how energy is propagated, stored, and dissipated in the astrophysical systems described above. Such considerations motivate an idealised plasma physics problem: how does a static fluid with a statistically homogeneous and isotropic Maxwell stress respond to an imposed large-scale impulse? It is this question that we aim to address in this chapter, subject to some important simplifying assumptions.

We will treat the problem in the setting of non-resistive MHD, i.e., assuming perfect flux freezing, and thus the invariance of the magnetic field topology. Physically, this means assuming that the small-scale magnetic tangle is itself always at scales that are sufficiently large for magnetic dissipation to be negligible. In pursuit of maximal simplicity, we will also assume that the tangled magnetic field represents an equilibrium state. While this assumption is unrealistic for MHD turbulence, the dynamics of the tangled equilibrium field are sufficiently complex to warrant investigation, and we anticipate that the lessons learned here will inform future study of the more realistic, non-equilibrium case.

The plan of this chapter is as follows. In Section 5.2, we formally motivate the problem from the equations of ideal MHD, and describe previous work that modelled the equilibrium Maxwell stress as "perfectly" homogeneous and isotropic at all scales. Using this model, Moffatt (1986) argued that tangled fields should support waves whose restoring force is the isotropic elasticity afforded by the magnetic field– these "magnetoelastic" waves are the isotropic analogue of Alfvén waves on a straight magnetic field. Later, magnetoelastic waves were rederived by Gruzinov & Diamond (1996) in the same approximation, and were suggested (in a somewhat modified form) by Schekochihin *et al.* (2002) and Maron *et al.* (2004) as a possible mechanism for the saturation of the turbulent MHD dynamo. Williams (2004) has speculated on the importance of magnetoelasticity in astrophysical systems in which the presence of magnetic fields is traditionally modelled by magnetic viscosity. More recently, Chen & Diamond (2020) have developed a theory of potential vorticity mixing in the solar tachocline, accounting for the effect of a tangled magnetic field elasticity using a similar model. Experimentally, elastic waves have been observed in viscoelastic flows of polymer solutions (Qin *et al.*, 2019), which obey a system of equations closely related to MHD (Ogilvie & Proctor, 2003).

However, treating the field as perfectly homogeneous naturally precludes the possibility of the large-scale waves driving small-scale motions. In Section 5.3, we show that such motions feed back on the large scales, thereby modifying the dispersion relation of magnetoelastic waves, even when the small scale motions are strongly damped

by viscosity (although not, as we will discover, when the small-scale motions are *hyper*viscously damped). In particular, we show that if the field configuration is stable (though this may be an idealisation), this effect always results in a decrease of the wave frequency from the perfectly homogeneous value.

In Section 5.3.3, we develop a mean-field formalism based on an approximation that assumes the coupling of different Fourier modes of the small-scale motions to each other to be small. This treatment is equivalent to the First-Order Smoothing Approximation (FOSA) commonly employed in large-scale dynamo theory (Moffatt 1978; Krause & Raedler 1980; Brandenburg & Subramanian 2005; see Rincon 2019 for a review), and allows the dispersion relation for magnetoelastic waves to be expressed in terms of statistical properties of the magnetic-field configuration. In Section 5.3.4, we use the FOSA to solve the inital-value problem for a magnetoelastic pulse in a viscous fluid. We find that accounting for intermittency gives anomalously fast viscous damping due to the development of small-scale motions.

An important caveat to modelling tangled magnetic fields by equilibrium configurations is that such equilibria appear to be generally *unstable*. Even in the case of periodic, linear force-free equilibria, which have been shown to be stable to wide class of perturbations (Woltjer, 1958; Molodensky, 1974; Moffatt, 1986), East *et al.* (2015) have shown that it is often, perhaps always, possible to find ideal perturbations that decrease the total energy. Whether there are any non-trivial cases of periodic magnetostatic equilibria that are stable is an open question. We provide a review of the instability of linear force-free equilibria in Appendix 5.A. The theory that we develop here applies to the idealised stable case, or to the case where viscous damping (which proceeds via motions at the scale of the tangled field) is sufficient to delay the onset of the instability.

In Section 5.4, we present the first (to our knowledge) numerical simulations of isotropic magnetoelasticity. We introduce a sinusoidal velocity perturbation to periodic magnetostatic equilibria, and measure the evolution of the induced standing waves. The results are in excellent agreement with the predictions of our mean-field-theory treatment.

5.2 A perfectly homogeneous tangle

The equations of ideal (non-resistive), incompressible MHD are

$$\frac{\partial \boldsymbol{u}}{\partial t} + \boldsymbol{u}\cdot\boldsymbol{\nabla}\boldsymbol{u} = -\boldsymbol{\nabla}P + \boldsymbol{B}\cdot\boldsymbol{\nabla}\boldsymbol{B} + \nu\nabla^2\boldsymbol{u}, \tag{5.1}$$

$$\frac{\partial \boldsymbol{B}}{\partial t} + \boldsymbol{u}\cdot\boldsymbol{\nabla}\boldsymbol{B} = \boldsymbol{B}\cdot\boldsymbol{\nabla}\boldsymbol{u}, \tag{5.2}$$

$$\boldsymbol{\nabla}\cdot\boldsymbol{u} = 0, \tag{5.3}$$

$$\boldsymbol{\nabla}\cdot\boldsymbol{B} = 0, \tag{5.4}$$

where P is the total (thermal + magnetic) pressure, determined by (5.3); ν is the kinematic viscosity; $\boldsymbol{u}$ is the fluid velocity; and the magnetic field $\boldsymbol{B}$ is measured in velocity units.

For our purposes, it is convenient to eliminate $\boldsymbol{B}$ from these equations in favour of the Maxwell stress, $M_{ij} = B_iB_j$. Then, in index notation, (5.1) becomes

$$\partial_t u_i + u_j\partial_j u_i = -\partial_i P + \partial_j M_{ij} + \nu\partial_j\partial_j u_i, \tag{5.5}$$

while taking the outer product of (5.2) with $\boldsymbol{B}$ gives

$$\partial_t M_{ij} = \mathcal{D}_{ij}\left(M,u\right) \equiv M_{ik}\partial_k u_j + M_{jk}\partial_k u_i - u_k\partial_k M_{ij}, \tag{5.6}$$

where $\mathcal{D}_{ij}(M,u)$ may be recognised as the negative of the Lie derivative of M along $\boldsymbol{u}$. In other words, $\mathcal{D}_{ij}(M,u)$ is the bilinear operator that gives the rate of change of the components M_{ij} of a tensor M frozen into (i.e., Lie dragged by) the flow $\boldsymbol{u}$.

This rewriting of the MHD equations is possible only because we have assumed non-resistive MHD: it would not be possible to write a closed system of evolution equations for $\boldsymbol{u}$ and M if there were a resistive term of the form $\eta\nabla^2\boldsymbol{B}$ in (5.2). Physically, this is because non-resistive MHD is insensitive to the directed nature of magnetic field lines. This is manifest in the fact the Maxwell stress B_iB_j is unchanged by a reversal of the sign of $\boldsymbol{B}$. Magnetic diffusion is, of course, sensitive to such direction reversals; a magnetic-field configuration with a sudden direction reversal can be subject to resistive instabilities.

A simple model of a tangled equilibrium state is obtained by linearising (5.5) and (5.6) about the equilibrium state $M_{ij} = v_{\rm E}^2 \delta_{ij}$, where $v_{\rm E}$ is a constant. A small amount of algebra yields

$$\frac{\partial^2 \boldsymbol{\xi}}{\partial t^2} = v_{\rm E}^2 \nabla^2 \boldsymbol{\xi} + \nu \nabla^2 \frac{\partial \boldsymbol{\xi}}{\partial t}, \tag{5.7}$$

where $\boldsymbol{\xi}$ is the displacement field defined by $\partial_t \boldsymbol{\xi} = \boldsymbol{u}$. This is a wave equation for (viscously damped) magnetoelastic waves with wave speed $v_{\rm E}$, i.e., waves whose restoring force is the isotropic elasticity of the tangled magnetic field. The corresponding dispersion relation is

$$\omega = \pm k v_{\rm E} \sqrt{1 + \left(\frac{\nu k}{2 v_{\rm E}}\right)^2} - \frac{1}{2} i \nu k^2. \tag{5.8}$$

In the absence of viscosity, magnetoelastic waves have dispersion relation $\omega = \pm k v_{\rm E}$, and can be thought of as the isotropic equivalent of Alfvén waves. Like Alfvén waves, magnetoelastic waves are transverse, as $\boldsymbol{\nabla} \cdot \boldsymbol{u} = 0$ implies $\boldsymbol{k} \cdot \boldsymbol{\xi} = 0$.

The dispersion relation (5.8) was first obtained via a similar derivation by Moffatt (1986), and later by Gruzinov & Diamond (1996). However, it is an idealisation because no vector field can satisfy $B_i B_j \propto \delta_{ij}$ at all scales. In the next section, we develop a theory of magnetoelastic waves for a magnetic tangle that is homogeneous and isotropic at large scales, but accounting for its inhomogeneous small-scale structure, and, therefore, the possibility of generating motions at the scale of the magnetic tangle. We find that the dispersion relation (5.8) is modified by an order-unity factor, even in the limit that the magnetic tangle scale is vanishingly small compared to the scale of the magnetoelastic wave.

5.3 Analytic theory of an inhomogeneous tangle

Returning to the MHD equations, we now separate all quantities into large- and small-scale parts, assuming a scale separation between the typical scales of the wave motions and the magnetic tangle. We denote the wavenumbers associated with these scales by $k_{\rm w}$ and $k_{\rm t}$, respectively, and take $k_{\rm w}/k_{\rm t} \equiv \epsilon$ to be a small parameter. We use the notation $X = \overline{X} + \widetilde{X}$, where $\overline{X}$ is the spatial average of the quantity X over some

intermediate scale that is large compared to the scale of the tangle but small compared to the scale of the wave motion, and $\widetilde{X}$ is the remaining small-scale part.

Denoting equilibrium fields by a subscript zero, we linearise (5.5) and (5.6) about a static equilibrium that satisfies

$$\overline{M}_{0ij} \equiv v_{\mathrm{E}}^2 \delta_{ij} \tag{5.9}$$

for constant v_{E}, while for the moment remaining agnostic about the form of $\widetilde{M}_{0ij}$, but expecting that $\widetilde{M}_0 \sim \overline{M}_0 \sim v_{\mathrm{E}}^2$ because locally there may be an order-unity deviation of the Maxwell stress from its large-scale average. According to this definition, we have $v_{\mathrm{E}}^2 = \frac{1}{3}\overline{v_A^2}$, where $v_A = v_A(\boldsymbol{r})$ is the local Alfvén speed, i.e. the speed at which small-scale Alfvén waves would propagate along the local magnetic field.

Equation (5.9) implies that the equilibrium Maxwell stress has no structure on the scale of wave motions, therefore our treatment precludes the possibility of treating stochastic fields with structure on all length scales. We note that, while it is possible to generate a wide class of synthetic stochastic magnetic fields satisfying (5.9), this assumption may prove too restrictive to model the fields generated by isotropic MHD turbulence. We shall address this and other differences with the turbulent case in a future publication.

The linearised equations are

$$\partial_t^2 \overline{\xi}_i = -\partial_i \overline{P} + v_{\mathrm{E}}^2 \partial_j \partial_j \overline{\xi}_i + \partial_j \overline{\mathcal{D}}_{ij}(\widetilde{M}_0, \widetilde{\xi}) + \nu \partial_j \partial_j \partial_t \overline{\xi}_i, \tag{5.10}$$

$$\partial_t^2 \widetilde{\xi}_i = -\partial_i \widetilde{P} + v_{\mathrm{E}}^2 \partial_j \partial_j \widetilde{\xi}_i + \partial_j \mathcal{D}_{ij}(\widetilde{M}_0, \overline{\xi}) + \partial_j \widetilde{\mathcal{D}}_{ij}(\widetilde{M}_0, \widetilde{\xi}) + \nu \partial_j \partial_j \partial_t \widetilde{\xi}_i. \tag{5.11}$$

5.3.1 The coupling to small scales is always formally non-negligible

Let us first ask whether it is possible to find a regime in which the coupling to small scales caused by the $\partial_j \overline{\mathcal{D}}_{ij}(\widetilde{M}_0, \widetilde{\xi})$ term in (5.10) can be neglected in comparison with the isotropic restoring force $v_{\mathrm{E}}^2 \partial_j \partial_j \overline{\xi}_i$. This would require $k_{\mathrm{t}}\, \widetilde{\xi} \ll k_{\mathrm{w}}\, \overline{\xi}$, i.e., $\widetilde{\xi} \ll \epsilon\, \overline{\xi}$. Under this ordering, there are no terms in (5.11) that can balance $\partial_j \mathcal{D}_{ij}(\widetilde{M}_0, \overline{\xi})$ apart from the viscous term. Such a balance implies $k_{\mathrm{w}} k_{\mathrm{t}} v_{\mathrm{E}}^2 \overline{\xi} \sim \nu k_{\mathrm{t}}^2\, \omega \widetilde{\xi} \ll \nu k_{\mathrm{t}}^2\, \omega \epsilon\, \overline{\xi}$, i.e., $v_{\mathrm{E}}^2 \ll \nu\omega$. Assuming that the large-scale response is indeed elastic gives $\omega \sim k v_{\mathrm{E}}$

as before, which leaves us with $v_{\mathrm{E}} \ll \nu k_{\mathrm{w}}$. However, this is precisely the condition for the magnetoelastic wave's viscous damping rate to be large compared to the wave frequency, a contradiction to the assumed scaling $\omega \sim k v_{\mathrm{E}}$. Hence we find that *the coupling to small scales is always non-negligible if the field is to respond elastically, i.e., if* $\omega \sim k v_{\mathrm{E}}$.

This conclusion is a result of the arithmetics of powers of k in each of the terms in (5.10) and (5.11): essentially, viscosity with its k^2 scaling does not 'switch on' fast enough at larger k to prevent the driving of dynamically important small-scale motions. Quenching them requires a viscous damping that scales with k *faster* than k^2, i.e., a hyperviscosity. In Section 5.4.3.1, we will present numerical experiments with tangle scales hyperviscously damped, which do indeed show precise agreement with (5.8).

That the coupling to small scales should be formally non-negligible is, in fact, clear on intuitive physical grounds; a set of disconnected 'blobs' of magnetic field may well satisfy $\overline{M}_{0ij} \propto \delta_{ij}$, but will not be able to support a net tension on scales much larger than the typical blob size. In this case, the term describing the coupling to small scales $\partial_j \overline{\mathcal{D}}_{ij}(\widetilde{M}_0, \widetilde{\xi})$ in (5.10) will be non-negligible and its effect will be to cancel the large-scale elasticity term, $v_{\mathrm{E}}^2 \partial_j \partial_j \overline{\xi}_i$. This intuition also suggests that the effect of the coupling to small scales should *reduce* the effective elasticity, an expectation that is confirmed by the analysis in the next section. Hyperviscosity modifies this picture by preventing any differential motion on small scales, so the fluid behaves as though the magnetic blobs were connected by rigid rods that allow the large-scale tension to be maintained.

5.3.2 Normal-mode analysis

Some general statements can be made regarding the elastic response of an inviscid tangle by conducting a normal-mode analysis. The essential result of this section is that for a stable field configuration, the frequency of magnetoelastic waves is always decreased from $k_{\mathrm{w}} v_{\mathrm{E}}$ as a result of intermittency of the Maxwell stress.

We expand the displacement field and Maxwell stress in Fourier modes, viz., $\xi_i = \sum_{\boldsymbol{k}} \xi_i(\boldsymbol{k}) e^{i(\boldsymbol{k}\cdot\boldsymbol{r} - \omega t)}$ and $M_{0ij} = \sum_{\boldsymbol{k}} M_{0ij}(\boldsymbol{k}) e^{i\boldsymbol{k}\cdot\boldsymbol{r}}$, define the projection operator $\mathcal{P}_{ij}(\boldsymbol{k}) =$

$\delta_{ij} - k_i k_j/k^2$, and define the matrix elements $A_{ij}(\boldsymbol{k}, \boldsymbol{k}')$ of the operator $\mathcal{P}_{il}\partial_j \mathcal{D}_{lj}\,(M_0,\, \bullet\,)$ in the Fourier basis so that

$$-\,\omega^2 \xi_i(\boldsymbol{k}) = \sum_{\boldsymbol{k}'} A_{ij}(\boldsymbol{k}, \boldsymbol{k}')\xi_j(\boldsymbol{k}'). \tag{5.12}$$

The explicit form of $A_{ij}(\boldsymbol{k}, \boldsymbol{k}')$ can be obtained straightforwardly from the definition (5.6) of $\mathcal{D}$, viz.,

$$\begin{aligned} A_{in}(\boldsymbol{k}, \boldsymbol{k}') = -\mathcal{P}_{il}\,(\boldsymbol{k})\, k_j \,[&-(k_m - k'_m)\, M_{0lj}\,(\boldsymbol{k} - \boldsymbol{k}')\, \mathcal{P}_{mn}\,(\boldsymbol{k}') \\ &+ M_{0lm}\,(\boldsymbol{k} - \boldsymbol{k}')\, k'_m \mathcal{P}_{jn}\,(\boldsymbol{k}') + M_{0jm}\,(\boldsymbol{k} - \boldsymbol{k}')\, k'_m \mathcal{P}_{ln}\,(\boldsymbol{k}')]\,. \end{aligned} \tag{5.13}$$

Importantly, $A_{ij}(\boldsymbol{k}, \boldsymbol{k}')$ is Hermitian, i.e., $A_{ij}(\boldsymbol{k}, \boldsymbol{k}') = [A_{ji}(\boldsymbol{k}', \boldsymbol{k})]^*$[1]. Let us prove this explicitly. The Hermitian conjugate of (5.13) is

$$\begin{aligned} [A_{ni}(\boldsymbol{k}', \boldsymbol{k})]^* = -\mathcal{P}_{nl}\,(\boldsymbol{k}')\, k'_j \,[&-(k'_m - k_m)\, M_{0lj}\,(\boldsymbol{k} - \boldsymbol{k}')\, \mathcal{P}_{mi}\,(\boldsymbol{k}) \\ &+ k_m M_{0lm}\,(\boldsymbol{k} - \boldsymbol{k}')\, \mathcal{P}_{ji}\,(\boldsymbol{k}) + k_m M_{0jm}\,(\boldsymbol{k} - \boldsymbol{k}')\, \mathcal{P}_{li}\,(\boldsymbol{k})]\,. \end{aligned} \tag{5.14}$$

Taking $m \leftrightarrow l$ in the first term of (5.13), and $j \leftrightarrow l$ in the second term, then subtracting (5.14) from (5.13) gives

$$\begin{aligned} &A_{in}(\boldsymbol{k}, \boldsymbol{k}') - [A_{ni}(\boldsymbol{k}', \boldsymbol{k})]^* = \\ &\qquad \mathcal{P}_{il}\,(\boldsymbol{k})\, \mathcal{P}_{nj}\,(\boldsymbol{k}')\, (\delta_{lp}\delta_{jq} - \delta_{lq}\delta_{jp})\, \left(k_q - k'_q\right)\, (k_m - k'_m)\, M_{0pm}\,(\boldsymbol{k} - \boldsymbol{k}')\,, \end{aligned} \tag{5.15}$$

which is zero, as $\delta_{lp}\delta_{jq} - \delta_{lq}\delta_{jp} = \epsilon_{rlj}\epsilon_{rpq}$, and $\epsilon_{rpq}\left(k_q - k'_q\right)(k_m - k'_m)\, M_{0pm}\,(\boldsymbol{k} - \boldsymbol{k}') = 0$ because the equilibrium field must satisfy $\boldsymbol{\nabla} \times (\boldsymbol{\nabla} \cdot \boldsymbol{M}_0) = 0$ (see equation 5.5). Therefore, $A_{ij}(\boldsymbol{k}, \boldsymbol{k}') = [A_{ji}(\boldsymbol{k}', \boldsymbol{k})]^*$, q.e.d.

When $\boldsymbol{k}' = \boldsymbol{k}$, (5.13) reduces to $A_{ij}(\boldsymbol{k}, \boldsymbol{k}) = -M_{0ll}(\boldsymbol{0})k^2\delta_{ij} = -k^2 v_{\mathrm{E}}^2 \delta_{ij}$, so each Fourier mode is subject to the large-scale isotropic restoring force, as in (5.11). Terms with $\boldsymbol{k}' \neq \boldsymbol{k}$ describe the coupling of different Fourier modes: indeed, from (5.13), we see that Fourier modes of the displacement field $\boldsymbol{\xi}$ with wavevectors $\boldsymbol{k}$ and $\boldsymbol{k}'$ are coupled to each other only when $M_{0jm}\,(\boldsymbol{k} - \boldsymbol{k}')$ is non-zero. This observation shows that two large-scale Fourier modes with $\boldsymbol{k}$, $\boldsymbol{k}' \sim k_{\mathrm{w}}$ are not coupled by (5.13), because

[1] This is a consequence of a general result in MHD that the linearised force operator $\boldsymbol{F}$, defined by $\rho_0\, \partial_t^2 \boldsymbol{\xi} = \boldsymbol{F}\,[\boldsymbol{\xi}]$, is self-adjoint (see Kulsrud, 2005), viz., for any $\boldsymbol{\xi}$ and $\boldsymbol{\eta}$, $\int \mathrm{d}^3\boldsymbol{r}\, \boldsymbol{\eta} \cdot \boldsymbol{F}\,[\boldsymbol{\xi}] = \int \mathrm{d}^3\boldsymbol{r}\, \boldsymbol{\xi} \cdot \boldsymbol{F}\,[\boldsymbol{\eta}]$.

$M_{0ij}(\boldsymbol{k}) = 0$ for $\boldsymbol{k} \sim k_\mathrm{w}$, by (5.9). In principle, these large-scale Fourier modes can still be coupled as a result of each of them coupling individually to small scales. The condition for two large-scale Fourier modes to be coupled in this way is the existence of a path in Fourier-space between them, along the wavevectors of M_0. This is precisely the condition for the Fourier modes of M_0 to 'beat' at the magnetoelastic-wave scale — we shall assume such beating is always weak and therefore neglect this possibility in our analysis. Therefore, different large-scale Fourier modes are completely decoupled. We will also assume that large-scale modes with the same $\boldsymbol{k}$ but different spatial directions are decoupled, which is a natural consequence of statistical isotropy. This discussion implies that it is sensible to decompose the large-scale perturbation into its constituent Fourier modes, each of which will independently drive small-scale motions that feed back on the particular large-scale Fourier mode that caused them, but not on any other large-scale modes.

If we take M_0 to have a finite number of non-zero Fourier modes[2], then $A_{ij}(\boldsymbol{k}, \boldsymbol{k}')$ can be considered as a Hermitian *matrix* whose elements $A_{(\boldsymbol{k},i)(\boldsymbol{k}',j)}$ describe the coupling of the mode $\xi_i(\boldsymbol{k})$ with $\xi_j(\boldsymbol{k}')$. Since a large-scale mode may couple to small-scale modes but *not* to other large-scale modes, the matrix representation of A is block diagonal, with each block corresponding to one particular large-scale mode and the small-scale modes to which it couples. Let $\mathcal{A}$ be the block of size $(N+1)\times(N+1)$ corresponding to a particular large-scale mode $\xi_z(\boldsymbol{k}_\mathrm{w})$, taken to be in the z-direction without loss of generality, that is coupled to N small-scale modes. The general structure of $\mathcal{A}$ is

$$\mathcal{A} = \begin{pmatrix} -k_\mathrm{w}^2 v_\mathrm{E}^2 & \boldsymbol{f}^\dagger \\ \boldsymbol{f} & \mathcal{B} \end{pmatrix}. \tag{5.16}$$

where the element $\mathcal{A}_{(\boldsymbol{k}_\mathrm{w},z)(\boldsymbol{k}_\mathrm{w},z)} \equiv A_{zz}(\boldsymbol{k}_\mathrm{w}, \boldsymbol{k}_\mathrm{w}) = -k_\mathrm{w}^2 v_\mathrm{E}^2$ describes the isotropic elastic restoring force on the large-scale mode; $\mathcal{A}_{(\boldsymbol{k},i)(\boldsymbol{k}_\mathrm{w},z)} \equiv A_{iz}(\boldsymbol{k}, \boldsymbol{k}_\mathrm{w}) \equiv f_{(\boldsymbol{k},i)}$ for $|\boldsymbol{k}| \sim k_\mathrm{t}$ is an N-dimensional vector that gives the coupling of the small-scale modes to the large-scale mode; and $\mathcal{A}_{(\boldsymbol{k},i)(\boldsymbol{k}',j)} \equiv A_{ij}(\boldsymbol{k}, \boldsymbol{k}') \equiv \mathcal{B}_{(\boldsymbol{k},i)(\boldsymbol{k}',j)}$ for $|\boldsymbol{k}|, |\boldsymbol{k}'| \sim k_\mathrm{t}$ is the $N \times N$ Hermitian matrix representing the coupling of the relevant small-scale modes to each other. The sizes of these three components are respectively $k_\mathrm{w}^2 v_\mathrm{E}^2$, $k_\mathrm{w} k_\mathrm{t} v_\mathrm{E}^2$ and $k_\mathrm{t}^2 v_\mathrm{E}^2$.

[2]Any field configuration can be approximated to arbitrary accuracy by making this number large.

The $N+1$ normal modes of the system have frequencies ω_μ satisfying $\det\left(\mathcal{A}+\omega_\mu^2 I_{N+1}\right)=0$, where I_{N+1} is the identity matrix of size $N+1$. To leading order in ϵ, the fast, small-scale motions with frequency $\omega_\mu \sim k_\mathrm{t} v_\mathrm{E}$ satisfy

$$\det\begin{pmatrix}\omega_\mu^2 & \boldsymbol{f}^\dagger \\ \boldsymbol{f} & \mathcal{B}+\omega_\mu^2 I_N\end{pmatrix} = \omega_\mu^2 \det\left(\mathcal{B}+\omega_\mu^2 I_N\right)=0 \implies \det\left(\mathcal{B}+\omega_\mu^2 I_N\right)=0, \tag{5.17}$$

so that the fast frequencies are unaffected by the coupling of large and small scales. Equation (5.17) has N solutions for ω_μ^2, which we denote by $\mu=1,...,N$. The remaining slow, large-scale solution with frequency $\omega_0 \sim k_\mathrm{w} v_\mathrm{E}$ represents a magnetoelastic wave, and satisfies

$$\det\begin{pmatrix}\omega_0^2-k_\mathrm{w}^2 v_\mathrm{E}^2 & \boldsymbol{f}^\dagger \\ \boldsymbol{f} & \mathcal{B}\end{pmatrix}=0. \tag{5.18}$$

Defining the block matrix

$$T=\begin{pmatrix}1 & 0 \\ 0 & U\end{pmatrix}, \tag{5.19}$$

where U is the $N\times N$ unitary matrix that diagonalises the matrix $\mathcal{B}$, and using the invariance of the determinant under the basis transformation defined by T, we obtain

$$\det\begin{pmatrix}\omega_0^2-k_\mathrm{w}^2 v_\mathrm{E}^2 & (U\boldsymbol{f})^\dagger \\ U\boldsymbol{f} & \Lambda\end{pmatrix}=0, \tag{5.20}$$

where $\Lambda = U\mathcal{B}U^\dagger = \mathrm{diag}\left(\lambda_1,\ldots,\lambda_N\right) = \mathrm{diag}\left(-\omega_1^2,\ldots,-\omega_N^2\right)$ is the diagonal matrix of eigenvalues of $\mathcal{B}$, which are the N (negative squared) frequencies of the small-scale system. Since Λ is diagonal, the determinant is simple to evaluate, and (5.20) leads to

$$\omega_0^2 = k_\mathrm{w}^2 v_\mathrm{E}^2 - \sum_{\mu=1}^{N} \frac{|\left(U\boldsymbol{f}\right)_\mu|^2}{\omega_\mu^2}. \tag{5.21}$$

Equation (5.21) shows that the effect of the coupling to small-scale motions is to *reduce* the frequency of large-scale waves, as long as the equilibrium is stable, i.e., as long as all $\omega_\mu^2>0$. Furthermore, since the components of U and $\boldsymbol{f}$ are ~ 1 and $\sim k_\mathrm{w}k_\mathrm{t}v_\mathrm{E}^2$ respectively, while $\omega_\mu \sim k_\mathrm{t}v_\mathrm{E}$ for $\mu \geq 1$, the frequency is reduced by a factor of order unity. Physically, this is akin to the elastic response of a tangled ball of elastic string compared to a solid elastic block: a deformation will generally produce a smaller restoring force in the elastic ball because the strings can move relative to each other to reduce the elastic energy (this is not possible in a hyperviscous fluid as small-scale motions are suppressed).

Of course, there is no reason that the right-hand side of (5.21) should be positive; if it is not, (5.21) describes a growing perturbation at large scales. This result shows that it is in principle possible for an *unstable* magnetic tangle to relax via motions on *large* scales rather than small scales. However, we have found no example of this in our numerical studies, where the effect of the tangled field on large-scale modes was always restoring, with instability proceeding only via motions at small scales.

The eigenvectors of $\mathcal{A}$ can be obtained to leading order by noting that $\mathcal{A}\left(0, \boldsymbol{e}_\mu\right)^{\mathrm{T}} = \lambda_\mu \left(0, \boldsymbol{e}_\mu\right)^{\mathrm{T}} + O\left(\epsilon\right)$, where $\boldsymbol{e}_\mu$ is the μth eigenvector of the matrix $\mathcal{B}$. The final eigenvector with associated frequency ω_0 is uniquely constrained by orthogonality to be $\left(1, \boldsymbol{0}\right)^{\mathrm{T}} + O\left(\epsilon\right)$. Therefore, a magnetoelastic wave consists primarily of a large scale oscillation, together with small-amplitude (vanishing as $\epsilon \to 0$), slow (frequency ω_0), small-scale oscillations. Physically, these small-scale oscillations represent the rearrangement of small-scale structures to reduce the elastic energy and, therefore, the large-scale tension. Despite having small amplitude, these small-scale motions are by no means negligible – as we have found, the magnetoelastic wave frequency is changed by a factor of order unity in their absence.

5.3.3 The First-Order Smoothing Approximation (FOSA)

In this section, we describe an approximate method to obtain the wave frequency ω_0 in terms of statistical properties of the magnetic tangle, by assuming that the coupling between different small-scale Fourier modes is small. This approximation is equivalent to neglecting the term $\partial_j \widetilde{\mathcal{D}}_{ij}(\widetilde{M}_0, \widetilde{\xi})$ in (5.11); in the context of large-scale kinematic dynamo theory, it is often called the First-Order Smoothing Approximation (FOSA) or the Second-Order Correlation Approximation (SOCA). In the dynamo-theory context, it is employed in the small-scale part of the induction equation to neglect a similar 'fluctuating part of the product of two fluctuations' term, allowing the small-scale induction equation to be solved for the small-scale magnetic field, which can then be used to compute the growth of the large-scale field (for a review, see Rincon, 2019). Our use of this approximation is directly complementary: instead of solving an equation for the small-scale magnetic field given a prescribed flow, we use the FOSA to solve an

equation for a small-scale flow given a known small-scale magnetic-field configuration, M_0.

Much like in the dynamo-theory context, where the FOSA is rigorously justified only when either the velocity correlation time is small, or Rm $\ll 1$, the assumption of weak coupling between modes is unlikely to be well satisfied in any real magnetic tangle. However, the FOSA remains a useful tool, and we show in Section 5.4 that it provides a remarkably good description of numerical simulations of large-scale waves in tangled-magnetic-field equilibria.

Under the FOSA, we neglect all off-diagonal terms of the matrix $\mathcal{B}$ in (5.18), so that the coupling of large and small scales is retained, but the small-scale modes do not couple to each other. This simplifies (5.21) considerably because now $U = I_N$ and $\omega_\mu = k_\mu v_\mathrm{E}$ for $\mu = 1, ..., N$, where k_μ are the wavenumbers of the N small-scale modes, so that (5.21) becomes

$$\omega_0^2 = k^2 v_\mathrm{E}^2 - \sum_{\boldsymbol{k}' \neq \boldsymbol{k}_\mathrm{w}} \frac{A_{zp}(\boldsymbol{k}_\mathrm{w}, \boldsymbol{k}') A_{pz}(\boldsymbol{k}', \boldsymbol{k}_\mathrm{w})}{k'^2 v_\mathrm{E}^2}. \tag{5.22}$$

With $i \to z$ and $\boldsymbol{k} \to \boldsymbol{k}_\mathrm{w}$, (5.13) gives

$$\begin{aligned} A_{zn}(\boldsymbol{k}_\mathrm{w}, \boldsymbol{k}') = -\mathcal{P}_{zl}\left(\boldsymbol{k}_\mathrm{w}\right) k_{\mathrm{w}j} \big[&- \left(k_{\mathrm{w}m} - k'_m\right) M_{0lj}\left(\boldsymbol{k}_\mathrm{w} - \boldsymbol{k}'\right) \mathcal{P}_{mn}\left(\boldsymbol{k}'\right) \\ &+ M_{0lm}\left(\boldsymbol{k}_\mathrm{w} - \boldsymbol{k}'\right) k'_m \mathcal{P}_{jn}\left(\boldsymbol{k}'\right) + M_{0jm}\left(\boldsymbol{k}_\mathrm{w} - \boldsymbol{k}'\right) k'_m \mathcal{P}_{ln}\left(\boldsymbol{k}'\right) \big]. \end{aligned} \tag{5.23}$$

With $|\boldsymbol{k}'| \sim k_\mathrm{t}$, the first term in the square brackets vanishes to leading order in ϵ because $k'_m \mathcal{P}_{mn}\left(\boldsymbol{k}'\right) = 0$. Relabelling $n \to p$, then swapping $m \leftrightarrow j$ and $m \leftrightarrow l$ in the second term, we obtain

$$\begin{aligned} A_{zp}(\boldsymbol{k}_\mathrm{w}, \boldsymbol{k}') &= -\mathcal{P}_{zl}\left(\boldsymbol{k}_\mathrm{w}\right) k_{\mathrm{w}m} M_{0lj}\left(\boldsymbol{k}_\mathrm{w} - \boldsymbol{k}'\right) k'_j \mathcal{P}_{mp}\left(\boldsymbol{k}'\right) \\ &\quad - \mathcal{P}_{zm}\left(\boldsymbol{k}_\mathrm{w}\right) k_{\mathrm{w}j} M_{0jl}\left(\boldsymbol{k}_\mathrm{w} - \boldsymbol{k}'\right) k'_l \mathcal{P}_{mp}\left(\boldsymbol{k}'\right)', \\ &= -k_{\mathrm{w}n} k'_l \mathcal{P}_{zq}\left(\boldsymbol{k}_\mathrm{w}\right) \mathcal{P}_{mp}\left(\boldsymbol{k}'\right) \left(\delta_{nm}\delta_{jq} + \delta_{nj}\delta_{mq}\right) M_{0lj}\left(\boldsymbol{k}_\mathrm{w} - \boldsymbol{k}'\right). \end{aligned} \tag{5.24}$$

An analogous expression for $A_{pz}(\boldsymbol{k}', \boldsymbol{k}_\mathrm{w})$ can be obtained directly from (5.14), but the derivation is much more involved. Instead, we can use the fact that A is Hermitian:

$$\begin{aligned} A_{pz}(\boldsymbol{k}', \boldsymbol{k}_\mathrm{w}) &= \left[A_{zp}(\boldsymbol{k}_\mathrm{w}, \boldsymbol{k}')\right]^* \\ &= -k_{\mathrm{w}n} k'_l \mathcal{P}_{zq}\left(\boldsymbol{k}_\mathrm{w}\right) \mathcal{P}_{mp}\left(\boldsymbol{k}'\right) \left(\delta_{nm}\delta_{jq} + \delta_{nj}\delta_{mq}\right) M_{0lj}\left(\boldsymbol{k}' - \boldsymbol{k}_\mathrm{w}\right) \\ &= -k_{\mathrm{w}n} k'_j \mathcal{P}_{zm}\left(\boldsymbol{k}_\mathrm{w}\right) \mathcal{P}_{qp}\left(\boldsymbol{k}'\right) \left(\delta_{nq}\delta_{lm} + \delta_{nl}\delta_{mq}\right) M_{0lj}\left(\boldsymbol{k}' - \boldsymbol{k}_\mathrm{w}\right), \end{aligned} \tag{5.25}$$

where to obtain the final expression we have swapped $l \leftrightarrow j$ and $q \leftrightarrow m$. With (5.24) and (5.25), (5.22) becomes:

$$\omega_0^2 = k_{\mathrm{w}}^2 v_{\mathrm{E}}^2 - \left(\delta_{nm}\delta_{jz} + \delta_{nj}\delta_{mz}\right)\left(\delta_{zl'}\delta_{n'q'} + \delta_{l'n'}\delta_{zq'}\right) k_{\mathrm{w}n} k_{\mathrm{w}n'} R_{mq'jl'}, \tag{5.26}$$

where

$$R_{mq'jl'} = \sum_{\boldsymbol{k}'} \frac{k_l' k_{j'}'}{k'^2 v_{\mathrm{E}}^2} \mathcal{P}_{q'm}\left(\boldsymbol{k}'\right) \widetilde{M}_{lj}\left(-\boldsymbol{k}'\right) \widetilde{M}_{l'j'}\left(\boldsymbol{k}'\right), \tag{5.27}$$

to leading order in ϵ. The rank-four tensor $R_{pq'jl'}$ is a statistical property (in the sense of volume averaging) of the magnetic tangle. Since we have assumed statistical isotropy, the most general form it can take is $R_{pq'jl'} = a\delta_{pq'}\delta_{jl'} + b\delta_{pj}\delta_{q'l'} + c\delta_{pl'}\delta_{q'j}$. Noting from (5.27) that $R_{pq'jl'}$ is symmetric in p and q' and vanishes on contraction of p with l', we find

$$R_{pq'jl'} = \frac{1}{30 v_{\mathrm{E}}^4}\left(4\delta_{l'j}\delta_{pq'} - \delta_{l'p}\delta_{jq'} - \delta_{l'q'}\delta_{jp}\right)\left(\left\langle P_0^2\right\rangle - \left\langle P_0\right\rangle^2\right). \tag{5.28}$$

where we have used the equilibrium condition $k_j M_{0ij}\left(\boldsymbol{k}\right) + k_i P_0\left(\boldsymbol{k}\right) = 0$, where P_0 is the equilibrium total pressure distribution, and identified

$$\sum_{\boldsymbol{k}'} \left|\widetilde{P}_0\left(\boldsymbol{k}'\right)\right|^2 = \left(\left\langle P_0^2\right\rangle - \left\langle P_0\right\rangle^2\right), \tag{5.29}$$

where angled brackets indicate spatial averages. On substitution of this result into (5.26) and contraction of the many Kronecker deltas, we finally arrive at

$$\omega_0^2 = k^2 v_{\mathrm{E}}^2\left(1 - \chi\right), \tag{5.30}$$

where

$$\chi = \frac{1}{5 v_{\mathrm{E}}^4}\left(\left\langle P_0^2\right\rangle - \left\langle P_0\right\rangle^2\right). \tag{5.31}$$

We therefore find that under the FOSA, the effect of the small-scale structure of the magnetic tangle is to reduce the frequency of magnetoelastic waves by an amount proportional to the variance of the total pressure. This is really a statement about the magnetic field, since the total pressure must balance the magnetic tension force in equilibrium, so (5.31) shows that *more intermittent magnetic fields are less elastic*. This is precisely in agreement with the intuitive reasoning of Section 5.3.1, where we

argued that a field configuration consisting of disconnected magnetic 'blobs' would not support a large-scale tension – such a field would have a large value of χ.

In the special case of a force-free magnetic tangle, i.e., when only magnetic pressure balances the magnetic tension, $P_0 = B_0^2/2$, so

$$\chi = \frac{9}{20}\left(\frac{\langle B_0^4\rangle}{\langle B_0^2\rangle^2} - 1\right). \tag{5.32}$$

5.3.4 Magnetoelastic waves in a viscous fluid

In this section, we develop a theory for magnetoelastic waves propagating through a viscous fluid. As we found in Section 5.3.2, a magnetoelastic wave in an inviscid fluid is a large-scale oscillation, accompanied by slow ($\omega \sim k_{\rm w} v_{\rm E}$), small-amplitude oscillations associated with the relaxation of small-scale structures in response to the large-scale tension. In the viscous case, these small-scale structures will be damped by viscosity; their presence therefore results in an anomalous viscous damping of magnetoelastic waves.

For definiteness, we take the initial condition to be a large-scale velocity perturbation u_z along z with wavevector $\boldsymbol{k}_{\rm w}$. We solve the inital value problem by taking a Laplace transform in time:

$$p^2\xi_z(\boldsymbol{k}_{\rm w}) - u_z\left(\boldsymbol{k}_{\rm w}, t=0\right) = -k_{\rm w}^2 v_{\rm E}^2 \xi_z(\boldsymbol{k}_{\rm w}) + \sum_{\boldsymbol{k}'} A_{zj}(\boldsymbol{k}_{\rm w}, \boldsymbol{k}')\xi_j(\boldsymbol{k}') + \nu k_{\rm w}^2 p \xi_z(\boldsymbol{k}_{\rm w}). \tag{5.33}$$

where p is the Laplace conjugate variable to time (analogous to $i\omega$)

In the FOSA, an inititally unperturbed small-scale mode with wavenumber $k' \gg k_{\rm w}$ satisfies

$$p^2\xi_j(\boldsymbol{k}') = -v_{\rm E}^2 k'^2 \xi_j(\boldsymbol{k}') + A_{jz}(\boldsymbol{k}', \boldsymbol{k}_{\rm w})\xi_z(\boldsymbol{k}_{\rm w}) + \nu k'^2 p \xi_j(\boldsymbol{k}'). \tag{5.34}$$

Solving this algebraic equation for $\xi_j(\boldsymbol{k}')$, and substituting into (5.33), we obtain

$$\begin{aligned} p^2\xi_z(\boldsymbol{k}_{\rm w}) - u_z\left(\boldsymbol{k}_{\rm w}, t=0\right) = &-k_{\rm w}^2 v_{\rm E}^2 \xi_z(\boldsymbol{k}_{\rm w}) \\ &+ \sum_{\boldsymbol{k}'} \frac{A_{zj}(\boldsymbol{k}_{\rm w}, \boldsymbol{k}')A_{jz}(\boldsymbol{k}', \boldsymbol{k}_{\rm w})}{p^2 + v_{\rm E}^2 k'^2 + \nu k'^2 p}\xi_z(\boldsymbol{k}_{\rm w}) + \nu k_{\rm w}^2 p \xi_z(\boldsymbol{k}_{\rm w}). \end{aligned} \tag{5.35}$$

where the sum is over all small-scale modes.

With $p \sim \omega_0 \sim k_\mathrm{w} v_\mathrm{E}$, the p^2 in the denominator of the coupling term in (5.35) is small compared to $v_\mathrm{E}^2 k'^2$.[3] Neglecting it, we can use (5.24) and (5.25) analogously to the inviscid case to write

$$p^2 \xi_z(\boldsymbol{k}_\mathrm{w}) - u_z\left(\boldsymbol{k}_\mathrm{w}, t=0\right) = -k_\mathrm{w}^2 v_\mathrm{E}^2 \xi_z(\boldsymbol{k}_\mathrm{w}) + \frac{\chi}{1+\nu p/v_\mathrm{E}^2}\xi_z(\boldsymbol{k}_\mathrm{w}) + \nu k_\mathrm{w}^2 p \xi_z(\boldsymbol{k}_\mathrm{w}). \quad (5.36)$$

Note that, as predicted in Section 5.3.1, the term representing coupling to small scales remains finite as $\epsilon \to 0$, and can only be neglected when $\nu p/v_\mathrm{E}^2 \sim \nu k_\mathrm{w}^2/k_\mathrm{w} v_\mathrm{E} \gg 1$, i.e., when wave motions are strongly damped. In contrast, in the hyperviscous case, the number of powers of k' is increased in the viscosity term in the denominator of the coupling term in (5.35), so that it is sufficient for *small* scales to be strongly damped for the coupling term to be negligible as $\epsilon \to 0$. We therefore recover the simple wave equation (5.7) in the hyperviscous case, as predicted in Section 5.3.1.

Finally, we invert the Laplace transform using Cauchy's residue theorem. The solution is a sum of Laplace modes $\overline{u}_i(t) = \left(\sum_n A_n e^{p_n t}\right)\overline{u}_i(0)$ with amplitudes

$$A_n = \mathrm{Res}\left[\frac{p}{D(p)}, p \to p_n\right], \quad (5.37)$$

where 'Res' denotes the residue and $\{p_n\}$ are the roots of the dispersion relation

$$D(p_n) \equiv p_n^2 + \left(1 - \frac{\chi}{1+\nu p_n/v_\mathrm{E}^2}\right) v_\mathrm{E}^2 k^2 + \nu k^2 p_n = 0. \quad (5.38)$$

It is instructive to consider the case where the viscous damping rate is finite but small compared to the wave frequency, i.e., $\hat{\nu} \equiv \nu k_\mathrm{w}/v_\mathrm{E} \ll 1$. The solutions of (5.38) in this

[3] The p^2 is only non-negligible if the large-scale Fourier mode under consideration has motions on the *fast* timescale, i.e., $p \sim k_\mathrm{t} v_\mathrm{E}$. In the inviscid case, we found that a purely large-scale perturbation is *almost* a normal mode – the true (slow) normal mode is a large-scale perturbation with accompanying small-amplitude (vanishing as $\epsilon \to 0$) small-scale perturbations. Therefore, a purely large-scale initial perturbation can be decomposed into the slow normal mode and small-amplitude fast modes. Similarly, fast modes are *almost* pure small-scale motions, but do have an accompanying small-amplitude *large*-scale motion. This means that in principle, there will be a fast, large-scale response to an imposed perturbation at large scales, but its amplitude will be vanishingly small compared to the amplitude of the slow response. In the presence of viscosity, we do not expect this conclusion to be modified – intuitively, viscosity should further suppress the amplitude of fast motions. In Appendix 5.B, we verify this conclusion by explicitly showing that the amplitude of any Laplace mode with $p \sim k_\mathrm{t} v_\mathrm{E}$ vanishes in the limit $\epsilon \to 0$.

limit are

$$p_1 = +iv_{\rm E}k_{\rm w}\sqrt{1-\chi} - \frac{1}{2}\nu k_{\rm w}^2\left(1+\chi\right) + O\left(\hat{\nu}^2\right), \tag{5.39}$$

$$p_2 = -iv_{\rm E}k_{\rm w}\sqrt{1-\chi} - \frac{1}{2}\nu k_{\rm w}^2\left(1+\chi\right) + O\left(\hat{\nu}^2\right), \tag{5.40}$$

$$p_3 = -v_{\rm E}^2/\nu + O\left(\hat{\nu}\right), \tag{5.41}$$

with corresponding amplitudes

$$A_1 = \frac{1}{2} + O\left(\hat{\nu}\right), \quad A_2 = \frac{1}{2} + O\left(\hat{\nu}\right), \quad A_3 = \chi\hat{\nu}^2 + O\left(\hat{\nu}^3\right). \tag{5.42}$$

In the first two solutions, p_1 and p_2, given by (5.39) and (5.40), we find the wave modes of the previous section, but now with a damping rate that is larger than in the perfectly homogeneous case by a factor of $1+\chi$. This increased damping rate is expected: it is a consequence of the viscous damping of the small-scale motions associated with magnetoelastic waves. It may appear odd that a damping associated with small-scale motions has a rate $\propto \nu k_{\rm w}^2$, especially as the condition $\hat{\nu} \ll 1$ does not exclude the possibility of fast, small scale motions being over-damped by viscosity. The resolution is that the small-scale motions associated with a magnetoelastic wave are *slow* (frequency $\sim k_{\rm w}v_{\rm E}$), not fast, and therefore they are not viscously dominated when $\hat{\nu} \ll 1$, as $\nu\partial_j\partial_j\partial_t\widetilde{\xi}_i \sim \nu k_{\rm t}^2\omega_0\widetilde{\xi} \sim \hat{\nu}k_{\rm t}^2v_{\rm E}^2\widetilde{\xi} \ll v_{\rm E}^2\partial_j\partial_j\widetilde{\xi}_i \sim k_{\rm t}^2v_{\rm E}^2\widetilde{\xi}$. These motions satisfy the balance $v_{\rm E}^2\partial_j\partial_j\widetilde{\xi}_i \sim \partial_j\mathcal{D}_{ij}(\widetilde{M}_0,\overline{\xi})$, which gives $\widetilde{\xi} \sim \epsilon\overline{\xi}$. The rate of energy dissipation associated with them is therefore $\sim \nu k_{\rm t}^2\omega_0^2\widetilde{\xi^2} \sim \nu k_{\rm w}^2\omega_0^2\overline{\xi}$, which is consistent with the anomalous damping rate in (5.39) and (5.40).

The third mode, p_3, given by (5.41), describes the case where the slow, small-scale motions associated with the waves *do* become viscously-dominated, so obey the balance $v_{\rm E}^2\partial_j\partial_j\widetilde{\xi}_i \sim k_{\rm t}^2\partial_t\widetilde{\xi}$, giving a damping rate of $v_{\rm E}^2/\nu$. As above, these motions become viscously-dominated only when $\hat{\nu} \sim 1$, explaining the vanishing amplitude of this mode when $\hat{\nu} \ll 1$[4].

[4]In the FOSA, there is only one mode of this type because all overdamped small-scale motions relax at the same rate, $v_{\rm E}^2/\nu$. This is because, in the notation of Section 5.3.2, the equation of motion of the over-damped, small-scale system is $\nu k^2\partial_t\widetilde{\xi}_i(\boldsymbol{k}) = \sum_{(\boldsymbol{k}',j)}\mathcal{B}_{(\boldsymbol{k},i)(\boldsymbol{k}',j)}\widetilde{\xi}_j(\boldsymbol{k}')$. In the FOSA, $\mathcal{B}$ is diagonal, with elements $\mathcal{B}_{(\boldsymbol{k},i)(\boldsymbol{k},i)} \propto k^2$, so that the viscous relaxation time has no k dependence. In the exact system, $\mathcal{B}$ is not diagonal, lifting the degeneracy. Then, p_3 is replaced by many Laplace modes for each of the possible viscous relaxation timescales, all with frequencies $\sim v_{\rm E}^2/\nu$.

5.4 Numerical study

5.4.1 Ideal instability of tangled magnetic field equilibria

The analysis in the preceeding sections has been idealised because real tangled magnetic equilibria are generically *unstable*, even to ideal perturbations (Er-Riani *et al.*, 2014; East *et al.*, 2015). The instability typically proceeds via motions at small scales that are fast compared to the magnetoelastic wave motions, but are inhibited by the presence of viscosity. However, the growth rate associated with viscously-dominated, small-scale unstable modes is $\sim v_{\rm E}^2/\nu$, which becomes comparable with the wave frequency when $\hat{\nu} = \nu k_{\rm w}^2/k_{\rm w}v_{\rm E} \sim 1$, i.e., when magnetoelastic waves are strongly damped by viscosity. The question then arises as to whether any static, tangled-magnetic-field equilibrium will persist long enough for waves to propagate through it, even with strong viscosity. In fact, we have found in our numerical study that when the equilibrium state is a *linear force-free* magnetic field (see next section) the growth rate of the instability is sufficiently slow for the equilibrium configuration to persist for many wave periods.

The existence of an instability of linear force-free magnetic fields in ideal MHD has only recently been appreciated, and indeed many inaccurate statements have historically been presented in the literature. For the interested reader, we present a short review of this instability in Appendix 5.A.

5.4.2 Simulation setup

In order to test the analytic predictions derived in the previous sections, we conduct simulations of standing magnetoelastic waves on periodic, linear, force-free magnetic-field equilibria with different values of the parameter χ.

The linear force-free magnetic field condition is $\boldsymbol{\nabla}\times\boldsymbol{B} = \alpha\boldsymbol{B}$, where α is a constant. Taking the curl and using $\boldsymbol{\nabla}\cdot\boldsymbol{B} = 0$, we get a Helmholtz equation for the magnetic field, $\nabla^2\boldsymbol{B} = -\alpha^2\boldsymbol{B}$, which shows that the modes in the Fourier expansion of $\boldsymbol{B}$ must all have $|\boldsymbol{k}| = \alpha$. The linear force-free equilibrium must then have $i\boldsymbol{k}\times\boldsymbol{B}_{\boldsymbol{k}} = \alpha\boldsymbol{B}_{\boldsymbol{k}}$, or

$$\hat{\boldsymbol{k}}\times\mathrm{Re}\left(\boldsymbol{B}_{\boldsymbol{k}}\right) = \mathrm{Im}\left(\boldsymbol{B}_{\boldsymbol{k}}\right). \tag{5.43}$$

To generate tangled magnetic equilibria, we take $\boldsymbol{k} = 2\pi\,(12, 6, 0)^{\mathrm{T}}$, together with all its permutations and negations. This means that the magnetic-field structure is periodic on a scale of 1/6 of the box size, which ensures the scale separation between the box scale and the scale of the tangled field. We then generate real vectors $\mathrm{Re}\,(\boldsymbol{B}_{\boldsymbol{k}})$ subject to the condition $\mathrm{Re}\,(\boldsymbol{B}_{\boldsymbol{k}}) = \mathrm{Re}\,(\boldsymbol{B}_{-\boldsymbol{k}})$, so that $\boldsymbol{B}$ is real, and to (5.43), so that it is force-free, using a numerical optimisation procedure to ensure $\overline{M}_{0ij} \propto \delta_{ij}$ and to produce fields with different values of the parameter χ[5]. The magnetic-field configurations thus obtained with $\chi = 0.17$ and $\chi = 0.98$ are shown in Figure 5.1. Curiously, we have been unable to generate a field with $\chi > 1$ using this optimisation procedure, which is the condition for the large-scale mode to become unstable in the FOSA.

For each equilibrium configuration, we introduce a sinusoidal velocity shear $\boldsymbol{u} = 0.05\,\langle v_A^2\rangle^{1/2}\sin(2\pi x/\lambda)\hat{\boldsymbol{z}}$, where $\lambda = 2\pi/k_{\mathrm{w}}$ is the box size and $\langle v_A^2\rangle^{1/2} = \langle B_0^2\rangle^{1/2} = \sqrt{3}\,v_{\mathrm{E}}$ is the r.m.s. Alfvén speed, and we measure the evolution of the amplitude of this mode in the Fourier representation of $\boldsymbol{u}$.

The 3D, incompressible MHD equations are solved using the Dedalus[6] code (Burns *et al.*, 2020) at 128^3 resolution (padded for de-aliasing according to the 2/3 rule). We take the resistivity $\eta = 0$, and thus our simulations are only valid in describing the evolution at early times when the small-scale instability of the equilibrium field configuration has not yet developed and hence the magnetic field structure is still well-resolved.

[5]This process of generating magnetic equilibria is not guaranteed to produce fields that are statistically isotropic, despite satisfying $\overline{M}_{0ij} \propto \delta_{ij}$. As a consequence, we calculate χ directly from the tensor R defined in Section 5.3.3, rather from the isotropic expression (5.31). Anisotropy on small-scales could in principle cause large-scale modes with the same $\boldsymbol{k}$ but different spatial directions to couple. However, for all configurations that we have tested the off-diagonal terms of the matrix $\sum_{\boldsymbol{k}'} A_{ip}(\boldsymbol{k},\boldsymbol{k}')A_{pr}(\boldsymbol{k}',\boldsymbol{k})$ are small (for the fields presented in Figure 5.1, they are small compared to the diagonal terms by a factor of 2×10^{-3} for $\chi = 0.17$ and 3×10^{-4} for $\chi = 0.98$). We have also checked that in our simulations, negligible energy is transferred into any large-scale mode other than the originally perturbed one.

[6]Dedalus is available at http://dedalus-project.org

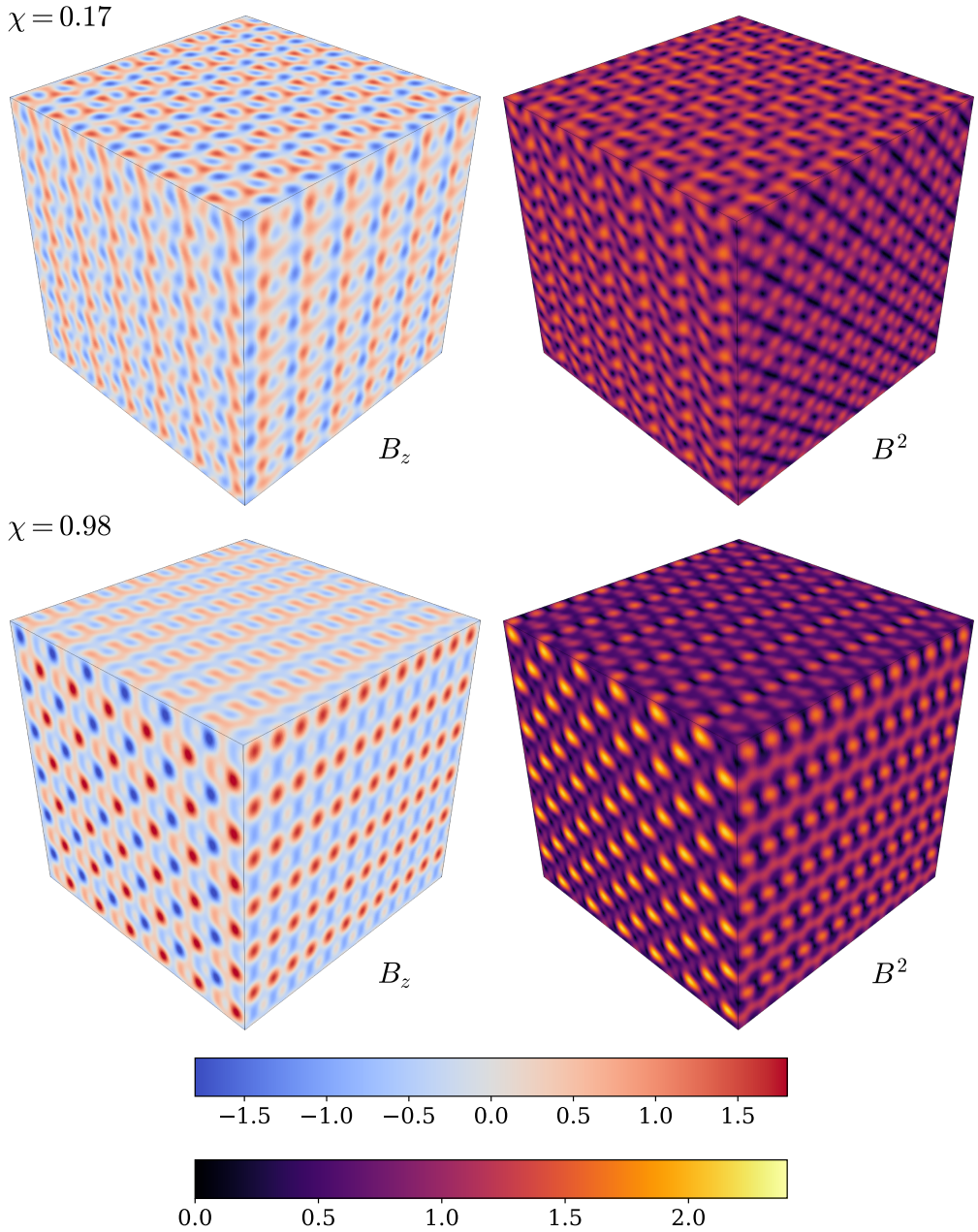

Figure 5.1: Magnetic-field structure of two force-free equilibria resulting from the numerical optimisation procedure described in Section 5.4.2. The upper colour bar describes the plots of B_z, while the lower colour bar describes the plots of B^2, in units of $\langle v_A^2 \rangle^{1/2}$ and $\langle v_A^2 \rangle$ respectively. Note that the configuration with $\chi = 0.17$ has smaller variation in the magnetic field strength than the configuration with $\chi = 0.98$. Indeed, the $\chi = 0.98$ configuration is hardly 'tangled' at all; it more closely resembles a collection of magnetic 'blobs' (cf. the discussion in Section 5.3.1).

5.4.3 Results

5.4.3.1 Hyperviscous regime

As the simplest 'control' case, we first present the results of simulations with hyperviscosity, i.e., with the viscous dissipation term in (5.1) replaced by $\nu\nabla^6\boldsymbol{u}$, with the tangled magnetic field at a smaller scale than the hyperviscous cutoff scale. As shown in Section 5.3.1, the small-scale motions cannot develop in this regime, therefore we expect an imposed sinusoidal shear flow to evolve according to (5.7), which might now be called the ZOSA prediction (Zeroth-Order Smoothing Approximation), independently of the small-scale structure of the magnetic field. This is indeed observed, as shown in Figure 5.2, where the evolution of the wave amplitude is plotted for $\chi = 0.17$ and $\chi = 0.98$. There is a small relative deviation of $\sim 10^{-3}$ between the two curves and the prediction of the ZOSA (5.7) that is not visible on this plot.

5.4.3.2 Effect of increasing χ

We now turn to the case of Laplacian viscosity. Figure 5.3 shows the wave evolution for a number of different values of χ, at a range of Laplacian viscosities. When the viscosity is not very small, the evolution is qualitatively in agreement with the FOSA theory developed in Section 5.3.4, i.e., a larger χ results in a longer wave period and increased damping. At small viscosity, the evolution is dominated by the onset of the instability of the periodic force-free field, which results in a transfer of energy from small to large scales via mergers of magnetic structures (see Appendix 5.A.3) that disrupts the waves (this process is not well-resolved in our simulations). We note that the time taken for the instability to develop becomes smaller as χ increases.

5.4.3.3 Comparison with the analytic theory at different viscosities

Figure 5.4 shows the evolution of the wave for $\chi = 0.51$ and for four different Laplacian viscosities, with the predictions of the ZOSA and FOSA plotted for comparison. We find that the FOSA gives a better prediction in each case, with excellent agreement for large viscosities, correctly capturing the longer wave period and the increased damping observed.

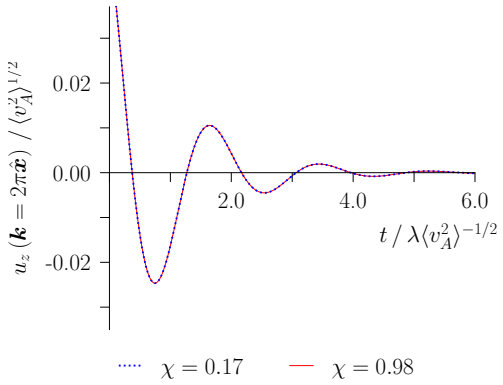

Figure 5.2: Wave amplitude against time for the field configurations with $\chi = 0.17$ and $\chi = 0.98$ (see Figure 5.1 for the structure of these fields) and using sixth-order hyperviscosity with $\nu_6 k_{\mathrm{w}}^6 = (0.048\lambda\langle v_A^2\rangle^{1/2})k_w^2$. Despite the difference in the magnetic-field configuration, both fields show an almost identical response to the imposed wave perturbation and evolve according to (5.7), as anticipated by the theory in Section 5.3.1.

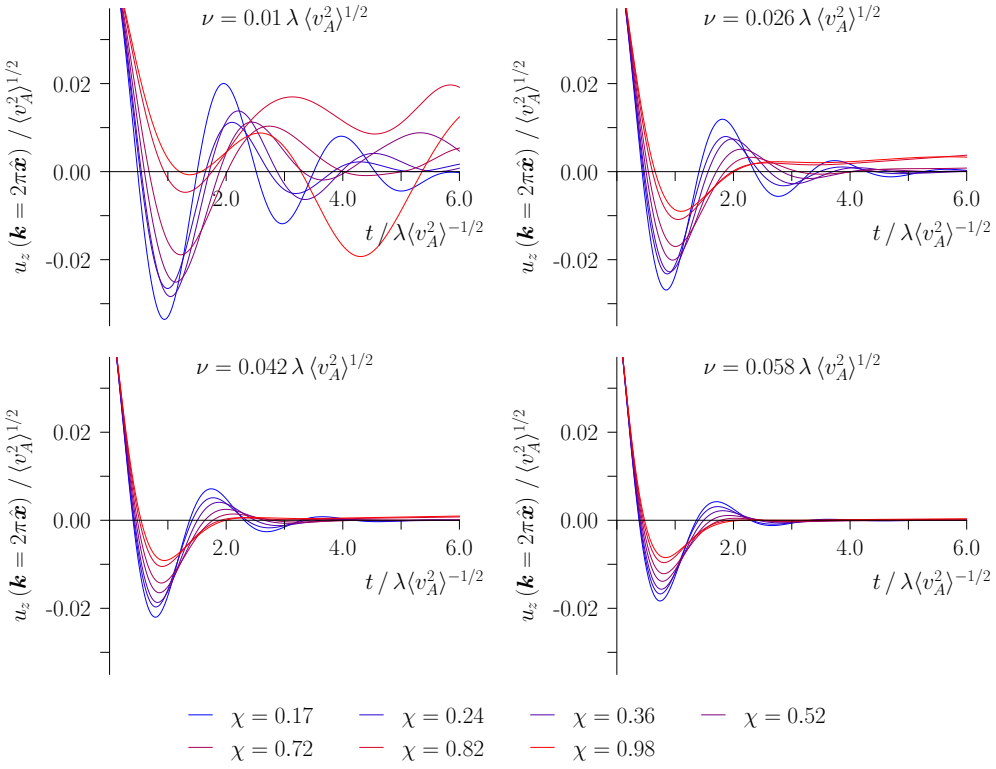

Figure 5.3: Wave amplitude against time for a range of values of χ, plotted for different viscosities. At large viscosity, fields with larger values of χ support waves with larger period and increased damping, in accordance with Section 5.3.4. At small viscosities, the evolution is dominated by the onset of the instability of the equilibrium field (see Appendix 5.A).

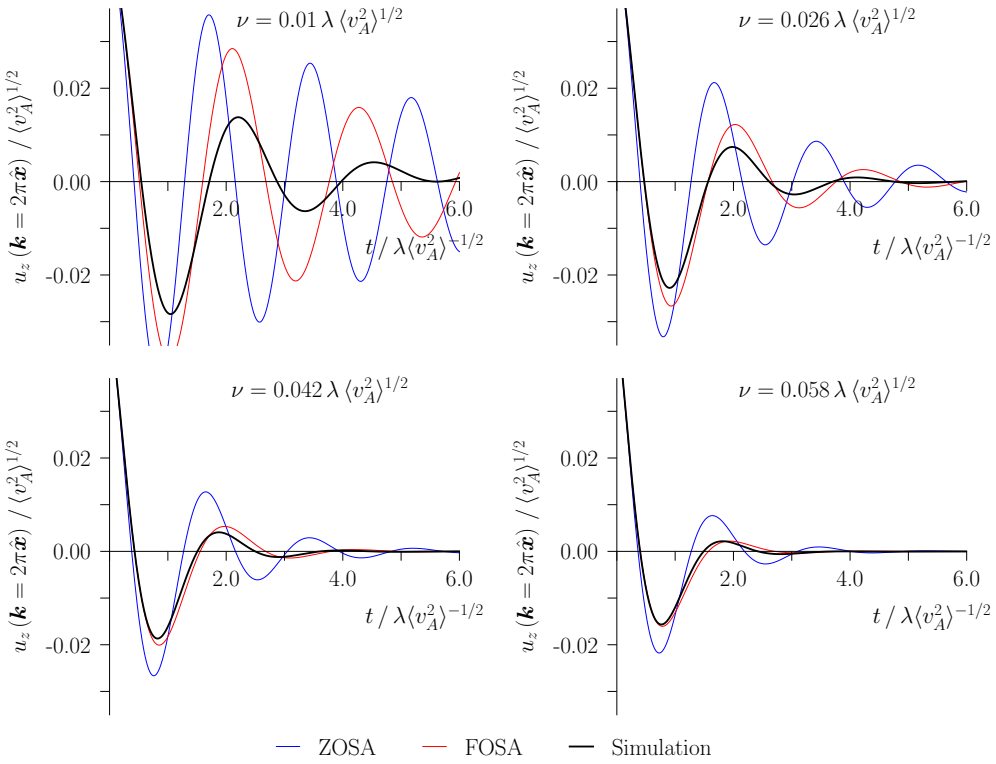

Figure 5.4: Wave amplitude against time for $\chi = 0.51$ at a range of viscosities (black), together with the predictions of the ZOSA, (equation 5.7; blue), i.e., neglecting all small-scale motions, and the FOSA (equation 5.37; red).

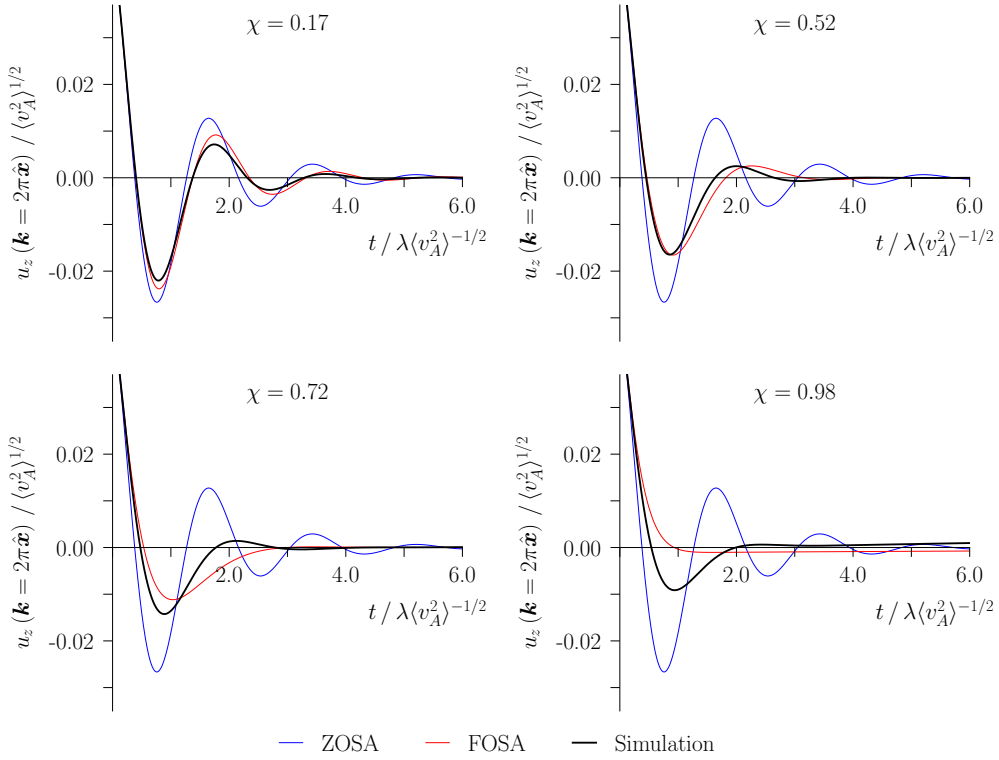

Figure 5.5: Wave amplitude against time for different values of χ at fixed viscosity $\nu = 0.03\lambda\langle v_A^2\rangle^{1/2}$, together with the predictions of the ZOSA, (equation 5.7; blue), i.e., neglecting all small-scale motions, and the FOSA (equation 5.37; red).

5.4.3.4 Comparison with the analytic theory at different values of χ

Finally, Figure 5.5 shows the evolution of the wave for different values of χ at fixed viscosity, $\nu = 0.03L\langle v_A\rangle^{1/2}$, with the predictions of the ZOSA and FOSA theories plotted for comparison. Again, we find that the FOSA gives a better prediction in each case, although at large values of χ it fails to predict the numerical result accurately.

5.4.4 Discussion

Our numerical experiments show that the analytical theory presented in Section 5.3.4 gives a good description of the dynamics of magnetoelastic waves either in the limit of small χ or of large viscosity. This is a natural result, as the FOSA assumes greatly simplified small-scale dynamics. Describing the small-scale motions precisely is most important when viscosity is small, because they are less-strongly damped, and when χ

is large, because χ encodes the strength of the coupling of large and small scales.

5.5 Conclusion

In this chapter, we have studied the large-scale elastic dynamics of MHD equilibrium states with statistically homogeneous and isotropic tangled magnetic-field configurations. We have extended the model presented by Moffatt (1986) to consider how the inevitable small-scale inhomogeneity of the magnetic field structure modifies the dynamics. We have found that in the idealised case of a stable equilibrium state, the frequency of magnetoelastic waves is necessarily reduced as a result of accounting for the inhomogeneity, as a result of relaxation of small-scale structures, which reduces the elastic tension. By employing the First-Order Smoothing Approximation (FOSA), where couplings between small-scale motions are neglected, we have been able to derive a dispersion relation for magnetoelastic waves in terms of statistical properties of the magnetic-field structure. A key finding is that more intermittent fields are less elastic (see equation 5.32), with the controlling parameter being the variance of the total (thermal + magnetic) pressure. By solving the initial-value problem for a large-scale pulse applied to a viscous fluid, we have further shown that the viscous damping rate of magnetoelastic waves in a magnetic tangle with small-scale inhomogeneity is greater than for a perfectly homogeneous and isotropic Maxwell stress, because the small-scale motions are themselves subject to viscous damping. As we found in Section 5.3.1, these effects are not present in a hyperviscous fluid because dynamically significant motions on the scale of the tangle are prevented.

This work is a first step towards our ultimate goal of understanding the dynamic effect of tangled magnetic field on large-scale motions. In the future, we plan to investigate how the conclusions reached here apply to more general field configurations and to MHD turbulence. The outstanding questions that we hope to address include:

- How restrictive is the equilibrium assumption? In this study, we have frequently utilised the Hermitian nature of the force operator (see Section 5.3.2), which relies on the unperturbed field being an equilibrium state. While turbulent magnetic fields may be far from equilibrium, simulations of isotropic MHD turbulence have

shown an excess of magnetic energy ('residual energy') at large scales [Müller & Grappin (2004, 2005); the same was true for the simulations presented in Chapter 2], hinting that at these scales, the field may organise itself into quasi-equilibrium structures.

- How restrictive is assuming that the magnetic field has no structure at large scales? In writing (5.9), we assumed that the equilibrium Maxwell stress M_0 had no component at the scale of the magnetoelastic-wave motions. Furthermore, in Section 5.3.2 we neglected coupling between large-scale modes via their mutual couplings to small-scale modes — strictly, this required that positive integer powers of M_0 also had negligible structure at large scales. These assumptions are justified for synthetic fields of the sort investigated numerically in Section 5.4, but may not be realistic for MHD turbulence — real turbulent fields can have a significant component of energy in modes with $k < k_\mathrm{t}$, as Chapter 4 illustrates.

- What is the effect of magnetic reconnection? Despite the key role of magnetic reconnection in MHD decay — see Chapter 2 (Hosking & Schekochihin, 2021) — we have exclusively considered flux-frozen magnetic fields in this chapter. This is because, as discussed in Section 5.2, the MHD equations cannot be written as closed evolution equations for the Maxwell stress when resistive effects are included. Intuitively, reconnection of magnetic field lines would reduce the magnetic tension that can be maintained at large scales, so we expect reconnecting magnetic fields to be less elastic.

Appendices

5.A Ideal instability of linear force-free fields

5.A.1 Existence of an ideal instability

Force-free magnetic fields are an important class of magnetostatic equilibria characterised by a vanishing Lorentz force. Such fields satisfy the equation

$$\boldsymbol{\nabla} \times \boldsymbol{B} = \alpha \boldsymbol{B}, \tag{5.44}$$

where $\alpha\,(\boldsymbol{r})$ is a scalar function of position, constrained to satisfy

$$\boldsymbol{B} \cdot \boldsymbol{\nabla} \alpha = 0, \tag{5.45}$$

by the divergence-free nature of $\boldsymbol{B}$. Force-free magnetic fields have long enjoyed prominence in plasma astrophysics as a natural relaxed state for magnetically dominated systems. The first such suggestion appears to be by Lüst & Schlüter (1954), in an effort to explain early investigations that indicated pressure gradients and gravity might be insufficient to balance strong fields in stellar media.

Special significance of *linear* force-free (LFF) fields, i.e., those for which $\alpha =$ constant, was first recognised by Chandrasekhar & Woltjer (1958), who showed that LFF fields are among the fields that minimise the total Joule heating subject to fixed magnetic energy, and argued on thermodynamic grounds that magnetically-dominated systems should relax to this minimum-dissipation state. This argument was refined somewhat by Woltjer (1958), who showed that ideal MHD evolution conserves a quantity that later became known as the magnetic helicity,

$$H = \int \mathrm{d}^3 \boldsymbol{r}\, \boldsymbol{A} \cdot \boldsymbol{B}, \tag{5.46}$$

and further showed that extremising the magnetic energy subject to the constraint of fixed magnetic helicity produced LFF fields. This *extremisation* was interpreted as a *minimisation* of the magnetic energy, and therefore a proof of the stability of LFF equilibria against ideal (helicity-conserving) perturbations. In a later paper, Woltjer (1959) argued that this conclusion had been incorrect, because the extremisation process was not guaranteed to produce minima, only extrema. Nonetheless, one state was guaranteed to be stable, the global minimum of the magnetic energy subject to fixed helicity. Substitution of (5.44) into (5.46) gives

$$H = \frac{1}{\alpha} \int \mathrm{d}^3\boldsymbol{r}\, B^2 = \frac{2E_M}{\alpha}, \tag{5.47}$$

and hence the magnetic energy is $E_M = \alpha H/2$. The force-free state with the smallest magnetic energy for a given magnetic helicity is therefore the one with the smallest value of α consistent with the boundary conditions; this state is guaranteed to be stable[7].

While the question of the stability of states with larger values of α is not resolved by the extremisation argument, theorems have been proposed regarding the stability of such states. These theorems mostly rely on the energy principle of Bernstein *et al.* (1958), which states that an MHD equilibrium state is stable if the second-order change in the total energy

$$\delta W_2 = \frac{1}{2} \int \mathrm{d}^3\boldsymbol{r} \left[(\boldsymbol{\xi} \cdot \boldsymbol{\nabla} p_0)\, \boldsymbol{\nabla} \cdot \boldsymbol{\xi} + \gamma p_0 \left(\boldsymbol{\nabla} \cdot \boldsymbol{\xi}\right)^2 + (\boldsymbol{\nabla} \times \boldsymbol{B}_0) \cdot (\boldsymbol{\xi} \times \delta\boldsymbol{B}) + |\delta\boldsymbol{B}|^2 \right] \tag{5.48}$$

is positive for any displacement field $\boldsymbol{\xi}$, where γ is the adiabatic index, p is the thermal pressure, the subscript zero refers to equibrium quantities, and $\delta\boldsymbol{B} = \boldsymbol{\nabla} \times (\boldsymbol{\xi} \times \boldsymbol{B}_0)$.

[7]These early arguments were later refined by Taylor (1974), who provided justification that conservation of magnetic helicity was indeed the correct constraint under which MHD fluids should relax. Taylor argued that the magnetic-field-topology-preserving nature of the MHD equations meant that any topological invariant of the magnetic field should be conserved during the evolution. This condition can be expressed as the conservation of $H_V = \int_V \mathrm{d}^3\boldsymbol{r}\, \boldsymbol{A} \cdot \boldsymbol{B}$ where V is any flux tube; physically, this integral is the total (signed) flux linked by the flux tube V. However, when even small topology breaking terms are introduced to the induction equation, H_V will no longer be conserved by the MHD evolution. The sum $H_{V_1} + H_{V_2}$ is nonetheless conserved when the tubes V_1 and V_2 'unlink', and hence the sum $\sum_i H_{V_i}$ over all flux tubes will still be a conserved quantity, as long as the evolution can be taken to be ideal outside of these unlinking events. The quantity $\sum_i H_{V_i}$ is just the total helicity, which, Taylor argued, justifies its priviledged role as the only topological invariant conserved in MHD relaxation.

The first term is zero for a force-free equilibrium, while the second is positive definite, but can always be made small by taking $p_0 \to 0$. Hence, the only terms relevant to the stability of force-free fields are the final two. Substituting the force free condition, (5.44), into (5.48), we obtain

$$\delta W_2 = \frac{1}{2} \int \mathrm{d}^3 \boldsymbol{r} \left[(\boldsymbol{\nabla} \times \delta \boldsymbol{A})^2 - \alpha \, \delta \boldsymbol{A} \cdot (\boldsymbol{\nabla} \times \delta \boldsymbol{A}) \right], \tag{5.49}$$

where $\delta \boldsymbol{A} = \boldsymbol{\xi} \times \boldsymbol{B_0}$. From this or equivalent expressions, it has been shown that more-or-less restricted classes of perturbations will give $\delta W_2 > 0$ for more-or-less restricted classes of LFF fields, and hence those equilibria are stable to such perturbations[8]. Classes of perturbations to which LFF fields have been shown to be stable (for any constant α) include: radial expansions; displacements along one spatial direction (i.e., $\boldsymbol{\xi} = \xi(\boldsymbol{r})\, \boldsymbol{n}$, where $\xi(\boldsymbol{r})$ is an arbitrary scalar function of position and $\boldsymbol{n}$ is a constant vector); axisymmetric perturbations (of axisymmetric LFF fields only); and perturbations that vanish outside of a region with spatial extent $d < 1/|\alpha|$ (Woltjer, 1958; Molodensky, 1974). To each of these perturbations it is possible to add any component along $\boldsymbol{B}_0$, because this does not change $\delta \boldsymbol{A}$.

Voslamber & Callebaut (1962), however, showed by means of a counterexample that not all LFF fields are stable; they found that there exist axisymmetric field configurations that are unstable to a class of non-axisymmetric perturbations. This dashed the hopes of proving a general stability theorem for LFF fields until the problem was revisited by Moffatt (1986), who showed by expanding $\boldsymbol{B}_0$ and $\boldsymbol{\xi}$ in Fourier modes that arbitrary periodic LFF equilibria are stable to arbitrary periodic perturbations. Indeed, the stability of LFF fields was the motivation for the consideration of the magnetoelastic wave problem by Moffatt (1986). Despite the apparent conflict between Voslamber & Callebaut's result and Moffatt's stability theorem, it was not until much more recently that a counterexample was explicitly presented by Er-Riani *et al.* (2014), who showed that there exist periodic force-free fields that are unstable to ideal periodic perturbations, as long as these perturbations are allowed to have wavevectors smaller

[8]This language, common in the literature, is a little imprecise, because a field perturbed by a displacement field $\boldsymbol{\xi}$ for which $\delta W_2 > 0$ will not necessarily tend to return to its original equilibrium state, unless the field is indeed stable to all perturbations.

than α[9]. Soon after, East *et al.* (2015) were able to find energy-decreasing peturbations for a number of LFF fields by numerical minimisation of (5.48) under variation of the Fourier coefficients in the expansion of $\boldsymbol{\xi}$. Indeed, they reported that they were able to find energy-decreasing peturbations for *every* LFF field that they considered, when Fourier modes with wavenumbers smaller than α were allowed. We too have encountered instability in each of the fields that we have investigated numerically in this study.

We note that there *do* exist stable periodic LFF fields, though only in the restricted case of no magnetic curvature. An example is the field $\boldsymbol{B} = B_0\,(0, \sin\alpha x, \cos\alpha x)$ which represents a uniform magnetic field in any plane of constant x, with direction rotating as x is varied. The stability of this configuration against a restricted class of periodic perturbations was demonstrated by Vekshtein (1989); here, we note that for a general periodic perturbation $\boldsymbol{\xi}\,(\boldsymbol{r}) = (\xi_x\,(\boldsymbol{r})\,,\, \xi_y\,(\boldsymbol{r})\,,\, \xi_z\,(\boldsymbol{r}))^{\mathrm{T}}$ it is possible to show via an elementary (though somewhat tedious) calculation that

$$\delta W_2 = \frac{1}{2}B_0^2 \int \mathrm{d}^3\boldsymbol{r} \left[\left(\cos\alpha x\, \frac{\partial \xi_x}{\partial x} + \cos\alpha x\, \frac{\partial \xi_y}{\partial y} - \sin\alpha x\, \frac{\partial \xi_z}{\partial y} \right)^2 + \left(\sin\alpha x\, \frac{\partial \xi_x}{\partial x} + \sin\alpha x\, \frac{\partial \xi_z}{\partial z} - \cos\alpha x\, \frac{\partial \xi_y}{\partial z} \right)^2 + \left(\sin\alpha x\, \frac{\partial \xi_x}{\partial y} + \cos\alpha x\, \frac{\partial \xi_x}{\partial z} \right)^2 \right]. \tag{5.50}$$

The integrand is manifestly positive definite, so this configuration is stable to ideal perturbations, for any α[10].

Whether there exist any periodic LFF configurations with magnetic curvature that are stable to arbitrary perturbations is, at present, unknown, as there have been no general theorems of instability (see Zrake & East 2016 for speculations that stable structures may exist in the *nonlinear* force-free case). The existence of stable force-free

[9]This is to say, a periodic LFF field with periodicity 2π ($\alpha = 2\pi$), in the 3-torus (or periodic box) with periodicity 2π *will* be stable. This is guaranteed to be so because 2π is the smallest value of α consistent with the periodicity of the domain, and hence the field must be stable by the variational result of Woltjer (1958).

[10]In fact, the same result is valid for $\alpha\, x \to \Phi\,(x)$, $\Phi'\,(x) \to \alpha\,(x)$, so a nonlinear force-free configuration corresponding to a non-constant rate of rotation of the magnetic field direction is also stable.

configurations would highly significant for astrophysical systems where magnetic-field structures are smaller than the system size, such as the hot, rarified plasma between galaxies in clusters.

5.A.2 Physical nature of the instability

Since its (re)discovery in 2014, the instability of LFF fields has attracted attention as a means of studying particle acceleration by magnetic reconnection in a more realistic setting than the typical Harris-type current sheet configuration[11] (Nalewajko *et al.*, 2016; Lyutikov *et al.*, 2017).

Lyutikov *et al.* (2017) have proposed a mechanism for the instability of two-dimensional LFF fields, by arguing that these fields describe a regular array (in the xy plane) of alternating currents (directed along z). Since like currents attract, this configuration is unstable, with similarly-directed currents ultimately merging.

In this study, we have been primarily motivated by the manifestation of the Lorentz force as a local magnetic tension in incompressible MHD. It is therefore instructive to see how the instability arises in this picture. Figure 5.6 shows the ideal instability of the 2D LFF given by

$$\boldsymbol{B} = B_0 \left(-\sin 4\pi y,\ \cos 4\pi x,\ \cos 4\pi y - \sin 4\pi x\right), \tag{5.51}$$

which has $\alpha = 4\pi$. Since the field is translationally invariant in z, only its component in the xy plane contributes to the magnetic tension. An unstable perturbation can be obtained by trialling a truncated Fourier series in (5.48); evaluation of the integral gives a quadratic form in the coefficients of the Fourier modes, which can be diagonalised and the perturbation that minimises δW obtained. By carrying out this proceedure, we find that $\xi_x = 7.34754\cos(2\pi x+2\pi y) - 7.34754\sin(2\pi x+2\pi y)) + 1.30549\cos(2\pi x - 6\pi y)) - 1.30549\sin(2\pi x-6\pi y)) + 0.447807\cos(6\pi x-2\pi y)) + 0.447807\sin(6\pi x-2\pi y)) + \sin(6\pi x+6\pi y)) + \cos(6\pi x+6\pi y))$, $\xi_y = -7.34754\cos(2\pi x+2\pi y) + 7.34754\sin(2\pi x + 2\pi y) + 0.435165\cos(2\pi x - 6\pi y) - 0.435165\sin(2\pi x - 6\pi y) + 1.34342\cos(6\pi x - 2\pi y) +$

[11] We stress that the instability is ideal in nature, but current sheets naturally form in its nonlinear evolution.

$1.34342\sin(6\pi x - 2\pi y) - \sin(6\pi x + 6\pi y) - \cos(6\pi x + 6\pi y)$ gives $\delta W_2 < 0$. This perturbation is shown in Figure 5.6, together with the perturbed magnetic-field structure. We observe that the perturbation represents a non-trivial deformation of the magnetic field structure that mostly consists of the "magnetic cells" that make up the field configuration sliding past each other in layers, with smaller perturbations to the field at the boundaries of each cell that generate a magnetic tension force whose net direction is along the direction of the displacement of the layer, preventing the configuration from returning to its original state.

The timescale for the development of instability can be estimated analytically using energy conservation for the truncated system:

$$\frac{\mathrm{d}}{\mathrm{d}t}\left(\frac{1}{2}\int \mathrm{d}^3\boldsymbol{r}\,\dot{\xi}^2 + \delta W\right) = -\nu\int \mathrm{d}^3\boldsymbol{r}|\boldsymbol{\nabla}\boldsymbol{\xi}|^2. \tag{5.52}$$

When the fluid is inviscid, the timescale can be estimated by balancing the kinetic and potential energy terms and solving the resulting eigenvalue problem for the growth rate of the unstable mode. For a viscously-dominated fluid, the rate of change of potential energy is balanced with the rate of energy dissipation by viscosity.

Solving the eigenvalue problem for the truncated system, we find growth rates of $0.0930196\,\alpha B_0$ for the inviscid case, and $0.0135899\,B_0^2/\nu$ for the viscous case. The dimensional form of these results is inevitable, but the numerical prefactors turn out to be small, particularly in the viscous case, indicating that the growth rate of the instability should be slower than a naïve estimate of the kind made in Section 5.4.1 would indicate. The reason for this is apparent from Figure 5.6, which shows that force responsible for driving the relative motions of the layers of magnetic cells is mostly generated by the perturbations to the field at the boundary of each cell, and the component of this force along the direction of motion of the layer is small. The viscous growth rate is further suppressed by the fact that the perturbations at the boundaries of each cell that are responsible for generating forces are at a smaller scale than the cell size, and hence are damped more strongly by viscosity.

Similar considerations may apply to the more complicated 3D 'tangled' equilibria that we have considered in the main text, explaining why the small-scale instability develops slowly in our simulations. Lyutikov *et al.* (2017) have also argued that 3D

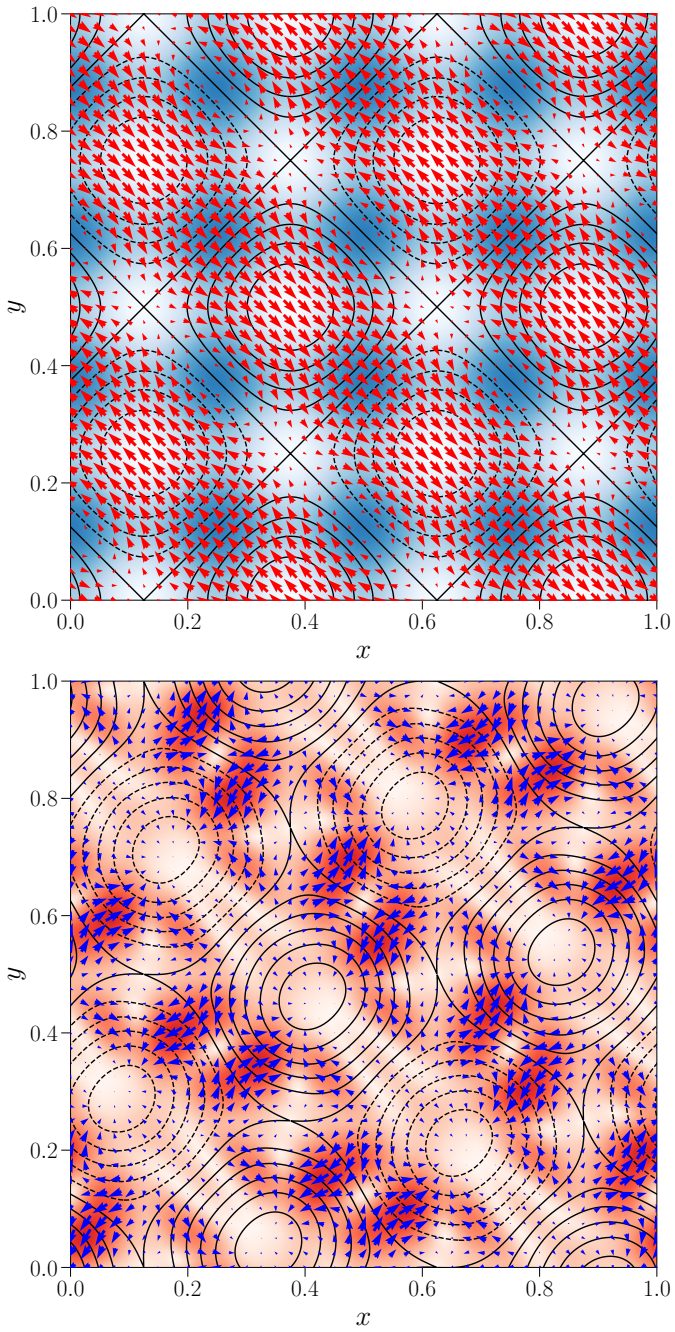

Figure 5.6: Upper panel: Black lines are level lines of B_z for the field defined by (5.51). By the LFF condition and z-independent nature of the field, these are also the field lines of the dynamically-important xy-plane field. Solid black lines have $B_z > 0$, so the in-plane field has anticlockwise circulation, while dashed black lines have $B_z < 0$, so the in-plane field has clockwise circulation. The strength of the in-plane field is shown in blue. Red arrows show a perturbation for which $\delta W < 0$. Lower panel: The field configuration obtained by applying this perturbation. Black lines again show the xy-plane field, while blue arrows show the non-compressive part of the magnetic tension force, with the size of this force shown in red.

magnetic configurations should be *more* stable than 2D ones because the field cannot be naturally decomposed into sliding layers.

5.A.3 Nonlinear evolution

The nonlinear evolution of the instability has been extensively studied using both force-free electrodynamics (FFE) simulations (East *et al.*, 2015; Zrake & East, 2016; Lyutikov *et al.*, 2017) and kinetic simulations (Nalewajko *et al.*, 2016; Yuan *et al.*, 2016; Lyutikov *et al.*, 2017; Nalewajko, 2018) of simple LFF configurations, the so-called Arnold-Beltrami-Childress (ABC) fields, of which (5.51) is an example.

In these studies, the late-time evolution is characterised by an "untangling" and merging of magnetic flux tubes, with an associated transfer of magnetic energy from small to large scales. Indeed, Blandford *et al.* (2017) suggested that the particle acceleration that occurs during such an untangling may power dramatic flares in high energy astrophysical sources. The ultimate state of the system is the stable LFF state with the smallest α compatible with the size of the box, in accordance with JB Taylor Relaxation (see Appendix 5.A.1). Interestingly, in 2D, Zrake & East (2016) have found with FFE simulations that the system does not relax to a LFF state, but instead to a configuration of *nonlinear* force-free magnetic 'bubbles', which they argue is a consequence of the existence in 2D of invariants additional to magnetic helicity. East *et al.* (2015) found indications that it is possible for the nonlinear system to evolve into a transient LFF state with α larger than the smallest value permitted by the geometry, though this does not appear to have been reproduced in later studies.

5.B Proof that the amplitudes of fast Laplace modes of the large-scale motion vanish as $\epsilon \to 0$

In this appendix, we show that the Laplace amplitudes of any fast motion on large scales vanishes compared to the amplitude of slow motions, as $\epsilon \to 0$. This justifies the neglect of p^2 in the denominator of the coupling term in (5.35).

Retaining p^2 in (5.35), the dispersion relation (5.38) becomes

$$D(p_n) \equiv p_n^2 + v_{\mathrm{E}}^2 k^2 - \sum_{\boldsymbol{k}'} \frac{A_{zj}(\boldsymbol{k}_{\mathrm{w}}, \boldsymbol{k}') A_{jz}(\boldsymbol{k}', \boldsymbol{k}_{\mathrm{w}})}{p_n^2 + k'^2 v_{\mathrm{E}}^2 + \nu k'^2 p_n} + \nu k^2 p_n = 0. \tag{5.53}$$

Using the non-dimensionalisation $\hat{\nu} = \nu k_{\mathrm{w}}/v_{\mathrm{E}}$, $\hat{p} = p/k_{\mathrm{w}} v_{\mathrm{E}}$, we can write (5.53) as

$$\hat{p}^2 + 1 - \sum_{\boldsymbol{k}'} \frac{A_{zj}(\boldsymbol{k}_{\mathrm{w}}, \boldsymbol{k}') A_{jz}(\boldsymbol{k}', \boldsymbol{k}_{\mathrm{w}})/k'^2}{\epsilon_{k'}^2 \hat{p}^2 + 1 + \hat{\nu}\hat{p}} + \hat{\nu}\hat{p} = 0. \tag{5.54}$$

where $\epsilon_{k'} = k/k' \sim \epsilon$, and, as before, $\epsilon \sim k_w/k_t \ll 1$.This equation has $2W + 2$ solutions, where W is the number of distinct wavenumbers among the small-scale modes to which the large-scale perturbation couples – this corresponds to the number of distinct small-scale frequencies that are possible[12]. To evaluate the Laplace amplitude according to (5.37), it is helpful to factorise the dispersion relation. Factoring out $1/(p^2 + 1/\epsilon_{k'}^2 + \hat{\nu}\hat{p}/\epsilon_{k'}^2)$ for each of the W terms in the sum in (5.54) leaves a polynomial whose leading coefficient is 1, and whose roots are all the solutions of (5.54): this polynomial can be factorised as $\prod_m (\hat{p} - \hat{p}_m)$, i.e.,

$$\hat{p}^2 + 1 - \sum_{\boldsymbol{k}'} \frac{A_{zj}(\boldsymbol{k}_{\mathrm{w}}, \boldsymbol{k}') A_{jz}(\boldsymbol{k}', \boldsymbol{k}_{\mathrm{w}})/k'^2}{\epsilon_{k'}^2 \hat{p}^2 + 1 + \hat{\nu}\hat{p}} + \hat{\nu}\hat{p} = \prod_{k'} \frac{1}{p^2 + 1/\epsilon_{k'}^2 + \hat{\nu}\hat{p}/\epsilon_{k'}^2} \prod_{m=1}^{2W+2} (p - p_m), \tag{5.55}$$

where the first product is over the W distinct values of $k' = |\boldsymbol{k}'|$.

According to (5.37), the Laplace amplitudes are computed according to

$$\begin{aligned} A_n &= \mathrm{Res}\left[\frac{p}{D(p)}, p \to p_n\right] \\ &= \lim_{\hat{p} \to \hat{p}_n} \frac{\hat{p}\,(\hat{p} - \hat{p}_n) \prod_{k'} \left(\hat{p}^2 + 1/\epsilon_{k'}^2 + \hat{\nu}\hat{p}/\epsilon_{k'}^2\right)}{\prod_{m=1}^{2W+2} (\hat{p} - \hat{p}_m)}, \\ &= \frac{\hat{p}_n \prod_{k'} \left(\hat{p}^2 + 1/\epsilon_{k'}^2 + \hat{\nu}\hat{p}/\epsilon_{k'}^2\right)}{\prod_{m=1,\, m \neq n}^{2W+2} (\hat{p}_n - \hat{p}_m)}. \end{aligned} \tag{5.56}$$

[12] $W \neq N$ if the large-scale perturbation couples to both of the small-scale modes $\boldsymbol{\xi}_i(\boldsymbol{k})$ and $\boldsymbol{\xi}_j(\boldsymbol{k}')$ where $|\boldsymbol{k}| = |\boldsymbol{k}'|$ but $\boldsymbol{k} \neq \boldsymbol{k}'$ or $i \neq j$.

The scaling of A_n with ϵ will depend on the ordering of $\hat{\nu}$ with respect to ϵ – this determines whether or not the small-scale magnetic field is viscously dominated. Generally, we can write $\hat{\nu} = O\left(\epsilon^{\beta}\right)$ and consider the scaling of A_n for different values of β.

If $\beta \geq 1$, the small-scale field is not overdamped by viscosity. Any solution for which $\epsilon_{k'}^2 \hat{p}^2$ is not negligible in the denominator of (5.54) is a balance of $\epsilon_{k'}^2 \hat{p}^2$ and 1 (and $\hat{\nu}\hat{p}$, if $\beta = 1$), so $p \sim \epsilon^{-1}$. We then have

$$\prod_{m \neq n} (p_n - p_m) \sim \epsilon^{-(2W+1)}. \tag{5.57}$$

Each term in the product $\prod_{k'} \left(p^2 + 1/\epsilon_{k'}^2 + \hat{\nu}\hat{p}/\epsilon_{k'}^2\right)$ is $\sim 1/\epsilon^2$ apart from one, which is that for which p_n is an approximate root. The leading-order scaling of this term will be ϵ^2, in order to balance the other terms in (5.54). Therefore,

$$\prod_{k'} \left(p^2 + 1/\epsilon_{k'}^2 + \hat{\nu}\hat{p}/\epsilon_{k'}^2\right) \sim \epsilon^{-2(W-1)}\epsilon^2 = \epsilon^{4-2W}. \tag{5.58}$$

With these scalings, (5.56) gives $A_n \sim \epsilon^4$.

Alternatively, if $\beta < 1$, the small-scale field is strongly damped by viscosity. We argue similarly to before: any solution for which $\epsilon_{k'}^2 \hat{p}^2$ is not negligible in the denominator of (5.54) is a balance of $\epsilon_{k'}^2 \hat{p}^2$ and $\hat{\nu}\hat{p}$, so $p \sim \epsilon^{\beta-2}$. We then have

$$\prod_{m \neq n} (p_n - p_m) \sim \left(\epsilon^{\beta-2}\right)^{2W+1}, \tag{5.59}$$

while

$$\prod_{k'} \left(p^2 + 1/\epsilon_{k'}^2 + \hat{\nu}\hat{p}/\epsilon_{k'}^2\right) \sim \left(\epsilon^{2\beta-4}\right)^{W-1} \epsilon^{4-2\beta} \sim \left(\epsilon^{\beta-2}\right)^{2W-4}. \tag{5.60}$$

With these scalings, (5.56) gives $A_n \sim \epsilon^{8-4\beta}$.

In both cases, $A_n \to 0$ as $\epsilon \to 0$.

Chapter 6

Conclusions and future directions

Chapter 2 of this thesis introduced a number of "generalised Saffman-type invariants" that constrain the evolution of the magnetic field in decaying MHD turbulence. Beyond this, Saffman-type invariants appear to be an extremely general tool allowing consideration of sign-indefinite conserved quantities in the 'selective decay' framework for decaying turbulence. In those physical systems where conserved quantities have a topological character, reconnection of the relevant fields is likely to be the key physical process whereby the decay occurs. Marrying this insight to the constraints imposed by the invariants appears to be a winning strategy for constructing decay theories, as it proved to be in the MHD turbulence regimes that we considered in Chapter 2.

There are many different types of fluid turbulence to which Saffman-type invariants might be usefully applied — a number of them are reviewed in Davidson (2013), and there are likely to be others, especially in the large variety of plasma systems increasingly of interest in the context of various types of space or astrophysical turbulence [see, e.g., Schekochihin *et al.* (2019); Milanese *et al.* (2020); Meyrand *et al.* (2021)]. We anticipate that the particular invariant I_H, upon which Section 2.3 focused, should remain an invariant in the cases of compressible (Mac Low *et al.*, 1998; Stone *et al.*, 1998), relativistic (Zrake, 2014) and/or kinetic dynamics (Nalewajko *et al.*, 2016; Yuan *et al.*, 2016; Lyutikov *et al.*, 2017; Nalewajko, 2018), as magnetic helicity remains a conserved quantity in these contexts. This means that the invariance of I_H (and the physical principle of conservation of local magnetic-helicity fluctuations from which it follows) should provide a constraint on decaying turbulence in a wide variety of

magnetised astrophysical systems. Examples might include turbulence in star-forming molecular clouds (Mac Low *et al.*, 1998; Gao *et al.*, 2015) and galaxy clusters (Subramanian, 2016; Sur, 2019); the generation of seed fields for galactic dynamo (Zhou *et al.*, 2020); as well as the evolution of primordial magnetic fields in the early Universe (Banerjee & Jedamzik, 2004; Durrer & Neronov, 2013; Subramanian, 2016), which was the subject of Chapter 3.

It is interesting to consider whether Saffman-type invariants play a role in determining the dynamics of *forced*, rather than decaying, turbulence. A first venture towards understanding whether they do was presented in Chapter 4, where we showed that turbulent diffusion of linear momentum can lead to hydrodynamic turbulence resembling the Saffman sort, even when the rate of injection of the Saffman integral by the forcing is formally zero. This process provides a physical understanding of the formation of large-scale equilibrium states in hydrodynamic turbulence (Dallas *et al.*, 2015; Cameron *et al.*, 2017; Alexakis & Biferale, 2018; Alexakis & Brachet, 2019). An intriguing separate possibility, to be explored in future work, is that Saffman-type invariants might somehow be used to impose constraints on inertial-range, rather than integral-scale, dynamics. That they could is suggested by observation of multi-scale alignment between (i) velocity and magnetic perturbations in the inertial range of MHD turbulence with a strong mean field (Perez & Boldyrev, 2009), and (ii) velocity and vorticity in the inertial range of hydrodynamic turbulence (Levich, 2009). These can be interpreted as patches of maximal cross- and kinetic helicity respectively — quantities for which Saffman-type invariants are a natural construction, and whose development and dynamics might therefore be controlled by scale-dependent analogues of Saffman-type invariants, if such objects could be meaningfully constructed.

In the context of the large-scale dynamics of MHD turbulence, one might wonder what the dynamical effect of statistically isotropic and homogeneous magnetic fields are on the medium hosting them. This was the subject of Chapter 5, where we showed that certain types of approximately isotropic magnetic equilibria support the propagation of large-scale "magnetoelastic waves", demonstrating their existence in a numerical simulation for the first time, and confirming that a mean-field theory based on "First-Order Smoothing" gave a reasonable estimate of their dispersion relation. On the other hand,

the static-equilibrium magnetic-field configurations are unlikely to be realistic models of real turbulent environments in astrophysics. Determining whether magnetoelastic waves play a role in facilitating energy transport in the turbulent intra-cluster medium (which was, in fact, the original motivation for my DPhil project) or in the primordial plasma of the early Universe is therefore a subject that we must leave for future work.

References

Adzhemyan, L. Ts., Antonov, N. V., Mazzino, A., Muratore-Ginanneschi, P. & Runov, A. V. 2001*a* Pressure and intermittency in passive vector turbulence. *Europhys. Lett.* **55**, 801.

Adzhemyan, L. Ts., Antonov, N. V. & Runov, A. V. 2001*b* Anomalous scaling, nonlocality, and anisotropy in a model of the passively advected vector field. *Phys. Rev. E* **64**, 046310.

Alexakis, A. & Biferale, L. 2018 Cascades and transitions in turbulent flows. *Phys. Rep.* **767**, 1.

Alexakis, A. & Brachet, M.-E. 2019 On the thermal equilibrium state of large-scale flows. *J. Fluid Mech.* **872**, 594.

Antonov, N. V., Hnatich, M., Honkonen, J. & Jurčišin, M. 2003 Turbulence with pressure: anomalous scaling of a passive vector field. *Phys. Rev. E* **68**, 046306.

Arponen, H. 2009 Anomalous scaling and anisotropy in models of passively advected vector fields. *Phys. Rev. E* **79**, 056303.

Banerjee, R. & Jedamzik, K. 2003 Are cluster magnetic fields primordial? *Phys. Rev. Lett.* **91**, 251301.

Banerjee, R. & Jedamzik, K. 2004 Evolution of cosmic magnetic fields: From the very early Universe, to recombination, to the present. *Phys. Rev. D* **70**, 123003.

Batchelor, G. K. & Proudman, I. 1956 The large-scale structure of homogeneous turbulence. *Philos. Trans. R. Soc. A* **248**, 369.

Bennett, C. L., Halpern, M., Hinshaw, G., Jarosik, N., Kogut, A., Limon, M., Meyer, S. S., Page, L., Spergel, D. N., Tucker, G. S. & others 2003 First-year Wilkinson Microwave Anisotropy Probe (WMAP) observations: preliminary maps and basic results. *Astrophys. J. Suppl.* **148**, 1.

Benzi, R., Biferale, L. & Toschi, F. 2001 Universality in passively advected hydrodynamic fields: the case of a passive vector with pressure. *Eur. Phys. J. B* **24**, 125.

Berera, Arjun & Linkmann, Moritz 2014 Magnetic helicity and the evolution of decaying magnetohydrodynamic turbulence. *Phys. Rev. E* **90**, 041003.

Berger, M. A. 1984 Rigorous new limits on magnetic helicity dissipation in the solar corona. *Geophys. Astrophys. Fluid Dyn.* **30**, 79.

Bernstein, I. B., Frieman, E. A., Kruskal, M. D. & Kulsrud, R. M. 1958 An energy principle for hydromagnetic stability problems. *Proc. R. Soc. Lond.* **244**, 17.

Bhat, P., Zhou, M. & Loureiro, N. F. 2021 Inverse energy transfer in decaying, three-dimensional, non-helical magnetic turbulence due to magnetic reconnection. *Mon. Not. R. Astron. Soc.* **501**, 3074.

Bhattacharjee, A., Huang, Y.-M., Yang, H. & Rogers, B. 2009 Fast reconnection in high-Lundquist-number plasmas due to the plasmoid Instability. *Phys. Plasmas* **16**, 112102.

Biskamp, D. & Bremer, U. 1994 Dynamics and statistics of inverse cascade processes in 2D magnetohydrodynamic turbulence. *Phys. Rev. Lett.* **72**, 3819.

Biskamp, D. & Müller, W.-C. 1999 Decay laws for three-dimensional magnetohydrodynamic turbulence. *Phys. Rev. Lett.* **83**, 2195.

Biskamp, D. & Welter, H. 1989 Dynamics of decaying two-dimensional magnetohydrodynamic turbulence. *Phys. Fluids B* **1**, 1964.

Blandford, R., Yuan, Y., Hoshino, M. & Sironi, L. 2017 Magnetoluminescence. *Space Sci. Rev.* **207**, 291.

Boyarsky, A., Cheianov, V., Ruchayskiy, O. & Sobol, O. 2021 Equilibration of the chiral asymmetry due to finite electron mass in electron-positron plasma. *Phys. Rev. D* **103**, 013003.

Braginskii, S. I. 1965 Transport processes in a plasma. *Rev. Plasma Phys.* **1**, 205.

Brandenburg, A., Enqvist, K. & Olesen, P. 1996 Large-scale magnetic fields from hydromagnetic turbulence in the very early Universe. *Phys. Rev. D* **54**, 1291.

Brandenburg, A. & Kahniashvili, T. 2017 Classes of hydrodynamic and magnetohydrodynamic turbulent decay. *Phys. Rev. Lett.* **118**, 055102.

Brandenburg, A., Kahniashvili, T., Mandal, S., Pol, A. R., Tevzadze, A. G. & Vachaspati, T. 2019 Dynamo effect in decaying helical turbulence. *Phys. Rev. Fluids* **4**, 024608.

Brandenburg, A., Kahniashvili, T. & Tevzadze, A. G. 2015 Nonhelical inverse transfer of a decaying turbulent magnetic field. *Phys. Rev. Lett.* **114**, 075001.

Brandenburg, A. & Subramanian, K. 2005 Astrophysical magnetic fields and nonlinear dynamo theory. *Phys. Rep.* **417**, 1.

Burns, K. J., Vasil, G. M., Oishi, J. S., Lecoanet, D. & Brown, B. P. 2020 Dedalus: A flexible framework for numerical simulations with spectral methods. *Phys. Rev. Res.* **2**, 023068.

Cameron, A., Alexakis, A. & Brachet, M.-E. 2017 Effect of helicity on the correlation time of large scales in turbulent flows. *Phys. Rev. Fluids* **2**, 114602.

Campanelli, L. 2004 Scaling laws in magnetohydrodynamic turbulence. *Phys. Rev. D* **70**, 083009.

Cassak, P. A., Liu, Y. H. & Shay, M. A. 2017 A review of the 0.1 reconnection rate problem. *J. Plasma Phys.* **83**, 715830501.

Chandrasekhar, S. & Woltjer, L. 1958 On force-free magnetic fields. *Proc. Natl. Acad. Sci. U.S.A.* **44**, 285.

Chen, C. & Diamond, P. H. 2020 Potential vorticity mixing in a tangled magnetic field. *Astrophys. J.* **892**, 24.

Chen, C. H. K., Mallet, A., Yousef, T. A., Schekochihin, A. A. & Horbury, T. S. 2011 Anisotropy of Alfvénic turbulence in the solar wind and numerical simulations. *Mon. Not. R. Astron. Soc.* **415**, 3219.

Cho, J., Lazarian, A. & Vishniac, E. T. 2002 Simulations of magnetohydrodynamic turbulence in a strongly magnetized medium. *Astrophys. J.* **564**, 291.

Christensson, M., Hindmarsh, M. & Brandenburg, A. 2001 Inverse cascade in decaying three-dimensional magnetohydrodynamic turbulence. *Phys. Rev. E* **64**, 056405.

Comisso, L. & Bhattacharjee, A. 2016 On the value of the reconnection rate. *J. Plasma Phys.* **82**, 595820601.

Dallas, V., Fauve, S. & Alexakis, A. 2015 Statistical equilibria of large scales in dissipative hydrodynamic turbulence. *Phys. Rev. Lett.* **115**, 204501.

Davidson, P. A. 2009 The role of angular momentum conservation in homogeneous turbulence. *J. Fluid Mech.* **632**, 329.

Davidson, P. A. 2011 The minimum energy decay rate in quasi-isotropic grid turbulence. *Phys. Fluids* **23**, 085108.

Davidson, P. A. 2013 *Turbulence in Rotating, Stratified and Electrically Conducting Fluids*. Cambridge University Press.

Davidson, P. A. 2015 *Turbulence: an Introduction for Scientists and Engineers*. Oxford University Press.

Davidson, P. A., Okamoto, N. & Kaneda, Y. 2012 On freely decaying, anisotropic, axisymmetric Saffman turbulence. *J. Fluid Mech.* **706**, 150.

Dobrowolny, M., Mangeney, A. & Veltri, P. 1980 Properties of magnetohydrodynamic turbulence in the solar wind. *Astron. Astrophys.* **83**, 26.

Dong, C., Wang, L., Huang, Y.-M., Comisso, L. & Bhattacharjee, A. 2018 Role of the plasmoid instability in magnetohydrodynamic turbulence. *Phys. Rev. Lett.* **121**, 165101.

Durrer, R. & Caprini, C. 2003 Primordial magnetic fields and causality. *J. Cosmol. Astropart. Phys.* **2003**, 010.

Durrer, R. & Neronov, A. 2013 Cosmological magnetic fields: their generation, evolution and observation. *Astron. Astrophys. Rev.* **21**, 62.

East, W. E., Zrake, J., Yuan, Y. & Bland ford, R. D. 2015 Spontaneous decay of periodic magnetostatic equilibria. *Phys. Rev. Lett.* **115**, 095002.

Er-Riani, M., Naji, A. & El Jarroudi, M. 2014 A note on the stability of Beltrami fields for compressible fluid flows. *Int. J. Non-Linear Mech.* **67**, 231.

Eyink, G. L. & Thomson, D. J. 2000 Free decay of turbulence and breakdown of self-similarity. *Phys. Fluids* **12**, 477.

Falkovich, G., Gawędzki, K. & Vergassola, M. 2001 Particles and fields in fluid turbulence. *Rev. Mod. Phys.* **73**, 913.

Frick, P. & Stepanov, R. 2010 Long-term free decay of MHD turbulence. *Europhys. Lett.* **92**, 34007.

Fromang, S., Papaloizou, J., Lesur, G. & Heinemann, T. 2007 MHD simulations of the magnetorotational instability in a shearing box with zero net flux. II. The effect of transport coefficients. *Astron. Astrophys.* **476**, 1123.

Galishnikova, A. K., Kunz, M. W. & Schekochihin, A. A. 2022 Tearing instability and current-sheet disruption in the turbulent dynamo, arXiv: 2201.07757.

Galli, S., Pogosian, L., Jedamzik, K. & Balkenhol, L. 2022 Consistency of Planck, ACT, and SPT constraints on magnetically assisted recombination and forecasts for future experiments. *Phys. Rev. D* **105**, 023513.

Gao, Y., Xu, H. & Law, C. K. 2015 Turbulence decay and cloud core relaxation in molecular clouds. *Astrophys. J.* **799**, 227.

Goldreich, P. & Sridhar, S. 1995 Toward a theory of interstellar turbulence. II. Strong Alfvenic turbulence. *Astrophys. J.* **438**, 763.

Gong, M., Ivlev, A. V., Zhao, B. & Caselli, P. 2020 Impact of magnetorotational instability on grain growth in protoplanetary disks. I. Relevant turbulence properties. *Astrophys. J.* **891**, 172.

Gruzinov, A. V. & Diamond, P. H. 1996 Nonlinear mean field electrodynamics of turbulent dynamos. *Phys. Plasmas* **3**, 1853.

Hatori, T. 1984 Kolmogorov-style argument for the decaying homogeneous MHD turbulence. *J. Phys. Soc. Jpn.* **53**, 2539.

Hosking, D. N. & Schekochihin, A. A. 2021 Reconnection-controlled decay of magnetohydrodynamic turbulence and the role of invariants. *Phys. Rev. X* **11**, 041005.

Hosking, D. N. & Schekochihin, A. A. 2022*a* Cosmic-void observations reconciled with primordial magnetogenesis, arXiv: 2203.03573.

Hosking, D. N. & Schekochihin, A. A. 2022*b* Emergence of long-range correlations and thermal spectra in forced turbulence, arXiv: 2202.00462.

Hosking, D. N., Schekochihin, A. A. & Balbus, S. A. 2020 Elasticity of tangled magnetic fields. *J. Plasma Phys.* **86**, 905860511.

Hossain, M., Gray, P. C., Pontius, D. H., Matthaeus, W. H. & Oughton, S. 1995 Phenomenology for the decay of energy-containing eddies in homogeneous MHD turbulence. *Phys. Fluids* **7**, 2886.

Ishida, T., Davidson, P. A. & Kaneda, Y. 2006 On the decay of isotropic turbulence. *J. Fluid Mech.* **564**, 455.

Jedamzik, K. & Pogosian, L. 2020 Relieving the Hubble tension with primordial magnetic fields. *Phys. Rev. Lett.* **125**, 181302.

Jedamzik, K. & Saveliev, A. 2019 Stringent limit on primordial magnetic fields from the cosmic microwave background radiation. *Phys. Rev. Lett.* **123**, 021301.

Ji, H., Daughton, W., Jara-Almonte, J., Le, A., Stanier, A. & Yoo, J. 2022 Magnetic reconnection in the era of exascale computing and multiscale experiments. *arXiv e-prints* p. arXiv:2202.09004.

Kadomtsev, B. B. & Pogutse, O. P. 1974 Nonlinear helical perturbations of a plasma in the tokamak. *Soviet Phys. JETP* **38**, 283.

Kazantsev, A. P. 1968 Enhancement of a magnetic field by a conducting fluid. *Soviet Phys. JETP* **26**, 1031.

Kolmogorov, A. N. 1941*a* Dissipation of energy in locally isotropic turbulence. *Dokl. Acad. Nauk SSSR* **32**, 16.

Kolmogorov, A. N. 1941*b* Local structure of turbulence in incompressible viscous fluid at very large Reynolds numbers. *Dokl. Acad. Nauk SSSR* **30**, 301.

Kraichnan, R. H. 1965 Inertial-range spectrum of hydromagnetic turbulence. *Phys. Fluids* **8**, 1385.

Kraichnan, R. H. 1968 Small-scale structure of a scalar field convected by turbulence. *Phys. Fluids* **11**, 945.

Kraichnan, R. H. 1973 Helical turbulence and absolute equilibrium. *J. Fluid Mech.* **59**, 745.

Kraichnan, R. H. 1994 Anomalous scaling of a randomly advected passive scalar. *Phys. Rev. Lett.* **72**, 1016.

Krause, F. & Raedler, K. H. 1980 *Mean-Field Magnetohydrodynamics and Dynamo Theory*. Elsevier.

Kulsrud, R. M. 2005 *Plasma Physics for Astrophysics*. Princeton University Press.

Kulsrud, R. M. & Anderson, S. W. 1992 The spectrum of random magnetic fields in the mean-field dynamo theory of the galactic magnetic field. *Astrophys. J.* **396**, 606.

Kunz, M. W. & Lesur, G. 2013 Magnetic self-organization in Hall-dominated magnetorotational turbulence. *Mon. Not. R. Astron. Soc.* **434**, 2295.

Kunz, Matthew W., Stone, James M. & Quataert, Eliot 2016 Magnetorotational turbulence and dynamo in a collisionless plasma. *Phys. Rev. Lett.* **117**, 235101.

Landau, L. D. & Lifshitz, E. M. 1959 *Fluid Mechanics*. Pergamon Press.

Lazarian, A., Eyink, G. L., Jafari, A., Kowal, G., Li, H., Xu, S. & Vishniac, E. T. 2020 3D turbulent reconnection: theory, tests, and astrophysical implications. *Phys. Plasmas* **27**, 012305.

Lee, E., Brachet, M. E., Pouquet, A., Mininni, P. D. & Rosenberg, D. 2010 Lack of universality in decaying magnetohydrodynamic turbulence. *Phys. Rev. E* **81**, 016318.

Lee, T. D. 1952 On some statistical properties of hydrodynamical and magnetohydrodynamical fields. *Quart. Appl. Maths* **10**, 69.

Lesieur, M. 2008 *Turbulence in Fluids*. Springer.

Lesieur, M., Métais, O. & Comte, P. 2005 *Large-Eddy Simulations of Turbulence*. Cambridge University Press.

Lesur, Geoffroy 2015 Snoopy: general purpose spectral solver, Astrophysics Source Code Library (ascl:1505.022).

Levich, E. 2009 Coherence in Turbulence: New Perspective. *Old and New Concepts of Physics* **6**, 239.

Loitsyansky, L. G. 1939 Some basic laws for isotropic turbulent flow. *Trudy Tsentr. Aero.-Gidrodin Inst.* **440**, 3.

Loureiro, N. F., Schekochihin, A. A. & Cowley, S. C. 2007 Instability of current sheets and formation of plasmoid chains. *Phys. Plasmas* **14**, 100703.

Lüst, R. & Schlüter, A. 1954 Kraftfreie magnetfelder. *Z. Astrophys.* **34**, 263.

Lyutikov, M., Sironi, L., Komissarov, S. S. & Porth, O. 2017 Particle acceleration in relativistic magnetic flux-merging events. *J. Plasma Phys.* **83**, 635830602.

Mac Low, M.-M., Klessen, R. S., Burkert, A. & Smith, M. D. 1998 Kinetic energy decay rates of supersonic and super-Alfvénic turbulence in star-forming clouds. *Phys. Rev. Lett.* **80**, 2754.

Mallet, A., Schekochihin, A. A. & Chandran, B. D. G. 2015 Refined critical balance in strong Alfvenic turbulence. *Mon. Not. R. Astron. Soc.* **449**, L77.

Maron, J. & Blackman, E. G. 2002 Effect of fractional kinetic helicity on turbulent magnetic dynamo spectra. *Astrophys. J. Lett.* **566**, L41.

Maron, J., Cowley, S. & McWilliams, J. 2004 The nonlinear magnetic cascade. *Astrophys. J.* **603**, 569.

Maron, J. & Goldreich, P. 2001 Simulations of incompressible magnetohydrodynamic turbulence. *Astrophys. J.* **554**, 1175.

Matthaeus, W. H. & Montgomery, D. 1980 Selective decay hypothesis at high mechanical and magnetic Reynolds numbers. *Annals of the New York Academy of Sciences* **357**, 203.

Matthaeus, W. H. & Montgomery, D. 1983 *Dynamic Alignment and Selective Decay in MHD*. Wiley NY.

Matthaeus, W. H., Pouquet, A., Mininni, P. D., Dmitruk, P. & Breech, B. 2008 Rapid alignment of velocity and magnetic field in magnetohydrodynamic turbulence. *Phys. Rev. Lett.* **100**, 085003.

Matthaeus, W. H., Zank, G. P. & Oughton, S. 1996 Phenomenology of hydromagnetic turbulence in a uniformly expanding medium. *J. Plasma Phys.* **56**, 659.

Melville, S., Schekochihin, A. A. & Kunz, M. W. 2016 Pressure-anisotropy-driven microturbulence and magnetic-field evolution in shearing, collisionless plasma. *Mon. Not. R. Astron. Soc.* **459**, 2701.

Meyrand, R., Squire, J., Schekochihin, A. A. & Dorland, W. 2021 On the violation of the zeroth law of turbulence in space plasmas. *J. Plasma Phys.* **87**, 535870301.

Michel, G., Pétrélis, F. & Fauve, S. 2017 Observation of thermal equilibrium in capillary wave turbulence. *Phys. Rev. Lett.* **118**, 144502.

Milanese, L. M., Loureiro, N. F., Daschner, M. & Boldyrev, S. 2020 Dynamic phase alignment in inertial Alfvén turbulence. *Phys. Rev. Lett.* **125**, 265101.

Moffatt, H. K. 1978 *Magnetic Field Generation in Electrically Conducting Fluids*. Cambridge University Press.

Moffatt, H. K. 1985 Magnetostatic equilibria and analogous Euler flows of arbitrarily complex topology. I - Fundamentals. *J. Fluid Mech.* **159**, 359.

Moffatt, H. K. 1986 Magnetostatic equilibria and analogous Euler flows of arbitrarily complex topology. II - Stability considerations. *J. Fluid Mech* **166**, 359.

Molodensky, M. M. 1974 Equilibrium and stability of force-free magnetic field. *Sol. Phys.* **39**, 393.

Montgomery, D., Turner, L. & Vahala, G. 1978 Three-dimensional magnetohydrodynamic turbulence in cylindrical geometry. *Phys. Fluids* **21**, 757.

Müller, W.-C. & Biskamp, D. 2000 Scaling properties of three-dimensional magnetohydrodynamic turbulence. *Phys. Rev. Lett.* **84**, 475.

Müller, W. C. & Grappin, R. 2004 The residual energy in freely decaying magnetohydrodynamic turbulence. *Plasma Phys. Control. Fusion* **46**, B91.

Müller, W. C. & Grappin, R. 2005 Spectral energy dynamics in magnetohydrodynamic turbulence. *Phys. Rev. Lett.* **95**, 114502.

Müller, W.-C., Malapaka, S. K. & Busse, A. 2012 Inverse cascade of magnetic helicity in magnetohydrodynamic turbulence. *Phys. Rev. E* **85**, 015302.

Nalewajko, K. 2018 Three-dimensional kinetic simulations of relativistic magnetostatic equilibria. *Mon. Not. R. Astron. Soc.* **481**, 4342.

Nalewajko, K., Zrake, J., Yuan, Y., East, W. E. & Blandford, R. D. 2016 Kinetic simulations of the lowest-order unstable mode of relativistic magnetostatic equilibria. *Astrophys. J.* **826**, 115.

Nazarenko, S. V. & Schekochihin, A. A. 2011 Critical balance in magnetohydrodynamic, rotating and stratified turbulence: towards a universal scaling conjecture. *J. Fluid Mech.* **677**, 134.

Neronov, A. & Vovk, I. 2010 Evidence for strong extragalactic magnetic fields from Fermi observations of TeV blazars. *Science* **328**, 73.

Ogilvie, G. I. & Proctor, M. R. E. 2003 On the relation between viscoelastic and magnetohydrodynamic flows and their instabilities. *J. Fluid Mech* **476**, 389.

Olesen, P. 1997 Inverse cascades and primordial magnetic fields. *Phys. Lett. B* **398**, 321.

Orszag, S. A. 1977 Lectures on the statistical theory of turbulence. In *Fluid Dynamics. Les Houches Summer School, 1973* (ed. R. Balian & J.-L. Peube), p. 235. Gordon and Breach, New York.

Oughton, S., Priest, E. R. & Matthaeus, W. H. 1994 The influence of a mean magnetic field on three-dimensional magnetohydrodynamic turbulence. *J. Fluid Mech.* **280**, 95.

Park, K. 2017 On the inverse transfer of (non-)helical magnetic energy in a decaying magnetohydrodynamic turbulence. *Mon. Not. R. Astron. Soc.* **472**, 1628.

Parker, E. N. 1957 Sweet's mechanism for merging magnetic fields in conducting fluids. *J. Geophys. Res.* **62**, 509.

Parra, F. I. 2019 Collisional plasma physics. *Lecture Notes for an Oxford MMath-Phys course.* `http://www-thphys.physics.ox.ac.uk/people/FelixParra/CollisionalPlasmaPhysics/CollisionalPlasmaPhysics.html`.

Perez, Jean Carlos & Boldyrev, Stanislav 2009 Role of cross-helicity in magnetohydrodynamic turbulence. *Phys. Rev. Lett.* **102**, 025003.

Qin, B., Salipante, P. F., Hudson, S. D. & Arratia, P. E. 2019 Upstream vortex and elastic wave in the viscoelastic flow around a confined cylinder. *J. Fluid Mech* **864**, R2.

Reppin, J. & Banerjee, R. 2017 Nonhelical turbulence and the inverse transfer of energy: a parameter study. *Phys. Rev. E* **96**, 053105.

Rincon, F. 2019 Dynamo theories. *J. Plasma Phys.* **85**, 205850401.

Riyopoulos, S., Bondeson, A. & Montgomery, D. 1982 Relaxation toward states of minimum energy in a compact torus. *Phys. Fluids* **25**, 107.

Ruzmaikin, A. & Akhmetiev, P. 1994 Topological invariants of magnetic fields, and the effect of reconnections. *Phys. Plasmas* **1**, 331.

Saffman, P. G. 1967 The large-scale structure of homogeneous turbulence. *J. Fluid Mech.* **27**, 581.

Schekochihin, A. A. 2020 MHD turbulence: a biased review, arXiv: 2010.00699.

Schekochihin, A. A., Cowley, S. C., Hammett, G. W., Maron, J. L. & McWilliams, J. C. 2002 A model of nonlinear evolution and saturation of the turbulent MHD dynamo. *New J. Phys.* **4**, 84.

Schekochihin, A. A., Cowley, S. C., Kulsrud, R. M., Hammett, G. W. & Sharma, P. 2005 Plasma instabilities and magnetic field growth in clusters of galaxies. *Astrophys. J.* **629**, 139.

Schekochihin, A. A., Cowley, S. C., Rincon, F. & Rosin, M. S. 2010 Magnetofluid dynamics of magnetized cosmic plasma: firehose and gyrothermal instabilities. *Mon. Not. R. Astron. Soc.* **405**, 291.

Schekochihin, A. A., Haynes, P. H. & Cowley, S. C. 2004 Diffusion of passive scalar in a finite-scale random flow. *Phys. Rev. E* **70**, 046304.

Schekochihin, A. A., Kawazura, Y. & Barnes, M. A. 2019 Constraints on ion versus electron heating by plasma turbulence at low beta. *J. Plasma Phys.* **85**, 905850303.

Schekochihin, A. A., Parker, J. T., Highcock, E. G., Dellar, P. J., Dorland, W. & Hammett, G. W. 2016 Phase mixing versus nonlinear advection in drift-kinetic plasma turbulence. *J. Plasma Phys.* **82**, 905820212.

Servidio, S., Matthaeus, W. H. & Dmitruk, P. 2008 Depression of nonlinearity in decaying isotropic MHD turbulence. *Phys. Rev. Lett.* **100**, 095005.

Son, D. T. 1999 Magnetohydrodynamics of the early Universe and the evolution of primordial magnetic fields. *Phys. Rev. D* **59**, 063008.

Spitzer, L. 1956 *Physics of Fully Ionized Gases*. Interscience Publishers.

Squire, J., Chandran, B. D. G. & Meyrand, R. 2020 In-situ switchback formation in the expanding solar wind. *Astrophys. J. Lett.* **891**, L2.

St-Onge, Denis A. & Kunz, Matthew W. 2018 Fluctuation dynamo in a collisionless, weakly magnetized plasma. *Astrophys. J. Lett.* **863**, L25.

Stawarz, J. E., Pouquet, A. & Brachet, M.-E. 2012 Long-time properties of magnetohydrodynamic turbulence and the role of symmetries. *Phys. Rev. E* **86**, 036307.

Stone, J. M., Ostriker, E. C. & Gammie, C. F. 1998 Dissipation in compressible magnetohydrodynamic turbulence. *Astrophys. J. Lett.* **508**, L99.

Strauss, H. R. 1976 Nonlinear, three-dimensional magnetohydrodynamics of noncircular tokamaks. *Phys. Fluids* **19**, 134.

Stribling, T. & Matthaeus, W. H. 1990 Statistical properties of ideal three-dimensional magnetohydrodynamics. *Phys. Fluids B* **2**, 1979.

Stribling, T. & Matthaeus, W. H. 1991 Relaxation processes in a low-order three-dimensional magnetohydrodynamics model. *Phys. Fluids B* **3**, 1848.

Subramanian, K. 2016 The origin, evolution and signatures of primordial magnetic fields. *Rep. Prog. Phys.* **79**, 076901.

Sur, S. 2019 Decaying turbulence and magnetic fields in galaxy clusters. *Mon. Not. R. Astron. Soc.* **488**, 3439.

Sweet, P. A. 1958 The neutral point theory of solar flares. In *Electromagnetic Phenomena in Cosmical Physics* (ed. B. Lehnert), , vol. 6, p. 123.

Taylor, A. M., Vovk, I. & Neronov, A. 2011 Extragalactic magnetic fields constraints from simultaneous GeV-TeV observations of blazars. *Astron. Astrophys.* **529**, A144.

Taylor, J. B. 1974 Relaxation of toroidal plasma and generation of reverse magnetic fields. *Phys. Rev. Lett.* **33**, 1139.

Taylor, J. B. 1986 Relaxation and magnetic reconnection in plasmas. *Rev. Mod. Phys.* **58**, 741.

Ting, A. C., Montgomery, D. & Matthaeus, W. H. 1986 Turbulent relaxation processes in magnetohydrodynamics. *Phys. Fluids* **29**, 3261.

Turok, Neil 1992 Electroweak bubbles: nucleation and growth. *Phys. Rev. Lett.* **68**, 1803.

Uzdensky, D. A., Loureiro, N. F. & Schekochihin, A. A. 2010 Fast magnetic reconnection in the plasmoid-dominated regime. *Phys. Rev. Lett.* **105**, 235002.

Vachaspati, T. 2001 Estimate of the primordial magnetic field helicity. *Phys. Rev. Lett.* **87**, 251302.

Vachaspati, T. 2021 Progress on cosmological magnetic fields. *Rep. Prog. Phys.* **84**, 074901.

Vekshtein, G. E. 1989 Magnetohydrodynamic stability of force-free magnetic fields in a rarefied plasma. *J. Exp. Theor. Phys.* **96**, 1263.

Vogt, C. & Ensslin, T. A. 2005 A Bayesian view on Faraday rotation maps — seeing the magnetic power spectra in galaxy clusters. *Astron. Astrophys.* **434**, 67.

von Kármán, T. & Howarth, L. 1938 On the statistical theory of isotropic turbulence. *Proc. R. Soc. Lond. A* **164**, 192.

Voslamber, D. & Callebaut, D. K. 1962 Stability of force-free magnetic fields. *Phys. Rev.* **128**, 2016.

Wagstaff, J. M. & Banerjee, R. 2016 Extragalactic magnetic fields unlikely generated at the electroweak phase transition. *J. Cosmol. Astropart. Phys.* **2016**, 002.

Wan, M., Oughton, S., Servidio, S. & Matthaeus, W. H. 2012 von Kármán self-preservation hypothesis for magnetohydrodynamic turbulence and its consequences for universality. *J. Fluid Mech.* **697**, 296.

Williams, P. T. 2004 Turbulent magnetohydrodynamic elasticity: Boussinesq-like approximations for steady shear. *New Astron.* **10**, 133.

Woltjer, L. 1958 A theorem on force-free magnetic fields. *Proc. Natl. Acad. Sci. U.S.A.* **44**, 489.

Woltjer, L. 1959 Hydromagnetic equilibrium II. Stability in the variational formulation. *Proc. Natl. Acad. Sci. U.S.A.* **45**, 769.

Yuan, Y., Nalewajko, K., Zrake, J., East, W. E. & Blandford, R. D. 2016 Kinetic study of radiation-reaction-limited particle acceleration during the relaxation of unstable force-free equilibria. *Astrophys. J.* **828**, 92.

Zel'dovich, Y. B., Ruzmaikin, A. A. & Sokoloff, D. D. 1983 *Magnetic Fields in Astrophysics*. Gordon and Breach.

Zhou, M., Bhat, P., Loureiro, N. F. & Uzdensky, D. A. 2019 Magnetic island merger as a mechanism for inverse magnetic energy transfer. *Phys. Rev. Res.* **1**, 012004.

Zhou, M., Loureiro, N. F. & Uzdensky, D. A. 2020 Multi-scale dynamics of magnetic flux tubes and inverse magnetic energy transfer. *J. Plasma Phys.* **86**, 535860401.

Zrake, J. 2014 Inverse cascade of nonhelical magnetic turbulence in a relativistic fluid. *Astrophys. J. Lett.* **794**, L26.

Zrake, J. & East, W. E. 2016 Freely decaying turbulence in force-free electrodynamics. *Astrophys. J.* **817**, 89.